UNIVERSITY OF SOUTHAMPTON
FACULTY OF PHYSICAL AND APPLIED SCIENCES
Optoelectronics Research Centre

Integrated Microlenses and Multimode Interference Devices for Microflow Cytometers

by

Hamish Cunha Hunt

Thesis for the degree of Doctor of Philosophy

December 2010

UNIVERSITY OF SOUTHAMPTON

ABSTRACT

FACULTY OF PHYSICAL AND APPLIED SCIENCES
OPTOELECTRONICS RESEARCH CENTRE

Doctor of Philosophy

INTEGRATED MICROLENSES AND MULTIMODE ITERFERENCE DEVICES FOR MICROFLOW CYTOMETERS

by Hamish Cunha Hunt

The convergence of microfabrication technologies, novel materials systems, and techniques for chemical and biochemical analysis is enabling the realisation of lab-on-a-chip technology. Products incorporating such technologies are expected to find widespread use, for example in personal medicine, food safety, water management and security. This research is driven by the demand for fast, low-cost, small, and automated chemical analysis using minimal sample and reagent volumes, in a multiplicity of applications including interrogation of individual particles such as biological cells or molecules by μflow cytometry.

Several promising optical detection methods are still in their infancy in terms of integration on to a single chip and improvements can be made to existing integrated methods. Manipulation of a free optical beam in microfluidic channels is identified as a major need to be able to realise more complex μflow cytometry detection systems. To achieve this, the integrated optics requires substantial advances. The approach in this thesis was to produce a microfluidic device with improved integrated optics, primarily for fluorescence and scattering particle detection, which can provide a platform from which to build more complex fully automated optical detection devices not yet realised. To manipulate the free beam, optical components such as waveguide lenses, both refractive and diffractive, were analytically designed and numerically simulated. An alternative device, the multimode interference device (MMI), which makes use of the self-imaging phenomenon in multimode waveguides, was also studied due to its less stringent fabrication tolerances. Optical components including channel waveguides, to route light on chip, were realised and integrated with microfluidic channels with a fabrication comprising a two-mask process developed in silica-based glass to integrate both optics and microfluidics on to a single chip. Spotsizes as low as 5.6 μm for paraxial kinoform lenses and 2.6 μm for MMIs have been measured at foci as far as 29.2 μm and 56.0 μm in a microfluidic channel. These devices pave the way to the full integration of more robust and complex microfluidic μflow cytometers.

To my family...

Contents

List of Figures

List of Tables

Declaration of Authorship

I, Hamish Cunha Hunt, declare that the thesis entitled 'Integrated Microlenses and Multimode Interference Devices for Microflow Cytometers' and the work presented in the thesis are both my own, and have been generated by me as the result of my own original research. I confirm that:

- this work was done wholly or mainly while in candidature for a research degree at this University;
- where any part of this thesis has previously been submitted for a degree or any other qualification at this University or any other institution, this has been clearly stated;
- where I have consulted the published work of others, this is always clearly attributed;
- where I have quoted from the work of others, the source is always given. With the exception of such quotations, this thesis is entirely my own work;
- I have acknowledged all main sources of help;
- where the thesis is based on work done by myself jointly with others, I have made clear exactly what was done by others and what I have contributed myself;
- parts of this work have been published as listed in the List of Publications.

Signed:

Hamish C. Hunt

15^{th} December 2010

List of Publications

H. C. Hunt and J. S. Wilkinson, "Microlenses for μflow cytometry," *Photon10*, Southampton, 23-26 Aug 2010.

W. Bolanos, J. J. Carvajal, X. Mateos, M. Aquilo, F. Diaz, G. S. Murugan, H. C. Hunt, A. Subramanian, J. S. Wilkinson, "Er-doped $KY_{1-x-y}Gd_xLu_y(WO_4)_2$ surface channel waveguides," *ECIO 2010*, Cambridge, 7-9 Apr 2010, ThP36.

C. Holmes, L. G. Carpenter, H. C. Hunt, J. C. Gates, "P. G. R. SmithMicrofluidic multimode interference device," *ECIO 2010*, Cambridge 7-9, Apr 2010.

H. C. Hunt and J. S. Wilkinson, "Integrated lenses for microfluidic systems," *MOC '09*,(15th Micro-optics Conference), Odaiba Japan, 25-28 Oct, 2009, J14.

H. C. Hunt and J. S. Wilkinson, "Optofluidic integration for microanalysis," *Microfluidics and Nanofluidics*, vol. 4, no. 1-2, pp. 53-79, 2008.

Acknowledgements

I would like to first and foremost thank my family for without their support I may not have pursued a doctorate. I also thank my supervisor, James Wilkinson, to whom I feel indebted for his guidance throughout my PhD. I wish to acknowledge my colleagues who have helped me during my project. I would like to thank Neil Session and Dave Sager for their invaluable help and advice in the cleanroom, Senthil Ganapathy, Ping Hua, Ananth Subramanian, Nicolas Perney for help and advice in the optical laboratory, Claudio Oton for help with prism coupling measurements, and Tim May-Smith for much advise on polishing glass, Michael Pollard for help with mask design, Edwin Weatherby and Simon Butler for making jigs and Owain Clark for help with ellipsometry measurements. I would also to like to acknowledge friends and colleges in and outside of the ORC who have helped me have the experience that I had throughput my PhD in Southampton.

Nomenclature

Symbols

A	Amplitude
A, B, C	Cauchy coefficients
a	Semi-major axis of hyperbola or ellipse
b	Semi-minor axis of hyperbola or ellipse
c	Speed of light in a vacuum
c_q	Diffraction order coefficients
c_v	Field excitation coefficients
D	Lens aperture
D_0	Spot diameter
d	Focal distance
d_q	Focal distances of diffracted order
$\mathbf{E}$	Electric field
E_x, E_y, E_z	Electric field components
E^x_{pq}, E^y_{pq}	Quasi-TE and quasi-TM modes
e	Eccentricity
F	F number
f_1	Length between channel waveguide and lens
f_2	Length between lens and microfluidic channel
$\mathbf{H}$	Magnetic field
H	Height of the microfluidic channel
H_x, H_y, H_z	Magnetic field components
h	Height of channel waveguide
h_m	Thickness of zone
I	Intensity
I_0	Peak intensity
i	Imaginary number
$\mathbf{K}$	Grating wavevector
k_0	Wavenumber in free space
k_x, k_y	Wavenumber in Marcatili's regions
L	Length of the grating

L	Length to image plane
L_C	Coupling loss
L_{MMI}	Length of MMI device
L_P	Propagation loss
L_T	Insertion loss
L_π	Beat length
M	Maximum number of zones
m	Zone number (of diffractive lens)
	Order of AWG grating
N	Number of images at plane
n	Refractive index distribution
	Refractive index contrast ratio
n_a	Refractive index of cladding
n_c, n_{co}	Refractive index of waveguide core
n_{ch}	Effective refractive index of channel waveguide
n_e, n_{cl}	Refractive index in the surrounding medium
n_{eff}	Effective refractive index
n_i	Refractive index of the incident medium
	Refractive index of region in Marcatili's method
n_p	Refractive index in the lens region
n_s	Refractive index of the substrate
n_t	Refractive index of the transmitting medium
n_{sl}	Effective refractive index of slab waveguide
n_w	Refractive index of water
P_i	Input light power
P_o	Output light power
Q	Q parameter
q	Diffraction order
R_p, R_s	Polarisation amplitudes
R_{sl}	Focal length of the slab region
$\mathbf{r}$	Ray vector
S	Spacing between the arrayed waveguides
s	Spacing between input or output waveguides
t	Transmission function
v	Mode number
W	Width of microfluidic channel
W_e	Effective mode width
W_{MMI}	Width of MMI
w	Width of channel waveguide
w_{eq}	Equivalent rectangular width
w_1	Top channel waveguide width

w_2	Bottom channel waveguide width
x, y, z	Spatial variables
x_m	Zone boundary position
z_c	Distance that the focus is in the microfluidic channel
z_R	Rayleigh range
$z(x)$	Kinoform profile
z_0	Shift of hyperbola or ellipse along z
α	Design mis-match ratio
β	Propagation constant
$\boldsymbol{\beta}_d$	Diffracted wavevector
$\boldsymbol{\beta}_i$	Incident wavevector
γ	Marcatili propagation constant
Δ	Ellipsometric phase difference
Δf	Frequency channel spacing
ΔL	Length difference between adjacent waveguides
Δn	Refractive index difference
$\Delta n(x)$	Grating index modulation
Δn_{max}	Maximum grating index difference
δ	Offset length
ζ	$\text{sgn}(1-n)$
η	Coupling efficiency
η_q	Diffraction efficiency
θ_i	Incidence angle
θ_{in}	Diverging angle into waveguide array
θ_d, θ_{diff}	Diffraction angle
θ_{lens}	Lens angle
θ_t	Transmittance angle
θ_{out}	Focussing angle out of waveguide array
κ, ξ, σ	Propagation constants of 2D waveguide
Λ	Grating period
λ	Actual effective wavelength (FZP)
	Actual input free-space wavelength (Paraxial kinoform)
λ_0	Wavelength in free space
λ_c	Central wavelength
λ_e	Effective wavelength (in design)
μ_0	Permeability in free space
ρ	Bragg grating coupling coefficient
Φ	Excited field distribution
ϕ	Phase change to a plane wave through the lens
	Mode field or excited field
ϕ, ψ	Phase offset of field distribution in 2D and 3D waveguides

Ψ	Arctangent of the ratio of polarisation amplitudes
ψ	Slant angle
$\omega(z)$	Spotsize along the propagation
ω	Angular frequency
ω_0	Spotsize at focus

Abbreviations

2D	Two dimensional
3D	Three dimensional
APD	Avalanche photodiode
ARROW	Anti-resonant reflecting optical waveguide
AWG	Arrayed waveguide grating
BNP	Brain natriuretic peptide
BPM	Beam propagation method
BSA	Bovine serum albumin
CCD	Charge-coupled device
CMOS	Complementary metal-oxide-semiconductor
CE	Capillary electrophoresis
DEP	Dielectrophoresis
DNA	Deoxyribonucleic acid
DRIE	Deep reactive ion etching
EB	Electron beam
EIM	Effective index method
FACS	Fluorescence-activated cell sorting
FASI	Field-amplified stacking injection fluorescene-5-isothiocyanate
FCCS	Fluorescence correlation spectroscopy
FCCS	Fluorescence cross-correlation spectroscopy
FDBPM	Finite difference beam propagation method
FDTD	Finite difference time domain
FFT	Fast Fourier transform
FFTBPM	Fast Fourier transform beam propagation method
FITC	Fluorescene-5-isothiocyanate
FP	Fabry-Perot
FRET	Fluorescence resonance energy transfer
FZP	Fresnel zone plate
GRIN	Gradient index
HSA	Human serum albumin

HSV	Herpes simplex virus
IPA	Isopropyl alcohol
IR	Infra-red
ITP	Isotachophoresis
LED	Light emitting diode
LIF	Laser induced fluorescence
LoC	Lab on a chip
LoD	Limit of detection
LTRS	Laser tweezer Raman spectroscopy
MEMS	Micro-electromechanical systems
MIP	Molecular imprinted polymer
MMI	Multimode interference (device)
MPA	Mode profile analyser
MZI	Mach-Zehnder interferometer
NA	Numerical aperture
OLED	Organic light emitting diode
PCR	Polymerase chain reaction
PDMS	Polydimethylsiloxane
PMMA	Polymethylmethacrylate
QD	Quantum dots
RF	Radio frequency
RIE	Reactive ion etching
SARS	Severe acute respiratory syndrome virus
SEB	Staphylococcal enterotoxin B
SEM	Scanning electron microscope
SERS	Surface enhanced Raman scattering
SERRS	Surface-enhanced resonance Raman
SNR	Signal-to-noise ratio
SPR	Surface plasmon resonance
TAMRA	Tetramethylrhodamine dye
TBC	Transparent boundary condition
TE	Transverse electric
TE	Transverse electromagnetic
TL	Thermal lens
TLM	Thermal lens microscope
TM	Transverse magnetic
TNT	Trinitrotoluene
UV	Ultraviolet
VCSEL	Vertical-cavity surface-emitting laser
YI	Young interferometer
ZE	Zone electrophoresis

μFACS	Micro-fluorescence-activated cell sorting
μTAS	Micro-total analysis systems

Chapter 1

Introduction

1.1 Integrated Optics and Microfluidics

Integrated optics has become a field of important technology, especially for optical telecommunications. It has scaled down bulk optical components allowing for signal processing to be performed on-chip to drive down costs and increase system functionality. Integrated optics allows the construction of optical circuits in or on planar substrates, guiding and processing light in dielectric thin films of elevated refractive index with structures defined using photolithography. Integrated optics has led to reducing light loss by having fewer optical interfaces, reducing the distances between components, and improving coupling and alignments between components. Since the components are fabricated on a single chip, there is an improvement to the temperature uniformity of the system and mechanical stability, meaning a decrease in variation in the optical properties (i.e. refractive index) of components resulting in increased optical stability and the reduction of noise.

Microfluidics is the study in behaviour of fluids at the microscale. It is also concerned with the design of systems in which such small volumes of fluids may be manipulated for various applications. Microfluidics technology has many foreseeable applications, particularly in chemistry and biology, which are now being realised. The structuring of such an integrated technology is in the micrometer scale to realise devices that control such small volumes of fluid. Basic structures, such as microfluidic channels (also known as microchannels or capillaries), can be fabricated allowing the controlled movement of fluid on the device. These capabilities have created the vision of lab-on-a-chip (LoC) technologies whereby microfluidics systems perform on-chip what is currently done in (bio)chemical laboratories, by exploiting denser integration of microfluidics [1].

There is much interest in combining the two fields and their technologies, which already share many of the microfabrication processes, as the major analysis methods for analytical chemistry and biochemistry are optical. In order to benefit from integration

both must be integrated on the same overall device, and thus substrate. Fabrication techniques for integrated optics have benefited much from those used in the microelectronics and micro-electro-mechanical systems (MEMS) fields. Until recently, most integrated optical circuits consisted of only one or two devices, but the field appears to be maturing with a drive for standardisation of materials, devices and interfaces, allowing much denser integration [2], and proposals for photonic circuit foundries which will allow "fab-less" researchers with design and measurement tools to access high-quality device fabrication.

1.2 Motivation

1.2.1 Optical Lab-on-a-Chip

This section will expand on the combining of integrated optics and microfluidics which some have termed "optofluidics" [3]. As its name suggests, LoC requires integration of many of the tools found in the (bio)chemistry laboratory. These may include the means for sample and reagent presentation such as channels, pumps and valves, chambers for mixing and reaction, heaters for reaction control, devices for trapping, separation and selection, devices for cell lysis, and for chemical analysis [4]. The convergence of microfabrication technologies, novel materials systems, and techniques for chemical and biochemical analysis is enabling the realisation of LoC or micro-total analysis system (μTAS) [5]. This research is driven by the demand for fast, low-cost, small, and automated chemical analysis using minimal sample and reagent volumes, in a multiplicity of applications [6], including interrogation of individual molecules [7]. The scale of integration, low cost and robustness of microfabrication approaches in microelectronics enabled the realisation of many modern devices: the mobile phone, hand-held computer and CCD camera, to name a few. It is often suggested that products incorporating LoC technology will find similarly widespread use, for example in personal medicine, food safety, water management and security. Cost and reliability for use by non-specialist personnel will be key issues in achieving this goal, which could advance personalised preventative medicine and public safety, and improve efficiency in food and water use.

The last decade has seen rapid growth in demonstrations of these functions in chips fabricated using either "hard lithography" in semiconductors or glass or "soft lithography" [8] in polymers such as PDMS. The former builds upon the functionality of silicon MEMS and the enormous infrastructure of the microelectronics industry and points to its example of cost reduction in complex electronic systems. The latter exploits the benefits of improved compatibility with biological systems and the simplicity of rapid prototyping in polymers. The emergence of preferred materials for the LoC will depend upon the degree to which components can be standardised and selected for integration to satisfy large-volume applications.

What can be achieved in LoC technology has been described in the literature for microfluidics [9] for cell manipulation and analysis [10, 11], biomolecule manipulation and analysis [12], μTAS [13–15], optical manipulation [16]. Optical approaches are the most widely used for chemical analysis in microsystems, as they have an excellent track-record in chemical analysis, usually show the lowest limits of detection [17] and provide the greatest chemical or morphological information on the species being analysed. Users of microfluidic systems for (bio)chemical analysis are familiar with conventional optical systems for chemical analysis. However, the majority of optical functions demonstrated in microfluidic systems use external micro-optical systems, or hybrid embedding of optical fibres, which, while providing much flexibility, do not offer the robustness, stability, operator-independence, and potential for mass manufacture of fully integrated approaches.

An inspiring visualisation from Balslev *et al.* [18] is shown in a photograph of the device in Figure 1.1. It is of a fully integrated microfluidic optical sensing system fabricated for use in analysis of particles in fluid flow. The device was monolithically microfabricated onto one substrate. The device boasts an on-chip dye laser which emits light at 576 nm, waveguides, microchannels, microfluidic passive diffusion mixers, and embedded photodiodes. Though this device was not fabricated with a specific application in mind, it has demonstrated how complex chips with microfluidic and optical components can be fully integrated. The design of such a device could be used to analyse the passing of particles that have been mixed on-chip. The particles would be analysed in the cuvette, by an array of waveguides irradiating light from the on-chip dye laser and collecting the fluorescence to the on-chip diodes to generate a direct electronic signal. Similar devices could be made for cell screening, drug screening, analysis of cellular function, analysis molecule interactions and reactions, or flow-cytometry. The confluence of integrated optics with microfluidics technology in the future of LoC shows great potential.

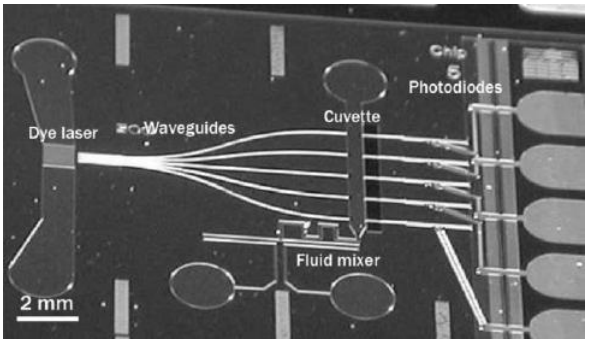

FIGURE 1.1: Balslev *et al.*'s [18] integrated chip with integrated dye laser, waveguides, cuvette, mixer, and photodiodes.

1.2.2 Micro-flow Cytometry

One major area that can benefit from integration is flow cytometry. It has been in use since the 1970s and is a technique for detecting, analysing, and sorting microscopic particles suspended in a stream of fluid. Conventional flow cytometers usually employ fluorescence activated cell sorting (FACS) systems which in a flow cytometer distinguishes between particles using chiefly fluorescence detection, but may also employ scattering to improve device analytical performance [19]. In fact, several optical quantities, such as fluorescence scattering and absorption, can be obtained from cells by irradiating light, and have the potential to be used for cell characterisation in these systems, as depicted in Figure 1.2(a). A typical detection process is illustrated in Figure 1.2(b). Cells in suspension are injected into a directed fluid stream forcing the cells to enter a small nozzle one at a time. The cells travel down the nozzle which is vibrated at an optimal frequency to produce drops at fixed distance from the nozzle. As the cells flow down the stream of liquid, they are irradiated by a laser and the fluorescence signal is acquired to identify the cell. Some of the laser light is scattered by the cells and this can be used to count the cells or to measure the size of the cells. An electrical charging ring is placed just at the point where the stream breaks into droplets. A charge is placed on the ring based on the immediately prior fluorescence intensity measurement (and maybe scattering information) and the opposite charge is trapped on the droplet as it breaks from the stream. The charged droplets then fall through an electrostatic deflection system that diverts droplets into containers based upon their charge.

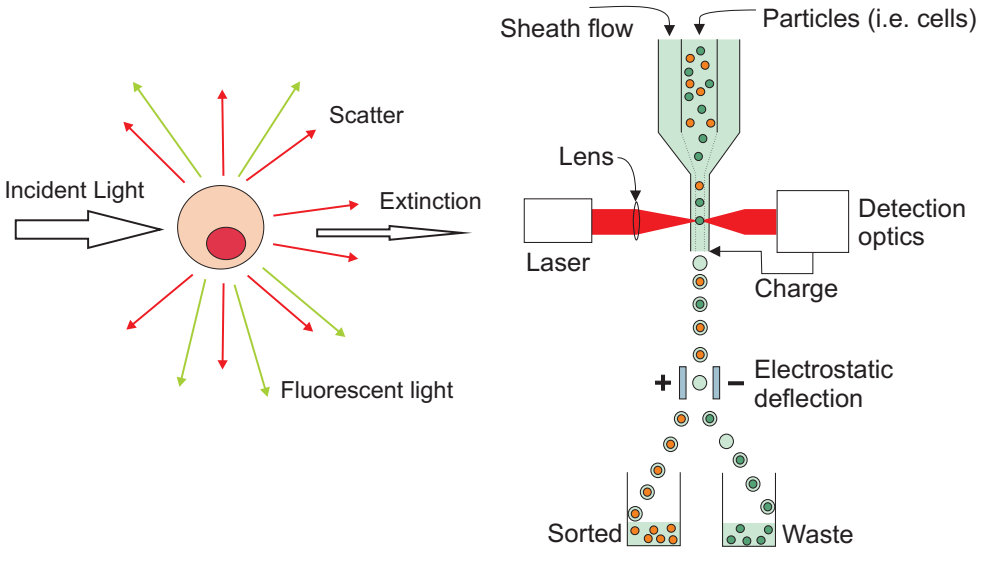

FIGURE 1.2: (a) Cell being irradiated by laser light. The cell's optical properties such as scattering, fluorescence, and extinction of light can be used to characterise it. (b) A bulk FACS system setup.

Flow cytometry can be used in the analysis and sorting or screening of cells [20]. Nowadays, the use of microfluidics and integrated optics is making it possible to realise a fully integrated system on a single chip [10], providing advantages over traditional flow cytometer systems which are bulky, costly, mechanically complex, and often require trained personnel for operation and maintenance. These "μflow" cytometry and "μFACS" systems offer advantages such as being less complex to use, thus being user friendly, cheaper to fabricate, more compact and robust. Developments have been underway in several research groups within the last 10 years [21–23]. In such systems manipulating individual cells with microfluidics will improve the ability to isolate rare cells for biologists, highlighted by Leary [24]. Toner and Irimia [25] studied how this LoC technology can be used to sort and manipulate cells in blood, commenting that if one could fabricate fully integrated cell sorters with the performance of their traditional bulk counterparts, these devices being smaller and cheaper, allowing one to have arrays of such devices splitting the incoming sample and processing it in parallel, thus increasing overall speed. As with electronics revolution, these devices will give an abstraction from the technology allowing researchers from other fields to do their research quicker by not being hindered of having to fully understand the technology they use.

1.3 Integrated Optics for μFlow Cytometers

This work has set out to improve the integrated optics in microfluidics devices used for microanalysis, specifically, in a μflow cytometer device. For such a device, the goal of how much integration is to be done is considered first. The integrated devices incorporating microfluidics and optics onto a single chip for detection can be split into subsystems. Due to time constraints, the project concentrated on the most crucial subsystems for analysis of microparticles only. The subsystem to be developed was for beam control, that is how the input light is delivered into the detection and analysis volume of a microfluidic channel. The importance of this in microanalysis in fluorescence techniques is that controlling spotsize, which defines the sample volume (or excitation volume), can reduce background signal and improve signal-to-noise ratio (SNR), improving sensitivity [26]. This is also the case not only for fluorescence, but scattering. Systems will struggle to detect smaller particles due to their scattering signals being too weak from such large beam dimensions [27].

Figure 1.3 shows the concept diagram of an integrated device that would focus a light beam into the middle of a microfluidic channel to have been realised in this work. The microfluidic channel depicted is the cross shape for hydrodynamic focussing. The waveguides can be used for inputting and guiding light on the chip. The optical function on the diagram corresponding to the function of an integrated optical device which is responsible for manipulating the light so as to focus it into the middle of a microfluidic channel. Solutions for integrated optics devices that can focus the light are described in

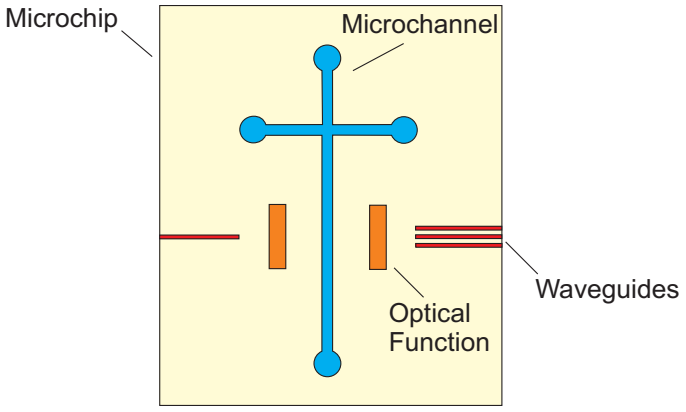

FIGURE 1.3: A microfluidics system with integrated waveguides for input and output and integrated optical devices providing optical function.

the thesis include: lenses, arrayed waveguide gratings (AWG), and multimode interference (MMI) devices. The optical functions appear on both sides as they are aimed to provide a collection subsystem on the output side. This system is required to be flexible primarily for doing fluorescent and scattering measurements of particles in the microfluidic channel and then, with little modification if any, to use for other optical techniques for particle detection and manipulation discussed in Chapter 2; some of which have had little or no optical integration at time of writing.

From the concept chip presented, the beam control by integrated optics and the microfluidic channel were realised in a SiO_2-based system; to make that transition, several steps had to be made. The project was started by reviewing the methods and phenomena used for optical detection for particles and the current level of integration of such methods to know what is required for a flexible system. The basic building block of most integrated optics is the waveguide, thus there was a study of a simple waveguide system with singlemode behaviour simulated. Singlemode behaviour allows for more complex devices to be added and focussing devices is the prime requirement in this work, so planar integrated lenses were studied and designs simulated. A paraxial kinoform lens was found by simulation to be most efficient to fabricate. Working at the microscale provides practical use of other phenomena, so AWGs and MMIs were considered and MMIs designs after simulations were fabricated. The studies of devices were done simultaneously with the development of the fabrication process. The designed paraxial kinoform lenses and MMIs were fabricated in a flexible two-mask photolithographic process. Realised devices were characterised and the chips using lenses and MMIs are able to focus light to a small spotsize further into the channel than a channel waveguide can, allowing for large improvements in optical detection systems and the higher integration of other methods with currently little integration or no integration form time of writing. The structure of the thesis detailing the work done is given in the next section.

1.4 Structure of Thesis

The thesis is structured as follows:

Chapter 1, this chapter, has introduced the use of integrated optics for microfluidics and given the motivation behind higher integration of optics for LoC, and specifically microanalysis of particles in μflow cytometer systems.

Chapter 2 is a review on the current state-of-the-art methods of optical detection in microfluidic devices and the level of current integration in such systems.

Chapter 3 presents a summary of planar waveguide theory, the mathematical tools used for waveguide design, and simulates the singlemode channel waveguides used to bring light to the microfluidic channel.

Chapter 4 gives a detailed theoretical description of the planar waveguide lenses to manipulate the excitation light to focus into the middle of a microfluidic channel and to improve collection of signal light. The analytical designs are outlined and candidate designs are justified and simulated for comparison in performance.

Chapter 5 introduces two alternative devices to lenses using other phenomena available at the microscale. The AWG and MMI devices, used in integrated optics, and how they can be designed as an alternative to using planar waveguide lenses to focus light into the middle of a microfluidic channel. MMIs were judged to be practical to fabricate at the wavelength required and to lower tolerances and designs were simulated.

Chapter 6 describes the establishment of a flexible two-mask fabrication process for planar devices integrated with optics and microfluidics on the same chip using GeO_2:SiO_2 waveguides.

Chapter 7 presents the characterisation results of the realised channel waveguides insertion, propagation losses, mode profiles and spotsizes. These are followed by characterisation results of the realised paraxial kinoform lenses and MMIs, images showing functioning devices focussing in the slab region and in the microfluidic channel and the Gaussian beam properties given.

Chapter 8 summarizes the conclusions of this work and proposes future advances based upon the work presented in the thesis.

Chapter 2

Optical Detection in Microfluidic Systems

2.1 Introduction

Detection and analysis of chemical and biochemical species in microfluidic systems is challenging due to short optical path-lengths, small sample volumes, and the need to analyse individual particles or molecules. For the LoC to fulfil its potential in terms of parallelism and throughput, high-speed, multiparameter and multiplexed detection is required, creating heightened demand for low noise, high specificity, miniaturization and ruggedness. Conventional optical techniques for macro-analysis such as fluorescence, absorption, and chemiluminescence have been applied to microfluidic systems, and good reviews have been published on optical detection methods for microfluidic devices [28, 29]. Less common methods for optical detection in microfluidic devices, such as Raman spectroscopy, are reviewed by [30]. The majority of optical detection systems in microfluidics address flow cytometry or capillary electrophoresis (CE). In common with demonstrations of optical trapping and propulsion in microsystems, most detection systems rely upon rather complex bulk optical systems external to the microchannel, such as confocal microscopes, or hybrid integration by embedding optical fibres, rather than the full on-chip integration of optical functions likely to be required for highly-functional integrated systems [7]. While the majority of demonstrations use optical transmission directly through the microfluidic channel, a few exploit evanescent field configurations where heterogeneous detection at a surface is carried out, exploiting the rapid diffusion to surfaces which occurs in thin laminar flow channels. There are undoubtedly some challenges in applying evanescent sensing techniques, and integrated optical waveguides [31], to microfluidic systems, such as the robustness and reversibility of chemically-specific films and surface fouling, but biosensor research and microfluidics research appear artificially distinct at present. This section reviews optical detection

schemes for chemical analysis in microfluidic systems, divided according to the principal optical phenomena employed: scattering, absorption, refractive index, fluorescence, Raman spectroscopy, and thermal lensing. This review is limited to microfluidic systems, but there are many sophisticated optical systems which have been applied to biosensing and chemical analysis which use less advanced fluidics, but which have potential for future incorporation in the lab-on-the-chip.

2.2 Scattering

Light scattering techniques applied to collections of particles, such as turbidimetry, are well established, but microfluidics enables scattering measurements to be made on individual particles of size comparable with the wavelength, with high throughput. Scattering is probably the simplest method for cell counting in a microchannel, but can be extended to yield information on cell size, shape and internal and external structure according to the angular scattering spectrum, and is commonly combined with fluorescence measurements to yield chemically-specific information. This is a natural extension of traditional bulk flow cytometry systems where scattering may be employed to increase detection reliability and the resolvability of fluorescent signals. Laser light is focussed on a detection volume and the scattering caused by a refractive index contrast between the particle entering that volume and the surrounding fluid allows detection of particles. Large angle scattering can give information on a particle's surface roughness and internal structures; whilst small angle or forward scattering can yield information of a particle's size. Scattering is surprisingly underutilised in microfluidic devices, perhaps due to the fact that most implementations are dependant on alignment of bulk external optics at the necessary angles.

Nevertheless, miniaturisations of flow cytometers using microfluidics have been developed, taking advantage of light scattering from particles. Schrum *et al.* [32] used scattering from fluorescently-labelled 2 μm diameter and unlabelled 1 μm diameter polystyrene latex particles to demonstrate flow cytometry in a microfluidic device, distinguishing them through fluorescence and size, and counting them at a rate of 13.5 Hz, using radiation from an Ar ion laser. Subsequently, McClain *et al.* [33] extended this work to perform flow cytometry on fluorescently-labelled *E. coli* at a rate of up to 85 Hz, observing marginally better particle resolution using scattering. Witek *et al.* [34] studied electromigration of *E. coli* and red blood cells in polymer microflow channels, using backscatter from focussed light from a 680 nm laser diode to monitor cell transport.

Pamme *et al.* [27] analysed polystyrene microspheres of diameters between 1 μm and 9 μm in a microflow channel using scattering alone from incident light at a wavelength of 633 nm. Optical fibres to collect scattering were fixed externally on top of the microfluidic device at 15° and 45° to the incident light beam, as shown in Figure 2.1. While

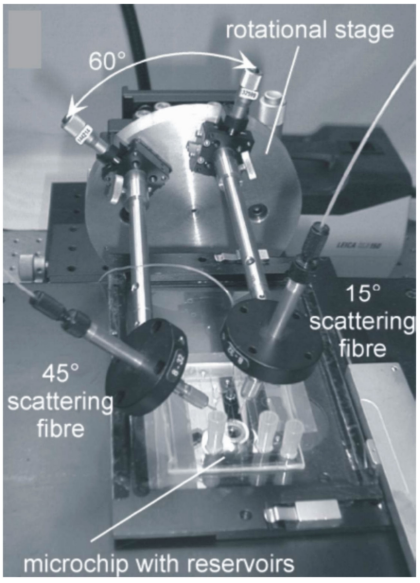

FIGURE 2.1: Photograph of the microfluidic particle scattering apparatus; two optical fibres were mounted above the microchip for scattering detection. Taken from [27].

particles between 3 and 9 μm diameter were readily distinguished at throughputs of order 150 Hz, the lower scattering intensities from smaller particles reduced the signal-to-noise ratio (SNR) to the point where 1 μm and 2 μm particles could not be reliably distinguished. The same group then analysed magnetic particles of diameter 2.8 μm and 4.5 μm under magnetophoretic separation. Similar apparatus was used as before but with scatter collection angles of 25° and 35° to the incident light [35].

Wang *et al.* [36] incorporated optical waveguides aligned photolithographically across the flow channel to perform scattering measurements on polystyrene microspheres of diameters 2.8 μm, 4.6 μm, 5.8 μm and 9.1 μm, avoiding the need for optical alignment and improving mechanical stability of the device. An integrated microlens was used to control the beam shape of incident light being delivered to the microchannel, and optical fibres were connected at the input and outputs. The channel, waveguides and lens were realised in a single SU-8 photoresist processing step. Measurements of forward scattering were made by collection in an output waveguide at an angle of 5°, and the particles of different size were clearly distinguished. The design allowed for optical extinction and large-angle scattering to be measured, but this was not discussed in detail. Incorporating this approach in a dielectrophoresis structure the authors were subsequently able to separate and count viable and non viable yeast cells [37]. Integration of further components close to the scattering particles may be expected to yield more detailed information on cells.

2.3 Absorption Detection

Detection through optical absorption is common in chemical analysis, employing either direct absorption in the UV/visible wavelength range or a colorimetric assay, for example. Its simplicity, and the lack of need for chemical derivitisations for fluorescent tagging, has led to it being the most widely used detection technique in conventional microseparations. However, the short optical path length inherent in miniaturization of fluidic channels leads to weak optical absorption competing with a high background transmission, and consequent difficulty in achieving low detection limits. This has been addressed in conventional capillary systems using Z-shaped and U-shaped channels (e.g. [38]) with longitudinal transmission. The problem becomes more severe in on-chip systems, and several approaches to increasing the absorption have been demonstrated, such as liquid-core waveguiding, multipass configurations, hollow prism cells, integrated waveguides and slow light. Detection limit depends upon good stability and reduced noise as much as increased sensitivity, rendering waveguiding approaches attractive.

To enhance absorption in microfluidic devices, Liang *et al.* [40] microfabricated a planar U-shaped absorption cell, with the base of the U placed between excitation and collection fibres in photolithographically-defined channels, and achieved a 10-fold increase in absorbance, using a path length of 140 μm compared with transverse measurement through the 20 μm depth of the channel. Mogensen *et al.* [41] integrated planar channel waveguides into a U-channel design for the coupling of light into the detection region, to overcome alignment issues observed with optical fibres, and used a larger optical path length of 750 μm, increasing this to 1000 μm in a subsequent polymer device [42]. They further increased this to an effective optical path length of 1.2 mm using novel pure silica integrated waveguides shown in Figure 2.2 [39]; using absorbance at a wavelength of 254 nm a detection limit of 3 μg mL^{-1} was achieved for paracetamol, and electrophoretic

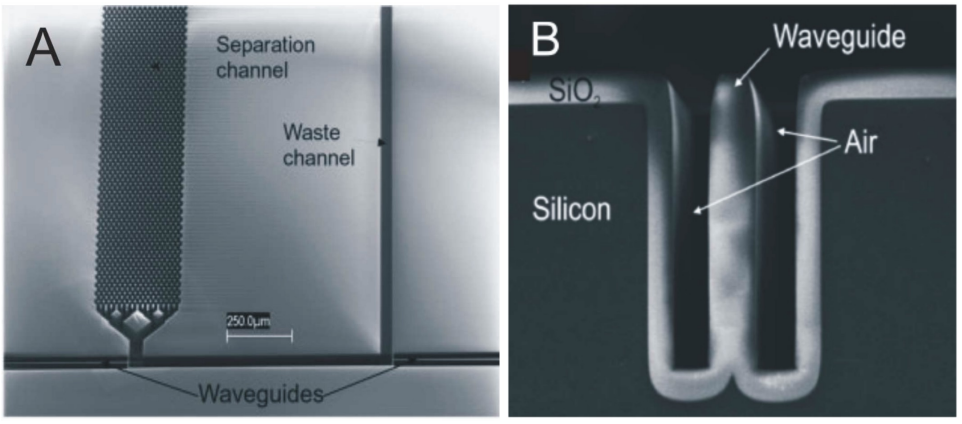

FIGURE 2.2: (a) Scanning electron micrograph of the detection region of U-channel absorption device after etching and oxidation (top view) (b) Stripe of SiO2 that acts as a waveguide. Taken from [39].

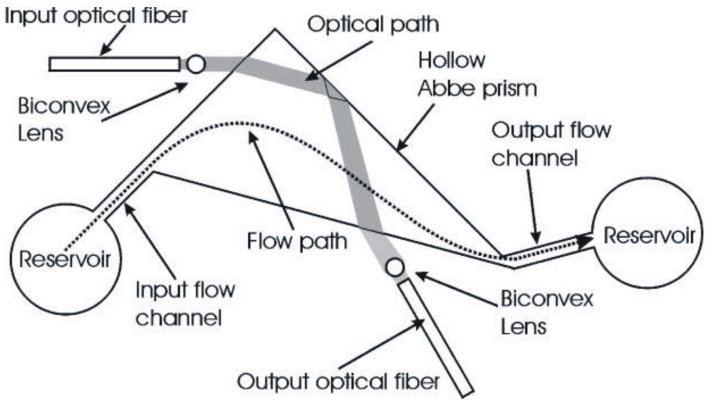

FIGURE 2.3: Schematic of the system for detection with a hollow Abbe prism. Taken from [50].

separation allowed caffeine, paracetamol, and ketoprofone to be distinguished. Launching and collecting light across long path-length channels has also been achieved using total internal reflection from micromachined V-grooves placed either side of the fluidic channel [43] and used for a glucose assay on whole blood, where a limit of detection (LoD) of 200 μM was achieved.

Salimi-Moosavi *et al.* [44] reported a multi-reflection cell, achieving five to ten-fold enhancements of optical path lengths. Mortensen and Xiao [45] have recently modeled the use of slow light structures for optical path-length enhancement. Periodic structures such as liquid-infiltrated photonic crystals could be incorporated within a flow channel and potentially yield large enhancements particularly near the band edges. Duggan *et al.* [46] achieved an optical path length of 5 mm by using a Teflon fluoropolymer capillary as both the flow channel and a liquid-core waveguide, and Teflon AF coated waveguiding microflow channels in silicon have also been realised [47]. However, extending the physical path-length along the direction of flow also degrades the spatial resolution of species in capillary separation systems, resulting in a trade-off between enhancement and resolution. Performance of absorbance based measurements can also be improved by incorporating additional on-chip optical components, such as microlenses and micro-apertures, to reduce in stray light and hence increase the effective optical path length [48]. Zhu *et al.* [49] improved collection efficiency by incorporating bare silicon detectors within the PDMS fluidic chip and reported a LoD for bovine serum albumin of 1 μg mL^{-1} with channels of 60 to 400 μm depth. Llobera and co-workers developed monolithically integrated hollow prism microchannels combined with optical components in a single-step PDMS microfabrication process [50, 51]. The device, shown schematically in Figure 2.3, consisted of channels to embed input and output fibres and cylindrical biconvex microlenses to collimate the light, pass it through the hollow prism filled with analyte, reflecting from a prism wall to enhance path-length, and refocus it on the output fibre. LoDs of 1.83 μM and 0.683 μM were achieved for fluorescein and methyl orange respectively, and pH measurements performed using methyl orange.

An alternative approach to overcoming the low UV absorptions obtained in microchannel separations due to the short optical path-length is to preconcentrate the sample. Isotachophoretic (ITP) preconcentration has been combined with zone electrophoresis (ZE) to lower the LoD on detection of two flavonoids down to 1.2 μg mL^{-1} and 0.2 μg mL^{-1} [52], a 32-fold enhancement compared with zone electrophoresis alone.

Jiang and Pau [53] fabricated an SU-8 rib waveguide in a PDMS microchannel with a spiral geometry resulting in a length of 110 mm within a chip area of 4 cm^2. The fluid to be sensed acts as a cladding and its spectroscopic properties are probed using the evanescent field. Hu *et al.* [54] realised a chalcogenide glass waveguide in a PDMS microchannel, in principle allowing transmission and evanescent absorption spectroscopy at mid-IR wavelengths. Special waveguide designs can achieve higher sensitivity for evanescent detection than "free-space" designs of the same physical path length [55], rendering them potentially attractive in on-chip labs.

2.4 Fluorescence Detection

Fluorescence techniques are by far the most commonly used for optical detection in microfluidic devices, having the prime advantage that the signal is usually readily separable from the scattered incident light. Compared to other detection techniques, fluorescence delivers high sensitivity, allowing detection of single molecules as reviewed by Dittrich and Manz [14], and has gained wide acceptance in conventional bulk instruments. In some cases, the autofluorescence of species (molecules, viruses, cells, *etc*) may be detected; otherwise a fluorophore or quantum dot must be attached to act as a tag to be detected. Tagging has the disadvantage that additional sample preparation must be carried out, but usually yields lower fluorescent background and improved confidence in the measurement. Due to the vast literature on this topic, in this section only work published within the last five years will be discussed to highlight the most recent advances in applications of fluorescence in microfluidic systems.

A wide variety of light sources are used for excitation, including lasers, LEDs and lamps. Lasers and laser-induced fluorescence (LIF) are most commonly employed in microfluidics, due to diffraction-limited focussing and the potential for 2-photon excitation. The increasing range of wavelengths, continually reducing cost due to use in consumer electronics, good stability, ease of switching, and low power requirements when using semiconductor lasers reinforce this trend. Longer wavelength fluorophores (600 nm $< \lambda_{abs} <$ 800 nm) tend to be gaining ground due to the reduced background fluorescence and wider availability of high-quality compact optical components at these wavelengths.

Recent research has emphasised electrokinetic methods for concentrating species to be detected, thereby improving LoD, with most using conventional external optical apparatus such as confocal microscopes. It has been shown that field-amplified stacking

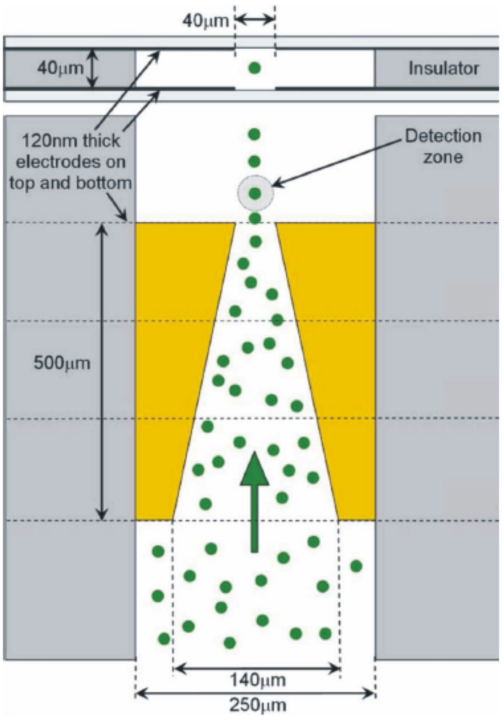

FIGURE 2.4: Schematic diagram of flow cytometer chip, showing the four focussing electrodes in top-down and cross-sectional views and the position of the optical detection zone and how the particles are focussed into this region by the electrodes. Taken from [56].

injection (FASI) in microfluidic capillary electrophoresis devices can increase sensitivity of detection of fluorescent dyes [57]. Using a microfluidic chip with several channel networks, detection of immunoassays of insulin secretions from multiple independent pancreatic islets can be continuously monitored with an LoD of 10 nM [58]. Sun and Yin [59] reported a multi-depth microfluidic device for single cell analysis. Human carcinoma cells which tend to aggregate and settle were separated using this device and the cell constituents separated by CE and analysed using LIF. Flow cytometry is an important function to benefit from microfluidics technology, with many continuous-flow microfluidic devices demonstrating fluorescent-activated cell sorting (μFACS). Morgan and co-workers [56, 60] reported devices that used dielectrophoresis (DEP) to focus particles in a microchannel stream. Figure 2.4 shows a micro flow cytometer chip which focused particles in both the vertical and horizontal dimensions and detected 6 μm diameter fluorescent latex particles. Using careful optimisation of the excitation intensity to limit fluorophore saturation, Jung *et al.* [61] obtained an extremely low LoD of 100 aM, and single molecule detection, of Alexa Fluor 488 by LIF in a CE chip flow with isotachophoretic separation. Hydrodynamic focussing has also been applied in microfluidic systems with fluorescence detection. Yang *et al.* [62] realised a portable system incorporating a microfluidic device with hydrodynamic focussing and on-chip pumping and applied it to detection and sorting of fluorescent dye-labelled human lung cancer cells,

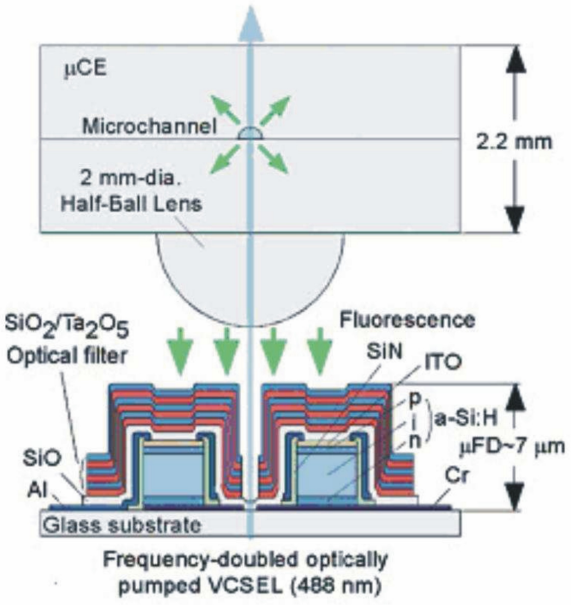

FIGURE 2.5: Cross-sectional view of the fluorescence detection platform on which a capillary electrophoresis chip is mounted. Laser light is introduced from below through an aperture. Taken from [64].

with a count rate of 120 min^{-1} and an error rate better than 2%. Simonnet and Groisman [63] created high-throughput flow cytometers (17,000 s^{-1}) in molded PDMS with 3D hydrodynamic focussing, and applied them to tagged yeast cells. Kamei and Wada [64] built upon earlier work [65] demonstrating microfluidic separation of biomolecules, and realised a detection platform shown in Figure 2.5, which included a 2 mm diameter half-ball lens for fluorescence collection, a microstructured interference filter deposited directly on a pin photodiode, and an aperture through the centre of the detector and filter via which excitation light from a 488 nm frequency-doubled vertical-cavity surface-emitting laser (VCSEL) was introduced. A planar microfluidic CE device was placed in contact with the half-ball lens, exciting fluorescein in the microchannel and allowing fluorescence to be collimated, filtered and collected. The device achieved an LoD of 7 nM fluorescein and was used to demonstrate the separation and detection of HaeIII digest of øX174 bacteriophage DNA. Breakthrough of scattered excitation light is often the limiting factor in performance of fluorescence-based systems. Fu *et al.* [66] performed a detailed study of the directionality of scattered excitation light and fluorescence which enabled maximization of the fluorescent to scattered power ratio by selecting the fluorescence collection angle. Excitation light was incident orthogonally to the microfluidic substrate and collected in the plane of the substrate from the chip sidewall, as shown in Figure 2.6, with angles of 45° and 135° to the flow-channel exhibiting the best performance. An LoD of 1.1 pM fluorescein was achieved, and the device demonstrated CE of tagged arginine and phenylalanine.

Waveguiding structures have been exploited for fluorescence-based detection in microfluidic systems. Mazurczyk *et al.* [67] realised ion-exchanged waveguides in soda-lime glass

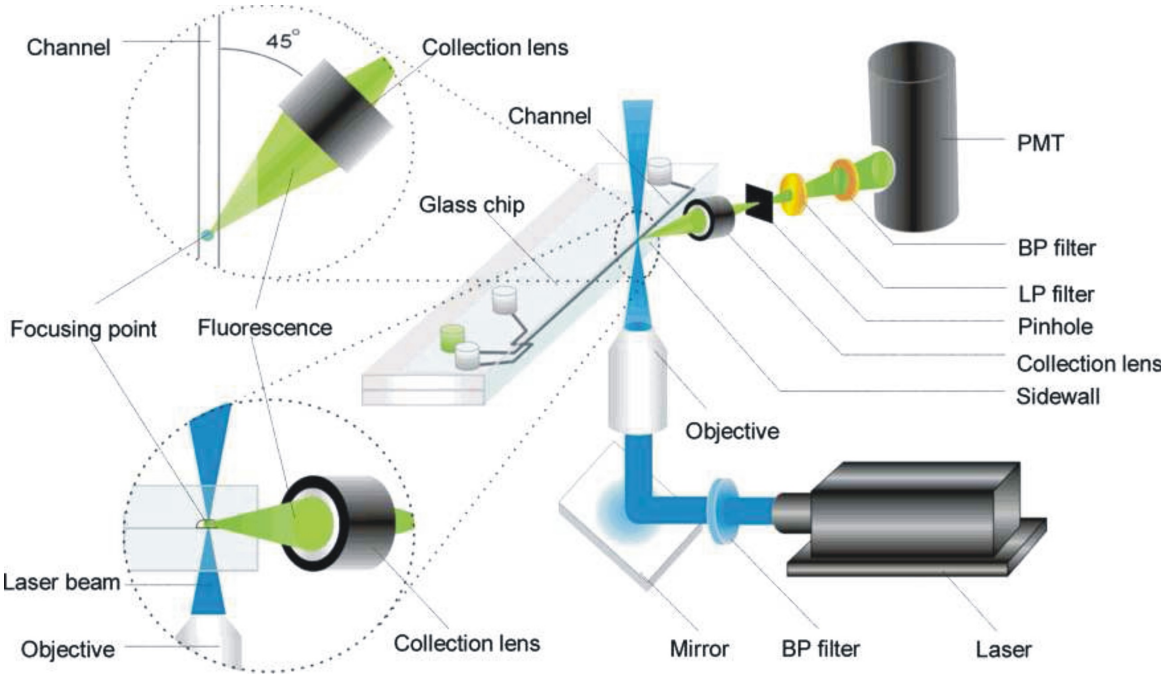

FIGURE 2.6: Schematic diagram of angle-resolved fluorescence detection apparatus. Taken from [66].

integrated with etched microfluidic channels and used fibre-coupled laser light at 532 nm for excitation of the Cy3 dye. Collection was carried out orthogonally from the top of the chip using a lens or bonded fibre, achieving an LoD as low as 0.5 nM Cy3, and collinearly in a waveguide on the opposite side of the channel, achieving an LoD of 1 μM Cy3. The orthogonal configuration was then used to demonstrate CE of Cy3 and Cy3-tagged streptavidin. Bernini *et al.* [68] used antiresonant reflecting optical waveguide (ARROW) structures to realise microfluidic channels that guided excitation light in the liquid, an alternative approach to the Teflon-clad waveguides described above. Although the liquid core has a lower refractive index than the surrounding media, the dual-layer cladding forms a high reflectivity mirror, which traps the light without invoking total internal reflection. Laser light was coupled into the flow channel via a fibre inserted into the hydrodynamically focused sample stream and two detector fibres were inserted in microchannels perpendicular to the main channel to capture fluorescent light from passing particles. The system was tested with human T leukaemia cells with diameters of about 20 μm.

The rapid, low-cost, detection of bacteria in food and drink is an important application for micro flow cytometry. Small numbers of *pseudomonas* cells in milk [69] and *E. coli* in buffer [70] were detected using fluorescence microscopy following attachment of fluorescent dyes. A more portable PDMS immunoassay system that detects the *E. coli* O157:H7 bacterial antigen with an LoD of 0.3 ng μL^{-1} has been reported [71]. A laser diode and optical fibre-based fluorescence excitation and collection module was employed, with the distal end of the multimode fibre placed against the bottom side of the thin glass fluidic

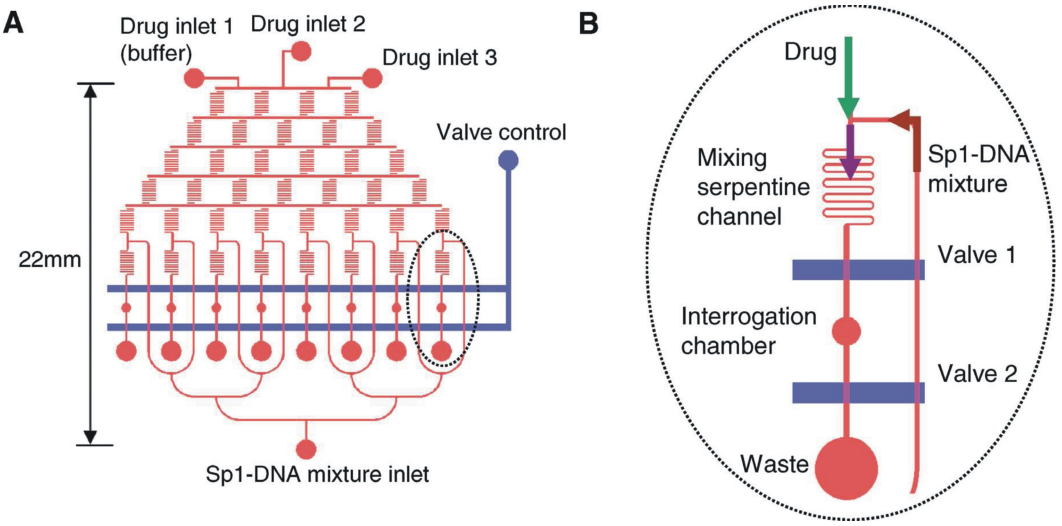

FIGURE 2.7: The PDMS-based microfluidic chip used for investigation of the dissociation of Sp1-DNA complex by DOX. (a) The layout of microchannels (red) and the mechanical on-off valves (blue). (b) A zoom-in of the mixing portion on the microfluidic chip. Taken from [73].

substrate. Li *et al.* [72] employed an optical fibre embedded in an etched channel in the substrate and a blue (470 nm) laser diode for detection of fluorescene-5-isothiocyanate (FITC)-tagged neurotransmitters dopamine and epinephrine in a micro CE chip.

Fluorescence correlation spectroscopy (FCS) is a powerful technique for the determination of the physical properties of small numbers of fluorescent or dye-tagged molecules. To ensure that only small numbers of molecules are studied at one time, the excitation volume is minimised by focussing to a small volume and using confocal detection. A correlation analysis of the temporal fluorescence fluctuations of particles entering the optical detection volume yields information on the diffusion characteristics and other physical properties of the molecules under study. Yeh *et al.* [73] assembled an FCS system with a complex PDMS microfluidic network, consisting of on-chip serpentine channels for mixing, interrogation chambers, reservoirs and valves, as shown in Figure 2.7. In a single flow-chip, the drug doxorubicin was mixed to produce eight parallel streams of different concentration; each stream was then mixed with a complex of DNA with transcription factor Sp1, and incubated in eight parallel interrogation chambers. Sp1-DNA dissociation was then determined by FCS, exploiting the different diffusion kinetics of differently-sized entities to determine the fractions of bound and unbound DNA. The resultant dose-response titration curve yielded the Sp1-DNA binding inhibition versus drug concentration. Rapid detection of low numbers of viruses for medical diagnostics is an important field of application of microfluidics. Zhang *et al.* [74] detected dengue virus with fluorescence crosscorrelation spectroscopy (FCCS), using dengue-specific antibody in a PDMS microfluidic array structure. The virus and antibody were fluorescently labelled with two different fluorophores, excited at 488 nm and 633 nm, and the emission separated by a dichroic filter onto two avalanche photodiodes (APDs). Viruses bound

to antibodies entering the detection volume exhibited positively cross-correlated fluorescence signals due to their motion being coupled. This study suggests that detection of a single virus is achievable with this system. Hollars *et al.* [75] also performed a cross-correlation of two fluorescence labelled probes excited and emitting at different wavelengths, in a flowing system. In this case total internal reflection was used to excite the dye-tagged analyte in an evanescent field in the microchannel. Short non-amplified DNA sequences were measured to sub 100 pM levels in less than one minute.

Advances have also been made in systems employing conventional lamps, which allow great flexibility in excitation wavelength by using wavelength filters, but generally show poorer limits of detection. Yan *et al.* [76] used an Hg-lamp with excitation wavelengths from 300 nm to 600 nm and a carefully engineered detection system with a microfluidic CE chip to achieve an LoD for FITC of 7×10^{-10} M and for FITC-tagged cystine of 9.6 nM. Götz and Karst [77] used a xenon arc lamp as an excitation source combined with a spectrograph and CCD, providing more detailed information through the complete emission spectrum in the visible wavelength range (350-800 nm). Three rhodamine dyes were used to characterise the system, applied to a standard microfluidic chip performing CE for separation of analytes. Peaks in the elution spectra could be assigned to different pure analytes and unexpected impurities were detected both by CE separation and within an elution peak using spectral information. Using similar apparatus the group were then able to detect thiols found in cosmetics with an LoD of 2 μM [78] and taurine found in drinks with concentrations as low as 60 aM [79]. Mitra *et al.* [80] fabricated a microdischarge device stacked on top of a microfluidic device as an alternative excitation light source producing emission in the UV for intrinsic fluorescence excitation. The microdischarge is created in an air gap between a metal anode and saturated salt solution in a reservoir acting as a cathode.

Light-emitting diodes (LEDs) are attractive sources for microfluidic measurements as they are cheap, compact, and efficient and may have higher brightness than conventional lamps. Destandau *et al.* [81] have reported a simple Y-shaped microfluidic channel and a simple LED and PMT detecting potassium with a LoD of 0.5 mM using calyx-bodipy dye, which has fluorescence intensity sensitive to potassium concentration. Kim *et al.* [82] realised a highly integrated fluorescent microfluidic detection chip comprising the microfluidic channels, silicon detector with interference filter, and an integrated organic LED (OLED) deposited directly on to glass as a thin-film structure. The microchannels were etched in glass with dimensions 70 μm width and 20 μm depth, and the OLED, emitting at 530 nm, was deposited on the reverse of the substrate. A p-i-n photodiode with a deposited interference filter were buried in PDMS which was then bonded to the glass microchannel. The device was characterised using tetramethylrhodamine dye (TAMRA) and achieved an LoD of 10 μM. Hofmann *et al.* [83] realised microchannels in a PDMS slab which had been doped with lysochrome dye and acted as a high-quality filter itself. One millimetre thick samples doped with 1200 μg mL^{-1} Sudan II, for

example, showed $< 0.01\%$ transmission at 500 nm and $> 80\%$ transmission above 570 nm. Irawan *et al.* [84] realised microchannels for use as fluorescence detection cells in PMMA optical fibre and plastic clad silica optical fibre by laser ablation. Microchannels of dimension 100 μm width by 210 μm depth were etched into the fibre cores and fluorescein, excited by a blue LED (centre wavelength at 470 nm), measured with an LoD of 5 ng L^{-1}.

Protein and DNA detection and manipulation are major fields of application in microfluidic systems due to the benefits of rapidity, flow control and small sample and reagent volumes at these scales. Shen *et al.* [85] developed an array of CE microchannels connected to reservoirs in soda-lime glass to perform parallel detection of fluorescent-tagged biomolecules. Light from a diode-pumped solid-state laser at 473 nm was line-focussed across the parallel measurement and reference channels and a CCD camera with filter was used to detect fluorescence simultaneously from all channels. Parallel CE separation allowed simultaneous detection of many fluorescently labelled molecules such as amino acids, proteins and nucleic acids. A similar system was realised in PMMA by Liu *et al.* [86], working in the same group, and successfully applied to rapid detection of multiplex PCR products for severe acute respiratory syndrome virus (SARS) and hepatitis B. Huang *et al.* [87] fabricated a sophisticated microfluidic network in PDMS to analyse low-copy number proteins in a single cell by single molecule detection. Individual cells were trapped, lysed, and the proteins in the lysate bound with fluorescently labelled antibodies and then separated using CE. A line-focused laser beam ensured that all molecules across the width and depth of the detection microchannel (40 μm $\times$ 1.8 μm) were detected, while in the direction of flow it was still tightly focussed to reduce background fluorescence. Edgar *et al.* [88] performed detection of fluorescein-labelled amino acids contained in 10 fL droplets. The device consisted of a T-channel 3 μm wide by 3 μm deep that separates a CE channel (50 μm wide by 50 μm deep) from the droplet generation input by using an immiscible liquid. LIF is then performed in the CE channel. Oh *et al.* [89] genetically engineered *E. coli* cells to cause them to express capture proteins and present them at the membrane surface. DEP cell traps were used to immobilise the cells in 200 μm wide microchannels, which then captured fluorescently labelled target molecules. Dual wavelength fluorescence measurements were performed on the cells to detect the bound molecules and reference to the number of capture ligands. This technique provides a convenient method to produce surfaces with immobilised capture molecules. Direct UV-excited fluorescence offers the potential for label-free protein analysis in individual cells. Hellmich *et al.* [90] performed direct UV fluorescence measurements on amino acids and proteins, using a frequency-quadrupled Nd:YAG laser and photomultiplier. Individual cells were optically trapped and electrically lysed on an PDMS/quartz chip, and the lysate separated by CE. Optimisation of the confocal optics and addition of carbon black into the PDMS led to a reduction in background florescence and an LoD of 25 nM for tryptophan.

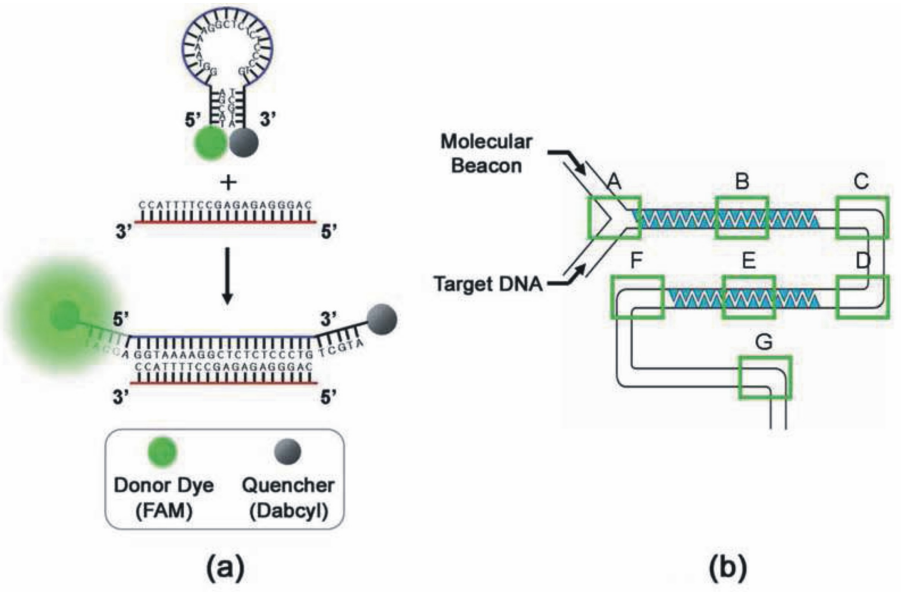

FIGURE 2.8: (a) Schematic representation of the molecular beacon and its operating principle. Target hybridization leads to the separation of the fluorophore (FAM) and quencher (DABCYL) and a consequent fluorescent signal. (b) Schematic representation of an alligator-teeth-shaped PDMS microfluidic channel. Taken from [92].

DNA hybridisation to a free DNA probe sequence in solution is much faster than to immobilised DNA sequences, due to the diffusion-limited kinetics of the latter. Thus detection of hybridisation of target and probe in a microflow system, with suitable mixing, presents considerable advantages in terms of speed. Lee and co-workers [91, 92] implemented a fluorescence resonance energy transfer (FRET) system in a PDMS microfluidic device with an alligator teeth structure for efficient mixing in otherwise laminar flow, shown in Figure 2.8(b). As the probe and hybridised target is not immobilised, washing cannot be used to remove the unbound target, so an alternative labelling scheme is required. Yea *et al.* [91] employed a system where both the target DNA and probe strands were labelled, and relative intensities yielded the fraction of hybridised DNA. To avoid the need to label the target DNA, Kim *et al.* [92] then employed a molecular beacon, shown in Figure 2.8(a), where one end of a single-stranded oligonucleotide has a fluorophore attached and the other end has a quencher attached. In the absence of the target sequence, emission is quenched as the probe sequence forms a loop and the fluorophore and quencher are in close proximity. Hybridisation of the complementary target causes the loop to open, the fluorophore and quencher to separate and fluorescence to be observed. Liu *et al.* [93] report a portable genetic analysis system for forensic applications and have validated it using samples extracted from oral swabs and human bone extracts. The glass microfluidic chip performed the polymerase chain reaction (PCR) and capillary electrophoresis followed by parallel four-wavelength fluorescence detection using a 488 nm frequency-doubled diode laser and confocal optics, with optical fibre as confocal aperture.

Multiplexed analysis with multiple fluorescent labels is limited by the spectral overlap

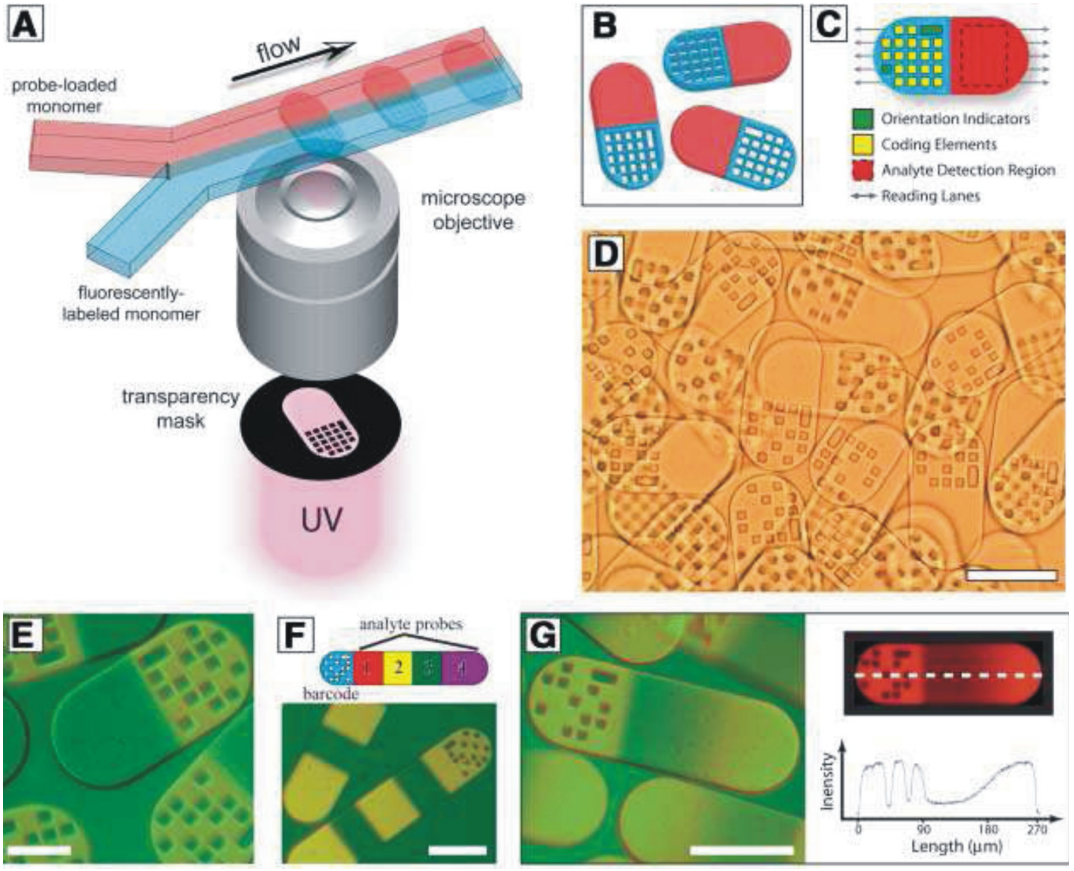

FIGURE 2.9: (a) Schematic diagram of dot-coded particle synthesis showing polymerization across two adjacent laminar streams to make single-probe, half-fluorescent particles [shown in (b)]. (c) Diagrammatic representation of particle features for encoding and analyte detection. (d) Differential interference contrast (DIC) image of particles generated by using the scheme shown in (a). (e to g) Overlap of fluorescence and DIC images of single-probe (e), multiprobe (f, bottom), and probe-gradient (g, left) encoded particles. Scale bars indicate 100 mm in (d), (f), and (g) and 50 mm in (e). Taken from [94].

of fluorophore emission. Pregibon *et al.* [94] created single and multi probe particles encoded with a spatial fluorescent pattern for multiplexed detection of DNA oligomers at 500 attomoles. The encoded particles were created in a continuous microflow system, shown in Figure 2.9(a), where laminar fluorescently-labelled monomer and probe-labelled monomer flows are introduced adjacently. Elongated polymer particles ($\sim$ 90 μm wide by 30 μm deep by up to 270 μm long) were formed in the channel by exposing the monomers to 30 ms bursts of UV to photopolymerise them. The shape of the particles was defined by a mask in the UV projection system, which included the 20-dot pattern at one end, yielding more than one million possible codes. The resultant particles, which have a fluorescent graphically-encoded region and covalently-coupled probe-carrying regions, as shown in Figure 2.9(b), are collected in a reservoir. After incubation with the fluorescent-labelled target the particles are read by passing them through a microfluidic channel a little wider than the particle width. The particles are hydrodynamically focused and aligned along the channel and when they pass through the detection region

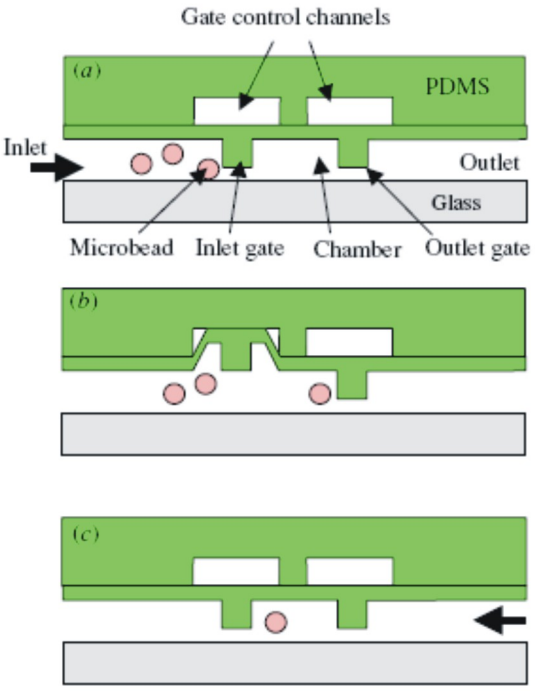

FIGURE 2.10: Schematic view of each step in capturing of a single microbead: (a) bead introduction, (b) inlet gate opens by applying a vacuum to the gate control channel and (c) gate closed by stopping the vacuum on the gate control channel resulting in a single bead captured for sensing. Taken from [96].

the fluorescent intensities are detected using a CCD camera and analysed in five lanes along the particles, corresponding to the rows of dots in the code, so that the particles code is read and the presence of the target is detected. The external optics employed in microfluidic LIF systems is often complex. Huang *et al.* [95] performed on-chip PCR and CE in PDMS/PMMA/glass multilayer device with an embedded optical fibre for fluorescence collection to reduce the complexity of collection. They detected *S. pneumoniae* bacteria and the dengue-2 virus by separating and detecting amplified DNA products.

Suitably modified microbeads may be used as probes for biomolecular detection in microfluidic systems. For example, the beads may be functionalized with antibodies and binding of the fluorescent-tagged antigen enables fluorescent detection in a microfluidic device, with multiplexing being achieved using beads containing different fluorophores. Detection on beads means that the antibody does not have to be immobilised in the microfluidic device, and the beads can be readily manipulated within a microflow system. Yun *et al.* [96] realised physical PDMS gate valves within a microfluidic channel to isolate individual beads, as shown in Figure 2.10. Using 10 μm diameter polystyrene beads modified with human IgG specifically bound to protein A on the bead surface, an LoD of 0.1 μg mL^{-1} for anti-human IgG conjugated with CdSe/ZnS quantum dots (QDs) was achieved, using a fluorescence microscope to excite and detect. Riegger *et al.* [97] performed sandwich immunoassays for hepatitis A and tetanus in a centrifugally-propelled

disk-based microfluidic system with an LED light source. CdSe QDs were used to identify the beads and fluorescent polystyrene microspheres were used to identify presence of the bound antigen. Haes *et al.* [98] achieved an LoD of 1 fM for staphylococcal enterotoxin B (SEB) detection using a microfluidic device with a system of microchannels and micro-weirs. Displacement assays were carried out on a glass chip using LIF and electrokinetic fluid pumping. Silica beads modified with antibodies specific to SEB were trapped in the weirs, and fluorescent-tagged SEB bound to these in situ. The displacement assay was carried out by introducing the sample containing SEB and observing fluorescence from displaced tagged SEB downstream from the beads. The beads could be replaced, for repeated assay, or used again a limited number of times.

2.5 Refractive Index Techniques

Refractive index based techniques are more prone to influence by non-specific effects than fluorescence techniques but are extremely attractive for chemical and biochemical sensing due to the lack of need for a label. However, rather few papers describe integration of refractive index based detection techniques with true microfluidic systems, and key examples are reviewed in this section.

Costin *et al.* [99] demonstrated measurement of diffusion coefficients and molecular masses in a microfluidic chip, which could play a useful role in on-chip CE and HPLC systems. The sample stream and mobile phase stream were merged in a detection channel and interdiffusion between the streams was monitored using the angular deflection of laser light by the resultant refractive index gradient. Two detection points, one just as the streams merge and one downstream, were used to monitor the extent of diffusion over the length of the channel, and the relative deflections yielded information on analyte diffusion coefficient and molecular weight. Leung *et al.* [100] analysed bubbles in microchannels 40 μm wide and 30 μm deep, for application in online reaction monitoring and safety applications. As a bubble passes through the microchannel the deflection of laser light due to the refractive index perturbation is recorded using a position-sensitive detector. Performing statistical analysis on the data the system is able to determine bubble size and formation frequency. Using a hollow Abbe prism as a microfluidic chamber, as described above for absorption monitoring (Figure 2.3), Llobera *et al.* [50] were able to detect changes in refractive index through dispersion of the prism, as well as the absorption of a liquid. The device consisted of channels to embed input and output fibres, biconvex microlenses to focus the light, reservoirs, and the Abbe prism monolithically integrated in PDMS.

The spectral transmission of a Fabry-Perot (FP) cavity is highly sensitive to intracavity refractive index and may enable imaging of refractive index distributions. Shao *et al.* [101] fabricated a FP microfluidic cavity in which microchannels of up to 30 μm deep and

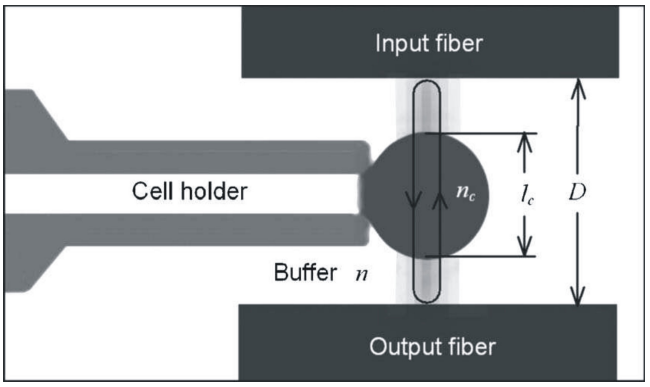

FIGURE 2.11: Schematic showing microfluidic Fabry-Prot cavity for cell detection. The cell holder holds a cell in position as the cavity resonates. Taken from [102].

200 μm wide were etched in Pyrex and the top and bottom coated with 35 nm thick gold layers to serve as reflectors. Using an LED as a broadband source and measuring the transmission spectrum of the device, they performed intracavity measurements on single particles such as yeast cells; human red and white blood cells could be distinguished, although improved quantification is needed. Song *et al.* [102] realised a microfluidic network incorporating a dual-fibre Fabry-Perot, with channels for insertion of cells and two buffer solutions, two single mode fibres with high reflectivity gold-coated ends crossing the fluid channel to act as the FP cavity and as optical input and output, and a pressure-based cell-holder to trap the cell between the two fibres, as shown in Figure 2.11. The cavity was 35.5 μm long and two buffer solutions having different refractive indices were alternated while the cell was trapped in position by the cell holder. The differences in the spectra with the two buffer media were reported to yield the effective refractive index of the cell with a standard deviation of $\mp 0.2\%$, and cell size with an SD of $\mp 4\%$ for repeated measurements of the same cell, being released and retrapped.

There is a vast literature on evanescent wave refractive index based biosensing, based on dielectric waveguides or on surface plasmon resonance, for instance, and these are subject of excellent recent reviews by Lambeck [31] and Phillips and Cheng [103]. Integration of these sensors with microfluidic circuits is essential for repeatable performance, integration of reference sensors, enhanced interaction of analyte and surface, and low-cost manufacture, and the lab-on-the-chip may benefit greatly from these welldeveloped techniques. Mach-Zehnder interferometers (MZIs) are one of the most sensitive waveguide devices for evanescent refractive index measurement [104], particularly if active electro-optic control is employed [105]. Lechuga and co-workers have reported the development of an MZI using CMOS compatible technology integrated with an SU-8 microfluidic channel [106, 107], achieving an LoD for bulk refractive index of 3.8×10^{-6}.

Ymeti *et al.* [108] realised a waveguiding Young interferometer (YI) on silicon with a glass microfluidic circuit. Light is inserted into a waveguide and is split into four channels. The outputs of the four waveguides are focused by a cylindrical lens to a

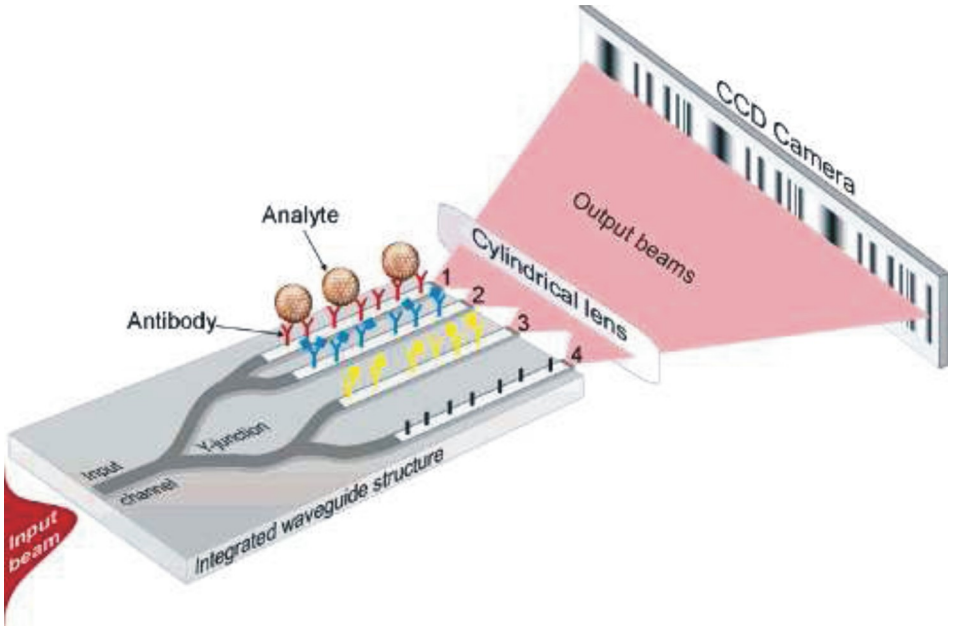

FIGURE 2.12: Four-waveguide integrated optical Young's interferometer sensor. Waveguides 1, 2, and 3 are sensing arms, and waveguide 4 is the reference arm. Taken from [109].

CCD camera to record the interference pattern. Each of the four waveguide channels is exposed in a sensing window, and microfluidic channels are realised on a separate wafer which is then bonded to the YI over the sensing windows. The device was used to analyse an immunoreaction between human serum albumin (HSA) and α-HSA and achieved a refractive index resolution of 6×10^{-8}. The authors later reported that a similar YI device, shown in Figure 2.12, could detect herpes simplex virus type 1 (HSV-1) at concentrations of 850 particles mL^{-1} and that the sensor may be able to achieve sufficient sensitivity to detect single virus binding [109]. In this case, a macrofluidic flow system was used, but the use of microfluidics was predicted to reduce the sample volume to a few microlitres and reduce time response to seconds.

Gratings are attractive components for interrogation of refractive index in microfluidic systems, as they allow relaxed optical alignment compared with direct end-coupling into waveguides [110]. Yuen *et al.* [111] realised a polymer H-shaped microfluidic device integrated with a grating for sensing, in which a reference fluid and analyte fluid could be passed over the grating under the same conditions and measured simultaneously. Laser light is incident through a polariser and focused via a lens to provide many angles to couple into the grating. Light is coupled into the waveguide at the angle where the grating provides phase-matching, and this angle changes depending on the refractive index of the material at the grating surface; the light then couples out of the waveguide and is recorded by a CCD camera. Tests with biotin/streptavidin assays were conducted to demonstrate detection of small molecule binding. Sarov *et al.* [112] employed a grating realised with a PMMA microprism on a glass microchannel lid, requiring multi-step fabrication. Laser light enters the prism under total internal reflection, so that the

grating is irradiated and an evanescent field penetrates the microchannel. Reflected and diffracted light exits the prism and the energy redistribution into the diffracted orders allows the determination of the refractive index and the absorption coefficient of the fluid. The device had an index sensitivity of 5×10^{-4} and an absorption coefficient sensitivity of 3.5×10^{6} m^{-1}. Choi and Cunningham [113] fabricated grating structures with a period of 550 nm as the sensors on the floor of a microchannel, by molding followed by deposition of a thin titania film. Using a white light source the grating is irradiated perpendicular to the grating with polarised light, and the reflected light, whose wavelength depends strongly on the refractive index of the medium in contact with the grating, is directed back to an imaging spectrometer. The key advantage of this approach is that an array of small sensor patches ($\sim 10 \times 10$ μm) can be imaged as independent sensors, allowing the potential for dense integration. The device detects changes of refractive index in the microchannel as a shift in the peak wavelength of reflection. Discrimination between chicken IgG and pig IgG was demonstrated using Protein A as the immobilised protein ligand.

Surface plasmon resonance is an alternative means of detecting refractive index changes in an evanescent field, which has achieved great success through the Biacore$^{\text{TM}}$ system [114]. Detection depends upon angle- or wavelength-dependent coupling to a lossy surface plasma wave at a metal surface, whose velocity changes with refractive index resulting in a change in reflected power. The potential for low reagent and sample volumes and fast reactions is driving further miniaturization and integration of SPR devices in microfluidic systems. Furuki *et al.* [115] realised photopatterned microchannels with floors coated with a gold film. The device was excited using a prism in the Kretschmann configuration where light is reflected from the 60 nm thick gold layer, tunneling through it to excite a surface plasmon on the liquid side of the film in each channel. A sequence of cysteamine, photobiotin, and avidin was bound to the surface and measured by SPR. The results were consistent with those measured by atomic force microscopy, and the channel sample volume was reduced to about 8 nL. Wheeler *et al.* [116] fabricated micro-flow cells designed to be attached to the commercial Spreeta$^{\text{TM}}$ SPR sensor by soft lithography in PDMS using conventional photoresist processing. Refractive index changes due to biotinylated bovine serum albumin, streptavidin, biotinylated protein A, and human immunoglobulin each bound to the preceding layer were monitored. Using volumes as low as 73 nL, the data were consistent those obtained with conventional flow cells of volume 8 μL. Recently more sophisticated microfluidic SPR devices have been reported. Huang *et al.* [117] realised a complex integrated flow circuit with many microfluidic components, and detection regions for three analytes in one channel. The optical excitation and detection was again achieved using an external prism in the Kretschmann configuration. Temperature control was incorporated into the device, as all refractive index based sensors are sensitive to temperature variations. Molecular imprinted polymer (MIP) films were used as the recognition element for specific biomolecules. MIPs specific to testosterone, cholesterol, and progesterone were pattered on the gold and detection of

these three analytes successfully demonstrated at physiologically normal concentrations. This microfluidic SPR system demonstrated direct detection of low molecular weight analytes, higher association rates between analyte and MIP compared with a conventional SPR system due to more efficient interaction between biomolecules and MIP films, and reduced sample consumption.

Lei *et al.* [118] integrated a microfluidic vortex pump into a hot embossed PMMA micro flow cell, with integrated SPR sensor. The gold layer was not deposited directly in the microchannel, but on the surface of a prism attached to an open microchannel, thereby sealing it. The sensitivity of the SPR technique was enhanced by exploiting the phase change on reflection as well as the amplitude change, in a bulk interferometer. An estimated sensitivity of ~ 10 ng mL^{-1} was achieved for the binding reaction of bovine serum albumin (BSA) antibodies to BSA immobilised molecules on the gold surface. Making use of a simple T-shaped PDMS microchannel on a glass wafer with gold patches, Kurita *et al.* [119] realised a portable SPR system with a concentration range of 5 pg mL^{-1} to 100 ng mL^{-1} for B-type natriuretic peptide, a marker of cardiovascular risk. This indirect measurement involved incubation with enzyme labelled antibody, attachment of the unbound antibody at a position upstream of the SPR sensor, production of thiocholine by interaction of enzyme and acetylthiocholine in solution, and accumulation of the thiocholine on the gold SPR pad.

2.6 Raman Spectroscopy

Light incident on a material may exhibit Raman scattering at shifted wavelengths (discovered by Raman in 1928 [120]) due to energy being lost to molecular vibrations (Stokes shift) or imparted by them (anti-Stokes shift). Raman spectroscopy thus provides molecular fingerprint information similar to that provided by IR spectroscopy, and is a powerful technique for highly specific label-free detection of species. Raman spectroscopy has the advantage that it may be carried out at wavelengths where the absorption of water is weak and where optical instrumentation is straightforward, but has the disadvantage that the scattered signals are very weak. Several approaches have been adopted to obtain measurable signals in microfluidic systems, including surface-enhanced Raman scattering (SERS), resonance Raman scattering, and long-term integration for a stationary particle. In this section two important types of Raman spectroscopy applied to microfluidic devices are discussed.

2.6.1 Surface-enhanced Raman Spectroscopy

Surface-enhanced Raman spectroscopy (SERS) exploits resonant excitation of surface plasmons on metallic surfaces to enhance Raman scattering by many orders of magnitude [121]. Metals with a large and negative real part and a small imaginary part of

dielectric permittivity, usually gold and silver, are required for efficient enhancement, and suitable surfaces for plasmon excitation include colloids, roughened and patterned films, and self-assembled structures. SERS is emerging as a competitor to fluorescence with the benefit that no tagging is required (although surface-enhanced resonance Raman (SERRS) may employ a tag) and Raman spectra show narrow lines characteristic of the material, allowing greater multiplexing. However, its application to microfluidic devices is complicated as, unlike fluorescence, the species under detection must be in close proximity to the metal surface for enhancement to take place. Reliable quantitative measurements are difficult to achieve as SERS enhancement is strongly dependent on the shape, size, and proximity of metallic features. For example, colloids are attractive enhancers in microfluidic systems as they may be analysed while flowing through the system and do not use a fixed surface within the flow channel which may become fouled. The highest enhancements using colloids occur in hot-spots where two particles are within a few nanometres of each other. Adequate control of measurement conditions such as the degree of colloid aggregation, particle sizes of the colloids, and the inhomogeneous distribution of molecules on a metal surface is challenging. Using a fixed patterned surface within the microflow channel has the advantage of providing a constant surface, with the disadvantage of its potential fouling and degradation.

Connatser *et al.* [122] vapour deposited ~ 20 nm silver onto PDMS microfluidic channels to create partially embedded clusters. Raman spectroscopy was performed in a conventional Raman microscope with 633 nm laser illumination for detection of riboflavin and resorufin following CE separation in the channel. The Raman spectra for riboflavin and resorufin gave readily distinguishable peaks at wavenumber shifts of 1200 cm^{-1} and 600 cm^{-1} respectively. Novel structures such as nanowells patterned by soft lithography in PDMS allow more controlled production of "hot spots" for SERS, yielding enhancement factors of 10^7 in a PDMS/glass microflow channel, configured as shown in Figure 2.13, compared to a device with a smooth PDMS surface [123].

Collection of SERS spectra from flowing colloids can provide more reproducible results because of temporal averaging of the geometry and improved heat dissipation. Nirode *et al.* [124] demonstrated direct on-column SERS in 100 μm diameter CE microcapillaries using silver colloids with nanomolar sensitivities for Rhodamine 6G. Flowing colloidal particles and analyte molecules show a tendency to adhere to microflow channel walls, contaminating subsequent measurements. Strehle *et al.* [125] performed analysis on aqueous droplets contained within flowing lipophilic tetradecane and moved along the channel by external pumps, thereby avoiding contact between colloid and the channel walls. Crystal violet detections within the 60 nL - 180 nL droplets were performed in a concentration range of 1×10^{-5} M to 1×10^{-6} M, and quantification achieved by recording the amplitude of the 1177 cm^{-1} Raman peak.

Lee and co-workers realised PDMS microfluidic chips where the colloidal silver solution is mixed with the analyte using the alligator-teeth structure (Figure 2.8(b)) in the

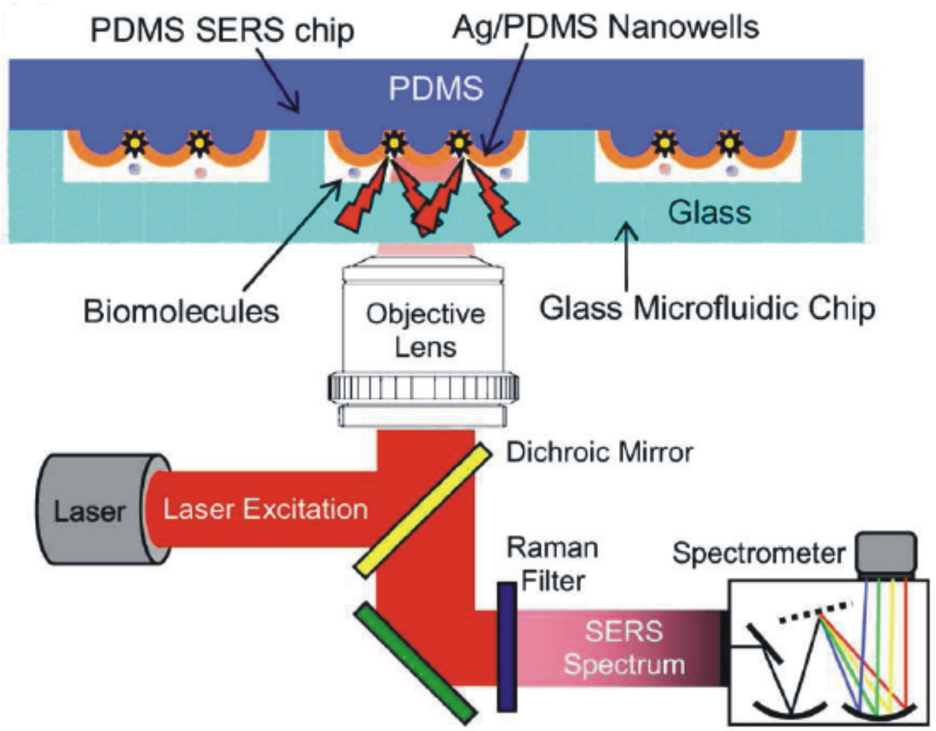

FIGURE 2.13: Schematic diagram of integrated microfluidic chip with nanowell structures for SERS, and the Raman detection apparatus. Taken from [123].

microchannel, and the Raman spectrum is acquired in a downstream detection region using a conventional Raman microscope and excitation at 514.5 nm. One device was used to detect cyanide anions for pollution monitoring using a Raman peak at 2100 cm^{-1}, achieving an LoD of 1.0 ppb or below [126]. Using similar devices this group also reported (i) detection of two different dye-labelled DNA nucleotides without the need for PCR or microspotting; TAMRA and Cy3 dyes were used for labelling with an LoD estimated at 10^{-11} M [127], and (ii) the detection of methyl parathion insecticide with an LoD of 0.1 ppm [128]. Recently, again using a similar device, molecular beacons were used to hybridise with the target DNA and detected using fluorescence and SERS. In the case of the SERS measurements, silver colloids were mixed with the beacon solution and the DNA to be hybridised was added through another inlet. The Raman signal was strongly reduced if the analyte was complementary to the beacon as the change in conformation of the beacon caused the SERS-active labels to be separated from the colloid [129].

Cooper and co-workers used surface-enhanced resonance Raman spectroscopy (SERRS) in a microfluidic system [130, 131]. The wavelength of the excitation source is selected to be at an analyte absorption, resulting in an increase in sensitivity and selectivity of the system, enabling improved discrimination of analytes from contaminants. A microfluidic device in glass was realised, in which silver colloid was formed on chip by insertion of an aqueous solution of $AgNO_3$ and of $NaBH_4$ in NaOH solution into two branches of a T-junction, producing a stream of aggregated colloids flowing down the centre of the third

branch [130]. The analyte was introduced at a downstream T-junction and 10 fmol of an azo dye derivative of trinitrotoluene (TNT) was detected using a conventional SERS system with 514 nm laser excitation. A similar microfluidic device was realised by the same group in PDMS, and yielded identification of up to three oligonucleotides of *E. coli* sequences labelled with different dyes [131].

2.6.2 Laser tweezer Raman spectroscopy

Laser beams can be made to function as optical traps, also known as optical tweezers. In the presence of a tightly focused laser beam nearby particles of higher refractive indices than the surrounding medium due to gradient forces are attracted towards the maximum optical intensity of the beam [132]. On the beam the particle is trapped near the focus as gradient forces and the "radiation pressure" forces which drive the particle along the propagation of the beam are balanced. Laser tweezer Raman spectroscopy (LTRS) exploits a single-beam optical gradient trap to hold and isolate a particle while performing Raman spectroscopy upon it. Such trapping applies to larger objects such as cells, where detection of Raman scattering is less problematic, and has the advantages that the object can be held away from surroundings, to limit background interferences, can be held stationary for extended periods and then released, to allow temporal integration of spectra and improved signal to noise ratio, and can be moved in and out of the Raman probe volume, to allow background subtraction and noise reduction. The optical gradient trap has been employed for some time to study Raman spectra of levitated objects [133]. However, it is only recently that LTRS has been used in conjunction with microfluidics. Xie *et al.* [134] fabricated a simple microfluidic system with two microfluidic chambers joined by a microchannel. Individual yeast cells and bacteria were trapped and identified from their Raman spectra in one chamber and then moved to separate regions in the collection chamber for subsequent processing using the tweezer.

Methods to improve the sensitivity of LTRS systems by reducing or cancelling background and environmental interferences are being continually refined and incorporated in microfluidic environments. The use of separate wavelengths for trapping and Raman scattering adds an extra dimension to LTRS systems. Creely *et al.* [135] realised a macrofluidic dual-wavelength LTRS system with excitation of the Raman spectra at 785 nm, and trapping at 1064 nm. Individual living yeast cells were trapped, a Raman spectrum obtained for between 0.2 s and 180 s, moved out of the Raman excitation beam so that a background measurement could be acquired under the same experimental conditions, and then the spectrum had the background subtracted. The approach employed a single microscope system using an excitation power and trapping power both < 10 mW, allowing live cells to be observed for over 2 hours, and detailed information on temporal changes in the cells to be obtained. Recently Rusciano *et al.* [136] have demonstrated a dual-beam microfluidic system, where the Raman probe beam is kept in

a fixed position whilst the trapping beam position oscillates so that the trapped object is moved through the Raman probe volume twice in each period of oscillation, thereby modulating the Raman signal by a frequency $2f$. This can then be demodulated with low noise using a lock-in amplifier, removing any stray light or unmodulated background fluorescence. The resultant signal includes a spurious component also modulated by $2f$ due to the photon scattering of the solvent volume. However, this second component is easily distinguished as it is shifted by $\pi/2$ radians with respect to the desired signal.

Dual-wavelength systems have also been realised, employing two separate microscopes, allowing greater independence in optimisation of trapping and Raman detection, and applied to red blood cells, yeast cells and resonance Raman spectroscopy of red blood cells [137, 138]. Ramser *et al.* [139] have developed their approach for application to a microfluidic chip for resonance Raman spectroscopy of red blood cells, allowing the oxygenation cycle of an individual erythrocyte to be studied.

In the case of detection of small numbers of biomolecules, laser tweezer Raman spectroscopy may be combined with SERS to enhance Raman signals by trapping micron-sized metal colloid clusters or metal-coated glass spheres [137, 140], and taking the Raman spectra of molecules absorbed on them.

2.7 Thermal Lens Detection

Light incident upon a liquid sample may be absorbed by the sample which then undergoes non-radiative relaxation and heats the surrounding volume. This heat changes the refractive index of the medium, usually lowering it. If a laser excitation beam is focussed on a small volume, the refractive index change is increased and a thermal lens (TL) is created by the thermal gradient. A laser probe beam can then be used to detect these changes. A thermal lens microscope (TLM) exploits this phenomenon by focussing a coaxial excitation beam and probe beam on the fluid through an objective lens, and detecting the power in the probe beam passing through a pinhole after filtering out the excitation wavelength, as shown for nanoparticle detection in Figure 2.14. A modulated excitation laser and synchronous detection is used to reduce noise and improve detection limit. Sensitivity to absorption is extremely high, as is required in microfluidic systems with small volumes, but TL is generally not able to distinguish between absorbing species, although thermal lens spectroscopy yields some compositional information. Kitamori *et al.* [141], writing on the principles of TLM and its application to imaging and microfluidics, observe that the chemical specificity obtainable through separation of analyte species in microfluidics is complemented by the great sensitivity of thermal lens detection. Further miniaturisation of the TLM is required for practical use in microfluidic systems as the optics used tends to be quite bulky.

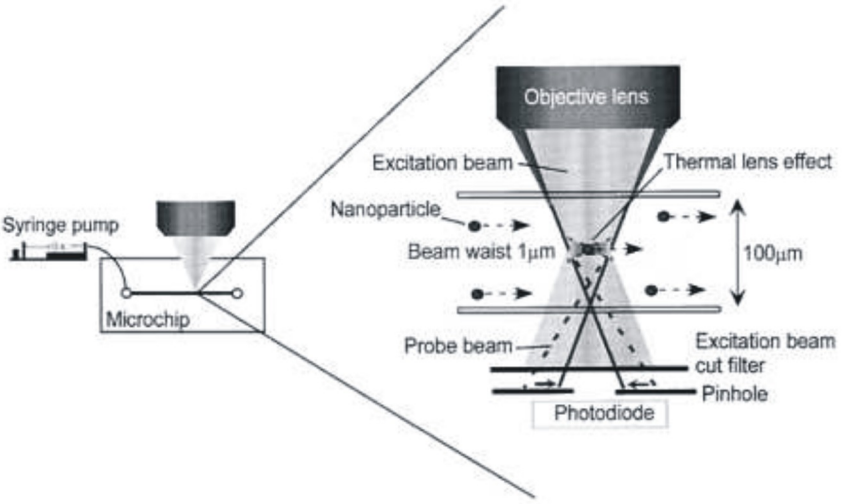

FIGURE 2.14: Principle of detection of individual nanoparticles by thermal lens microscopy. Taken from [142].

Kitamori and co-workers have made a large contribution to the development of continuous-flow chemical processing incorporating TLM in microfluidic devices, and demonstrated its potential applications, with 0.1 nM detection limits in 7 fL detection volumes, for example [143]. A three-dimensional microchannel network on chip with pressure-driven flow that produced multi-phase laminar flows was able to perform twenty micro operations such as mixing and liquid-liquid extraction. The device was used to extract and analyse Fe(II) and Co(II) ions using changes in absorption spectrum [144]. A simpler device which also makes use of multi-phased flows demonstrated an LoD of 7×10^{-8} M for carbaryl pesticide, two orders of magnitude lower than conventional spectrophotometric methods for [145]. These systems employed single wavelength excitation at 532 nm and detection at 633 nm. A tunable thermal lens spectrometer system using a Xe lamp and monochromator as excitation source [146] enabled determination of the thermal lens spectrum of non-scattering and turbid solutions, demonstrating a clear advantage over absorption detection by measuring the spectrum largely regardless of the strong light scattering background. The thermal gradient required for thermal lensing was obtained by exploiting rapid thermal conduction between the glass substrate and the liquid, rather than by tight focussing of the excitation beam. Application to cultured cells was demonstrated [147] by monitoring nitric oxide release from macrophage-like cells stimulated by lipopolysaccharide using a colorimetric reaction in a microfluidic device with localized temperature control. A successful assay was achieved within 4 hours using 3000 cells compared to 24 hours and 10^5 – 10^6 cells for conventional batch methods. UV excitation TLM at 266 nm was employed for detection of adenine aqueous solutions without labelling in a fused-silica microchip. The sensitivity obtained was 350 times higher than a conventional spectrophotometric method with an LoD of 1.4×10^{-8} M [148]. Detection of single and multiple 50 nm gold nanoparticles was demonstrated using TLM, as shown in Figure 2.14 and their optically-driven fixation to the wall of

the glass microchannel using the same beam was also demonstrated, having the potential for sensitive nanoparticles detection and production of microchip SERS substrates [142]. A glass microchip consisting of a microchamber for cell culture connected to a microchannel for TLM detection was used to monitor intercellular messengers [149]. Rat hippocampus nerve cells were cultured in the microchamber to form a neural network, and the retrograde messenger was then detected in the microchannel. Chirality of low-volume liquid samples was measured in a microfluidic device by using TLM in which the handedness of circularly-polarised excitation light was modulated [150]. Left- and right- circularly polarized light may be absorbed differentially in a chiral medium, and this is detected as a modulation of the detected TLM signal. Miniaturised thermal lens systems have been realised utilizing, for example, optical fibres, fibre wavelength multiplexer for the two diode laser sources (658 nm excitation and 785 nm probe) and SELFOC microlenses. LoDs of 3.7×10^{-8} M for sunset yellow and 7.7×10^{-9} M for nickel (II) phthalocyanine-tetrasulfonic acid, tetrasodium salt (NiP) were achieved, showing a rather small reduction in performance compared with the conventional bulk-optical detection system [151]. Employing both TLM detection and fluorescence in a microfluidic device with similar miniaturised optics yielded an LoD 6.3 nM for (NiP) and 3 nM for Cy5 [152].

Kakuta *et al.* [153] realised a semi-automated heterogeneous immunoassay system for brain natriuretic peptide (BNP), using TLM to detect BNP within a concentration range of 0.1100 pg mL^{-1} through reaction resulting in a blue-coloured product. Kitagawa *et al.* [153] used CE separation in silica fused capillaries connected to a microchannel on a chip. The system achieved an LoD of 3.6×10^{-7} M for the azo dye, Sudan Red, more than two orders of magnitude lower than that of conventional absorbance detection. Micellar electrokinetic chromatography with sample concentration by "sweeping" [154] reduced the LoD to 1.2×10^{-12} M. Mawatari *et al.* [155] used the sensitivity of the TLM signal to focusing position to optimise precise focusing in a portable TL apparatus, in a manner similar to the optical disk drive, using a micro-optical pick-up unit rather than a microscope. Adjustments of the depth were made by determination of the astigmatism of the reflected excitation beam, and the width by monitoring transmitted scattered light of the probe beam. An LoD of 30 nM was achieved for xylene cyanol solution, with a sensitivity between 20 – 100 times higher than that obtained by spectrophotometry. This laboratory then presented a similar miniaturised TLM system, but with reflective rather than transmissive optics, shown in Figure 2.15, reducing alignment complexity, and only requiring optical access from one side of the microfluidic chip. This was achieved by forming an aluminium mirror on the reverse of the microchip. The reflected probe beam was detected with 40 times higher sensitivity when compared to a spectrophotometer, with an LoD of 60 nM for xylene cyanol solution [156].

Ghaleb and Georges have reviewed and analysed the use of crossed-beam systems, in

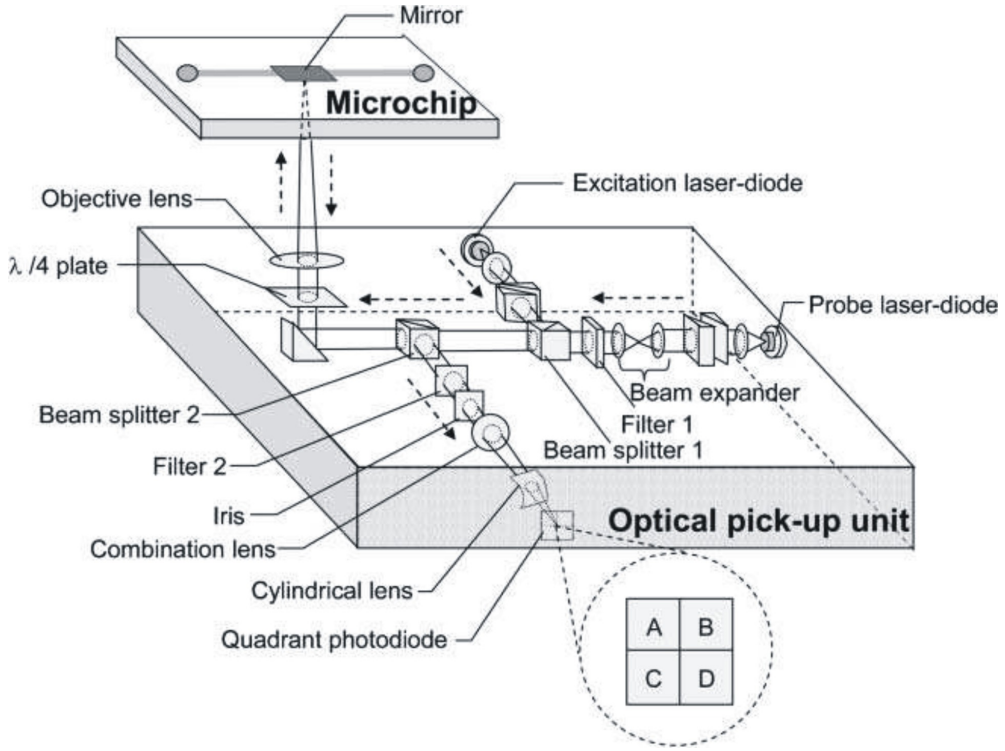

FIGURE 2.15: Illustration of the optical arrangement of a reflective thermal lens detection device. Taken from [156].

which the excitation beam and probe beam are perpendicular to each other, in comparison with the collinear approach normally used in TLM. In the former case, the heated sample acts as a cylindrical lens for the probe beam, and excitation light exhibits less interference with detection [157]. They subsequently performed a detailed optimization of crossed-beam systems for chopping frequency, sample size and flow rate in fused silica capillaries [158].

2.8 Conclusions

Optical detection techniques are preferred in microfluidic systems due to their high sensitivities. It is quite a challenge to develop optical detection systems for microfluidics as advantages that are associated with microfluidics technologies can place high specifications upon the optics, due to the sample volumes and optical path-lengths being extremely small. Most systems still perform the optical operations off-chip, and the optics tend to be bulk instruments, such as the much used confocal microscope. Although these allow the system to be highly configurable they hinder the progress of miniaturisation to portable, robust, cheaper, and even increased sensitivity LoC solutions.

Scattering has been used to acquire size and shape information on cells in flow cytometry, and progress appears to indicate further advances in interrogation of scattering distributions, and when combined with fluorescence may yield more powerful automated

μFACS systems. Absorption is a common method of detection in macrofluidic detection systems, which is attractive as it often does not require labelling; but absorption poses a problem in microfluidics due to short path lengths involved. Enhanced absorption in microfluidic devices has been achieved in several ways, such as "multipass" systems, improvements of on-chip integrated optics, and sample concentration steps. The most dominant technique in use for optical detection is fluorescence. Very often requiring labelling of particles to be detected with fluorophores it has such a high sensitivity that the sample preparation step is tolerated. Advances have been made in fluorescence systems such as moving on to more stable tags, such as quantum dots, and the use of longer-wavelength semiconductor sources for compactness, lower fabrication costs, and reduced background fluorescence. There have also been improvements in geometrical configurations by incorporating multipass parallel channels, optimisation of the fluorescence collection angles, and the realisation of compact multiwavelength detection microchip units. Refractive index measurements are used in several detection devices, such as microfabricated Fabry-Perot cavities for cell analysis, and evanescent field sensors using integrated dielectric waveguides or metal films supporting surface plasma waves within microchannels. Refractive index detection techniques are label-free but require sample separation methods such as CE to give adequate specificity of detection of particle species. The major attractiveness of evanescent devices is that many can be produced using standard microfabrication techniques ideal for mass-production and development of fully integrated systems. Raman spectroscopy is gaining ground as a competitor to fluorescence as a direct label-free methods for detection and identification of species. Normally the Raman signal is too weak and SERS needs to be used. SERS in microfluidic systems is implemented either by nanostructed metal films on the microchannel walls, which can degrade and become blocked, or by on-chip micromixing of sample and metallic nanoparticles but is not separated from the sample after analysis. Another method to perform Raman spectroscopy is the use of LTRS which may be used to trap and analyse larger particles such as cells without enhancement, or species attached to enhancing metallic particles, allowing for long signal integration times and trapped object being held away from interfering surfaces. The uses of a thermal lens for detection in absorption assays is making progress as a method for detection, because of not requiring long path lengths as absorption detection. The drawback as a method is that it must usually be combined with other complimentary detection methods or sample separation methods such as CE to have adequate specificity of detection of particle species.

The literature has shown that optical detection techniques are extremely useful for microfluidics, and *vice versa*. There is still much scope for development of integrated optics into LoC technology. Higher integration of optical components and different configurations is the route to achieving integration for optical detection methods with little or no integration yet, such as the thermal lens, LTRS, and SERS. Direct excitation as opposed to evanescent excitation methods are used in the majority of microfluidic systems as it provides a greater flexibility for a device that can incorporate many of the optical

methods available for detection. In the remainder of this thesis, absorption is not considered as it is very dependent on excitation region length and work on this has reached maturity. Refractive index methods using evanescent fields are also not considered as these are usually best suited for submicron-sized particle detection, and also have configurations where light is delivered via the evanescent field and not directly, differing from most other optical detection setups. The concepts and realised devices described in the following chapters are developed primarily for fluorescence and scattering detection measurements by manipulating the excitation beam into a focus in the middle of the microfluidic channel. Direct excitation rather than evanescent excitation are the most useful for flow cytometry, but direct excitation means that there is an unguided free-beam in the microfluidic channel. There is a great need for integrated approaches to free-beam in the microfluidic channel for low cost LoC and this is the need that the project addresses. This approach will demonstrate the potential for integration of many of the optical detection functions described in this review.

Chapter 3

Planar Waveguides for Microfluidics

3.1 Introduction

Integrated optics used for LoC technology has been shown in Chapter 2 to be very useful for detection, but is still in its infancy. Direct excitation of light by a free beam in a microfluidic channel offers a greater flexibility in design to incorporate most of the optical detection methods previously discussed. To understand what is needed from further integration of optics with microfluidics, a basic integrated optics system should be studied. The basic building block of integrated optics is the waveguide and is the first step in developing integrated optical detection systems [159–163]. This chapter gives a summary of planar waveguide theory followed by simulations of three dimensional (3D) optical waveguides, based on the material system given in Chapter 6.

The simulations were done using a commercial simulation package, *BeamPROP*$^{\text{TM}}$ (by RSoft Design Group Inc.), which makes use of the beam propagation method (BPM), to model channel waveguides for delivery and collection of light across a microfluidic channel. Simulations studying the channel waveguide modes and how the light diffracts from the end of the waveguide when entering the microfluidic channel are presented. The modelling concentrates on waveguides with single mode operation. Multimode waveguides for excitation and collection in the detection of particles with integrated optics are common in the literature. Though multimode waveguides are adequate for proof of concept for many detection systems, with singlemode waveguides one can predictably create more complex optical operations such as beam splitters, integrated lenses and gratings [164] or one can achieve smaller spotsizes with single mode waveguides when focussing the beam off-chip.

3.2 Two-Dimensional Waveguides

The theory of dielectric optical waveguides has been documented at length and explained in the literature for many years, and the reader is directed to references [164–169]. This section will give a concise summary of the analytical solutions in two dimensions (2D) which corresponds to the slab waveguide shown in Figure 3.1. The slab waveguide consists of a substrate and a film on top, called the core, of higher refractive index, with or without a cladding of lower refractive index. The core being of higher refractive index than the surrounding medium allows for light to be guided by total internal reflection at the interfaces of the mediums.

The 3D slab waveguide in Figure 3.1 is modelled in 2D in the y-z- plane with the light propagating in the z-axis. This geometry allows for two sets of solutions to Maxwell's equations of orthogonal polarisation defined by which field, electric or magnetic, is in the transverse plane (plane out of the page in the 2D model). The wave equation for the transverse electric (TE) polarisation is [165]

$$\frac{d^2E_x}{dy^2} + (k_0^2 n^2 - \beta^2)E_x = 0, \tag{3.1}$$

$$H_y = -\frac{\beta}{\omega\mu_0}E_x, \tag{3.2}$$

$$H_z = \frac{i}{\omega\mu_0}\frac{E_x}{dy}, \tag{3.3}$$

$$E_y = E_z = H_x = 0, \tag{3.4}$$

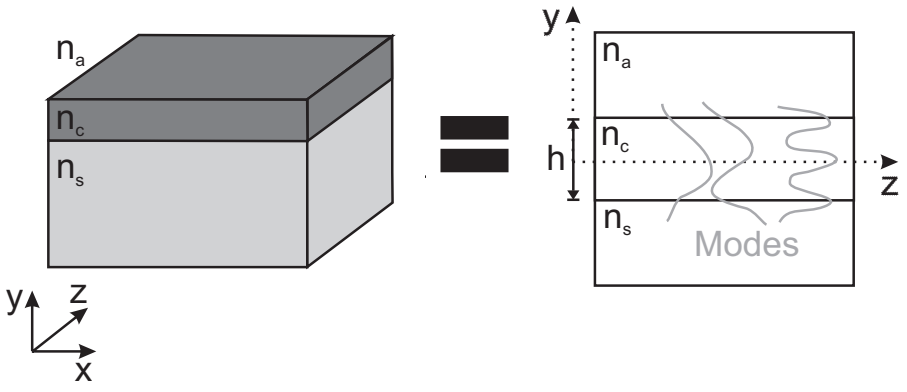

FIGURE 3.1: Slab waveguide model.

and for transverse magnetic (TM) polarisation

$$\frac{d}{dy}\left(\frac{1}{n^2}\frac{dH_x}{dy}\right)+\left(k_0^2-\frac{\beta^2}{n^2}\right)H_x=0, \tag{3.5}$$

$$E_y = \frac{\beta}{\omega\varepsilon_0 n^2}H_x, \tag{3.6}$$

$$E_z = -\frac{i}{\omega\varepsilon_0 n^2}\frac{H_x}{dy}, \tag{3.7}$$

$$H_y = H_z = E_x = 0. \tag{3.8}$$

Solutions to these equations in the form of $\tilde{\mathbf{E}} = \mathbf{E}(y)e^{i(\omega t-\beta z)}$ and $\tilde{\mathbf{H}} = \mathbf{H}(y)e^{i(\omega t-\beta z)}$ describe supported modes each with unique field profile. First the TE polarisation will be considered. The electric field across the boundaries is

$$E_x(y)=\begin{cases} A\cos(\kappa h/2-\phi)e^{-\sigma(y-h/2)} & (y>h/2)\\ A\cos(\kappa y-\phi) & (-h/2\le y\le h/2)\\ A\cos(\kappa h/2+\phi)e^{-\xi(y+h/2)} & (y<h/2)\end{cases} \tag{3.9}$$

where

$$\kappa = \sqrt{k_0^2 n_c^2-\beta^2} \tag{3.10}$$

$$\sigma = \sqrt{\beta^2-k_0^2 n_a^2} \tag{3.11}$$

$$\xi = \sqrt{\beta^2-k_0^2 n_s^2} \tag{3.12}$$

At the boundaries the transverse component of the electric field is continuous. Therefore,

$$\frac{dE_x(y)}{dy}=\begin{cases} -\sigma A\cos(\kappa h/2-\phi)e^{-\sigma(y-h/2)} & (y>h/2)\\ -\kappa A\sin(\kappa y-\phi) & (-h/2\le y\le h/2)\\ \xi A\cos(\kappa h/2+\phi)e^{-\xi(y+h/2)} & (y<h/2).\end{cases} \tag{3.13}$$

and from these equations at the boundary $y=\pm h/2$ the following equations are obtained

$$\kappa A \sin(\kappa h/2 + \phi) = \xi A \cos(\kappa h/2 + \phi) \quad (3.14)$$

$$\sigma A \cos(\kappa h/2 - \phi) = \kappa A \sin(\kappa h/2 - \phi) \quad (3.15)$$

and rearranging leads to

$$\tan(\kappa h/2 + \phi) = \frac{\xi}{\kappa} \quad (3.16)$$

$$\tan(\kappa h/2 - \phi) = \frac{\sigma}{\kappa} \quad (3.17)$$

giving eigenvalues equations

$$\kappa h = m\pi + \tan^{-1}\left(\frac{\xi}{\kappa}\right) + \tan^{-1}\left(\frac{\sigma}{\kappa}\right) \quad (3.18)$$

$$2\phi = m\pi + \tan^{-1}\left(\frac{\xi}{\kappa}\right) - \tan^{-1}\left(\frac{\sigma}{\kappa}\right). \quad (3.19)$$

Solving Equation 3.18 gives values of β and thus the modes that can be supported by the waveguide. For the TM modes, the same method can be applied to Equation 3.1 giving the eigenvalues equations

$$\kappa h = m\pi + \tan^{-1}\left(\frac{n_c^2\xi}{n_s^2\kappa}\right) + \tan^{-1}\left(\frac{n_c^2\sigma}{n_a^2\kappa}\right) \quad (3.20)$$

$$2\phi = m\pi + \tan^{-1}\left(\frac{n_c^2\xi}{n_s^2\kappa}\right) - \tan^{-1}\left(\frac{n_c^2\sigma}{n_a^2\kappa}\right). \quad (3.21)$$

Solutions to the eigenvalue equations can be obtained using modern programming environments such as MATLAB. Introducing boundaries in a second dimension makes analysing 3D planar waveguides more difficult than the 2D case. The next section addresses how this is done.

3.3 Three-Dimensional Waveguides

3.3.1 Waveguide Types

Slab waveguides have limited uses in planar integrated circuits and 3D waveguides are better suited because the light is confined in two dimensions stopping losses due to

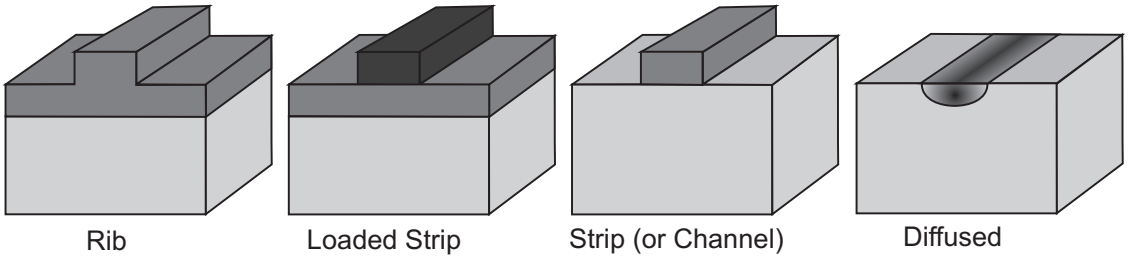

FIGURE 3.2: 3D waveguide types.

diffraction and allowing for guiding geometries that can steer the light on chip. 2D waveguides are simple and, as has been described in Section 3.2, the guiding is well understood. When the propagating wave is bound in two dimensions in a dielectric medium the problem is more difficult to analyse as the modes are not TE or TM polarised, but quasi-transverse electromagnetic (TEM) modes polarised in the x-axis and y-axis. Accurate approximations can be achieved by numerical calculations of which a comparison of numerical methods is found elsewhere [170].

Practical planar waveguides come in several geometries as shown in Figure 3.2. The rib waveguide is formed by not etching all the way through the higher refractive index film. The raised part in the film will have a higher effective refractive index than the etched parts allowing for total internal reflection. The loaded strip waveguide involves having a strip of higher refractive index than the substrate but lower than the film making the region in the film where the strip is has a higher effective refractive index than the rest of the film. The strip or channel waveguide can be thought of as a rib waveguide with the slab part of the film completely removed. This geometry has the advantage of being more symmetrical than the rib waveguide, thus simpler to analyse and gives more regular mode fields. The diffused waveguide is another alternative usually fabricated by diffusion or ion-exchange on the substrate giving rise to a higher refractive index distribution in the substrate.

The following subsection explains analytical approximations to modes of 3D waveguides.

3.3.2 Rectangular Cross-sections: Marcatili's Method

Marcatili [171] is credited with the earliest method, still effectively used, at giving analytical approximations of mode properties and field distributions. The method gives solutions to waveguides with rectangular cross-sections, dealing with both symmetric and asymmetric waveguides. The method involves first dividing the cross-section into regions as shown in Figure 3.3. The model is of a rectangular cross-section with a core region at the centre with height, h, and width, w, and are surrounded on the four sides

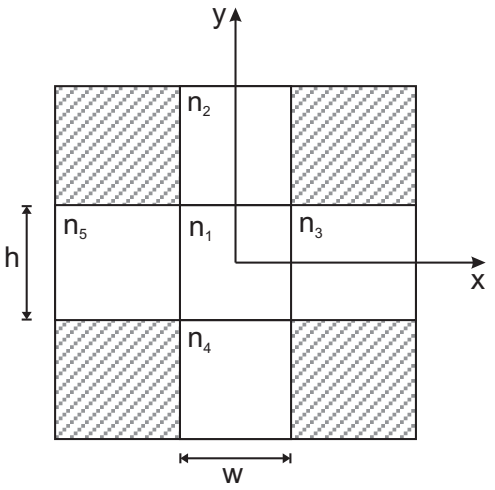

FIGURE 3.3: Marcatili's method for rectangular waveguides.

by other regions having different refractive indices. The region at the corners are neglected as there is an assumption that the modes will be confined mostly in the core, and so will only contribute to a negligible error.

The propagating wave bound in two dimensions does not have TE or TM modes as both polarisations. But, one polarisation will have $H_x = 0$ and setting this in Maxwell's equations gives a wave equation having a predominant E_x and H_y in both x-axis and y-axis and the other polarisation will have $H_y = 0$ with E_y and H_x predominant described as quasi-TE and quasi-TM, respectively. Marcatili gave the quasi-TE modes the notation E^x_{pq} and quasi-TM mode E^y_{pq}, where p and q relates to the number of field peaks in the mode. The lowest quasi-TE mode for example is E^x_{11}.

The solutions to quasi-TE modes are given here following the formulation by Okamoto [165], and are applicable for asymmetric, as well as symmetric waveguides, in both dimensions. The method involves analysing the regions 1, 3, 5 and regions 1, 2, 4 as slab waveguides in the x-axis and y-axis, respectively. The field solutions are given as

$$H_y(x,y) = \begin{cases} A\cos(k_x x - \phi)\cos(k_y y - \phi) & \text{region 1} \\ A\cos(k_x x - \phi)\cos(k_y h/2 - \psi)e^{-\gamma_{y2}(y-h/2)} & \text{region 2} \\ A\cos(k_x w/2 - \phi)\cos(k_y y - \psi)e^{-\gamma_{x3}(x-w/2)} & \text{region 3} \\ A\cos(k_x x - \phi)\cos(k_y h/2 + \psi)e^{\gamma_{y4}(y+h/2)} & \text{region 4} \\ A\cos(k_x w/2 + \phi)\cos(k_y y - \psi)e^{\gamma_{x5}(x+w/2)} & \text{region 5} \end{cases} \tag{3.22}$$

where the wavenumbers have the relation

$$
\begin{aligned}
-k_x^2 - k_y^2 + k^2 n_1^2 - \beta^2 &= 0 && (3.23)\\
\gamma_{xi} - k_y^2 + k^2 n_i^2 - \beta^2 &= 0 \quad i = 3,5 && (3.24)\\
\gamma_{yi} - k_x^2 + k^2 n_i^2 - \beta^2 &= 0 \quad i = 2,4. && (3.25)
\end{aligned}
$$

Therefore, the same treatment that is applied to 2D waveguides, Section 3.2, is used to obtain the eigenvalue dispersion equations

$$
\begin{aligned}
2\phi &= (p-1)\pi + \tan^{-1}\left(\frac{n_1^2\gamma_{x5}}{n_5^2 k_x}\right) - \tan^{-1}\left(\frac{n_1^2\gamma_{x3}}{n_3^2 k_x}\right) && (3.26)\\
2\psi &= (q-1)\pi + \tan^{-1}\left(\frac{\gamma_{y4}}{k_x}\right) - \tan^{-1}\left(\frac{\gamma_{y2}}{k_x}\right) && (3.27)\\
k_x w &= (p-1)\pi + \tan^{-1}\left(\frac{n_1^2\gamma_{x5}}{n_5^2 k_x}\right) + \tan^{-1}\left(\frac{n_1^2\gamma_{x3}}{n_3^2 k_x}\right) && (3.28)\\
k_y h &= (q-1)\pi + \tan^{-1}\left(\frac{\gamma_{y4}}{k_x}\right) + \tan^{-1}\left(\frac{\gamma_{y2}}{k_x}\right), && (3.29)
\end{aligned}
$$

allowing to obtain k_x and k_y using the relations

$$
\begin{aligned}
\gamma_{xi} &= k(n_1^2 - n_i^2) - k_x^2 \quad i = 3,5 && (3.30)\\
\gamma_{yi} &= k(n_1^2 - n_i^2) - k_x^2 \quad i = 2,4 && (3.31)
\end{aligned}
$$

obtained from the relations in Equations 3.23, 3.23 and 3.25. The propagation constant, β, of each mode can then be obtained by rearranging Equation 3.23

$$\beta^2 = k^2 n_1^2 - (k_x^2 + k_y^2). \tag{3.32}$$

The same treatment for quasi-TM modes, E_{pq}^y, can be applied. As with the analytical 2D waveguides, Marcatili's method can be implemented in most modern programming environments. Marcatili's method is not the sole method used for analytical analysis of 3D planar waveguides; another method which is discussed in the next section is the effective index method (EIM). There have been improvements made to the Marcatili method such as by perturbation theory, known as Kumar's method [172], to take into account the corner regions. Another notable improvement which also combines EIM and generalises the analysis is described by Chiang [173].

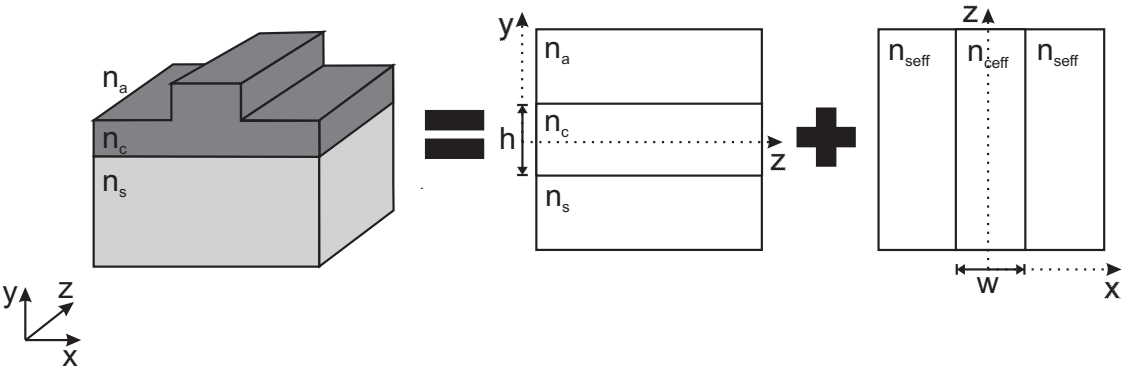

FIGURE 3.4: The effective index method applied to a rib waveguide.

3.3.3 Effective Index Method

Another useful, and simple, analytical method for mode solving is the effective index method (EIM) [165, 166, 169]. Though this method tends to give slightly less accurate results for rectangular waveguides than the aforementioned methods, it has the advantage that it can be used for waveguides with more complicated geometries such as the rib waveguide that Marcatili's method, for example, cannot analyse.

Essentially, the EIM converts the 3D structure of the planar waveguide into a 2D problem. A rib waveguide is given as an example in Figure 3.4 for EIM. The structure is divided into three parts in the x-z-plane corresponding to the structure's thicker film between two thinner film regions with effective refractive indices of n_{ceff} and n_{seff}, respectively. These effective refractive indices are obtained by solving for the effective refractive index the y-z-plane for each region which are 2D waveguides. Solving the 2D waveguide in the x-z-plane gives the 3D modes.

Another use of the EIM, due to its transformation of a 3D structure to a 2D structure, is to just perform this transformation. This then allows for many structures, not only single waveguides, to be analysed as a 2D problem in numerical simulation methods such as BPM. This speeds up numerical simulation time greatly without high loss of accuracy and uses less memory. This use of the EIM for transformation is only valid when the slab in the vertical dimension (y-axis) is singlemoded.

3.3.4 Trapezoidal Cross-sections

This subsection will introduce a concern that is relevant to rectangular cross-section waveguides. It is not uncommon that fabrication processes result in trapezoidal or quasi-trapezoidal cross-section waveguides when aiming for rectangular cross-section. Due to the nature of etching processes, the resulting feature will be the isosceles variety of trapezoid. Weakly-guiding waveguides of an isosceles trapezoidal cross-section have modes approximately equivalent to rectangular waveguides of width [174, 175], given by

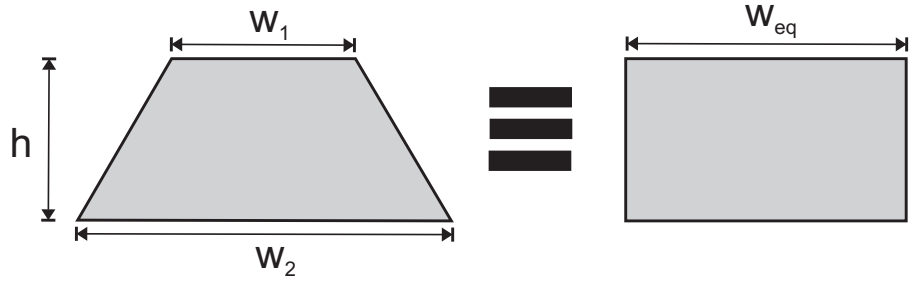

FIGURE 3.5: Trapezoidal cross-section and its equivalent rectangular cross-section.

$$w_{eq} = \frac{w_1 + w_2}{2}. \tag{3.33}$$

where w_1 and w_2 are the top and bottom widths of the trapezoid, depicted in Figure 3.5.

3.4 Beam Propagation Method

Analytical solutions for 2D and 3D waveguides have been presented. Numerical solutions can give more accurate analysis of optical structures, including waveguides, than analytical methods. The beam propagation method (BPM) is the numerical method presented here. Its used extensively in simulating the optical structures in this work and can handle waveguides well. It was chosen over the more commonly used finite difference time domain (FDTD) as it has lower computational complexity and lower memory usage with a trade-off of negligible error [165, 169].

BPM has limitations, for example, errors tend to increase in simulations with device dimensions greater than a few centimetres and BPM does not handle angled waveguides well [165], unless corrected by better function approximations such as the Padé approximations used in *BeamPROP*$^{\text{TM}}$ [176]. Calculation accuracy and time suffer when the majority of the light is propagating in the evanescent field because this requires a larger simulation window placing limits on memory.

The basic concepts of BPM are described in the following. BPM is a powerful technique to simulate wave propagation, explained in detail in the literature and the reader is referred to references [165, 169]. The 3D scalar wave equation is

$$\frac{\partial^2 E}{\partial x^2} + \frac{\partial^2 E}{\partial y^2} + \frac{\partial^2 E}{\partial z^2} + k^2 n^2(x, y, z) E = 0, \tag{3.34}$$

where E is the electric field, k the wavenumber, and n is the refractive index distribution. The electric field can be expressed in two parts, a slowly varying envelope ϕ, and a propagation term along z,

$$E(x, y, z) = \phi(x, y, z) \exp(-ikn_0 z). \tag{3.35}$$

Substituting Equation 3.35 into Equation 3.34

$$\nabla^2 \phi - i2kn_0 \frac{\partial \phi}{\partial z} + k^2(n^2 - n_s^2)\phi = 0 \tag{3.36}$$

where n_s is the refractive index of the substrate and

$$\nabla^2 = \frac{\partial^2}{\partial x^2} + \frac{\partial^2}{\partial y^2}. \tag{3.37}$$

Note that, the $\partial^2\phi/\partial z^2$ has been set to zero as it is considered that the field in the z direction is slow-varying. This allows the equation to be rearranged to give,

$$\frac{\partial \phi}{\partial z} = -i\frac{1}{2kn_s}\nabla^2\phi - i\frac{1}{2n_s}k(n^2 - n_s^2). \tag{3.38}$$

The first term is the free space propagation in a material with refractive index n_s. The second term is the effect the structure, usually a waveguide of refractive index n, has on the propagation. For small incremental distances, each term is treated independently and calculated from a given input field alternately, the first then the second term, to give the output field. This procedure is continued for all subsequent steps for the duration of the simulation.

Equation 3.38 is the principal equation of BPM and it is solved at each incremental step using numerical methods. The most commonly implemented is the split-step Fourier method, FFTBPM, making use of the fast Fourier transform (FFT). An alternative method is the finite difference method BPM (FDBPM) which is considered superior and which *BeamPROP*$^{\text{TM}}$ uses [176]. FDBPM also allows for the use of transparent boundary condition (TBC) which stop unwanted effects at the boundaries of the simulation window. The next section makes use of BPM in simulating waveguides and the excitation from a waveguide into a microfluidic channel.

3.5 Waveguide Simulations

3.5.1 Introduction

Waveguide optical properties and dimensions control the mode profiles within the waveguide. Singlemode waveguides make the system behaviour more predictable by only having the fundamental mode supported. This yields advantages for simpler characterisation of the system giving predictable spotsizes so that the light coupling between planar waveguide and singlemode fibres (usually ~ 2 μm spotsize [177]) can have better matched mode profiles, thus lowering coupling losses and divergence of a beam when it enters the unbound microfluidic channel.

This section presents simulations on the mode properties of planar channel waveguides, with cladding, in particular the waveguides that are realised in Chapter 6. The waveguides have substrate and cladding index $n_s = 1.458$ and core index $n_c = 1.474$, thus having a $\Delta n = 0.016$ where $\Delta n = n_c - n_s$ for a wavelength of 633 nm. This wavelength of 633 nm was used because it is a common wavelength used for fluorescence measurements as there are several standard fluorophores that are excited at this wavelength.

First, a study on channel waveguides with rectangular cross-sections is presented as the ideal channel waveguides in planar fabrication. However, in practice, planar fabrication leads to channel waveguides with trapezoidal or quasi-trapezoidal cross-sections. Therefore, for comparison with channel waveguides of rectangular cross-sections, a study on channel waveguides with trapezoidal cross-sections was done. The limitations placed by planar fabrication and the trade-off between making the waveguide as large as possible whilst operating in the fundamental mode, to make it easier to couple from optical fibre by having better mode matching, led to the decision of fabricating channel waveguide widths of 2 μm. Waveguides were fabricated in close proximity and the expected extent of coupling between them is studied here theoretically. Lastly, simulations of light entering a microfluidic channel perpendicular to a waveguide are proposed. Further simulations were done on the free beam which defines the excitation volume within a microfluidic channel and this is dependent on the divergence of the beam and limited by its Rayleigh range.

3.5.2 Rectangular Cross-section Waveguides

For waveguides of height, h, the spotsize of the fundamental mode, ω, is determined by the waveguide width, w, in two regimes illustrated in Figure 3.6. In the first regime, where w is small enough for the fundamental mode to be near cut-off, more light is guided in the evanescent field and the spotsize in both the x-axis and y-axis increases the smaller the waveguide. In the second regime, the fundamental mode is confined well

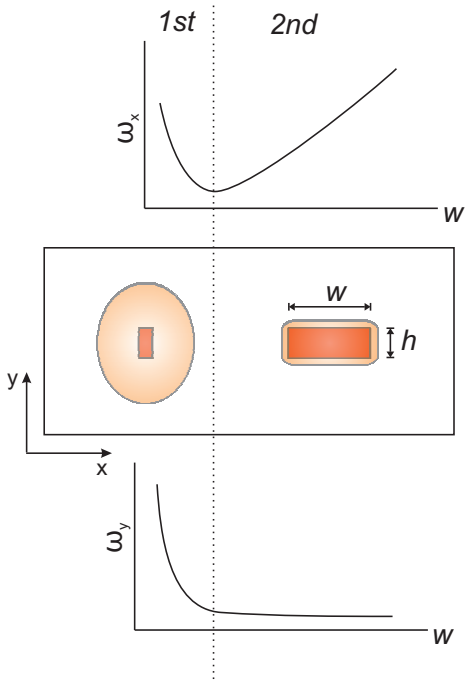

FIGURE 3.6: Diagram illustrating that in large width waveguides spotsize in vertical direction is independent on waveguide width. The opposite is true for small width waveguides.

in the core and follows w closely. The second regime is the preferred regime of operation as the waveguides are easier to fabricate being larger than for the first regime.

Figure 3.7 shows the dispersion of a rectangular of waveguide 2 μm height showing effective index of the waveguide, n_{eff}, with respect to waveguide width. This shows that

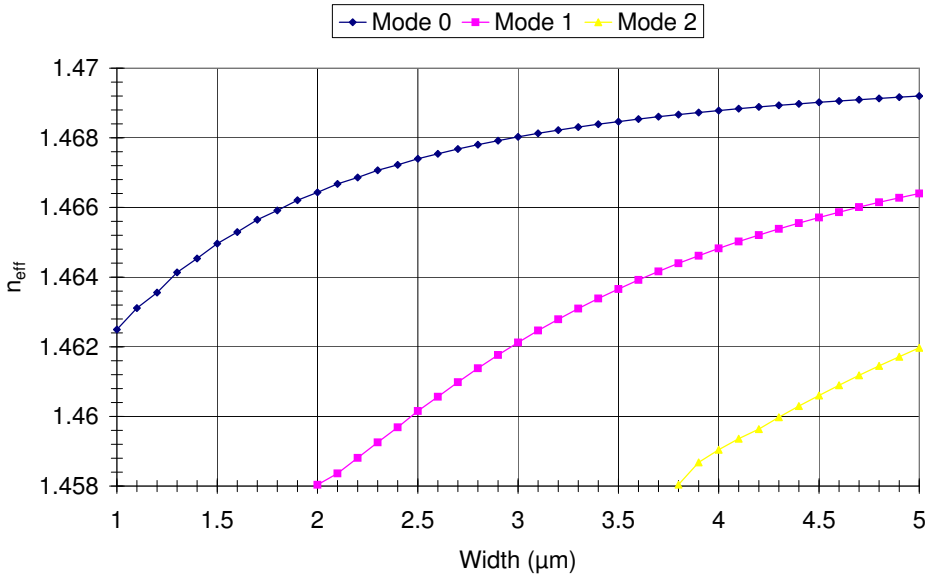

FIGURE 3.7: Mode dispersion graph with respect to rectangular waveguide width.

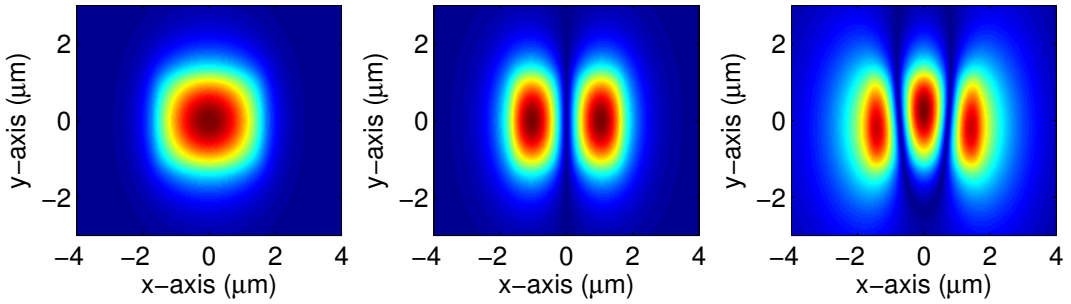

FIGURE 3.8: Mode profiles of a simulated rectangular waveguide with a 4 μm width and 2 μm height.

for singlemode operation the waveguide width should not exceed 2 μm, the cut-off of a second mode. The cut-off of a third mode is found at 3.8 μm.

If the waveguide is not singlemode, the first three modes expected are shown in Figure 3.8. These mode profiles are for a rectangular waveguide with 4 μm width to make sure that these modes are supported. The modes correspond to Maracatili's notation of E^x_{11}, E^x_{21} and E^x_{31}, but since the modes have peaks only on x-axis the modes are referred to as mode 0, mode 1, and mode 2, respectively.

Here, BPM simulations on the effects of waveguide dimensions on spotsize are presented. Figure 3.9 shows the spotsize of the fundamental mode in the x-axis versus the waveguide width with varying Δn for a rectangular waveguide of 2 μm height. The graph shows the behaviour described in Figure 3.6. The first regime moves below 1 μm with increasing Δn. For both regimes, the spotsize decreases with increasing Δn as the mode is confined more to the core. In the second regime, the spotsize increases almost linearly with increasing width. Figure 3.10 shows the spotsize of the fundamental mode in the y-axis versus the waveguide width with varying Δn for the same waveguide. The graph shows the two regimes. The first regime decreases with increasing Δn. In the second regime, the spotsize has practically converged on to a constant value.

The effect of changing the height on the waveguide with $\Delta n = 0.016$ is shown in Figure 3.11. There is a small increase in spotsize in the x-axis with decrease in height. Figure 3.12 shows the spotsize in the y-axis with varying height; the spotsize increases with increasing height.

The ideal waveguide for this project would be a rectangular cross-section waveguide. Singlemode behaviour is ideal and therefore the waveguide can only have a maximum width of 2 μm. The waveguide should be kept as large as possible for better coupling to fibre and made symmetrical to minimise birefringence due to geometry, therefore a width and thickness of 2 μm should be used. Furthermore, photolithography is made easier and more accurate if the waveguide dimensions are kept as large as possible. The properties of rectangular waveguides have been simulated, but the waveguides realised

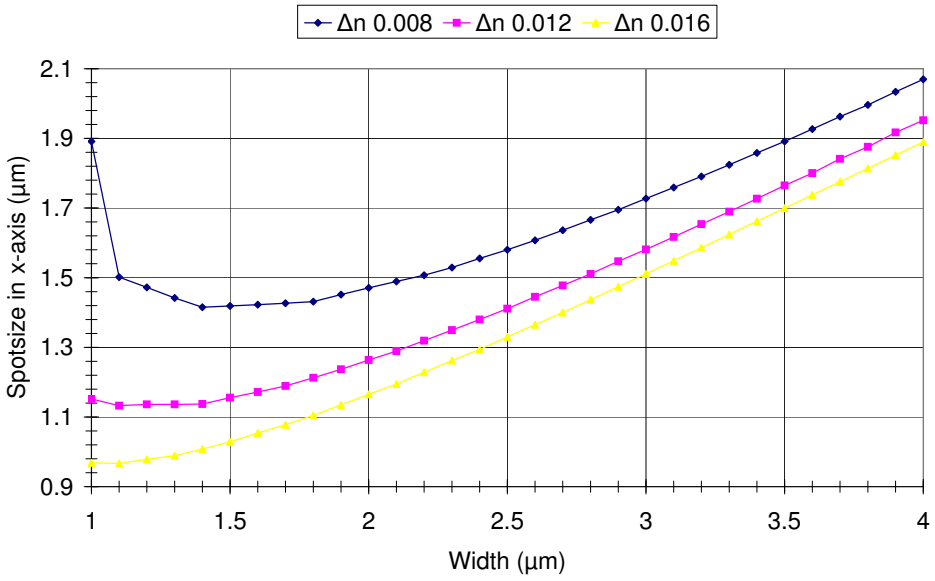

FIGURE 3.9: Spotsize of the fundamental mode in the x-axis versus the waveguide width of a rectangular waveguide of 2 μm height with varying Δn.

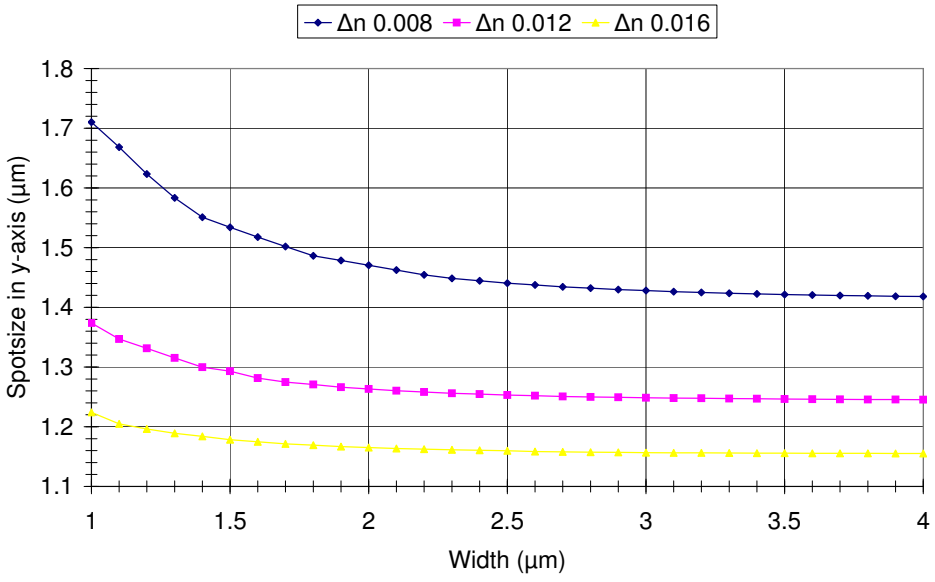

FIGURE 3.10: Spotsize of the fundamental mode in the y-axis versus the waveguide width of a rectangular waveguide of 2 μm height with varying Δn.

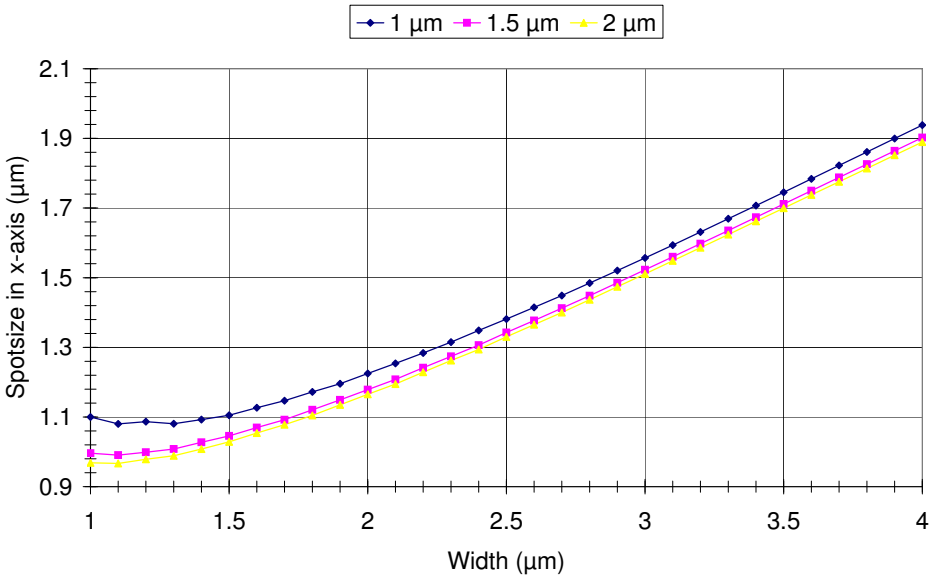

FIGURE 3.11: Spotsize of the fundamental mode in the x-axis versus the waveguide width of a rectangular waveguide of $\Delta n = 0.016$ with height of 1, 1.5, and 2 μm height.

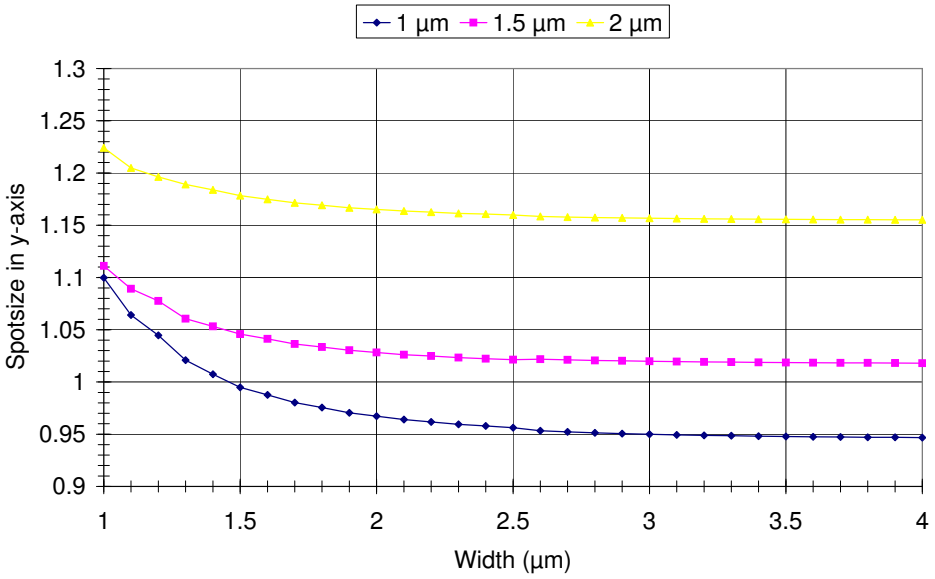

FIGURE 3.12: Spotsize of the fundamental mode in the y-axis versus the waveguide width of a rectangular waveguide of $\Delta n = 0.016$ with height of 1, 1.5, and 2 μm height.

are known to have trapezoidal or quasi-trapezoidal cross-sections. The next subsection simulates trapezoidal cross-section waveguides.

3.5.3 Trapezoidal Cross-section Waveguides

It was mentioned in Subsection 3.3.4 that for fabrication of real waveguides it is common for rectangular waveguides to exhibit trapezoidal or quasi-trapezoidal cross-sections. This is confirmed by the experimental results in Chapter 6. From the microscope images and the profiler measurements taken of the waveguides, a model of an isosceles trapezoid with dimensions of 2 μm top width, 5 μm bottom width, and 2 μm height was used for simulations. The trapezoid angles are kept the same throughout the simulations, so when the width of the top of the waveguide is changed, the bottom width changes by the same amount (e.g. 1 μm top width has a 4 μm bottom width).

Figure 3.13 shows the result of simulations of a trapezoidal cross-section waveguide showing effective index of the waveguide, n_{eff}, with respect to waveguide width. Modes 0, 1, and 2 have cut-offs below 1 μm which BPM was not able to simulate accurately. A waveguide with this cross-section geometry with Δn of 0.016 cannot be to be singlemode.

The first three modes to expect are shown in Figure 3.14. These mode profiles are for a rectangular waveguide with 4 μm width to make sure that these modes are supported. Comparing with Figure 3.8, the profiles are not symmetrical in the y-axis as the rectangular waveguides.

Simulations for the characteristics of the spotsize with varying parameters, as for rectangular waveguides, are presented here for trapezoidal waveguides as a comparison. The

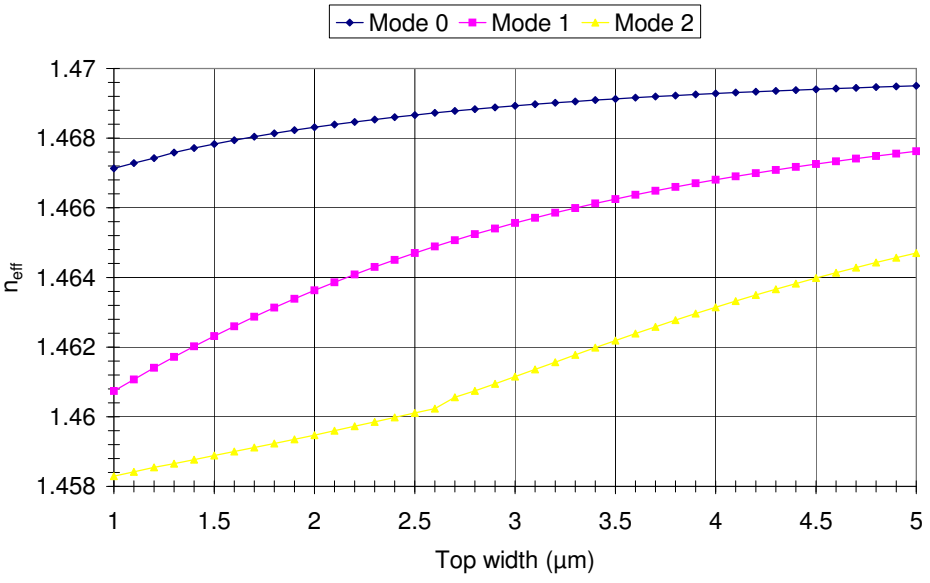

FIGURE 3.13: Mode dispersion graph with respect to trapezoidal waveguide width.

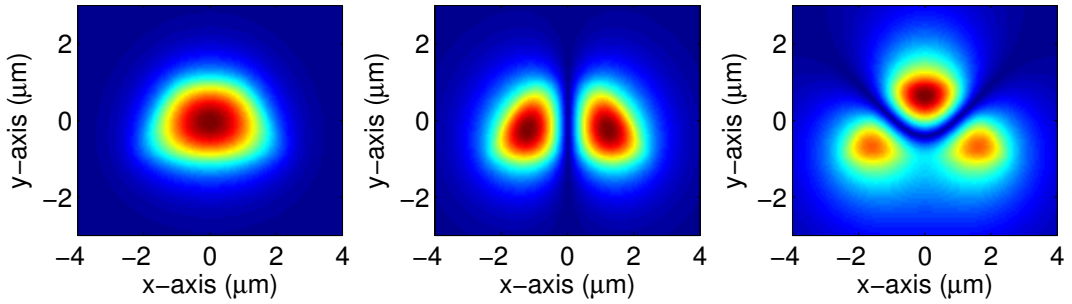

FIGURE 3.14: Mode profiles of a simulated trapezoidal waveguide with a 4 μm width and 2 μm height.

trapezoidal waveguide has a height of 2 μm. The spotsize in the x-axis versus the waveguide width with varying Δn is shown in Figure 3.15. For the range of widths from 1 μm to 4 μm, there is no visible first regime. Subsection 3.3.4 described how an approximation for trapezoidal waveguides into rectangular waveguides can be made. The approximation agrees well for the range of Δn given. Comparing Figure 3.9 with Figure 3.15 trapezoidal waveguides with top width from 1 to 3.5 μm linearly corresponds to w_{eq} of 2.5 μm to 4 μm.

Figure 3.16 shows the spotsize in the y-axis versus the waveguide width with varying Δn. The n_{eff} converges to a value with increasing width, but unlike the rectangular waveguides the convergence is increasing, not decreasing. Again, the approximation to a rectangular waveguide is good when comparing with Figure 3.10.

The effect of changing the height on the waveguide is shown in Figure 3.17. The Δn is 0.016 and the heights are 1, 1.5, and 2 μm. Figure 3.18 shows the spotsize in the y-axis for the different heights. The spotsize increases with increasing waveguide height in both x-axis and y-axis. This is the opposite behaviour for rectangular waveguides in the x-axis in Figure 3.11.

Trapezoidal waveguides show slight differences in optical behaviour to those of rectangular waveguides, and while an approximation can be made, the differences are notable, most noticeably in the mode profiles not being as symmetrical. The simulations have shown that the trapezoidal waveguides have three modes for a top width down to 1 μm with a 2 μm height. As with the rectangular waveguides simulated in Section 3.5.2, the trapezoidal waveguides should be as symmetrical as possible and as large as possible for better coupling to fibre and easier and more accurate photolithography. A practical aim, then, would be to make the waveguides with any top width up to 2 μm. However, the dimensions are ultimately limited by the fabrication process.

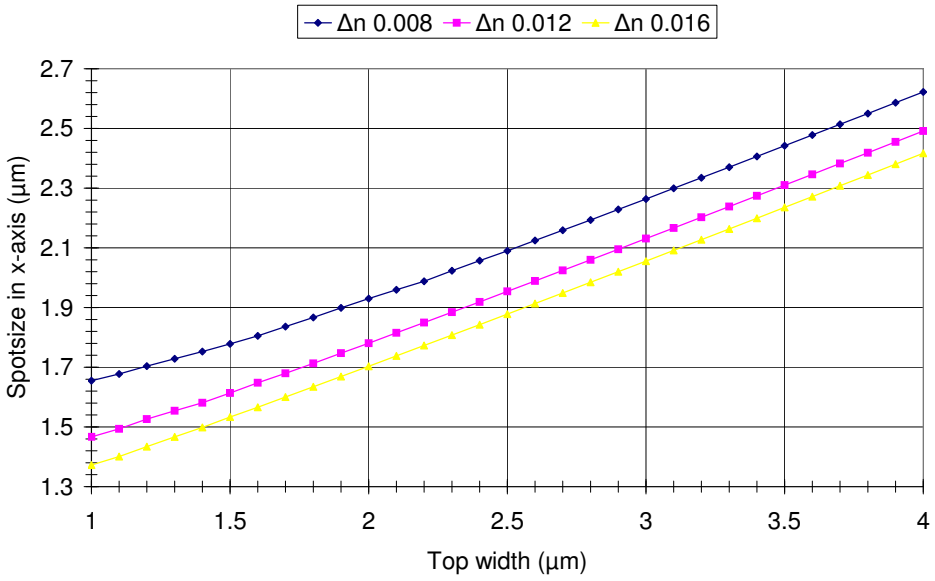

FIGURE 3.15: Spotsize of the fundamental mode in the x-axis versus the waveguide width of a trapezoidal waveguide of 2 μm height with varying Δn.

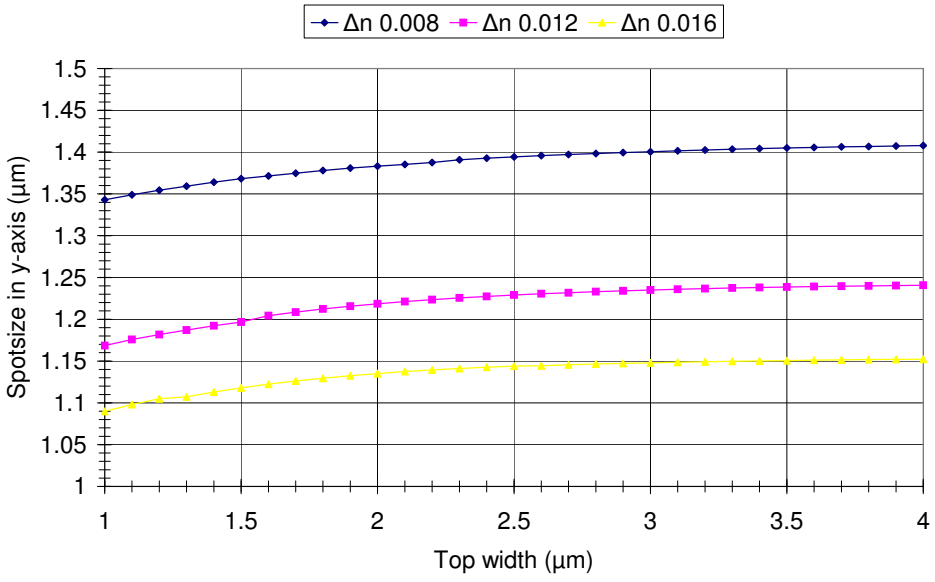

FIGURE 3.16: Spotsize of the fundamental mode in the y-axis versus the waveguide width of a trapezoidal waveguide of 2 μm height with varying Δn.

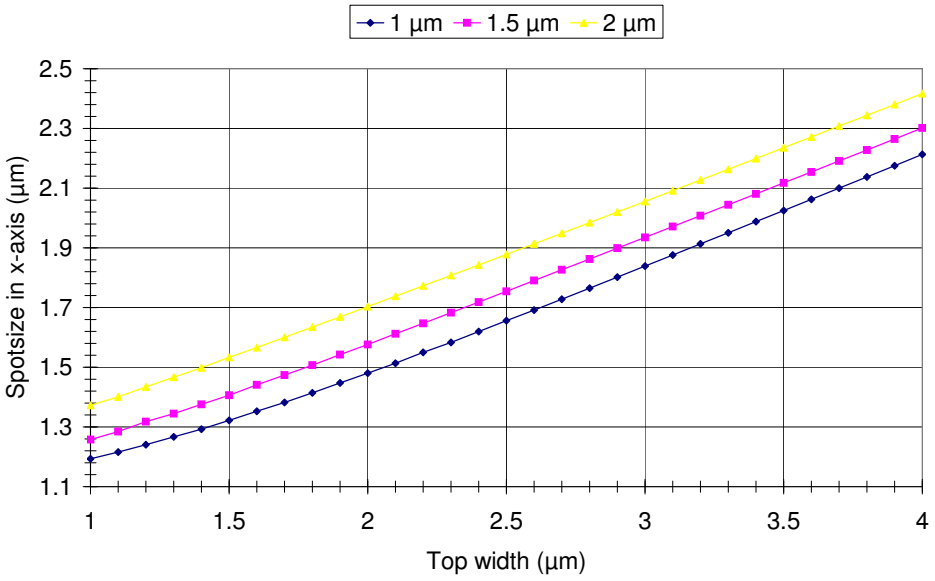

FIGURE 3.17: Spotsize of the fundamental mode in the x-axis versus the waveguide width of a trapezoidal waveguide of $\Delta n = 0.016$ with height of 1, 1.5, and 2 μm height.

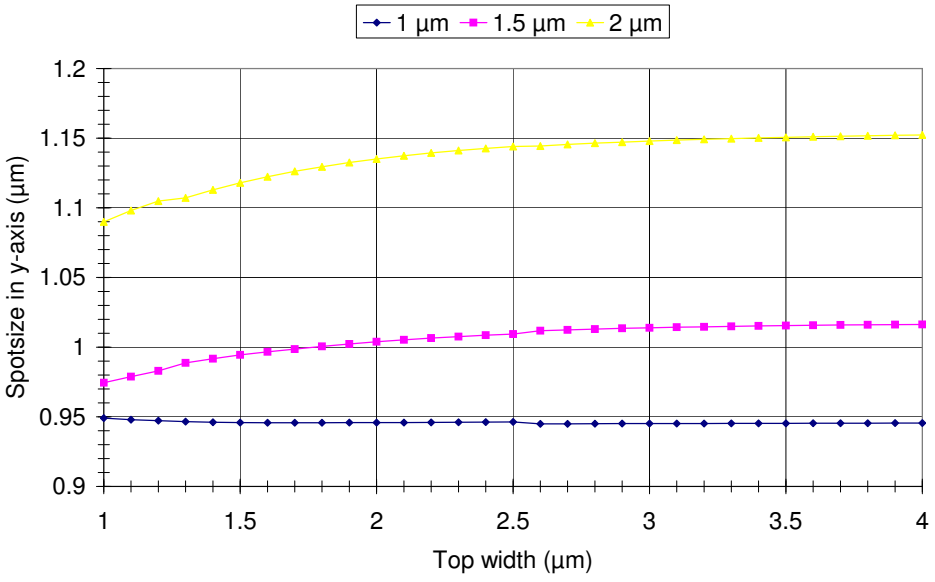

FIGURE 3.18: Spotsize of the fundamental mode in the x-axis versus the waveguide width of a trapezoidal waveguide of $\Delta n = 0.016$ with height of 1, 1.5, and 2 μm height.

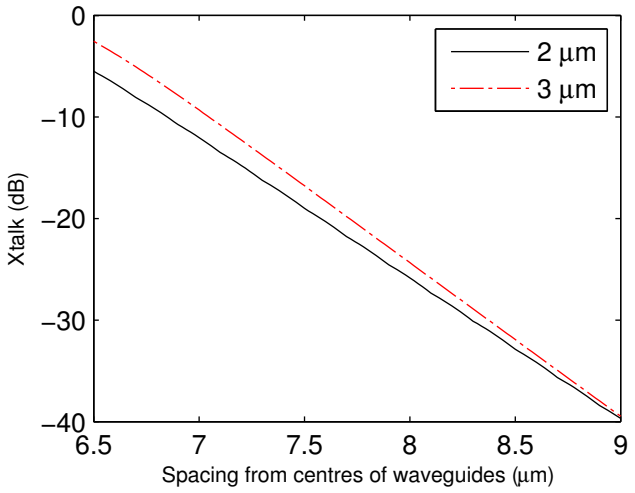

FIGURE 3.19: Crosstalk between two adjacent waveguides of 2 μm and 3 μm for a length of 50 mm.

3.5.4 Directional Coupling between Waveguides

Integrated optics often requires waveguides to be in close proximity. Therefore, it is valuable to know the coupling between the waveguides. An analytical method could be used to analyse the coupling such as mode coupling theory [164, 165, 169]. However, numerical BPM simulations give accurate results [165] and was the tool chosen as it was already in use in the project.

Figure 3.19 shows the loss in a waveguide due to coupling to another identical waveguide versus the spacing of the rectangular waveguides for widths of 2 and 3 μm for a length of 50 mm, which is the maximum length that realised waveguides were designed for. The minimum spacing is 6.5 μm as lower spacing gave very strong coupling. A minimum spacing between waveguides of 8 μm should be applied to mask designs as the coupling would be at an acceptable level of below -20 dB crosstalk.

3.5.5 Excitation in a Microfluidic Channel

This chapter has used BPM as a numerical tool for analysing waveguides, but the method is suitable to simulate complex integrated optics. This section describes a model of a system consisting of a rectangular channel waveguide perpendicular to a microfluidic channel. The rectangular waveguide is buried so that it is positioned at the middle of the microfluidic channel depth. The basic system in Figure 3.20 describes the layout and dimensional parameters. These are the waveguide dimensions width w and height h, and the microfluidic channel dimensions width W and height H. The waveguide has a Δn of 0.016 with the surrounding medium n_s of 1.458 and the liquid in the microfluidic channel refractive index, n_w, 1.33, since the fluid is assumed to be water.

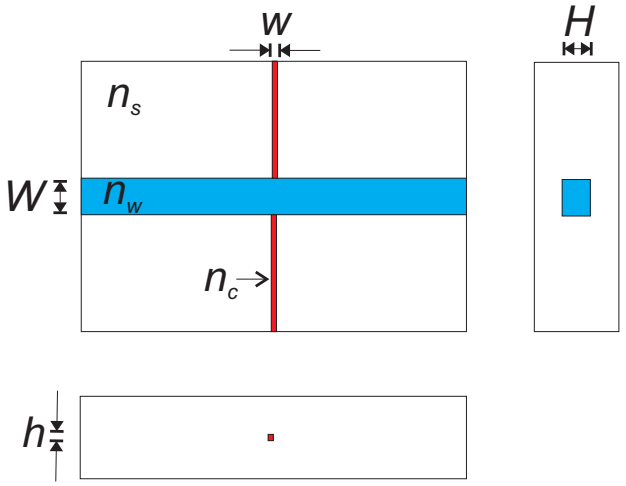

FIGURE 3.20: Model of rectangular waveguide buried on a substrate with cladding of same material crossed by a microfluidic channel filled with water. The microfluidic channel has a width W and height H and a refractive index n_w, the waveguides have a width w and a height h and refractive index n_c whilst that of the substrate is n_s.

The microfluidic channel dimensions must be determined primarily from the size of particles one expects to pass through the channel, which will depend on application. Default values were chosen for the simulations to reflect common values found in such a device. The microfluidic channel parameters W and H are varied up to 100 μm and set at 50 μm respectively, and the waveguide parameters w and h are both set at 2 μm because this was the ideal dimensions for the rectangular waveguide in Section 3.5.2. The values for the microfluidic channels are based on a microfluidic device being developed at this University's School of Electronics and Computer Science by Dr. Benazzi, itself based upon a previous device with a smaller microfluidic channel [178]. A wavelength of 633 nm is used in the simulations as this is a common wavelength value for biological analysis using LIF. The previously mentioned device uses this wavelength for detection of auto-fluorescent algae.

The integrated waveguides guide the light to the microfluidic channel sidewall and once it enters the microfluidic channel the light will no longer be guided and will diverge incurring one of the largest losses in the device. Due to this divergence, not all the light will be coupled to the waveguide at the other side of the microfluidic channel sidewall.

The BPM simulations in Figure 3.21 for coupling efficiency versus microfluidic channel width show that increasing microfluidic channel width increases the loss of transmitted light as expected. The waveguides simulated have a height of 2 μm and varying widths of 2, 3, and 4 μm. The graph shows that for a propagation length of 25 μm across the microfluidic channel the efficiency is below 0.5. The trend is that the wider waveguides have lower loss due to rate of divergence being lower because of larger spotsize from the waveguide. The graph also shows the analytically determined coupling efficiency due to the microfluidic channel of a Gaussian beam [168, 179]

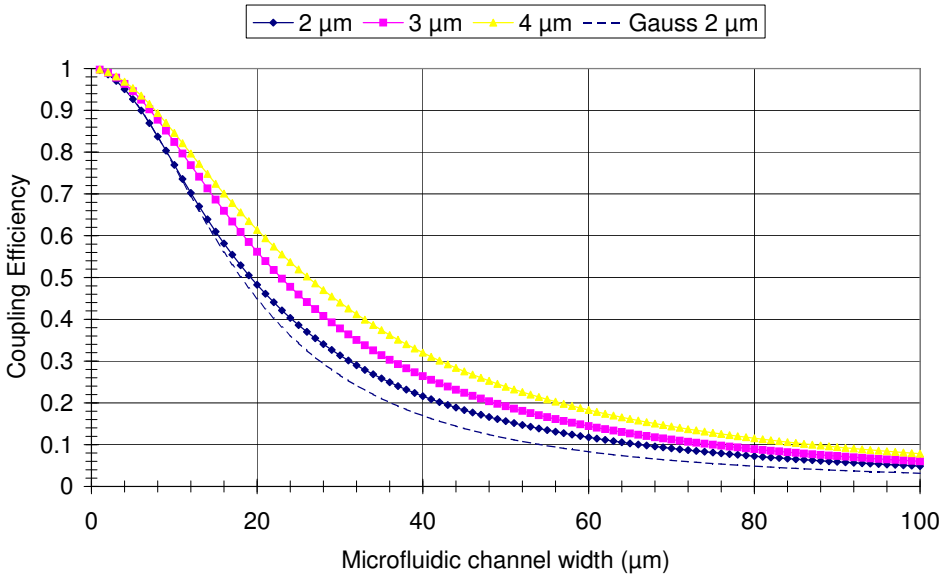

FIGURE 3.21: Coupling efficiency versus propagation length in a microfluidic channel for waveguides of 2, 3, and 4 μm. The graph shows the coupling efficiency also for a Gaussian beam with the same ω_0 as the 2 μm channel waveguide.

$$\eta = \left(1 + \left(\frac{W\lambda_0}{\omega_0^2}\right)^2\right)^{-1}, \tag{3.39}$$

with the same size spotsize, ω_0, as the rectangular waveguide of 2 μm width. It is a good approximation initially, but by 20 μm microfluidic channel width it differs due to the mode profiles not being exactly Gaussian.

The spotsize of the mode diverging from the waveguide end in the microfluidic channel is given in Figure 3.22. The simulated results of a rectangular waveguide of 2 μm height and 2 μm width is superimposed on to analytical the Gaussian beam solution with ω_0 the same as the channel waveguide.

The spotsize for the Gaussian beam is given as

$$\omega(z) = \omega_0\sqrt{1 + (z/z_R)^2} \tag{3.40}$$

where

$$z_R = \frac{n_w \pi \omega_0^2}{\lambda_0}. \tag{3.41}$$

The Gaussian beam is a good approximation for small propagation distances, but has a greater divergence than that of the channel waveguide. In terms of beam profile, the narrow waist is kept to the sidewall of the microfluidic channel. The Rayleigh range,

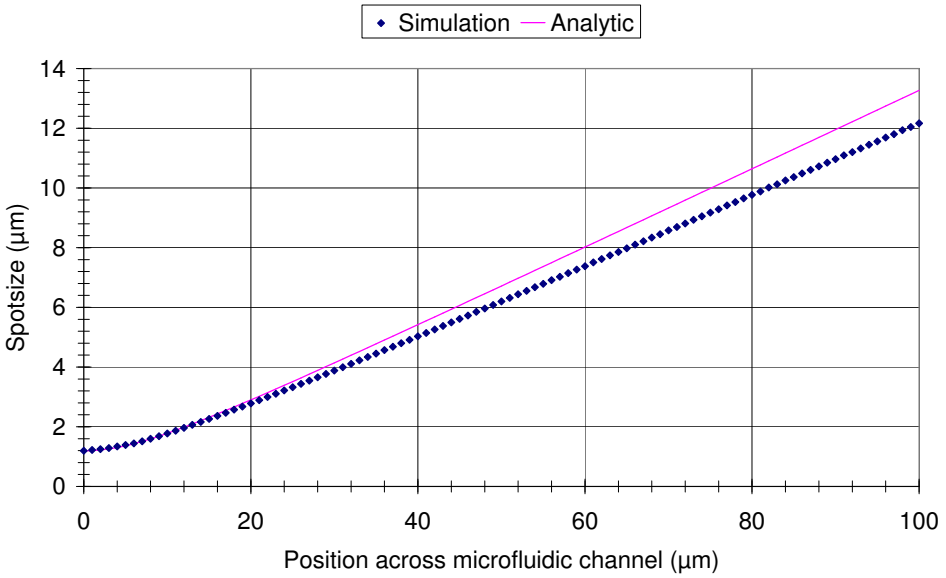

FIGURE 3.22: Simulated spotsize of light propagating the microfluidic channel compared to the analytical Gaussian beam equation versus propagation length.

z_R, is the distance where $\omega(z) = \omega_0\sqrt{2}$ and for the Gaussian beam approximation it is 9 μm. This should be the prime measure used as a figure of merit for microfluidic channel widths where the divergence is acceptable.

3.6 Conclusion

Further integration of optics into LoC technology is required for optical detection of particles in a microfluidic channel. The 3D waveguide is the basic building block for integrated optics and understanding waveguide properties allows for design of devices with predictable behaviour. A basic system for direct launching of a free beam in a microfluidic channel, using integrated optics, is to have a waveguide deliver the light into the microfluidic channel. However, 3D planar waveguides are difficult to model and analyse accurately due to their geometries. Whilst analytical solutions to 2D waveguides have been presented, analytical approximations to 3D planar waveguides must use methods such as Marcatili's or the EIM, but these methods are limited to certain geometries. The EIM has a second use for planar devices in general, which is to transform 3D problems into 2D problems. Numerical methods overcome the difficulties of analytical methods; BPM is one such tool. It has the benefit of also simulating more complex planar integrated optics structures, and so has been adopted in this thesis.

The ideal waveguide for the material system in Chapter 6 is a singlemode rectangular cross-section waveguide. However, the dimensions are ultimately limited by the fabrication process leading to practical waveguides having trapezoidal or quasi-trapezoidal cross-sections. The analytical methods give an intuitive feel to the nature of modes, but

for accuracy, the numerical BPM was used to analyse channel waveguides with rectangular and trapezoidal cross-sections. For rectangular cross-sections with a Δn of 0.016 and a substrate refractive index of 1.458, waveguides are singlemode up to a width of 2 μm. Simulations have also shown that trapezoidal waveguides have differences in some optical properties compared with those of rectangular waveguides, and while an approximation to a rectangular cross-section can be made, the most notable differences are that the mode profiles are not as symmetrical and the waveguide supports three modes for top widths down to 1 μm with a 2 μm height. It is difficult to realise singlemode waveguides with a Δn of 0.016 due to the trapezoidal cross-section. However, it is possible in practice to use waveguides with few modes in singlemode operation even for complex integrated optics [180]. Therefore, the practical waveguides to be adopted here should be made to be as rectangular in cross-section as possible and have a top width of 2 μm and a height of 2 μm, which for an ideal rectangular waveguide would keep dimensions as large as possible for better coupling to fibre, lowering fabrication tolerances, and make the cross-section symmetrical to minimise birefringence due to geometry.

To study micron-sized particles, such as biological cells, the microfluidic channels will need to be from a few microns up to a hundred microns in dimensions [181]; channel dimensions can be expected to be up to 100 μm to accommodate most cell sizes. A basic configuration of a buried channel waveguide delivering light into a microfluidic channel was simulated. Waveguides of 2 μm height and widths of 2, 3, and 4 μm the coupling efficiencies that drop to 0.5 after 25 μm of propagation along the microfluidic channel width. The beam profile in the microfluidic channel is not ideal for optical detection in microfluidics. The width of the microfluidic channel for acceptable free-beam loss from a waveguide is determined by the width of the waveguide to reduce divergence. However, this leads to either narrow microfluidic channels and larger spotsizes not ideal for fluorescent or scattering measurements. The Rayleigh range for 2 μm rectangular waveguide only has ~ 9 μm. The Rayleigh range should be the prime measure used for whether microfluidic systems need more complex optics than just a channel waveguide, but an increase of Rayleigh range involves increasing the spotsize which for many systems may be unacceptable. The maximum coupling loss due to beam divergence to the output waveguide, at the other side of the microfluidic channel width, for realised waveguides is expected to be more than 0.9. Integrated planar lenses should be built upon waveguides to focus the light compensating for the lateral divergence in the microfluidic channel and allow for wide microfluidic channels with small spotsizes where the waist could be moved to the middle of the microfluidic channel.

Chapter 4

Planar Waveguide Lenses

4.1 Introduction

A lens is a device which transmits light with an altered phase-front, thereby performing operations such as focussing or collimating. This is a necessary function for the on-chip optical analysis discussed in Chapter 1. This chapter describes the design of several planar waveguide lenses, both refractive and diffractive types, and discusses simulations which are suitable for integration into a generic planar particle detection device using the fabrication process described in Chapter 6. Lens types which are suitable for compact microfluidic systems are selected and design rules generated and structures simulated using the beam propagation method (BPM).

The use of integrated lens structures appears in the literature for the purpose of creating high intensity in the middle of a microchannel for fluorescence and scattering detection methods. Many examples are polymer devices using moulding or stamping methods of fabrication. Wang *et al.* [36] demonstrated a device consisting of waveguides and a single circular focussing lens protruding into the microfluidic channel wall for scattering measurements of microparticles, but with a drawback of perturbing the structure of the channel and thus its flow.

Integrated systems can be designed to have input and output fibres responsible for delivery of light directly to the lens [182] and can also be designed by simple moulding processes; the lenses do not interfere with microfluidic flow, as they are located away from the microchannel [183]. Seo and Lee [184] presented a disposable PDMS planar microfluidic device with aligned refractive circular microlenses fabricated in the same step as the microchannel. The device showed better sensitivity compared to a system with a single circular lens and without a lens. The lenses were arranged as a compound lens to reduce severe aberrations. The planar fabrication is simple and optical alignment with microchannels was done at fabrication. The disadvantage of the design was that the

light was unguided, yielding higher losses. Microfluidic lenses, made from microfluidic lens-shaped chambers with microfluidic channels as fluid connectors, have shown some interest as they can be tuned by changing the characteristics of the fluid in them [185] or the pressure of the fluid to modify the lens shape in the elastic polymers [186].

To achieve the phase changes required for a lens function either the geometries or the refractive index (GRIN) distribution within the lens or both may be varied. Since GRIN lenses are not considered for fabrication in this work they are also not considered in detail in this chapter, but will be referred to for completeness. Luneburg and geodesic lenses, though having the best performance compared to other waveguide lenses to date, shall not be considered as they are not fabricated using planar lithographic processes [164, 187–190].

When designing lenses four criteria should be considered: (1) high focussing efficiency (low aberrations and diffraction into one order if applicable), (2) predictable focal spot size and location, (3) low loss in the lens region, and (4) easy integration into existing fabrication processes. This chapter will not address the theory of aberrations as the lenses described are of *ideal* design and aberrations would be considered to be low or contributed by fabrication tolerances in real devices. For more in depth discussion of the theory of aberrations the reader is directed to the appropriate textbooks [120, 191–193]. In this chapter, the negative lens configuration is identified as the best suited for planar device. This involved having the general expressions for defining lenses, not just the positive lens formulations found in the literature. The use of BPM to compare candidate lenses finds that practically the paraxial kinoform lens is the most efficient of the candidate lenses to focus the end of a waveguide in the middle of a microfluidic channel.

4.2 Waveguide Lenses

Planar lenses can be fabricated without any integration to waveguides [184]. If a waveguide is employed to improve the configuration of the system, the lenses have to be designed with waveguide theory in mind taking into account modes and their effective refractive indices. Having waveguiding structures allows for lower losses on-chip and for other operations to be performed on the light by integrated devices.

Figure 4.1 illustrates the side cross-sections of candidate lens regions created in a slab waveguide, (a) a thicker waveguide region for a positive lens and (b) a thinner waveguide region for a negative lens. These have the advantage that the light is confined in the vertical dimension when passing through both regions. There will be an associated coupling loss between modes in the lens region and waveguide. Types (c) and (d) are weak guiding waveguides and need to be etched all the way through the waveguide for a practically large enough index change. This has the disadvantage of no guiding in the

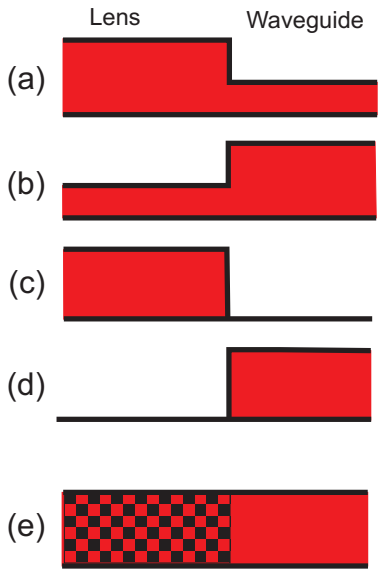

FIGURE 4.1: Cross-section along waveguide lenses in the z-axis.

etched region, thus increasing the losses at the interfaces. Type (e), for completeness, shows the index change created by ion exchange diffusion or implantation, for example.

4.3 The Refractive Lens

The refractive lens was the first type of lens to be developed by humans shaping transparent materials for useful optical functions. Refraction is caused by a wave changing its velocity upon entering a medium with a different refractive index to the incident medium. Refraction has been described by the well known Snell's Law,

$$n_i \sin\theta_i = n_t \sin\theta_t \tag{4.1}$$

where n_i and n_t are the refractive indices of the incident and transmitting mediums respectively, and θ_i and θ_t are the angles of incidence and transmittance of the wave respectively taken between the normal of the interface of the two materials and the ray.

A curvature to the interface between two media with different refractive indices has been commonly used to create lenses. Bulk refractive lenses are usually split into two groups with respect to their shape: aspherical and spherical. Spherical lenses have proven to be suitable for general purpose lenses but suffer from aberrations outside the paraxial approximation. These aberrations can be reduced using a combination of lenses [120]. Spherical lenses are not, therefore, optimum for certain functions a lens performs, such as collimating light from a point source. However, due to relative simplicity in bulk optics manufacturing, spherical lenses are much more commonly used than aspherical lenses.

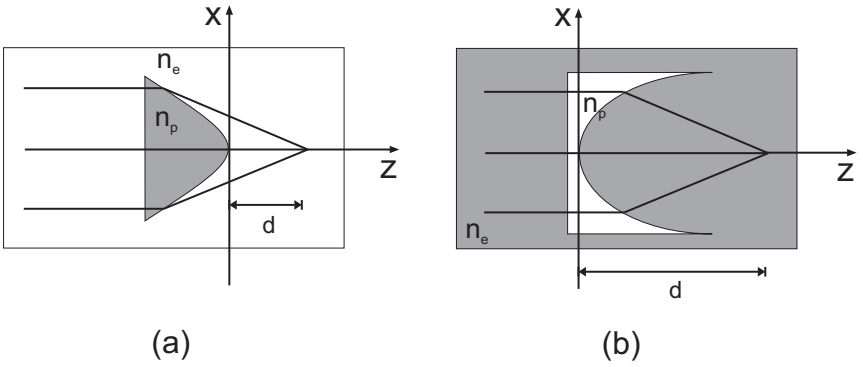

FIGURE 4.2: Hyperbolic (a) and elliptical (b) collimating refractive lenses. The shaded areas regions of higher effective refractive index. The vertices of the lenses are at the origin and rays illustrate its function.

In planar optics, since the lenses are modelled as two-dimensional (2D), the equivalent to spherical and aspherical lenses are referred as circular and acircular, respectively.

To create a planar waveguiding refractive lens, there must be a difference in the effective modal refractive indices. Refractive regions can be manufactured lithographically in a waveguide structure by either increasing or decreasing the height of a guiding layer or depositing another higher index layer on the guiding layer, or by doping the region. Since planar waveguide lens fabrication does not resemble that of bulk lens fabrication, difficulties in acircular compared to circular lens fabrication do not arise since the geometries of the lenses are determined by the masks used.

The function needed from a lens to focus a guided beam into a microchannel is to focus a diverging point source from the end of a channel waveguide. A simple case of collimating a point source which may then be used to perform such a function is presented. The optimum lens shape can be calculated from Fermat's principle which states that the optical path of a light ray travelling between two points is stationary with variations to the path taken [120, 193]. This means that the optical path will either be a minimum, maximum or point of inflection with respect to variations in the path.

The optimum shape for the profile of the lens is found to be a hyperbola or ellipse if the lens is of a higher (positive lens) or lower (negative lens) refractive index than the surrounding medium, respectively [194]. Such lenses are depicted in Figure 4.2 in Cartesian coordinates. For a plane wave propagating along the z-axis and with the vertex of the lens at the origin the lens profile is given by

$$\frac{(x-a)^2}{a^2} + \frac{z(x)^2}{\zeta b^2} = 1, \qquad x \leq a \tag{4.2}$$

$$a = d\left(\frac{1}{n+1}\right), \quad b = d\left(\frac{|1-n|}{1+n}\right)^{\frac{1}{2}}, \quad \zeta = \mathrm{sgn}(1-n), \tag{4.3}$$

where d is the focal distance from the lens vertex at the origin to the focal point, and $n = n_p/n_e$, n_p being the refractive index of the lens, and n_e the refractive index surrounding the lens. The thickness of the lens is determined by the eccentricity of the hyperbola or ellipse and is equal to n. Therefore, it is difficult to realise an efficient lens with low F number ($F = d/D$, D the aperture) without the lens thickness becoming impractically large because, in practice, the difference between n_p and n_e is likely to be small. To overcome this, kinoform lenses using refraction and diffraction will be introduced which provide larger aperture whilst keeping the lens thickness small and more suited to compact chip design. Refractive lenses are considered as candidate lenses for simulation in Section 4.9.

4.4 The Fresnel Zone Plate

This section describes the most basic type of diffractive lens, the Fresnel zone plate (FZP), which is the forerunner to both kinoforms and Bragg lenses. A propagating plane wavefront can be divided into zones by a an FZP so that the optical path difference between each consecutive zone to a point at distance d from the FZP is $\lambda_e/2$, where $\lambda_e = \lambda_0/n_e$ and λ_0 is the free space wavelength, as shown in Figure 4.3. If a device achieves this by blocking (by having a reflective or absorptive medium) every other zone, the diffracted light will interfere constructively at the focal point at distance d from the device. FZPs can function as lenses, though they are not considered efficient optical lenses as they have several focal points corresponding to diffraction orders. The diffraction efficiency (power of the desired diffracted order divided by the power in all diffracted orders) is only approximately 10% [195]. This does not fully quantify the efficiency of the system as aberrations are not taken into account.

To make FZPs more efficient, instead of blocking alternate zones, a transmissive structure (first made by R.W. Wood, as mentioned in reference [120]) is used, which retards the wave by a phase shift of π every alternate zone. This increases the irradiance at the focal point by a factor of four. This *phase* FZP is the basic structure to be built upon to design and make more efficient diffractive lenses in the following sections and is referred to as the FZP.

To design an FZP the relation of the zones for a known focal point, d, is the optical path of the diffracted ray at the zone edge, x_m, for constructive interference, is equal to the hypotenuse using Pythagoras' theorem. This and its approximation is given by [187, 195],

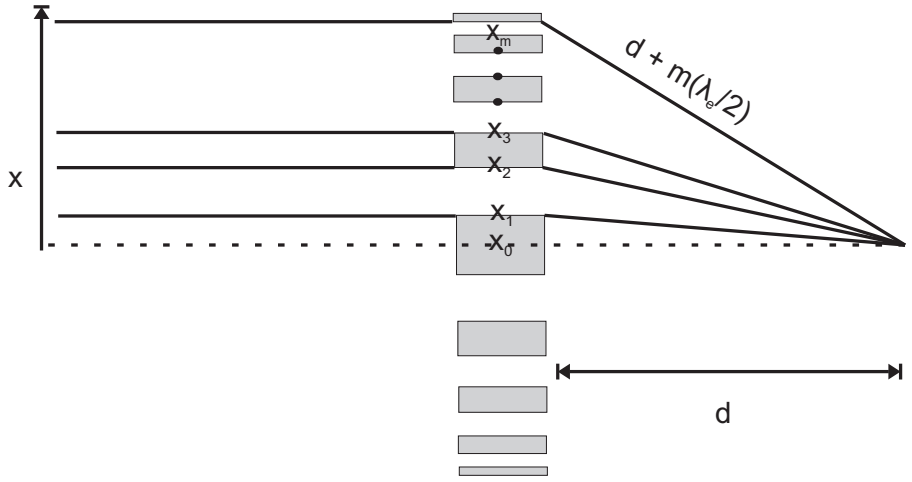

FIGURE 4.3: The geometry of an FZP in focussing a plane wave to a point.

$$x_m^2 + d^2 = \left(d + m\frac{\lambda_e}{2}\right)^2 \tag{4.4}$$

$$x_m^2 = m\lambda_e d + \left(\frac{m\lambda_e}{2}\right)^2 \tag{4.5}$$

$$\approx m\lambda_e d, \tag{4.6}$$

where m is the zone number and λ_e is the effective wavelength of the propagating waveguide mode. The paraxial approximation commonly made neglects the second order term in λ_e.

The diffraction efficiency, which describes how much power is contained in each diffracted order of a phase grating, can be calculated using Fourier optics [196]. Applying this method to the FZP shown in Figure 4.3 with a transmission function, t, defined by

$$t(x) = \begin{cases} +1 & \text{for} \quad x_m^2 \le x^2 < x_{m+1}^2 \\ -1 & \text{for} \quad x_{m+1}^2 \le x^2 < x_{m+2}^2. \end{cases} \tag{4.7}$$

The function is periodic, it can be decomposed into a Fourier series with complex coefficients as follows

$$t(x) = \sum_{q=-\infty}^{\infty} c_q \exp\left(i\frac{\pi q}{\lambda_e d}x^2\right) \tag{4.8}$$

$$c_q = \begin{cases} \frac{2}{i\pi q} & \text{for odd } q \\ 0 & \text{for even } q. \end{cases} \tag{4.9}$$

The diffraction efficiency η_q for diffraction order q is found as

$$\eta_q = c_q c_q^* = \left(\frac{2}{\pi q}\right)^2 \quad \text{for odd } q, \tag{4.10}$$

so that the maximum efficiency for diffraction into the first order is ∼40%.

The Fourier optics transmission function of a thin lens is used to find the focal distances of the FZP for an input effective wavelength λ [196]:

$$t = \exp\left(-i\frac{\pi}{\lambda d}x^2\right). \tag{4.11}$$

Comparing this equation with the transmission function given for the FZP in Equation 4.8, it is clear that the focal distances for the FZP are given by

$$d_q = -\frac{\lambda_e d}{\lambda q}, \quad q \quad \text{is odd.} \tag{4.12}$$

The focal distances are the diffraction orders of the FZP with the principal focus being the furthest from the lens at distance d and having the strongest power, shown in diagram in Figure 4.4. This is the main reason why FZPs suffer from high aberrations, as the observed wavefront at distance, d, will consist of a superposition of the unwanted diverged orders. The difference between λ and λ_e is that the former is the actual effective wavelength and the latter is the designed effective wavelength. The wavelength mismatch ratio, λ_e/λ, is useful as it describes the chromatic behaviour of the FZP as well as the effect of realising a different refractive index in the material system than

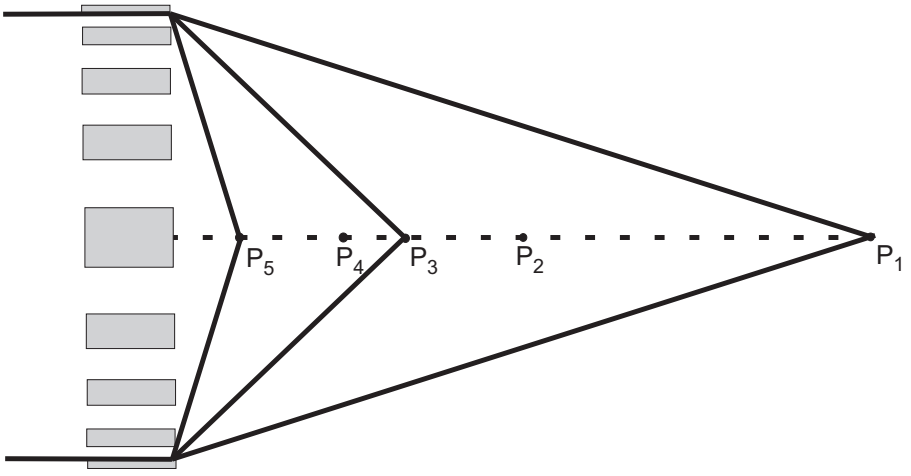

FIGURE 4.4: Diagram representing the FZPs first five diffraction order focal points, P_q. The FZP has several focal points corresponding to diffraction orders. Only the odd orders have light focussed into to them the evens have none.

that designed; the focussing orders do not change only the focussing distances of the FZP orders are affected by a change in actual effective wavelength from the designed effective wavelength. The minus sign is needed because counter-intuitively negative orders correspond to a positive lens and positive orders to a negative lens. A correction for this could be made by replacing q with $-q$ [197].

One may wonder if the other orders are of any use. As explained in the following sections, kinoform and Bragg lenses improve the diffraction efficiency by directing the power into one diffracted order. By diffracting power into a higher order the lens' F number (and its NA) is effectively increased and even allows for the design of efficient multiwavelength lenses with low chromatic aberrations, which is out of scope for this work. In this work diffracting only into the first order will allow for lower aberrations, as tolerances for fabrication are lowered. For a detailed discussion of the design of higher order lenses refer to [198–201]. The FZP will not be considered further as there are better alternatives, namely, the Bragg lens and kinoform lenses which are discussed in the proceeding sections.

4.5 The Bragg Lens

The operation of the FZP as a focussing lens and its major shortcomings in diffraction efficiency due to diffracting into many orders can be improved in design to be more efficient. In holography, gratings are designed with a sinusoidal modulation and as a thin grating gets thicker it goes from the Raman-Nath regime with many diffracted orders to the Bragg regime with one diffracted order [202].

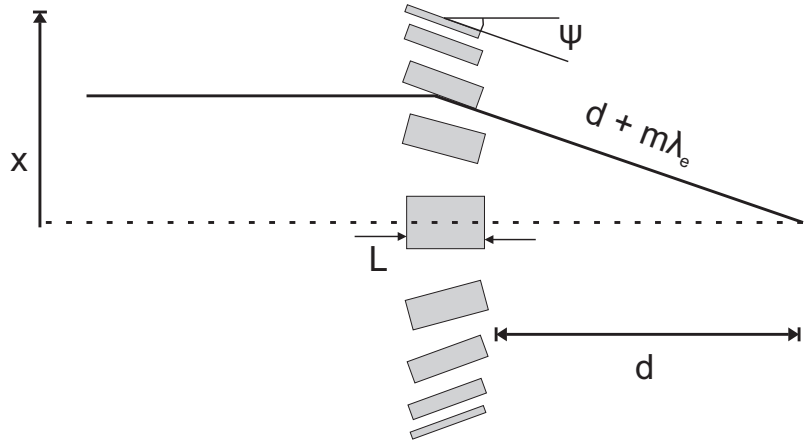

FIGURE 4.5: Bragg Lenses: A chirped Bragg grating with incident plane wave at an angle to the grating is focussed.

A lens with a sinusoidal modulation (known as a Gabor zone plate) has the well known first order maximum diffraction efficiency of $\eta_{\pm 1} = 33.8\%$ [164, 196], working in the so called Raman-Nath regime, has a poorer result than the FZP with its binary profile and a first order maximum diffraction efficiency of $\eta_{\pm 1} = 40\%$. However, if the grating is *thick* enough it operates in the Bragg regime and only diffracts into one order, so that the maximum efficiency can theoretically reach 100%.

The Q parameter gives an indication of whether a grating is in the Raman-Nath regime, where incoming light is diffracted into several orders, or in the Bragg regime, where the light is diffracted into one order,

$$Q = \frac{2\pi L \lambda_e}{\Lambda^2} \tag{4.13}$$

where L is the length of the grating, λ_e the surrounding material's effective index, and Λ the grating period. Bragg diffraction is a diffraction regime which occurs when $Q \gtrsim 10$ by making L large giving a *thick* grating. In Bragg diffraction, the diffracted ray into order q is

$$\boldsymbol{\beta}_d = \boldsymbol{\beta}_i + q\mathbf{K} \tag{4.14}$$

where $\boldsymbol{\beta}_d$ and $\boldsymbol{\beta}_i$ are the diffracted and incident wavevectors respectively and $\mathbf{K}$ the grating wavevector with its magnitude (modulus) $K = 2\pi/\Lambda$. For a thick grating $|q|$

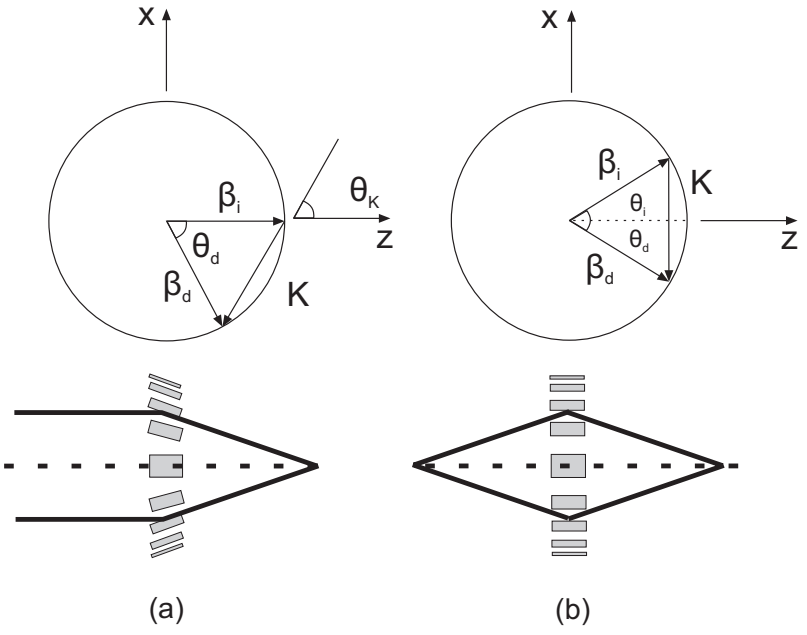

FIGURE 4.6: Wavevector diagrams depicting (a) focussing of a plane wave and (b) 1:1 imaging of a point source . $\boldsymbol{\beta}_d$ and $\boldsymbol{\beta}_i$ are the diffracted and incident wavevectors respectively and $\mathbf{K}$ the grating wavevector.

may be set to unity since only the first order is of interest. Equation 4.14 is illustrated in Figure 4.6.

A chirped Bragg grating of this type has a grating index modulation of [202]

$$\Delta n(x) = \Delta n_{max} \cos(\mathbf{K} \cdot \mathbf{r}) \tag{4.15}$$

where $\Delta n_{max} = n_p - n_e$ and $\mathbf{r}$ is the ray vector. The dot product in the cosine argument is

$$\begin{aligned} \mathbf{K} \cdot \mathbf{r} &= \beta(p_d - p_i) && (4.16) \\ &= k_0 n_e (d - \sqrt{x^2 + d^2}) && (4.17) \end{aligned}$$

where $p_i = x\cos(\theta_i) + y\sin(\theta_i)$ with $i = p, d$, the geometrical distances. The phase of the index modulation is the phase difference between the plane and converging wavefronts. Equation 4.15 becomes

$$\Delta n(x) = \Delta n_{max} \cos(k_0 n_e (d - \sqrt{x^2 + d^2})). \tag{4.18}$$

If a focussing Bragg lens is required, then the grating lines should be slanted by the angle

$$\psi(x) = -\left(\frac{1}{2}\right) \tan^{-1}\left(\frac{x}{d}\right) \simeq -\frac{x}{2d}, \tag{4.19}$$

so that the Bragg condition is met along the whole grating. The minus sign indicates the slanting for a converging lens and a plus sign for a diverging lens. Therefore, slanting the grating lines makes the lens converging for a plane wave in one direction and diverging for a plane wave in the opposite direction meaning that it is not a reciprocal lens.

The diffraction efficiency for a Bragg grating operating at the paraxial approximation is given by [164]

$$\begin{aligned} \eta_{\pm 1} &= \sin^2\left(\frac{\rho L}{\sqrt{\cos\theta_i \cos\theta_d}}\right) && (4.20) \\ &\approx \sin^2(\rho L) && (4.21) \\ \rho &= \pi \frac{\Delta n}{\lambda}, && (4.22) \end{aligned}$$

where ρ is the coupling coefficient. In the paraxial region, the thickness L does not affect the diffraction efficiency significantly, so a constant thickness can be assumed. It should be noted that the thickness should actually vary with diffracted angle because $\cos\theta_i = 1$ for a plane wave being focussed. For 100% diffraction efficiency the thickness should vary, but in practice this may be ignored in the paraxial regime.

$$\frac{\rho L}{\sqrt{\cos\theta_d}} = \frac{l\pi}{2}, \quad l = 1, 3, 5, \ldots \tag{4.23}$$

$$L(\theta_i) = \frac{l\pi\sqrt{\cos\theta_d}}{2}. \tag{4.24}$$

The best suited lens for use in microfluidics would achieve imaging of the end of a waveguide into the centre of the microchannel to integrate with optics devices which use waveguides to guide light on chip. Pfeiffer *et al.* [203] concluded on modelling FZPs for x-rays, that one-to-one imaging of a point source can be achieved with an FZP if it is thick enough to operate in the Bragg regime. The configuration for such a Bragg lens is shown by its wavevector diagram in Figure 4.6 (b) and requires no slanting of the planes because the incident angle $\theta_i = -\theta_d$ meaning that Equation 4.20 for this lens the diffraction efficiency simplifies to

$$L(\theta_i) = \frac{l\pi\cos\theta_i}{2}. \tag{4.25}$$

It can be difficult to meet the Bragg condition in the central zones as that is where the Λ is high and it is highest between the zeroth and first zone. This maximum grating period, taking into account the paraxial approximation, is given by

$$\Lambda_{max}^2 = (x_1 - x_0)^2 = 2\lambda_e d. \tag{4.26}$$

Substituting Λ_{max}^2 into Equation 4.13 and holding the Bragg condition to be $Q \gtrsim 10$. The required length must be

$$L \gtrsim \frac{10d}{\pi} \tag{4.27}$$

$$\approx 3.2d, \tag{4.28}$$

which is impossible as the central zone would have to extend over the object and image planes. One solution is an off-axis-focus chirped Bragg grating [204, 205]. This would be used at one end of the lens aperture, thus avoiding the central zones. The difficulty with

this is that alignments could be more difficult to optimise and fabrication tolerances would have to be more stringent than on-axis for the alignment.

The Bragg lens was not considered as a candidate lens for simulation because of the impracticality due to the central zones not meeting the Bragg condition and an off-axis alignment as an alternative would require high fabrication tolerances.

4.6 The Kinoform Lens

The FZP was not considered as a candidate lens for simulation due to poor efficiency and the Bragg lens was not considered as a candidate lens because of the central zones not meeting the Bragg condition. This section will introduce the kinoform as an alternative design.

Before defining kinoforms, a short discussion on nomenclature in the literature is given to clarify the terminology [192, 197]. The kinoform resembles a bulk Fresnel lens in its profile and, because it is based on the function of the FZP, it may be for these reasons that both devices are referred to as Fresnel lenses. In this thesis the term Fresnel lens will only apply to the bulk device.

The Fresnel lens has been in use for over a 150 years and has the advantage over a refractive lens in that it provides the same function without becoming thicker with increasing aperture. The Fresnel lens is a bulk optical component designed by taking the curve of a refractive lens and splitting it into arbitrary zones. Where the zones lie, thickness can be removed from the lens whilst retaining its ability to operate as a refractive lens for imaging or collimation of incoherent light because it is only the profile of the boundary between two media that is responsible for refraction.

The kinoform lens provides a similar thickness reduction advantage for refractive lenses as the Fresnel lens but at the micron scale, ideal for miniaturisation of integrated devices using planar waveguide lenses. It can be viewed as a phase hologram or, in the collimating case, as a blazed FZP. Kinoform operation is dependent on both diffraction and refraction and applies to coherent light so that its zones and thicknesses are precisely defined quantitatively and are dependent on the design wavelength.

The kinoform was first reported in the literature by researchers at IBM in 1969 [206] as a new form of numerical computer designed phase hologram. However, it will be shown in the following sections that for an ideal lens an analytical approach can be followed. The analytical design of planar waveguide kinoform lenses is given in this section using geometrical optics. Fermat's principle is used to define the surface relief of the kinoform and show the relation to the FZP zones and then the relationship of this design to a simpler paraxial design familiar in the literature is described.

4.6.1 The Kinoform Profile

The geometrical model for a kinoform collimating lens is illustrated in Figure 4.7. Analysis and design of a finite thickness kinoform profile for a positive lens has been presented in the literature [195, 197, 207, 208].

This section presents the derivation using Fermat's principle for the kinoform profile and its paraxial approximation, showing all steps based on the equations derived by Moreno *et al.* [195]. The derivation shows that the profile for the kinoform is made of segments of hyperbolas and ellipses and how this profile shape is dependent on the refractive index ratio of lens and surrounding medium.

To derive the kinoform profile using Fermat's principle the optical path length from the diffraction of the zones represented by BP and that from refraction within the zones given by AP must equate to have the plane wave diverge onto point P at a distance d from the lens vertex. This is given by

$$-n_p z(x) + n_e(d + m\lambda_e) = n_e\sqrt{(d - z(x))^2 + x^2}. \tag{4.29}$$

where all symbols have been previously defined. Defining $n = n_p/n_e$ and $d_\lambda = d + m\lambda_e$ the equation appears simpler

$$-nz(x) + d_\lambda = \sqrt{(d - z(x))^2 + x^2}. \tag{4.30}$$

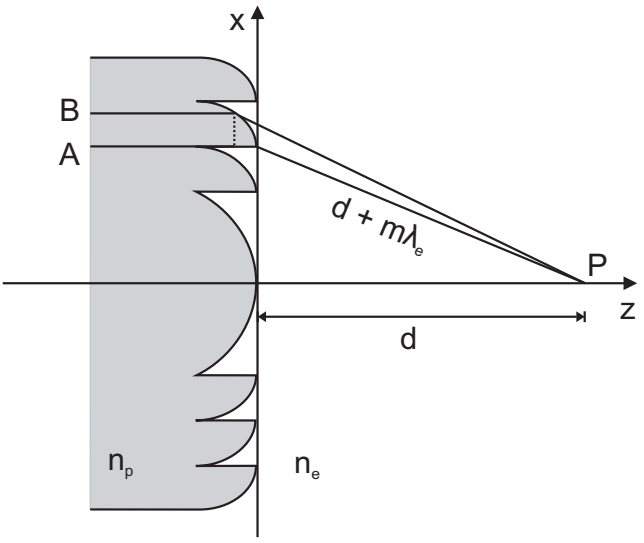

FIGURE 4.7: Illustration of a kinoform in Cartesian coordinates with rays in a zone focussing to a point where n_p is the lens and n_e the surrounding medium's effective refractive indices respectively.

Squaring both sides and expanding the brackets, it is possible to collect up the terms as

$$z^2(x)(n^2-1)+d_\lambda^2-d^2-2z(x)(nd_\lambda-d)=x^2. \tag{4.31}$$

Dividing through by n^2-1 and completing the square the equation becomes

$$\left\{z(x)-\left(\frac{nd_\lambda-d}{n^2-1}\right)\right\}^2-\left\{\frac{nd_\lambda-d}{n^2-1}\right\}^2+\left\{\frac{d_\lambda^2-d^2}{n^2-1}\right\}=\frac{x^2}{n^2-1}, \tag{4.32}$$

which simplifies to

$$\left\{z(x)-\left(\frac{nd_\lambda-d}{n^2-1}\right)\right\}^2-\left\{\frac{nd-d_\lambda}{n^2-1}\right\}^2=\frac{x^2}{n^2-1}. \tag{4.33}$$

In this form, it is clear that the equation is a hyperbola. Dividing through by $\{(nd-d_\lambda)/(n^2-1)\}^2$ and with a slight rearrangement the equation can be stated in standard form as a shifted hyperbola in the z-axis. Note that had the equation been rearranged to assume that n^2-1 is negative, and thus use $1-n^2$, it would show that the equation's general form is also a solution for a shifted ellipse. Therefore the general form can be stated as,

$$\frac{(z(x)-z_0)^2}{a^2}-\frac{x^2}{\zeta b^2}=1, \qquad z(x)\leq z_0, \tag{4.34}$$

where $\zeta=\mathrm{sgn}(n_p-n_e)$, which is a clear indicator of the profile shape by using the signum function equal to +1 for a hyperbola and -1 for an ellipse. The hyperbolic expressions for z_0, a, and b by resubstitution of n and d_λ are those given by Moreno *et al.*:

$$z_{0,hyper} = \frac{d(n-1)+nm\lambda_e}{n^2-1}, \tag{4.35}$$

$$a_{hyper} = \frac{d(n-1)-m\lambda_e}{n^2-1}, \tag{4.36}$$

$$b_{hyper} = \frac{d(n-1)-m\lambda_e}{\sqrt{n^2-1}}, \tag{4.37}$$

and for an ellipse, not given in the literature, are given by:

$$z_{0,ellip} = \frac{d(1-n) - nm\lambda_e}{1-n^2}, \tag{4.38}$$

$$a_{ellip} = \frac{d(1-n) + m\lambda_e}{1-n^2}, \tag{4.39}$$

$$b_{ellip} = \frac{d(1-n) + m\lambda_e}{\sqrt{1-n^2}}. \tag{4.40}$$

The thickness of the conic shape (and thus the lens) is dependent on its eccentricity which is equal to the refractive index ratio, n, defined as

$$e = \sqrt{1 + \frac{a^2}{\zeta b^2}} = n. \tag{4.41}$$

Equation 4.34 describes a family of curves, which may be illustrated by taking the hyperbolic profile ($n > 1$) which produces a family of hyperbolas, one for each zone as shown in Figure 4.8. McGaugh *et al.* [208] designed and simulated hyperbola kinoforms by introducing a line that crosses the hyperbolas behind the vertex as shown in Figure 4.8(a). This line is chosen to be the same distance from the vertex as in the case of the paraxial kinoform. This leaves the design of how to partition the hyperbolas to the designer by choosing a maximum lens thickness.

In this thesis, a different approach is proposed to partition the hyperbola by arranging the beginnings of all zone segments defined to be at the plane of the vertex as shown in Figure 4.8(b) by setting $z_m(x_m) = 0$. Rearranging the hyperbola equation and substituting in for $z_m(x_m)$, x^2 becomes,

$$x_m^2 = (n^2 - 1)(z_0^2 - a^2). \tag{4.42}$$

Using Equation 4.38 and Equation 4.39, x^2 for each zone can be rearranged to,

$$x_m^2 = 2m\lambda_e d + (m\lambda_e)^2. \tag{4.43}$$

This is the familiar zone formula encountered in the literature for a non-paraxial kinoform. The advantage of this approach is that the expression for the zone boundaries is simpler than with McGaugh *et al.*'s method [208] and the design may be more tolerant to fabrication errors as all zone boundaries start at the vertex line.

The thickness of the hyperbolic non-paraxial lens for each zone is given by,

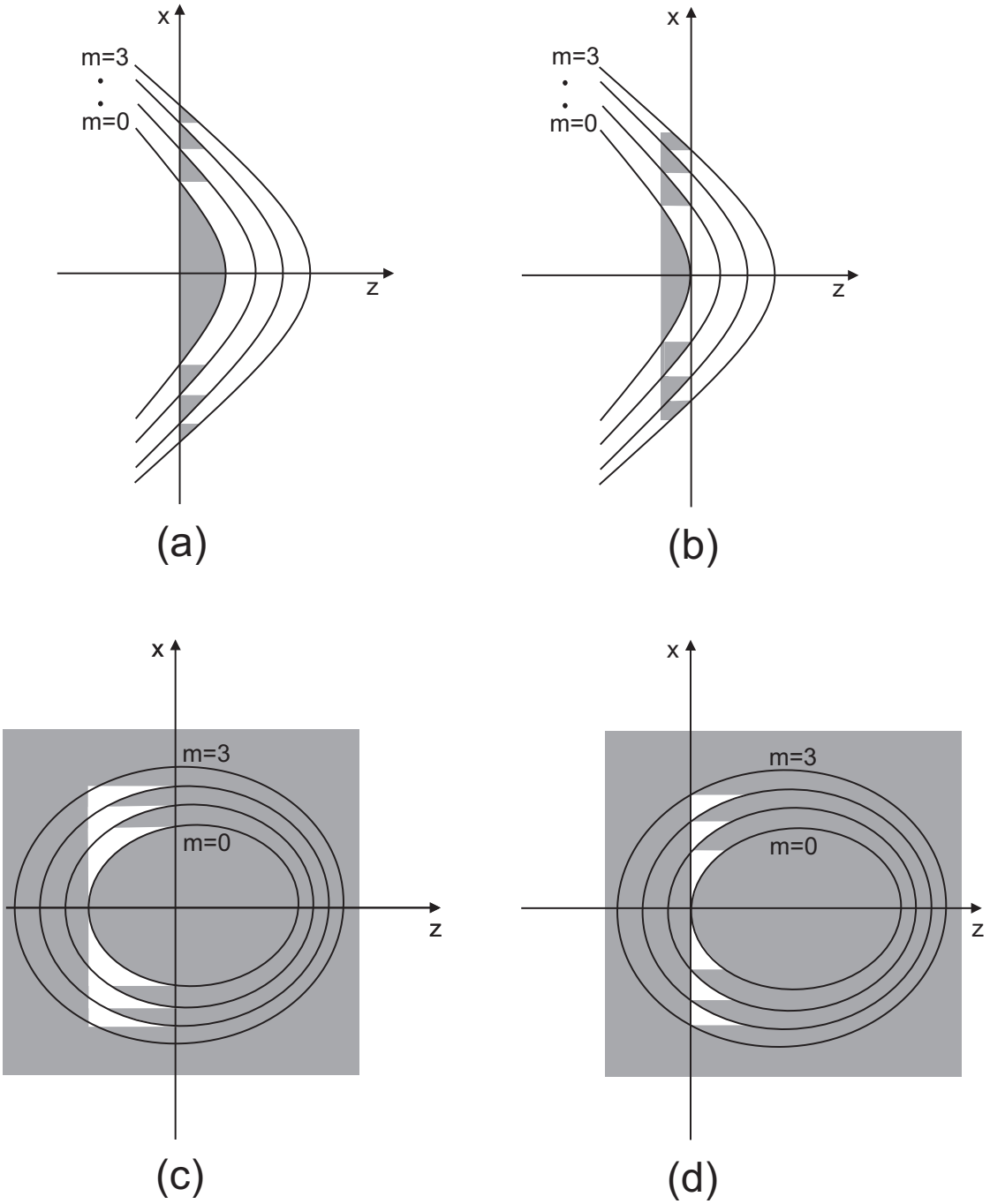

FIGURE 4.8: The hyperbola and ellipse curve families and their segmentation into kinoform zones. The schemes used are by McGaugh *et al.* [208] choosing an intersecting line behind the vertex to define and arbitrary maximum thickness for hyperbolas (a) and ellipses (c) and the scheme proposed in this chapter by having the line positioned on the vertex for hyperbolas (b) and ellipses (d) giving the familiar zone boundaries in the literature.

$$h_m = |z_m(x_{m+1}) - z_m(x_m)| = \left| \sqrt{\frac{x_m^2}{n^2-1} + a_m^2} - \sqrt{\frac{x_{m+1}^2}{n^2-1} + a_m^2} \right| \tag{4.44}$$

the difference of two square roots. It is difficult to visualise this equation since a_m and x_m are discrete functions of m. Nevertheless, it can be made clearer by noting that as h_m is a discrete function $\Delta x_m^2 = x_{m+1}^2 - x_m^2$ [209] the equation can be rearranged to

$$h_m = \left| \sqrt{\frac{x_m^2}{n^2-1} + a_m^2} - \sqrt{\frac{x_m^2}{n^2-1} + a_m^2 + \frac{\Delta x_m^2}{n^2-1}} \right|. \tag{4.45}$$

In this form, it is clear that it is the difference of two square root functions shifted relative to each other by $(\Delta x_m^2)/(n^2-1)$ where Δx_m^2 is given by

$$\Delta x_m^2 = ((2m+1)\lambda_e)^2 + 2\lambda_e d. \tag{4.46}$$

But, since $x_m^2 = (n^2-1)(z_{0,m}^2 - a_m^2)$ because $z_m(x_m) = 0$ as defined earlier,

$$h_m = |z_m(x_{m+1})| = \left| z_0 - \sqrt{\frac{x_{m+1}^2}{n^2-1} + a^2} \right|. \tag{4.47}$$

$$h_m = \left| z_0 - \sqrt{\frac{x_m^2}{n^2-1} + \frac{\Delta x_m^2}{n^2-1} + a^2} \right|. \tag{4.48}$$

Therefore, in this design, the maximum height for each zone can be viewed as a shifted hyperbola in both axes.

$$(z_m(x_{m+1}) - z_{0,m})^2 - (z_m(x_m) - z_{0,m})^2 = -\left(\frac{\Delta x_m^2}{n^2-1} \right). \tag{4.49}$$

For the designer it will be necessary to decide how many zones should be included in the lens design. There is a maximum aperture that the kinoform can take due to the geometrical definition of hyperbolas and ellipses, which is clearly evident in Equation 4.34, for a hyperbola $a_{hyper} > 0$ and for an ellipse $z_{0,ellip} \geq 0$. Hence the maximum number of zones, M, for real hyperbolic and elliptical lenses is

$$M_{hyper} < \frac{d(n-1)}{\lambda_e} \tag{4.50}$$

and

$$M_{ellip} \leq \frac{d(1-n)}{n\lambda_e}, \tag{4.51}$$

respectively.

When calculating the diffraction efficiency for the kinoform, Fresnel diffraction is used to establish the use of Fourier analysis in optical problems. Unfortunately, this derivation of the standard Fourier optics inherits the paraxial approximation [196]. Rigorous electromagnetic (EM) theory is normally used to calculate diffraction efficiency in a non-paraxial optical system, but Harvey *et al.* [210] have worked on a non-paraxial scalar Fourier transform theory of diffraction. This should allow for accurate estimation of the non-paraxial kinoform's diffraction efficiency. It may be shown that a solution for the diffraction efficiency using Harvey's method is close to the paraxial solution given in the following subsection i.e. $\eta_q \approx \mathrm{sinc}^2(\alpha + q)$.

The lenses chosen as candidate lenses were the elliptical kinoform and the elliptical McGaugh kinoform as they are considered the ideal non-paraxial kinoform lenses in terms of the way they are derived and designed.

4.6.2 The Paraxial Kinoform Lens

The general derivation for the kinoform given in the previous subsection yields a complex expression. In this section, a simpler expression for a kinoform profile is derived from the paraxial approximation to the non-paraxial kinoform profile already given. The paraxial approximation is valid for devices if, say, the F number is kept to ∼5 [164], the maximum angle of acceptance is then only ∼6° (Found by $\tan\theta = 1/2F$). The paraxial kinoform lens may also be derived by just considering the necessary phase difference, as it is often in the literature, as shown in the following subsection, by treating the lens as a negligibly thin device that only effects the phase at a certain plane.

To find the paraxial kinoform profile needed for the collimating operation we rearrange the kinoform profile, Equation 4.34 to,

$$z(x) = z_0 - a\sqrt{1 + \frac{x^2}{\zeta b^2}}. \tag{4.52}$$

In this form, a simplification can be made by realising that $(1/b)^2 \ll 1$ in a normal practical design because the values for $\lambda_e \ll d$ in the paraxial region [195]. Taking the Taylor series of the square root term, Equation 4.52 becomes

$$z(x) = z_0 - a\left(1 + \frac{1}{2\zeta}\left(\frac{x}{b}\right)^2 - \frac{1}{8\zeta}\left(\frac{x}{b}\right)^4 + \cdots\right). \tag{4.53}$$

If the lens is to be used in the paraxial region then terms higher than second-order terms are neglected simplifying it to,

$$z(x) = z_0 - a\left(1 + \frac{1}{2\zeta}\left(\frac{x}{b}\right)^2\right). \tag{4.54}$$

By rearranging as follows,

$$z(x) = z_0 - \left(a + \frac{ax^2}{2\zeta b^2}\right) \tag{4.55}$$

a further approximation $b^2/a \approx d(n-1)$ can be made as $\lambda_e \ll d$ in the paraxial region [195]. This leads to the parabolic kinoform profile commonly found in the literature,

$$\begin{aligned} z(x) &= z_{max}\left(m - \frac{x^2}{2\lambda_e d}\right), && (4.56)\\ z_{max} &= \zeta\frac{\lambda}{n_p - n_e}, && (4.57)\\ x_m^2 &= 2m\lambda_e d. && (4.58) \end{aligned}$$

Note that the square of the zone boundary position on the x-axis, x_m, is twice that of the paraxial FZP. The kinoform is then described by one parabolic profile modulated within a thickness given by z_{max}.

The diffraction efficiency is also described adequately using Fourier optics [196]. The phase change to a plane wave through the lens is

$$\begin{aligned} \phi &= \frac{2\pi}{\lambda}(n_p' - n_e')z(x) && (4.59)\\ &= \alpha 2\pi\left(m - \frac{x^2}{2\lambda_0 d}\right), && (4.60)\\ \alpha &= \frac{z_{max}}{\lambda}(n_p' - n_e') && (4.61)\\ &= \left(\frac{n_p' - n_e'}{n_p - n_e}\right)\frac{\lambda_0}{\lambda}, && (4.62) \end{aligned}$$

where λ is the input wavelength, n_p' the actual effective refractive index of the lens region, n_e' the actual effective refractive index of the surrounding medium and α the design mis-match ratio between the actual lens and the designed lens. The transmission function t is periodic. Taking the Fourier series

$$t(\phi) = \exp(i\phi) = \sum_{q=-\infty}^{\infty} c_q \exp\left(i\frac{2\pi q}{2\lambda_e d}x^2\right) \tag{4.63}$$

Substituting $\xi = x^2/2\lambda_e d$, for simplicity, the coefficients are calculated as

$$\begin{aligned} c_q &= \int_{-1/2}^{1/2} t(\xi) e^{-i2\pi q\xi}\, d\xi && (4.64)\\ &= e^{i2\pi\alpha m} \int_{-1/2}^{1/2} e^{-i2\pi\alpha\xi} e^{-i2\pi q\xi}\, d\xi && (4.65)\\ &= \frac{e^{i2\pi\alpha m}}{\pi(\alpha+q)} \frac{1}{2i}\left(e^{i\pi(\alpha+q)} - e^{-i\pi(\alpha+q)}\right) && (4.66)\\ &= \frac{e^{-i2\pi\alpha m}}{\pi(\alpha+q)} \sin(\pi(\alpha+q)). && (4.67) \end{aligned}$$

The diffraction efficiency is given by

$$\eta_q = c_q c_q^* = \mathrm{sinc}^2(\alpha+q) \tag{4.68}$$

where

$$\mathrm{sinc}(x) = \frac{\sin(\pi x)}{\pi x}. \tag{4.69}$$

It is clear from Equation 4.68 that a kinoform can diffract with a 100% efficiency into any diffraction order depending on the values of α and q, but for this work only the first order is of interest, as discussed in Section 4.4, and the objective is to achieve α as close to unity as possible so as to not diffract power into higher orders. The equation describes the chromatic behaviour of the paraxial kinoform lens because α is wavelength dependent. The simplest method to acquire an idea of tolerances is to plot the diffraction efficiency versus α for diffraction orders 0,-1,-2. Where the diffraction efficiency falls to 0.9 for the order -1 (the order of interest), α values can be read off. For a wavelength of, for example, 633 nm $\alpha \approx 0.82, 1.18$, which corresponds to actual wavelengths of 772 nm and 536 nm, respectively, assuming the actual refractive indices are the same as those designed. This gives a tolerance for the linewidth of light sources, for example an LED. A lower actual wavelength moves focussed power to a higher order ($|q|$) and a higher actual wavelength moves focussed power to a lower order. Chromatic aberrations worsen in both cases, but less so for an increase in actual wavelength because the power in the 0 diffraction order is not focussed by the lens, therefore the power will add a lower intensity to the first order focus than if it comes from a focussed order. Although the other kinoform lenses have not had a diffraction efficiency expression derived, it is

expected that an expression would be similar to Equation 4.68 as discussed in Subsection 4.6.1 and, thus, the lenses will show similar behaviour as that of the paraxial kinoform lens. However, a detailed study through simulation could confirm this.

While gradient index (GRIN) lenses are not considered in detail, the GRIN version of the kinoform should be mentioned for completeness as it is an alternative design reported in the literature [164, 188]. Parabolic GRIN kinoforms can be made by maintaining a constant thickness and varying the refractive index difference according to the modulation described by Equation 4.56. The literature does not appear to describe a treatment for GRIN kinoforms similar to that of Subsection 4.6.1 for finite thickness of thickness varying kinoforms.

The paraxial kinoform design, presented here, is a candidate lens for simulation of a compact microfluidic device as the system will operate close to paraxial regime and the true field distribution is Gaussian-like and therefore most of the power travels in the paraxial region. There is also a trade-off with approximation and lens thickness as diffraction in the actual lens region is reduced which means fewer phase errors at the second lens boundary.

4.6.3 Kinoform Derived via Phase Modulation

The design of a planar waveguide kinoform via the desired phase modulation is well documented in the literature [164, 188, 211, 212] and leads to the well known paraxial kinoform. This design sees the kinoform as a negligibly thin phase modulator to a plane wavefront and does not take the finite thickness into account as did the derivation in Subsection 4.6.1. So for completeness, this subsection will describe and discuss this method in a similar manner to Buralli *et al.* [197] and compare it with the previous profiles already defined. The phase modulation required to focus a plane wave is depicted in Figure 4.7. Taking the difference in the optical path lengths, the change to a plane wave due to the lens is

$$\phi(x) = \alpha 2\pi \left(m - \frac{\sqrt{d^2 + x^2} - d}{\lambda_e} \right). \tag{4.70}$$

Substituting with $\xi = (\sqrt{d^2 + x^2} - d)\lambda_e$ [197], the equation can be written in the form

$$\phi(\xi) = \alpha 2\pi (m - \xi). \tag{4.71}$$

This is the same form as Equation 4.59 and thus the diffraction efficiency for this kinoform will be $\eta_q = \mathrm{sinc}^2(\alpha + q)$. This kinoform has the same zone boundaries

$$x_m^2 = 2m\lambda_e d + (m\lambda_e)^2, \tag{4.72}$$

as those defined earlier for the non-paraxial kinoform in Subsection 4.6.1. Taking the Taylor series approximation and ignoring terms of x higher than second-order leads back to the paraxial kinoform previously discussed in Subsection 4.6.2. From other treatments [197, 207] it is found to be a hyperbola with different geometrical parameters compared with the general method described in section 4.6.1,

$$z_0 = \frac{d + m\lambda_e}{n-1}, \tag{4.73}$$

$$a = \frac{d}{n-1}, \tag{4.74}$$

$$b = d, \tag{4.75}$$

$$e = \sqrt{1 + (n-1)^2}. \tag{4.76}$$

The kinoform described here could be considered non-paraxial, but the difference between it and the non-paraxial kinoforms described in Subsection 4.6.1 is that the it does not take into account the finite thickness of the kinoform. Therefore, this kinoform was not considered a candidate lens.

4.7 Lens Aperture

For the lenses described in this chapter, light diffracting from the end of a channel waveguide must be re-focussed into the microfluidic channel. Consideration must be given to whether the aperture of the lens is large enough to capture the diffracting light efficiently; as a lens that does not capture the majority of the diffracting beam is not of practical use.

To generate an analytical method to model the efficiency of the lens aperture, some assumptions are required which are in line with common treatment in the literature [165]. A Gaussian intensity profile is assumed for the beam emerging from the waveguide end and the edge of the beam is chosen to be the spotsize (beam radius), ω, which means that more than 95% of the power is contained within the defined beam. Therefore, in considering the efficiency of a lens aperture not all the light power is taken into account as a Gaussian profile is of infinite extent. The lenses are designed using geometrical optics, thus an assumption that should be considered is that the beam has an approximate spherical wavefront beyond the Rayleigh range

$$z \gg z_R = \frac{\pi\omega^2}{\lambda_e}. \tag{4.77}$$

The condition that must be fulfilled for efficient collection of diffracted light for elliptical lenses is that the diffracted angle must be less than or equal to the lens aperture angle given by the definition of the geometrical shape and for hyperbolic lenses the diffracted angle must be less than the lens aperture angle (angle of the asymptotes), as shown in Figure 4.9. To obtain geometrical expressions, tangents of the angles may be compared to give simple expressions. Therefore, the condition on the tangents for a elliptical and hyperbolic lenses must be

$$\tan\theta_{diff} \leq \tan\theta_{lens}, \tag{4.78}$$

where angles θ_{diff} and θ_{lens} are shown in Figure 4.9.

The numerical aperture (NA) of the waveguide and lens, being a familiar parameter in optics, would appear to be useful in giving an intuitive expression for this condition. Unfortunately, the NA is dependent in the sine of the diffracted angle angle and not its tangent leading to more complicated expressions. As will be shown, the tangent of the angle gives simple expressions. For a diffracting beam emanating from the end of a waveguide the tangent of its angle of diffraction beyond the Rayleigh range is [165]

$$\tan\theta_{diff} = \frac{2\lambda_e}{\pi D_0} \tag{4.79}$$

where D_0 is the spot diameter, twice the spotsize ($D_0 = 2w_0$), of the waveguide. If the waveguide confines the fundamental mode well then D_0 can be approximated to the

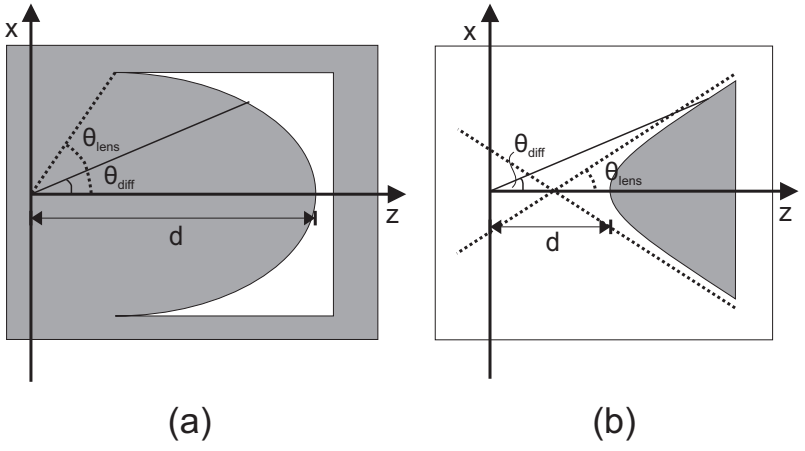

FIGURE 4.9: Lens aperture angle and diffraction angle for (a) elliptical and (b) hyperbolic geometries where the shaded regions are of higher refractive indices.

waveguide width. For the circular refractive lenses the tangent of the angle between the optical axis and half the lens aperture, and assuming the thin lens maker's formula, is

$$\tan\theta_{lens} = \frac{R}{d} \tag{4.80}$$

$$= n-1 \tag{4.81}$$

$$\frac{1}{d} = \frac{(n-1)}{R} \tag{4.82}$$

where R is the radius of the curvature of the lens. The tangent of the lens angle between the optical axis and half the lens aperture for an elliptical lens is

$$\tan\theta_{lens} = \frac{b}{an} \tag{4.83}$$

and for a hyperbolic lens is the gradient of its asymptotes,

$$\tan\theta_{lens} = \frac{b}{a}. \tag{4.84}$$

Substituting the above equations into the tangent inequalities in Equation 4.78, inequality expressions can be given which must be satisfied to ensure at least 95% of the power emerging from a channel waveguide with mode spotsize diameter, D_0, is captured by the lens aperture. For comparison, the more familiar thin and thick circular lens conditions are also described below. A circular refractive lens whose sides are made of intersecting similar circles the condition for a thin lens becomes

$$D_{0,thin} \geq \frac{2\lambda_e}{\pi}\frac{1}{(n-1)} \tag{4.85}$$

and for the thick lens

$$D_{0,thick} \geq \frac{2\lambda_e}{\pi}\frac{n}{(n-1)} \tag{4.86}$$

where $n = n_p/n_e$. For an elliptical lens

$$D_{0,ellip} \geq \frac{2\lambda_e}{\pi}\frac{n}{\sqrt{1-n^2}} \tag{4.87}$$

and for a hyperbola

$$D_{0,hyper} > \frac{2\lambda_e}{\pi} \frac{1}{\sqrt{n^2 - 1}} \tag{4.88}$$

Note that the kinoform will have the same limitations as those of elliptical and hyperbolic refractive lenses because the inequality shows it possible to have 95% of the power collected with a given value for n and λ_e. Therefore, the paraxial kinoform will be limited in practice by the same conditions.

Using numerical values approximate to the materials system being used in Chapter 6 with the elliptical condition with λ_0 at 633 nm, n_p of 1.458, n_e of 1.4658, the waveguide spot diameter, D_0, has to be greater than or equal to 2.65 μm for 95% of the waveguide power to be collected by the lens. Since full etching of the thickness of the optical waveguiding layer is assumed in the lens region there would be a loss from the unguided lateral dimension. This sets the minimum practical value for D_0 for this material system, in turn, placing a minimum width constraint of the channel waveguide for efficient collection of power by the lens.

4.8 Discussion on Lenses

Several planar waveguide lenses have been described so far. This section is a summary and discussion about which of the lenses were chosen as candidate lenses for simulation. The lenses fall into two categories: refractive, and diffractive based on the FZP. An ideal refractive lens, one which takes collimated light and focusses it, can be designed using geometrical optics and Fermat's principle. This procedure determines the lens profiles to be conic sections, namely, ellipses and hyperbolas depending on whether the lenses are positive or negative respectively. Section 4.2 explained that a negative lens design is preferred for lower losses because etching through the waveguide layer means that the etched region will not guide light in the lateral dimension (y-axis), which for negative lenses is limited to the lens region. Section 4.7 shows that for a weak-guiding system comprising waveguide lenses the features may need to be etched entirely through the guiding layer to achieve a practical aperture by increasing the index contrast between the lens region and surrounding medium. This has the effect that the propagating light will not be guided in the lens region which will increase loss in the system.

The FZP is inefficient (only 40% of light focussed into the first order) so was not considered as a lens for simulation, but it is the basis of other solutions, namely, the kinoform and Bragg lenses. Although Bragg lenses seem attractive, their central zones do not meet the Bragg condition and therefore Bragg lenses cannot be as efficient as kinoforms and the off-axis versions would require higher alignment tolerances in fabrication. Therefore, Bragg lenses were not considered for simulation. Kinoforms lenses may take several designs due to approximations, leading to the paraxial kinoform lens, or design

decisions on how to segment the zones, leading to the general kinoform lenses and the McGaugh kinoform lens.

The kinoforms are generally difficult to fabricate at the extremities of their apertures as feature size decreases [164]. D'Auria *et al.* [213] looked at the distance between the last two zones for paraxial kinoform lenses to estimate how the minimum feature size determines the maximum F number of the lens. However, this approach can be applied to the other kinoforms. Assuming that $m\lambda_e$ will be small because the maximum zone, M, will not be large in practice, the same paraxial approximation can be made,so that the small feature size, s_{min}, is related to the F number as $s_{min} \approx 2\lambda_e F$. The ideal smallest feature size for kinoforms is an impossible 0 μm because of the continuous profile in a zone coming to a sharp tip due to the zone boundary, but D'Auria *et al.*'s approach does not take this into account. A solution may be to use a hybrid of the the Bragg lens and a kinoform, where a kinoform profile is used in the central zones and a chirped Bragg grating in the higher zones [214]. This should be explored in future work once a basic kinoform has been established.

The lens profiles are all possible analytical solutions to imaging a focussed spot into the middle of a microfluidic channel, but it is the ease of fabrication and likely tolerances that determine the feasibility of making and using such lenses. Various planar processing techniques have been employed to make the lenses, such as electron beam (EB) lithography [187] for FZP fabrication extending to Bragg lens by EB lithography [215], photolithography [204] and ion exchange [205] and kinoforms by EB direct writing [188] and photolithography [189, 214, 216, 217] and by ion exchange [218] exotically by photo-imprinting [219].

In summary, the lenses to be simulated are all negative elliptical lenses because this configuration is better suited for fabrication than positive lenses in weak-guiding systems that require etching through the optical layer. The candidate lenses include: the elliptical refractive, the elliptical kinoform, the paraxial kinoform, and the elliptical McGaugh kinoform. There is a clear trade-off between refractive index contrast, n, that would allow for thinner lenses and higher collection efficiency from apertures; and lower refractive index contrast allowing designs to have larger dimensions increasing the fabrication tolerances using photolithography. Photolithography was chosen as it was the only patterning method available at the start of this work, and is widely available and suited to low cost mass production.

4.9 Simulations of Waveguide Lenses

4.9.1 Approach to Models

The candidate lenses chosen for simulation were the elliptical refractive, elliptical kinoform, paraxial kinoform, and McGaugh kinoform. Figure 4.10 shows the profiles, designed in MATLAB, of the candidate lenses with kinoform lenses of having 26 zones as this is the maximum possible for the elliptical kinoform lens. To determine which of the candidates is the best lens to be fabricated in the material system presented in Chapter 6, simulation results are presented to model the performance of imaging a spot from a channel waveguide into the middle of a microfluidic channel.

The quantity to be optimised for imaging a spot in the the middle of the microfluidic channel would logically be the spotsize. However, the spotsize does not give information on the amount of power transmitted along the device and, thus, does not give a measure of efficiency. The spotsize along a device may also be impossible to quantify as it is a construct based on Gaussian-like field distributions which may not be appear along all of the propagation length. The figure of merit chosen for the simulations is the power

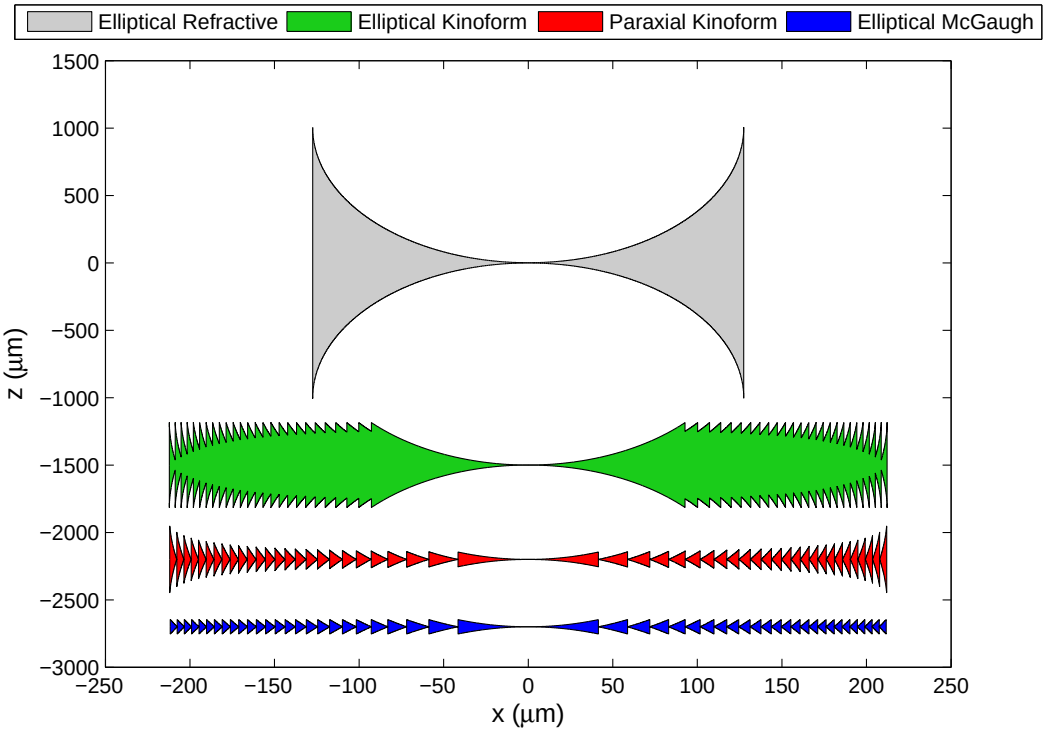

FIGURE 4.10: Comparison of differing profiles of candidate negative lenses designed for simulation in the material system described in Chapter 6. The lenses are negative in design and the coloured areas indicate regions of lower refractive index.

coupling efficiency of a launching waveguide mode at any point of interest along the device is given by the square of the overlap integral

$$\eta = \frac{\left(\int_{-\infty}^{\infty} \phi(x,0)\phi(x,z)dx\right)^2}{\int_{-\infty}^{\infty} \phi^2(x,z)dx} \tag{4.89}$$

where ϕ is the field distribution. This is a dimensionless figure of merit comparing what is desired and what is achieved that overcomes the difficulties with just using spotsize.

The effective index method (EIM) as described in Subsection 3.3.3 was used to transform 3D models into 2D prior to BPM simulation. The 2D simulations were necessary because 3D simulations, due to computational complexity, were too demanding on time and computer memory. The EIM transformation was performed using the refractive index values of the material system used in Chapter 6 at a wavelength of 633 nm. Essentially, regions in the 2D model were given effective refractive indices calculated from the analytical description of a slab waveguide given in Section 3.2. This is a valid approximation method because the symmetrical sandwich structure of slab waveguides that could be made are singlemoded. The lens profiles were generated using the MATLAB programming language, then imported into *BeamPROP*$^{\text{TM}}$ program for BPM simulations. There is also the benefit that in *BeamPROP*$^{\text{TM}}$ 2D simulations can have Padé order approximations to make wide angle calculations more accurate [176].

4.9.2 Focussing Ability in a Slab Waveguide

As a first step, simulations were performed on a slab waveguide structure for all candidate lenses shown in Figure 4.11. It is useful to define the distances before and after the lens under simulation. Define f_1 as the distance from the face of the input waveguide to the vertex of the lens. This model was created in *BeamPROP*$^{\text{TM}}$. An example is shown Figure 4.12 where the elliptical kinoform in *BeamPROP*$^{\text{TM}}$ CAD to be simulated. Figure 4.13 shows the simulation of the field strength of the device.

The lenses were designed to have an object plane and image plane at 2000 μm from the vertex. This value was chosen to keep the F number ~ 5 as found in the literature [164]. The kinoform lenses all consist of 26 zones as this is the maximum possible for the elliptical kinoform lens as given by Equation 4.51. Varying f_1, the efficiencies of focussing for the lenses were acquired. Figures 4.14(a) and 4.14(b) are the simulation results of coupling efficiency versus the offset from the designed 2000 μm focal distance for 2 μm waveguide, $\eta_{2\mu\text{m}}$ and 3 μm waveguide, $\eta_{3\mu\text{m}}$, respectively. Both show that the elliptical refractive lens has poor performance for the 1:1 operation compared to the kinoform lenses. An improvement is noticeable when the waveguide width increases from 2 μm to 3 μm, due to better aperture collection efficiency as discussed in Section 4.7.

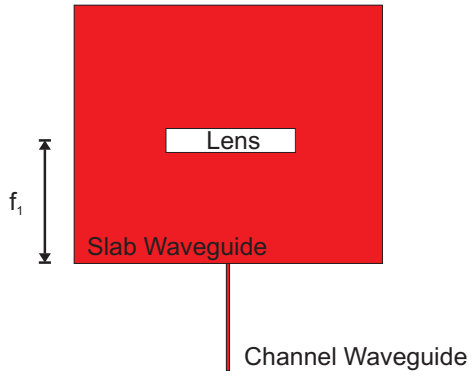

FIGURE 4.11: Slab model.

The McGaugh lens shows an interesting flat response with respect to the offset from the designed focal distance, 2000 μm. The paraxial kinoform showing the best performance of the candidate lenses.

The limit of 26 zones is only for the elliptical kinoform. The algorithm for generating the McGaugh lens leads to a design with a possible maximum number of 36 zones. The paraxial kinoform can have an infinite number of zones, although the further out the zones the less valid the paraxial approximation inherent in the design. Therefore, to see if there is a change in efficiency, the McGaugh and paraxial kinoform lenses of 36 and 37 zones, respectively, were simulated and the results are given in Figure 4.15. The

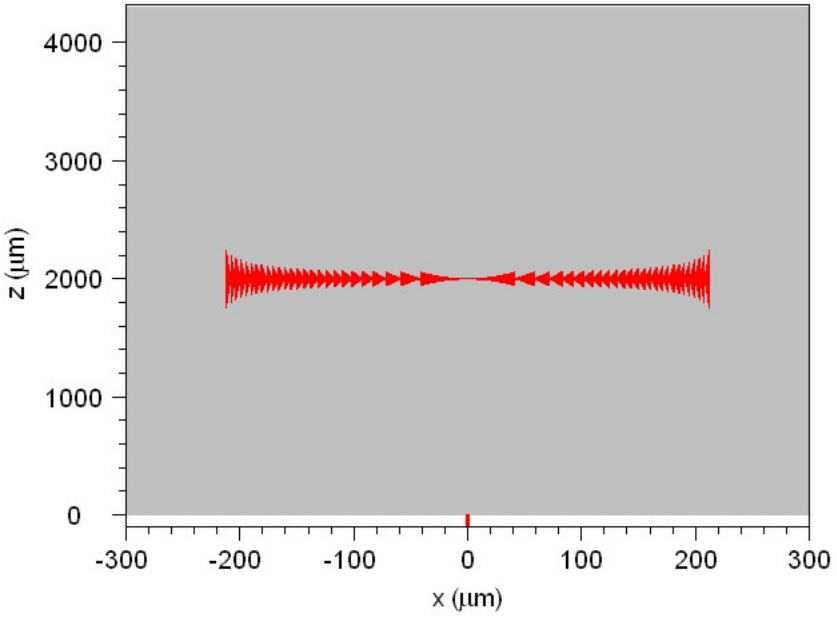

FIGURE 4.12: The elliptical kinoform in *BeamPROP*^{TM} CAD window to undergo simulation in a slab waveguide structure.

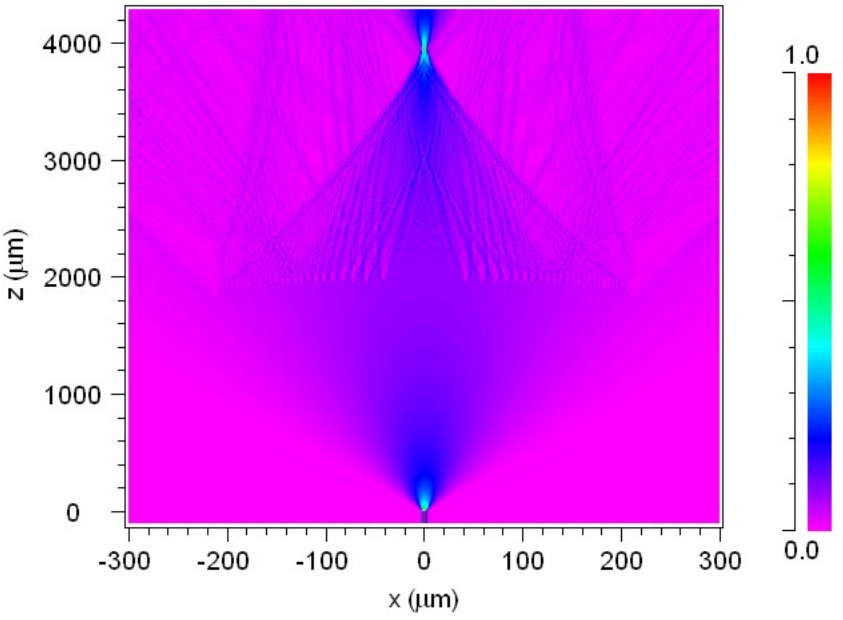

FIGURE 4.13: An example from the *BeamPROP*™ CAD window.

McGaugh lens retains the flat response, but the overall efficiency drops compared to its 26 zone version, whilst the change for the paraxial lens is negligible. It is clear that the elliptical refractive lens exhibits the worst performance of the candidate lenses and therefore was not considered for further simulations.

4.9.3 Focussing into a Microfluidic Channel

The next step involved simulating the structure in Figure 4.16 with the three remaining candidate lenses: the elliptical kinoform, paraxial kinoform, and McGaugh kinoform; all having 26 zones. The model was used to simulate the performance of the lenses focussing into the middle of the channel. The model has an additional distance f_2 defined as the distance from the second lens vertex to the middle of the microfluidic channel.

Figure 4.17 shows contour plots of f_1 versus f_2 and the efficiency, η for a 2 μm wide waveguide system, at the middle of the 20 μm wide microfluidic channel. The paraxial lens shows the highest efficiency compared to the elliptical kinoform and the elliptical McGaugh lenses but has a tighter tolerance. For example, at f_1 at the design focal distance of 2000 μm the efficiency is at 60% for f_2 at 2025 μm for a range of $\pm$15 μm. However, this tolerance is within photolithographic constraints of alignment. The graphs are also symmetrical allowing for f_1 and f_2 in the design to be made equal.

At this point, the decision was made that the paraxial kinoform lens was more practical for fabrication as it shows the highest efficiency in the simulations compared to the other

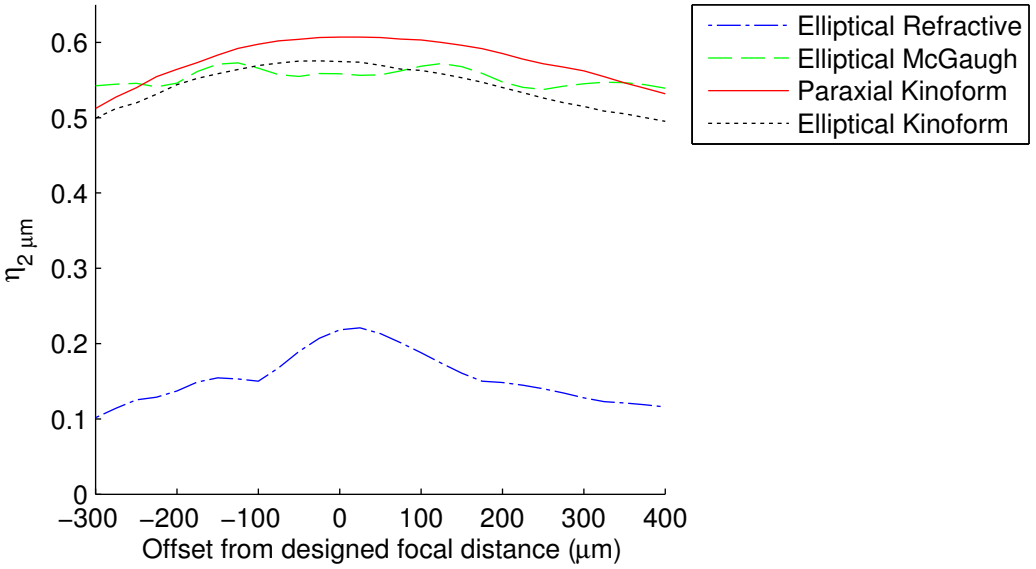

(a)

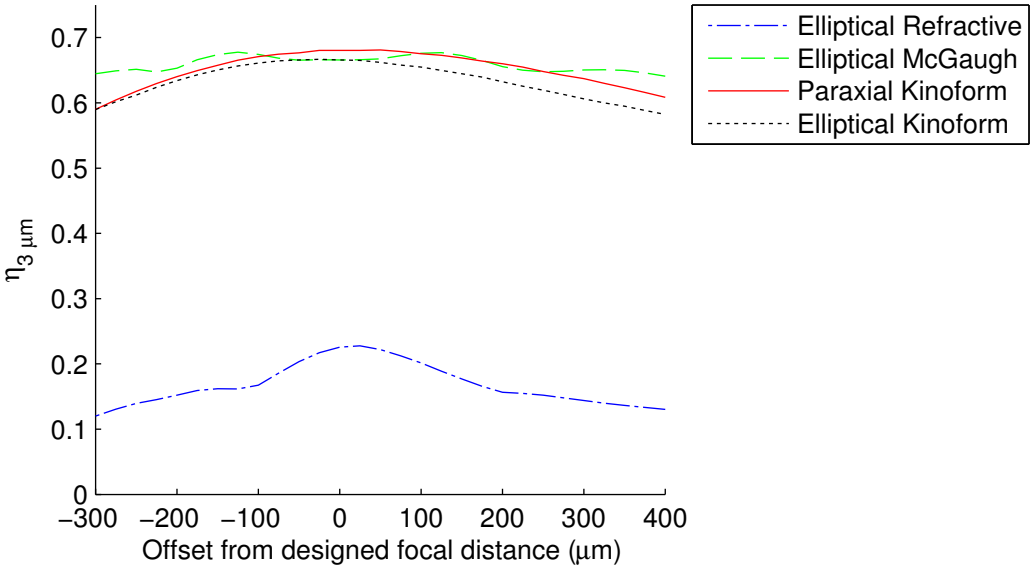

(b)

FIGURE 4.14: Efficiency versus offset from designed focal distance for (a) a two micron waveguide and (b) a three micron waveguide.

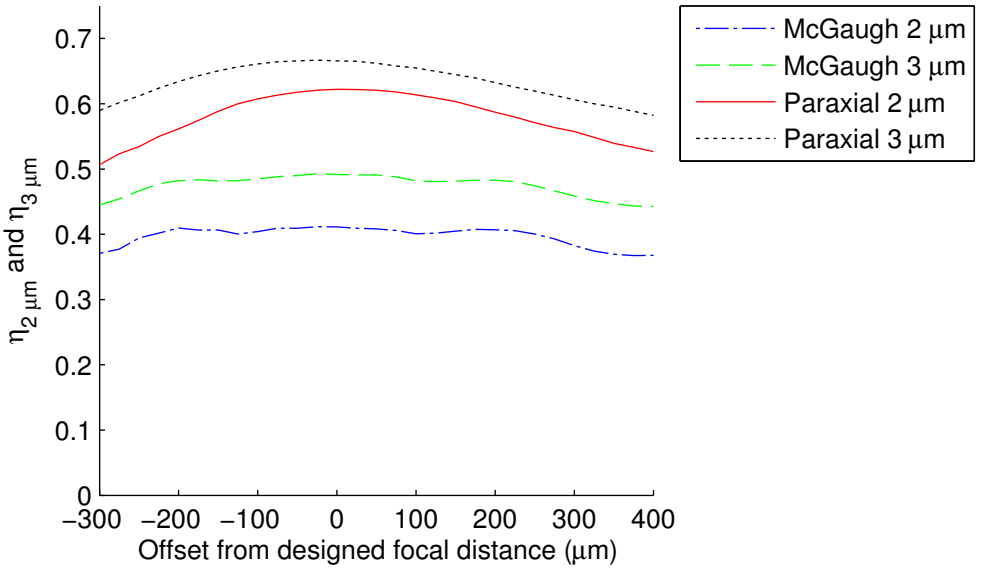

FIGURE 4.15: Efficiency versus offset from designed focal distance for waveguides of two and three microns for both McGaugh elliptical and paraxial elliptical lenses.

candidate lenses. The paraxial kinoform lens also has the thinnest profile and therefore will have a smaller unguided region.

4.9.4 Characteristics of Paraxial Kinoform Lens

After deciding to use a paraxial kinoform lens for fabrication further simulations were done to explore more of its properties. The lengths f_1 and f_2 were fixed at 2010 μm as this was the high efficiency configuration shown in Figure 4.17(a) near 2000 μm. Figure 4.18 shows that a change in the effective index of the slab waveguide in the model in Figure 4.11 effects the efficiency, $\eta_{2\mu m}$, of the lens. An increase on the effective refractive index of the slab can increase $\eta_{2\mu m}$, peaking at 64%. It is interesting to note that,

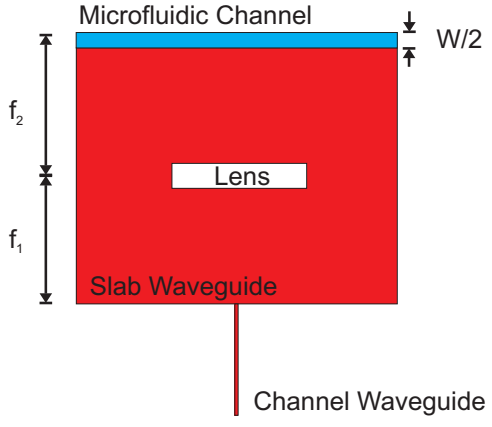

FIGURE 4.16: Simulation model for a lens in a slab region with a microfluidic channel.

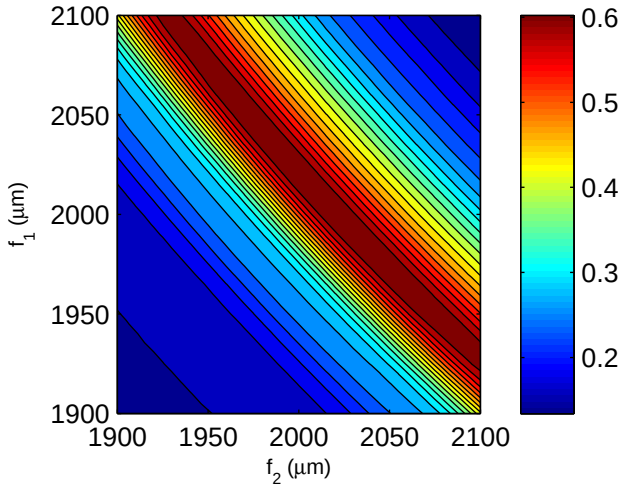

(a) Paraxial kinoform

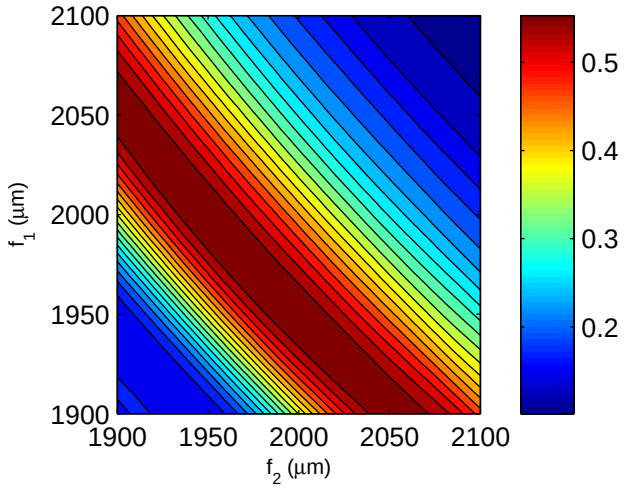

(b) Elliptical kinoform

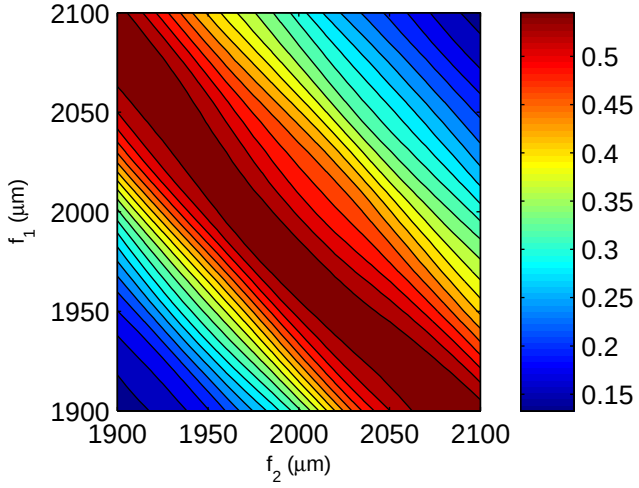

(c) McGaugh kinoform

FIGURE 4.17: Focussing efficiency with varying f_1 and f_2 for the (a) paraxial, (b) elliptical, and (c) McGaugh lenses.

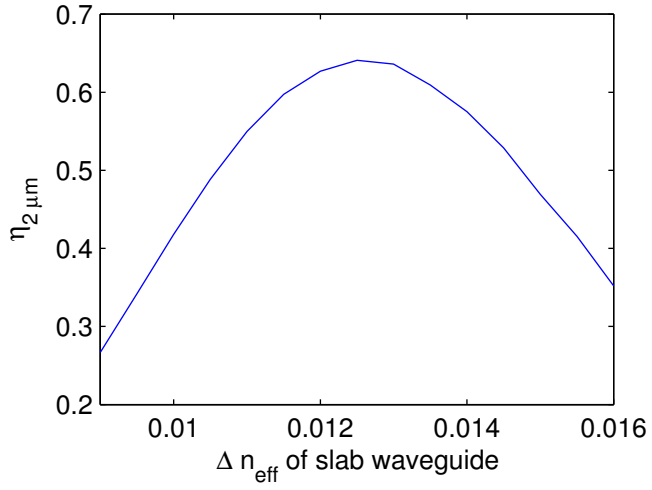

FIGURE 4.18: The effect on efficiency by change in the effective refractive index of the slab region in a paraxial kinoform lens.

if the relationship between the change in effective index of the slab and the change in temperature of the slab is empirically found then Figure 4.18 would describe the thermal stability of the lens.

The spotsize in the middle of the microfluidic channel of 20 μm width, though not the figure of merit for simulations, is, nonetheless, an important quantity for characterising the efficacy of the device. Figure 4.19 shows a launch field with a spotsize, ω_0, of 1.25 μm and a spotsize of 2.05 μm at the centre of the microchannel.

The lens is designed so far for a 20 μm wide microfluidic channel. However, varying the focal distance f_1 (with f_2 being equal to f_1), Figure 4.20 shows that for a focal distance of 2000 μm and 2010 μm the efficiency only differs by a few percent with respect to a microfluidic channel width from 20 to 200 μm. This potentially allows for scaling of the microfluidic channel width without change in the optical components.

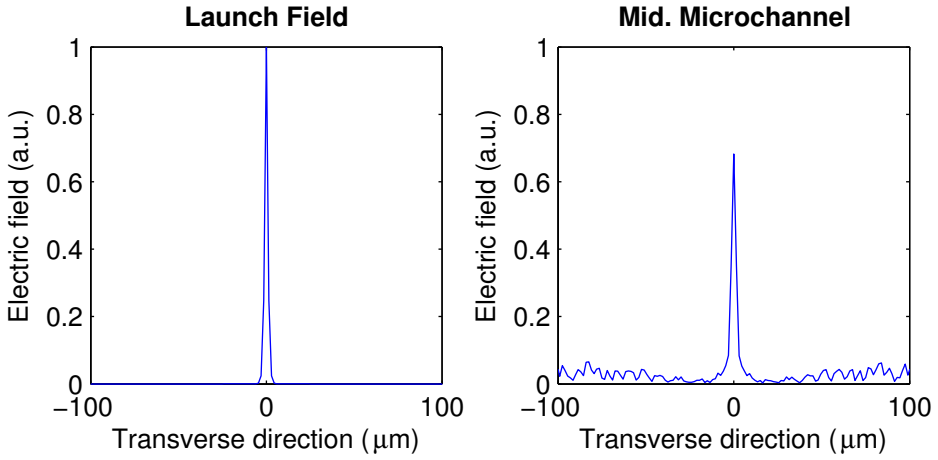

FIGURE 4.19: Launch field shown on the left and the resultant reformed spot in the middle of the microchannel after passing a paraxial kinoform lens.

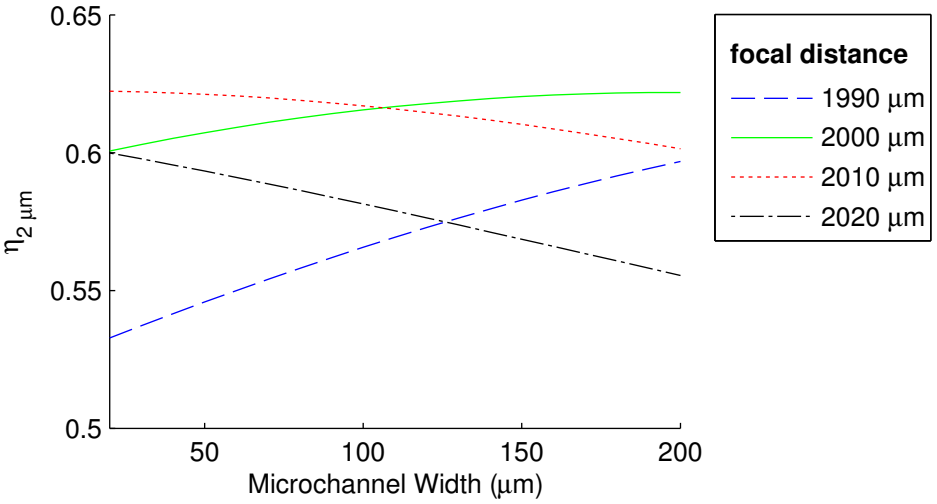

FIGURE 4.20: Efficiency versus microfluidic channel width.

4.9.5 Paraxial Kinoform Lens for Collection Optics

Placing a lens on the other side of the microfluidic channel allows for light to be collected. The model for this is shown in Figure 4.21. It is also interesting to know how collection is affected with changes to input by an offset in the lateral dimension (x-axis). Figure 4.22 is an example simulation of an input with a 10 μm offset. The focus in the microfluidic channel is shifted -10 μm from the centre. The second lens collects this light and refocusses it back into an output waveguide at 10 μm offset.

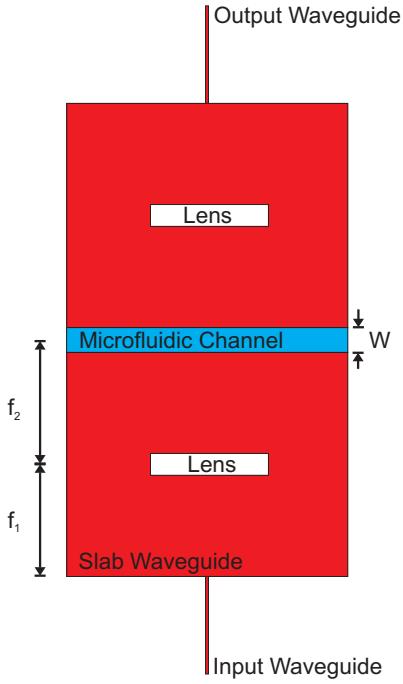

FIGURE 4.21: Simulation model for full device with a lenses for excitation and collection in a slab regions and a microfluidic channel in the centre.

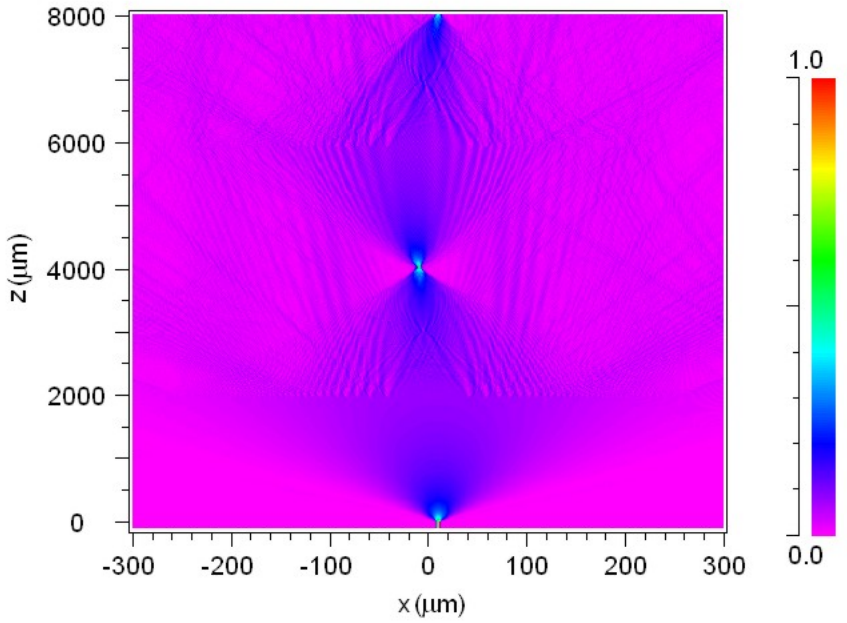

FIGURE 4.22: BPM simulation of the electric field when the input waveguide is moved by 10 μm.

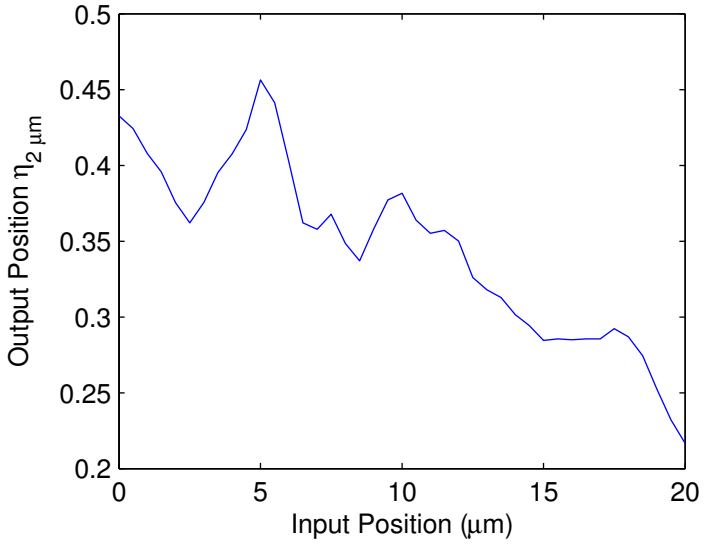

FIGURE 4.23: Efficiency at the output waveguide with the same position from centre as the input waveguide.

Moving the output waveguide with the same lateral offset as the input waveguide and observing its efficiency produces the graph in Figure 4.23. The efficiency has a general trend to decrease, though not smoothly, which may be due to aberrations caused by the lens being designed ideally as collimating a point source located on the optical axis.

These aberrations in imaging at the output waveguide can be further studied by laterally moving the output waveguide around the expected offset. Figure 4.24 shows for offsets

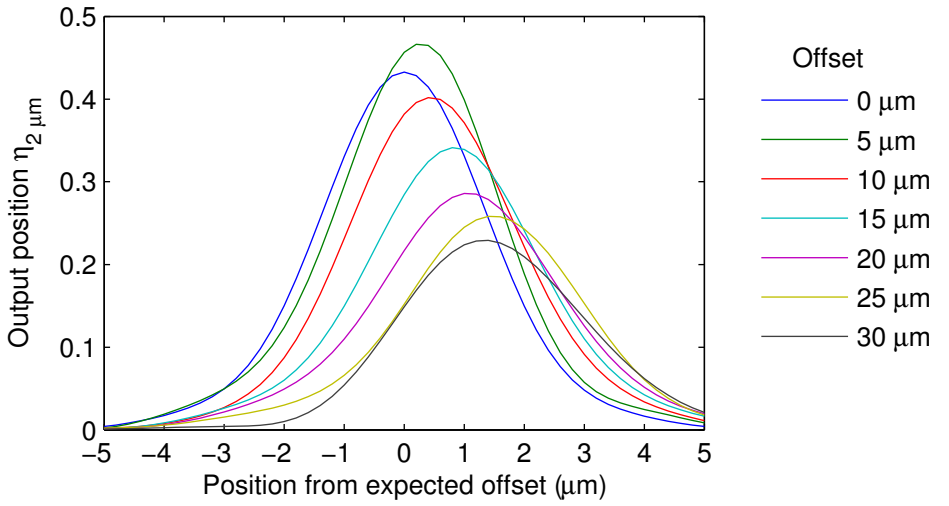

FIGURE 4.24: Efficiency at output waveguides at distances from the expected input lateral offsets.

0 μm to 30 μm how the efficiencies vary with varying the distance of the offset. Only the on-axis input peaks where it is expected. The trend is for efficiencies to peak up to 2 μm away from where expected.

4.9.6 Discussion

From amongst the candidate lenses, the paraxial lens was chosen for fabrication as simulations have shown it be the most efficient. The fabrication tolerances are not considered significantly more difficult than for the other candidate lenses. It was unexpected that the kinoform should perform better in simulations than the other candidate lenses, but it may be explained by the limitations in the analytical model for design. This is further discussed in section 4.10.

4.10 Limitations of the Analytical Model

The simulations have not shown 100% efficiency as expected from the theory used for design. There are two shortcomings in the analytical design which are discussed here. First, the analytical model does not take into account the effect of the diffraction of a plane wave in the lens itself, leading to errors on the second lens boundary through which the light passes. Second, the analytical model is based on the approximation that the lens receives a spherical wavefront at its input lens boundary.

The 2D simulations show the paraxial kinoform design to be the most efficient of the lenses. Having outlined the limitations of the analytical model, this could could be due to the paraxial kinoform being the thinnest of the lenses and the approximations

being adequate in practice. Furthermore, in practice, losses incurred from propagation, scattering from imperfections and mode mismatches at interfaces, are not included in the model or simulations because of the advantages of the use of EIM. To improve on the performance of the design, a more detailed analytical model could be developed with better or fewer approximations by including the effects of diffraction of a plane wave and focussed waves. Another option would be to run BPM with numerical optimisation methods, such as spline or genetic algorithms, which could improve the design and simulated performance with efficiencies approaching $\sim 90\%$, potentially achievable.

4.11 Conclusion

Integrated lenses can be used on chip to focus a beam into a small spotsize in the middle of a microfluidic channel by imaging the end of a channel waveguide. The planar integrated lenses discussed in this chapter have been of two types: refractive lenses and diffractive lenses.

Refractive lenses with circular or spherical profiles are commonly used in bulk designs due to manufacturing difficulties of such lenses. Ideal refractive lenses are designed by Fermat's principle giving ideal collimating and focussing lens geometries of hyperbolas for positive lenses and ellipses for negative lenses. Conic geometries are not troublesome for fabrication in a planar process allowing simple access to improved performance using these acircular lenses rather than the familiar circular lenses, lowering aberrations on the optical axis and increasing apertures.

Diffractive lenses were considered to overcome the problems with refractive lenses such as poor lens aperture collection and large *thickness*. Integrated diffractive lenses stem from the long established FZP, which is well known for its poor diffraction efficiency of only $\sim$40%. The Bragg lens is an extension of the FZP which can focus the light into one diffractive order, but operating in the Bragg regime. Unfortunately, the central zones of the lens do not meet the Bragg regime condition. This severely limits the practical efficiency of the lens. An alternative improvement on the FZP diffraction efficiency can be achieved by employing a kinoform profile which is essentially a blazing necessary to concentrate the power into one focussed order. This has a theoretical efficiency of 100%, but is limited by the analytical model used to design it and, of course, fabrication tolerances and imperfections.

Candidate lenses were chosen, namely, the elliptical refractive lens, the elliptical McGaugh kinoform lens, the elliptical kinoform lens, and the paraxial kinoform lens. Simulations by BPM have shown, unexpectedly, that the paraxial kinoform lens is the most efficient at imaging the end of a channel waveguide. The discrepancy is because of the limitations of the analytical method used for designing of the lenses. The paraxial lens was simulated to predict likely performance of focussing into the middle of a microfluidic

channel. The lens has the ability to focus into the middle of channels as wide as 200 μm with small change to efficiency.

The lens chosen to be fabricated using the material system in Chapter 6 is the paraxial kinoform. This lens from among the other candidate lenses was the most efficient in simulations; there was a 60% efficiency for imaging the end of a waveguide into the middle of a 20 μm microfluidic channel with a spotsize of 2.05 μm. At the micron scale, integrated optics offers potential for alternative planar devices that can image the end a waveguide. Chapter 5 describes such alternative devices, the AWG and MMI, which use diffraction and another phenomenon of self-imaging, respectively, to achieve focussing of a waveguide spotsize into a microfluidic channel.

Chapter 5

Alternative Waveguide Focussing Devices

5.1 Introduction

Integrated optical components are able to manipulate light on chip at the micronscale, leading to the motivation to combine it with microfluidics to further LoC performance. The state-of-the-art work being done in combining the two specifically for microanalysis has been reviewed in Chapter 2. This showed that an important function for optical integration is in controlling the free beam for direct excitation in the microfluidic channel enabling improvement to existing LoC optical detection systems and to incorporate other optical detection systems into LoC which so far have had little or no integration. Chapter 3 showed that channel waveguides delivering the light to the microfluidic channel is a poor solution for the wide microfluidic channels necessary in many microfluidic applications. Chapter 4 described how integrated planar waveguide lenses can be designed to focus light from the end of a waveguide into the middle of a microfluidic channel. This chapter introduces alternatives to planar waveguide lenses. Two other planar devices which can achieve the necessary function of 1:1 imaging of a point source into the middle of a microfluidic channel are described.

The first device considered is the arrayed waveguide grating (AWG) used for wavelength filtering and routing [220]. The equations used for designing a Rowland-type AWG are given and alternative designs discussed. The flexibility for direct excitation in microfluidics is discussed, but the AWG was not considered further due to fabrication tolerances being stringent. The second device is the multimode interference device (MMI) which is essentially a multimode waveguide which uses the *self-imaging* phenomenon and has been extensively used for power splitting [221]. The equations to design an MMI are given and, unlike the AWG, the MMI has high tolerances and was therefore fully designed and simulated using BPM for subsequent fabrication.

5.2 Arrayed Waveguide Grating

5.2.1 The Rowland-type AWG

By far the most common design of the AWG is based on two star couplers connected together by an array of waveguides of varying length,as depicted in Figure 5.1. The star coupler geometry is based on the Rowland mounting used in concave gratings. The AWG can be viewed as a transmission version of a concave grating [222]. Here, the Rowland-type AWG will be described in terms of its defining equations based on the literature [165, 222, 223].

Input waveguides connect to the first star coupler. The light from the end of an input waveguide diverges in the star coupler's slab region and couples into the arrayed waveguides. The arrayed waveguides are a phased array acting as a concave diffraction grating, which gives rise to the wavelength dispersion in an AWG device. The design of the array is such that the adjacent waveguides have a different length incremented by ΔL, leading to phase differences dependent on wavelength so that the interference pattern created by the emerging light from the grating into the second star coupler reconstructs focal points at shifted angles dependent on wavelength coupling to different output waveguides that lie on a circle. The function of the Rowland-type AWG is reciprocal.

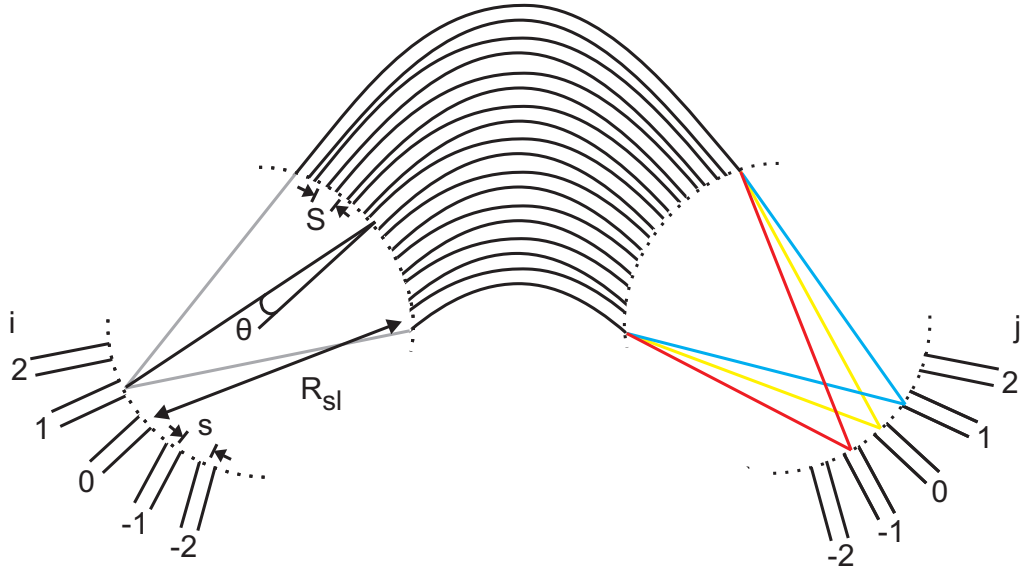

FIGURE 5.1: Schematic of AWG layout consisting of a phased grating between two star couplers. Light entering from an input channel waveguide diverges in the first star coupler and couples to the phased grating, then enters the second star coupler wavefront interfering in such a way as to refocus different wavelength on to the different output waveguides. The operation is reciprocal.

The defining equation for an AWG is its grating equation relating optical path length through the AWG to the wavelength, λ, and the grating diffraction order, m, describing its focussing and dispersive functions. The grating equation for the Rowland-type AWG is [223]

$$n_{sl} S \sin\theta_{in} + n_{ch}\Delta L + n_{sl} S \sin\theta_{out} = m\lambda, \tag{5.1}$$

where n_{sl} and n_{ch} are the effective refractive indices of the slab waveguide and the channel or rib waveguide, respectively, S is the spacing between the arrayed waveguides of the star coupler, and

$$\theta_{in} = is/R_{sl}, \quad \text{and} \quad \theta_{out} = js/R_{sl}, \tag{5.2}$$

where i and j are the waveguides integer positions for the input and output slab regions, respectively, s is the spacing between input or output waveguides, and R_{sl} is the focal length of the slab region. The difference in length between adjacent array waveguides determined by the central wavelength, λ_c (the wavelength with zero angular dispersion), is

$$\Delta L = \frac{m\lambda_c}{n_{ch}}. \tag{5.3}$$

The dispersive properties of the AWG are what makes the device extremely useful. The angular dispersion is derived by differentiating Equation 5.1 and taking into account the group effective refractive index, n_g, due to wavelength dispersion in the waveguides. Assuming $\theta_{in} \approx \theta_{out}$ and that the dispersion angle is small ($\sin\theta \approx \theta$) the angular dispersion is given by

$$\frac{d\theta}{df} = -\frac{m\lambda^2}{n_{sl} S c}\frac{n_g}{n_{ch}} \tag{5.4}$$

$$n_g = n_{ch} - \lambda\frac{dn_{ch}}{d\lambda}. \tag{5.5}$$

where c is the speed of light in a vacuum. From the angular dispersion, the frequency channel spacing for the AWG is then given by

$$\Delta f = \frac{s}{R_{sl}}\left(\frac{d\theta}{df}\right)^{-1} = \frac{s}{R_{sl}}\left(-\frac{m\lambda^2}{n_{sl} S c}\frac{n_g}{n_{ch}}\right)^{-1}. \tag{5.6}$$

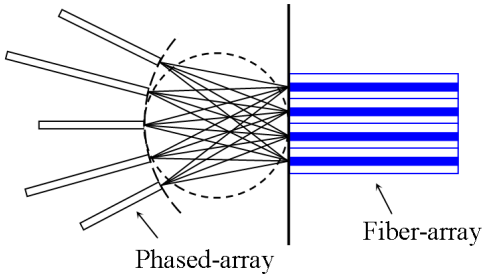

FIGURE 5.2: Flat focal AWG coupling into fibres, taken from [226].

The frequency channel spacing is the spacing between frequencies that can be demultiplexed by the AWG into the output waveguides.

5.2.2 Alternative AWG Types

The Rowland-type AWG focusses its output onto a circle. Other focal lines not based on a circle, but optimised for particular parameters are possible by using the aberration theory of AWGs [224] based on the stigmatic points used in reflective concave gratings [169, 225]. One such possible design is the flat-focal AWG, which has been realised in a polymer material system [226], focussing on a straight line that can be used to couple light directly from or to a fibre array, as illustrated in Figure 5.2, or to a photodiode array. This configuration would be very useful for microfluidics as the focal line could be located in the middle of the microfluidic channel being better suited for microfluidic straight channel geometry.

There are other types of AWGs which operate by replacing the star couplers with MMIs making use of the phenomenon of self-imaging to split power into the arrayed waveguides, these are known as MMI-AWGs. These are not considered in this chapter, but are discussed in Section 8.2.

5.2.3 Discussion on the AWG

The AWG can be used as a lens, performing a 1:1 imaging operation of a point source into a microfluidic channel with the spotsize determined by the input waveguide dimension and can perform better than a planar lens described in Chapter 4, with higher efficiencies, low aberrations, and can work efficiently at more than one wavelength. The fact that AWGs are used for the (de)multiplexing of wavelengths implies that they are ideal candidates for integrated planar spectrometers to be included in microfluidic systems as demonstrated in the modified AWG used by Komai *et al.* [227] to measure the spectral transmittance of liquids in the near infrared. This has also been achieved in the visible wavelength range [228, 229] with a recently developed AWG [180]. However, these devices involve having the microfluidic channel either in the middle of the slab

region or crossing an input waveguide before entering the AWG and do not achieve a focus with a small spotsize in the microfluidic channel, the objective of the present work.

Optical detection can be performed with AWGs, as with lenses. Excitation at the AWG's small focal point and the AWG's collection at a wide range of angles has the potential in acquiring the scattering distributions of particles flowing through the microfluidic channel. In addition, fluorescence measurements could be made and separated from the excitation light due to the AWG's angular dispersion.

The use of the AWG is flexible as it can be used for optical trapping, normally requiring bulk confocal lenses, in a microfluidic channel [230]. The AWG doing the optical trapping aids in creating more complex device configurations for optical detection methods which have few, if any, examples of integration to date. Laser tweezer Raman spectroscopy (LTRS) may be achievable as AWGs can multiplex and focus two wavelengths on the same focal point, one for trapping, the other for Raman excitation. Focussing several wavelengths to the same point would also make the AWG useful as an integrated thermal lens microscope (TLM). An area of motivation for scaling by using integrated optics to analyse submicron-sized particles is fluorescence correlation spectroscopy (FCS). An even more novel use would be an AWG working as a Young's interferometer for micro-scale interference pattern detection whereby several beams of the same wavelength are created along a focal line and a passing micron-sized particle affects the interference pattern.

AWGs would be a very flexible device, if integrated with a microfluidic channel. However, the first AWG operating in the visible part of the spectrum was only recently reported [180] by a group that have designed and fabricated AWGs for many years. AWGs tend to be difficult to fabricate requiring stringent tolerances in fabrication to function efficiently. The AWG was not be pursued further because of the tolerances in fabrication are considered too high for this work. The MMI, on the other hand, is simpler to design and has lower tolerances, since it is essentially a multimode waveguide. The MMI is presented in the next section.

5.3 Multimode Interference Device

5.3.1 Theory of Self-Imaging in Waveguides

The Talbot effect first described over 170 years ago [231], also known as self-imaging, is a familiar phenomenon in diffractive optics, but the phenomenon also arises in multimode optical waveguides and it is proposed here that it can be used to image a small spotsize beam into the middle of a microfluidic channel. This section gives the theory of self-imaging in step-index multimode waveguides as described by Soldano and Pennings [232]. When the multimode waveguide is designed so its length coincides with one of the self-imaging planes at its output, it is known as a multimode interference (MMI) device.

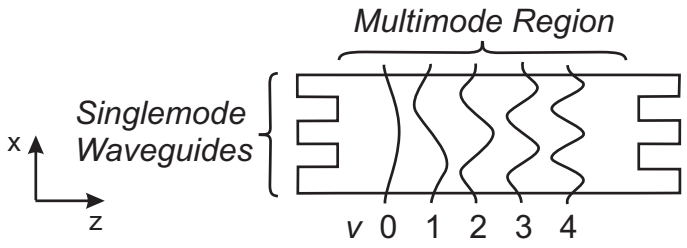

FIGURE 5.3: Schematic of an MMI supporting several modes.

The MMI device usually comprises one or more singlemode waveguides at the input and output of the multimode waveguide, referred to as the multimode region or slab region, as illustrated in Figure 5.3. Since the MMI is thin enough that the modal behaviour in the vertical dimension (y-axis) of the waveguide can be assumed to be singlemoded, the EIM, described in Subsection 3.3.3, can be employed to transform a 3D structure problem into a 2D structure problem. The 2D multimode waveguide supports m modes as depicted in Figure 5.3 with mode numbers assigned by $v = 0, 1, \ldots (m-1)$. The relationship between the horizontal wavenumber k_{xv}^2 and the propagation constant β_v^2 is given by the dispersion equation

$$\beta_v^2 + k_{xv}^2 = (k_0 n_{co})^2 \tag{5.7}$$

where $k_0 = 2\pi/\lambda_0$, n_{co} is the core index

$$k_{xv}^2 = \frac{(v+1)\pi}{W_{ev}}. \tag{5.8}$$

W_{ev} is the effective width corresponding to the Goos-Hähnchen shift. For high-contrast waveguides $W_{ev} \simeq W_{MMI}$. However, there will be little difference between the effective mode widths and the approximation $W_{ev} \approx W_e$ corresponding to the fundamental mode can be used. The effective width is

$$W_e = W_{MMI} + \frac{\lambda_0}{\pi}\left(\frac{n_{cl}}{n_{co}}\right)^{2\sigma}(n_{co}^2 - n_{cl}^2)^{-\frac{1}{2}} \tag{5.9}$$

where $\sigma = 0$ for TE and $\sigma = 1$ for TM, and n_{cl} is the refractive index of the surrounding medium. Applying a paraxial approximation, $k_{xv}^2 \ll (k_0 n_{co})^2$, on Equation 5.7, the dispersion equation,

$$\beta_v \cong k_0 n_{co} - \frac{(v+1)^2 \pi \lambda_0}{4 n_{co} W_e^2}. \tag{5.10}$$

West and Plant [233] explore optimising MMIs using a higher number of terms from the Taylor expansion. Returning to the paraxially designed MMI, the necessary length of the MMI is calculated below. The beat length between the two lowest order modes can be defined as

$$L_\pi = \frac{\pi}{\beta_0 - \beta_1} = \frac{4 n_{co} W_e^2}{3\lambda_0} \tag{5.11}$$

with the propagation constants spacing

$$(\beta_0 - \beta_v) \cong \frac{v(v+2)\pi}{3L_\pi}. \tag{5.12}$$

An input field $\Phi(x,0)$ at $z = 0$ can be decomposed into modes $\phi_v(x)$

$$\Phi(x,0) = \sum_{v=0}^{m-1} c_v \phi_v(x) \tag{5.13}$$

where c_v is the field excitation coefficients given by the overlap integral

$$c_v = \frac{\int_\infty^\infty \Phi(x,0)\phi_v(x)dx}{\sqrt{\int_\infty^\infty \phi_v^2(x)dx}} \tag{5.14}$$

The field can be described as

$$\Phi(x,z) = \sum_{v=0}^{m-1} c_v \phi_v(x) \exp(i(\omega t - \beta_v z)). \tag{5.15}$$

The $\exp(i\omega t)$ part can be ignored because it is implicit and the phase factor of the fundamental mode, $\exp(-i\beta_0 z)$, can be removed. The formula then becomes

$$\Phi(x,z) = \sum_{v=0}^{m-1} c_v \phi_v(x) \exp(i(\beta_0 - \beta_v) z) \tag{5.16}$$

and substituting Equation 5.12 the field at a distance $z = L$ is

$$\Phi(x,z) = \sum_{v=0}^{m-1} c_v \phi_v(x) \exp\left(i \frac{v(v+2)\pi}{3L_\pi} z\right). \tag{5.17}$$

By inspection, the condition for having 1:1 imaging of the input $\Phi(x,0)$ along the MMI is for *general self-imaging*

$$\exp\left(i\frac{v(v+2)\pi}{3L_\pi}z\right) = (-1)^v \tag{5.18}$$

where N-fold images are created at planes given by

$$L = \frac{p}{N}(3L_\pi), \quad p = 0, 1, 2, \ldots \tag{5.19}$$

General self-imaging is the general case for the self-imaging phenomenon. Unlike the general case where which modes are excited are irrelevant, in *restricted self-imaging* only certain modes are excited leading to imaging effects which can shorten the MMI length. *Symmetric interference* where the field at the input of the MMI is symmetrical provides possibly a useful device for the microfluidic device and imaging planes are given by

$$L = \frac{p(3L_\pi)}{4N}, \quad p = 0, 1, 2, \ldots \tag{5.20}$$

The design procedure for an MMI is relatively straightforward. Once the W_{MMI} is specified, then Equations 5.19 and 5.20 for MMI lengths of the general self-imaging and restricted self-imaging by symmetric interference, respectively. Both of these MMIs are simulated in the next section.

5.3.2 Simulations of MMI Devices

5.3.2.1 The MMI devices

The MMIs were designed to have three waveguide inputs and outputs of a width of 2 μm. Section 3.5.4 showed that a 10 μm waveguide spacing would avoid coupling, resulting in an MMI slab region of a width of 22 μm. The MMIs were designed for imaging into the middle of a 20 μm-wide microfluidic channel. The structure defined could then be simulated relatively quickly as was the case with the waveguides and lenses using BPM in Chapter 3 and Chapter 4, respectively.

The MMIs were simulated for the purposes of optical microanalysis based on the material system discussed in Chapter 6. The MMI structure was drawn into *BeamPROP*$^{\text{TM}}$ CAD window as shown in the simplified schematic given in Figure 5.4. The MMI consists of three input and three output waveguides. The figure of merit chosen for the simulations is the power coupling efficiency of a launching waveguide mode at any point of interest along the device is given by the square of the overlap integral

$$\eta = \frac{\left(\int_{-\infty}^{\infty}\phi(x,0)\phi(x,z)dx\right)^2}{\int_{-\infty}^{\infty}\phi^2(x,z)dx} \tag{5.21}$$

where ϕ is the field distribution. This is the same dimensionless figure of merit, used in the simulations of waveguide lenses in Chapter 4, comparing what is desired and what is achieved that overcomes the difficulties with just using spotsize.

The length of the general self-imaging MMI is given by substituting Equation 5.11 into Equation 5.19 for 1:1 imaging (N=1) at the shortest length possible (p=1),

$$L_{MMI} = \frac{4n_{co}W_e^2}{\lambda_0} + \delta, \tag{5.22}$$

where δ is the offset length needed because of the analytical approximations made. The L_{MMI} is 4988 μm with a δ of 40 μm for Figure 5.5.

Figure 5.5 shows contour plots of a propagating field amplitude in the general self-imaging case. Figure 5.5(a) shows the propagating field distribution when he input waveguide 1 is excited and results in the light coupling into output waveguide 3. Likewise, Figure 5.5(b) shows the middle input waveguide, waveguide 2, excited and the output coupling to output waveguide 2. Figure 5.5(c) shows the input waveguides 1 and 3 excited and coupling into the same positions at the output. All three input waveguides are excited in Figure 5.5(d) and couple into all three output waveguides. All four plots show varying amounts of initial loss into the multimode region because divergence of the light entering causes some of the light not to fulfil the total internal reflection condition, but this is negligible. Figures 5.5(b) - 5.5(d) show interference patterns that reconstruct the input 4 times along the length of the MMI because the inputs are symmetrical and exhibit having symmetrical interference as described in Subsection 5.3.1.

The field of the required spot to be imaged into the middle of a microfluidic channel is symmetrical. If the input field of the multimode region of the MMI is symmetrical about the middle of the MMI input, then only symmetrical modes are excited within the MMI leading to symmetrical interference. This has the effect of reproducing the symmetrical input field at one quarter of the length of an ideal general self-imaging MMI.

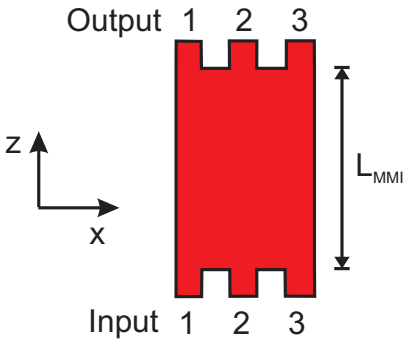

FIGURE 5.4: MMI model for simulation with 3 input and 3 output single mode channel waveguides.

The set of plots in Figure 5.5 is repeated in Figure 5.6 for the case of a symmetric restricted MMI. The length is calculated from substituting Equation 5.11 into Equation 5.20 for a 1:1 imaging (N=1) of shortest length needed (p=1),

$$L_{MMI} = \frac{n_{co} W_e^2}{\lambda_0} + \delta. \tag{5.23}$$

The difference between Equation 5.22 and Equation 5.23 is that the first term is 4 times larger in the case of the general self-imaging MMI. The restricted self-imaging MMI has a L_{MMI} of 1247 μm with a δ of 10 μm. Note that, in the case of Figure 5.6(a), where the input field is not symmetrical, the output does not couple efficiently into the output waveguides as it does not form a 1:1 image. All the other plots in the figure show coupling into the corresponding outputs.

Figures 5.5 and 5.6 show clearly the MMI function for general imaging and restricted imaging, respectively. The two designs for MMIs integrated with a microfluidic channel

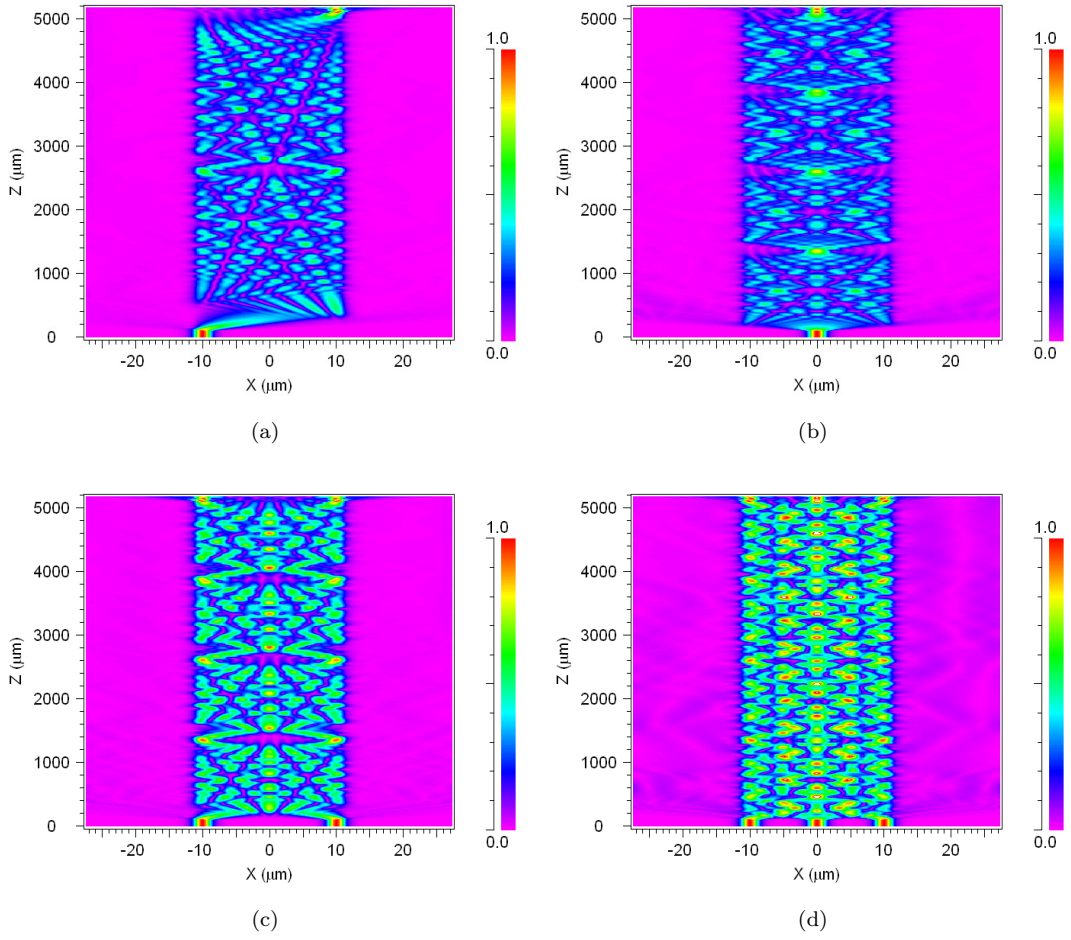

FIGURE 5.5: Field amplitude of a general imaging MMI with 2 μm waveguide input excitation at (a) waveguide 1, (b) the centre, waveguide 2, (c) waveguides 1 and 3, and (d) all three inputs.

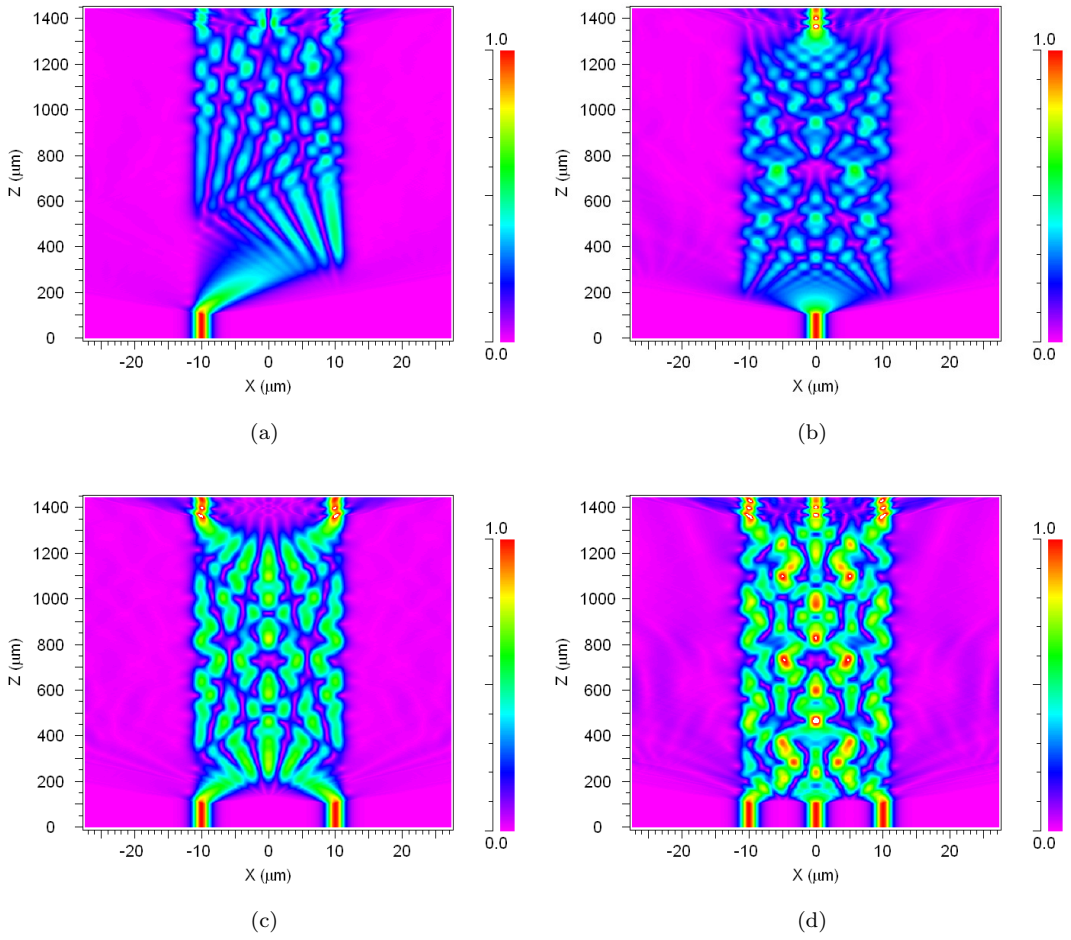

FIGURE 5.6: Field amplitude of a symmetrical restricted imaging MMI with 2 μm waveguide input excitation at (a) waveguide 1, (b) the centre, waveguide 2, (c) waveguides 1 and 3, and (d) all three inputs.

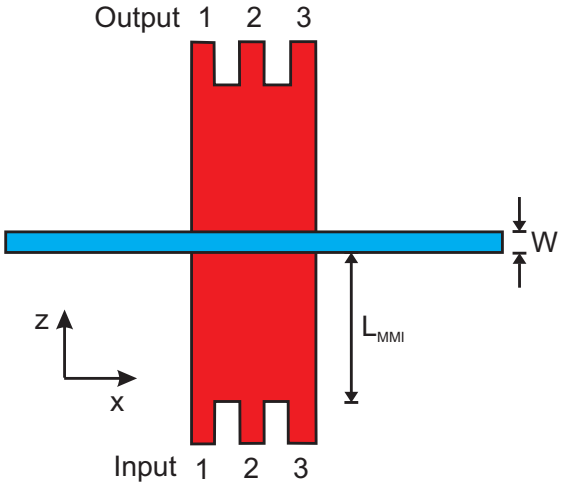

FIGURE 5.7: Simulation model of MMIs between a microfluidic channel of width W.

involve two MMIs either side of the microfluidic channel, one to image the waveguide inputs into the middle of the microfluidic channel and the other to collect from the middle of the microfluidic channel. Simulations can indicate how the system will behave with a water filled microfluidic channel. A simple schematic of such a design in *BeamPROP*™ is shown in Figure 5.7.

5.3.2.2 The general self-imaging MMI with microfluidic channel

The presence of the microfluidic channel affects the offset length needed for the MMI to function. Therefore, simulations of the coupling efficiency in the middle of the microfluidic channel were done for the general self-imaging MMI. Figure 5.8(a) shows the coupling efficiency for imaging into the middle of microfluidic channel versus the offset length between -100 and 100 μm with an efficiency peak at 0.76 for a 15 μm offset length. There is negligible light coupling into output positions 1 and 3. Moving inputs from waveguide 2 to 1 as shown in Figure 5.8(b), the efficiency peaks at 0.76, but with an offset length of 40 μm, again, with negligible power coupling to the other two output positions. Figure 5.8(c) shows the efficiency with all inputs active. The peak for position 2 is 0.93 at offset length of 25 μm, but the peak for the side positions 1 and 3 is 0.83 at 40 μm. The graphs in Figure 5.9 do not have their peaks in efficiency at the same offset lengths because of the approximations in the analytical designs and the Goos-Hähnchen shift. To choose the offset length necessary for maximum efficiency it was decided to take the peak for the side waveguides in Figure 5.8(c) because at this offset the efficiency at waveguide 2 is still higher than the side waveguides. Comparing this with the other graphs at offset length of 40 μm, the efficiency is still as high as 0.70 with only a side waveguide excited, Figure 5.8(b), or middle excitation, Figure 5.8(a).

Once imaging has been optimised for the middle of the microfluidic channel, then the spotsize expected at the middle of the channel is calculated. The lefthand column in Figure 5.9 show plots of the field amplitude propagating along the device and focussing into the microfluidic channel for different input waveguides excited and the righthand column shows the corresponding field amplitude distribution in the middle of the microfluidic channel. The case of excitation from waveguide input 1 is shown in Figure 5.9(a) resulting in a spotsize of 1.69 μm. Excitation from the middle waveguide, waveguide 2, is given in Figure 5.9(c) and gives a spotsize of 2.22 μm. Excitation from input waveguides 1 and 3 is given in Figure 5.9(e) resulting in a spotsize of 1.55 μm. The spotsizes for the different excitations are larger than the launch spotsize of 1.25 μm. This is due to the image not being perfectly reconstructed because of the accumulating relative phase shifts between modes due to the paraxial approximation and Goos-Hähnchen shift.

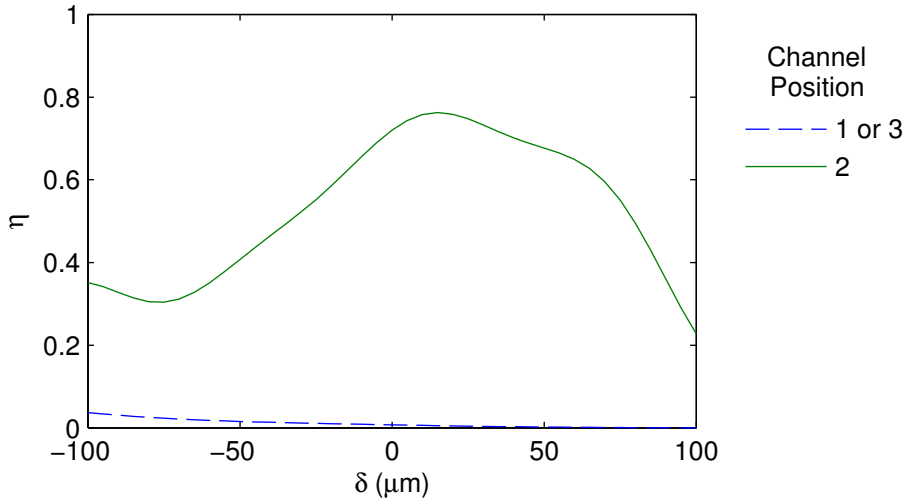

(a) middle excitation, input position 2

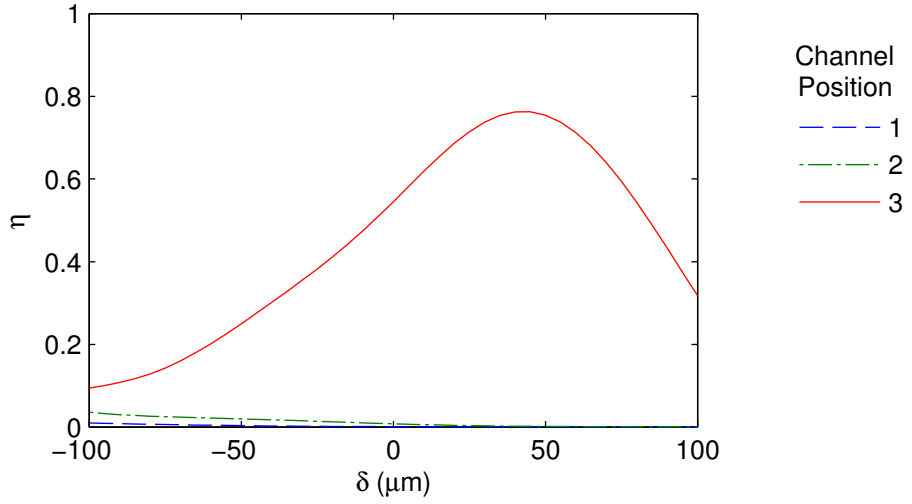

(b) side excitation, input position 1

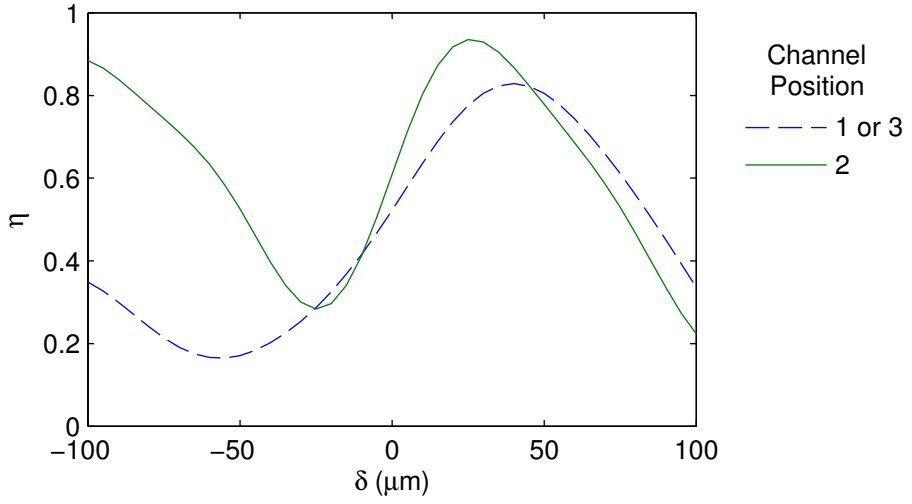

(c) excitation of all three inputs

FIGURE 5.8: Efficiency in the middle of the microfluidic channel versus offset length for a general self-imaging MMI with different inputs excited.

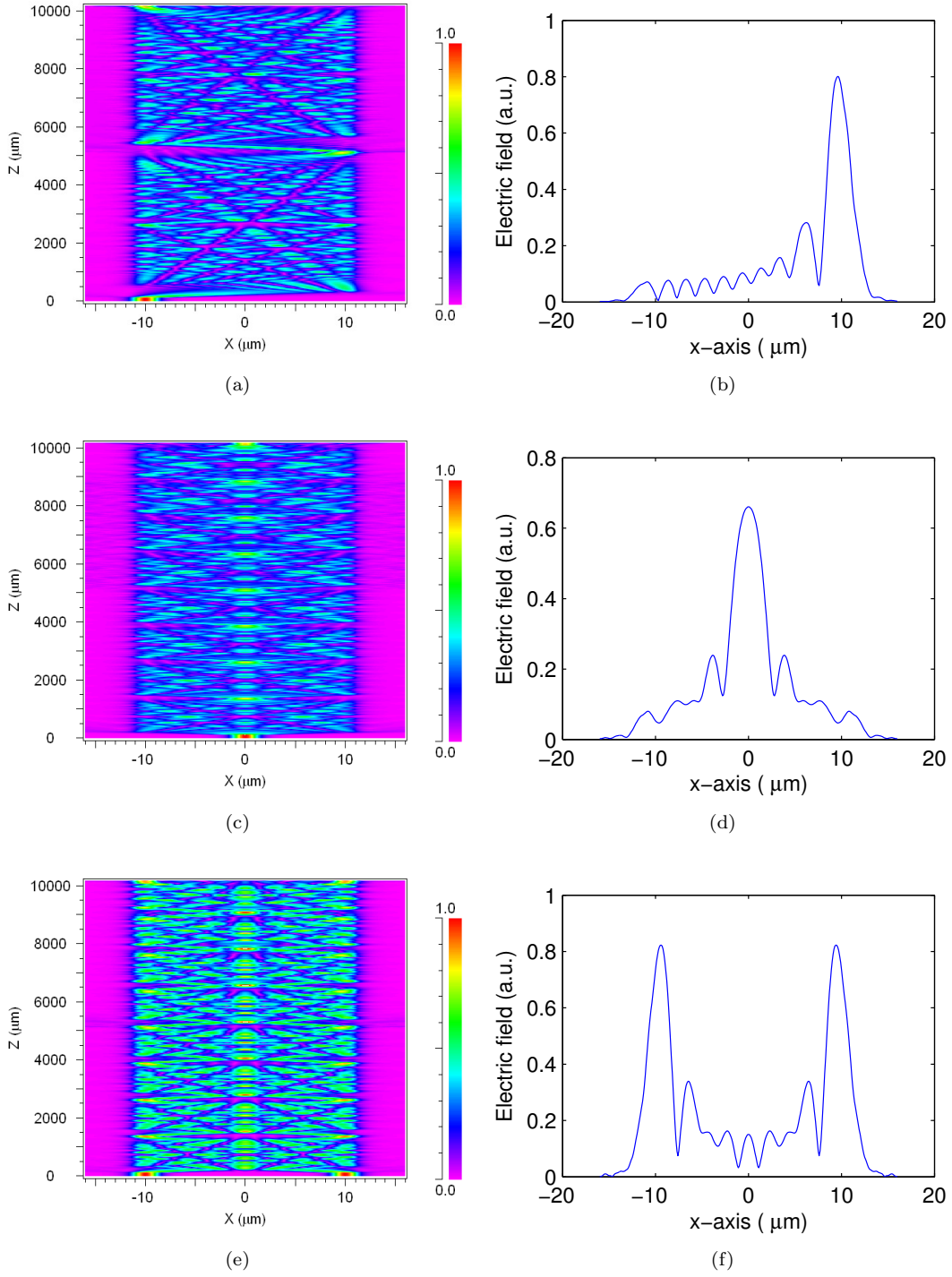

FIGURE 5.9: Field amplitude of the general imaging MMI.

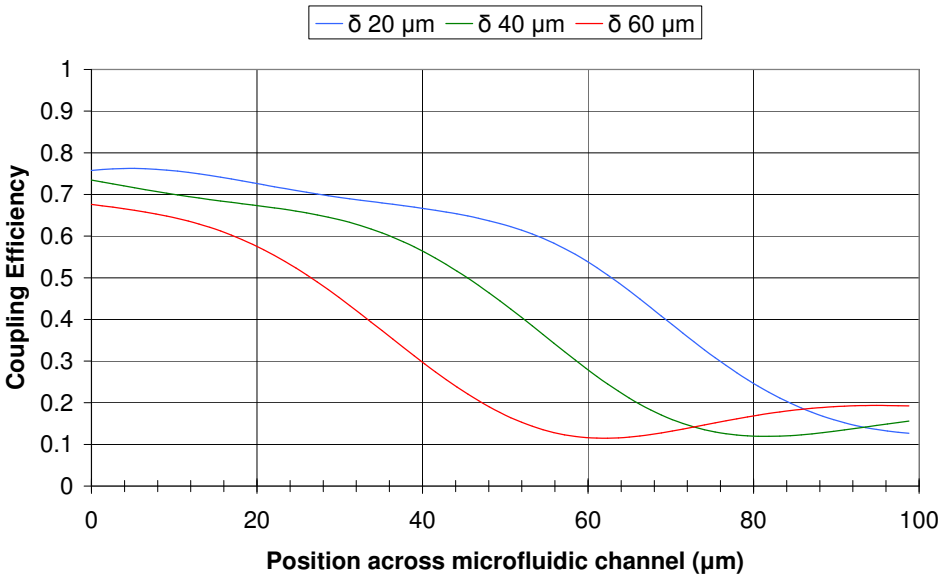

FIGURE 5.10: Coupling efficiency of general imaging MMI across the microfluidic channel for δ offset length of 20, 40, and 60 μm.

The microfluidic channel width in the model in Figure 5.7 was set to 100 μm. Figure 5.10 shows the coupling efficiency of a general self-imaging MMI across this microfluidic channel width for δ, the offset length, of 20, 40, and 60 μm for excitation at input waveguide 2. The MMI was optimised for a microfluidic channel of 20 μm width and corresponds well with the graph in Figure 5.8(a) with the offset length of 20 μm having the highest efficiency at 10 μm in the microfluidic channel (the middle of a 20 μm microfluidic channel). The shape of the curves gives information on the free beam across the microfluidic channel where lower efficiency from the peak efficiency corresponds to lower local peak intensity. The curves in the graph have similar shape, which is shifted by the offset length with approximately -1 μm shift in the microfluidic channel per 1 μm of offset length. Therefore, only the MMI offset needs to adjusted for a given microfluidic channel size and with increasing the microfluidic channel for this MMI will lead to negative offset length.

5.3.2.3 The restricted self-imaging MMI with microfluidic channel

The general self-imaging MMI was simulated for imaging into a microfluidic channel in the previous section. Here, the restricted self-imaging MMI is simulated for imaging into a microfluidic channel. Figure 5.11(a) shows the efficiency of imaging into the middle of microfluidic channel with an excited input at waveguide position 2. The peak efficiency for the output position 2 is 0.88 for an offset length of 10 μm. Figure 5.11(b) is the same but with the input at position 1 and the efficiency is not above 0.23 for any output position because this MMI can only image symmetrical input fields. For an excitation

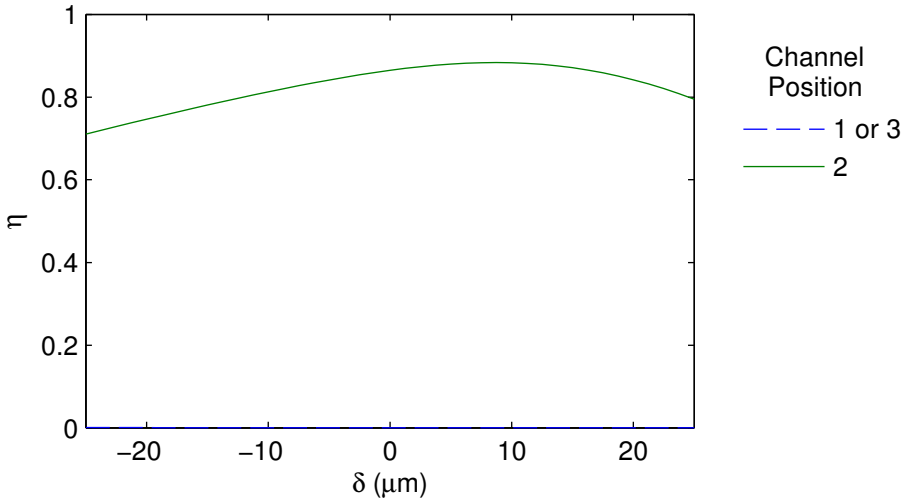

(a) middle excitation, input position 2

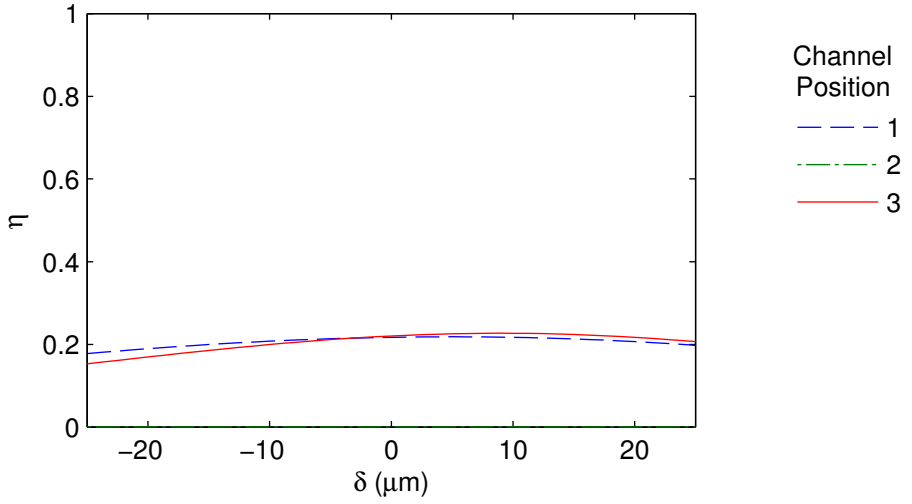

(b) side excitation, input position 1

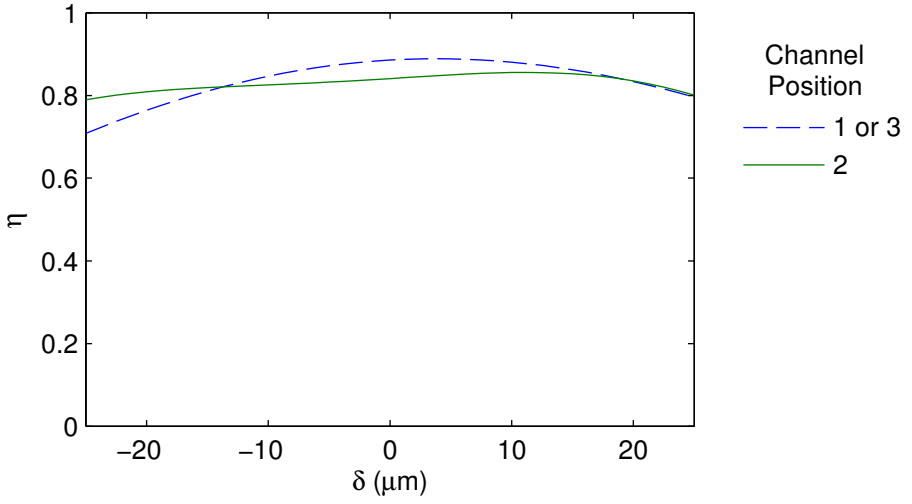

(c) excitation of all three inputs

FIGURE 5.11: Efficiency in the middle of the microfluidic channel versus offset length for a restricted self-imaging MMI with different inputs excited.

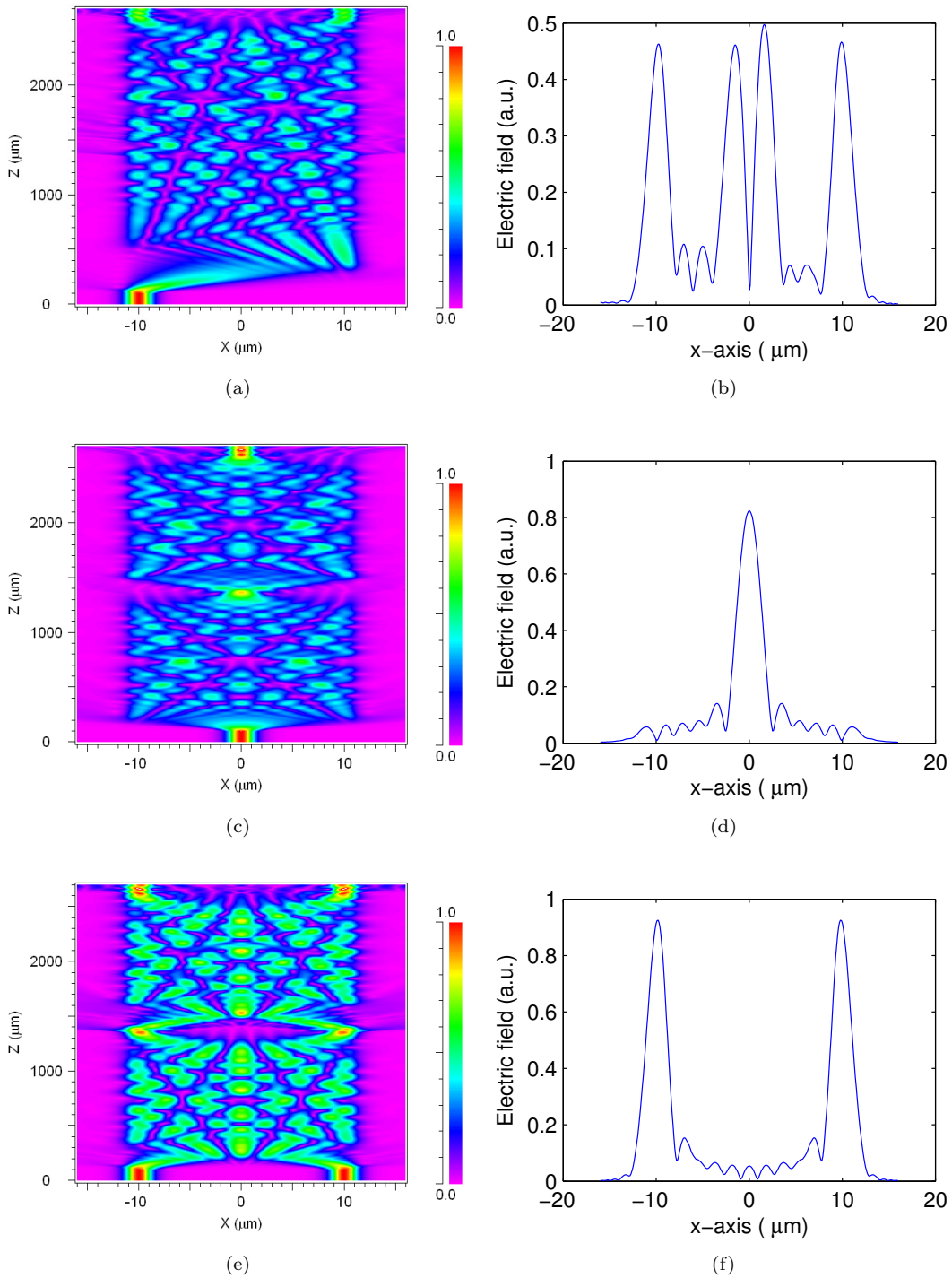

FIGURE 5.12: Field amplitude for the restricted imaging MMI.

of all inputs shown in Figure 5.11(c) the peak efficiency is 0.88 for an offset length of 5 μm for position 2 and peaks at 0.85 for an offset length of 10 μm for the side position, 1 and 3.

The spotsize expected at the middle of the channel for the restricted self-imaging MMI is given in Figure 5.12. The left column in Figure 5.12 shows plots of the field amplitude

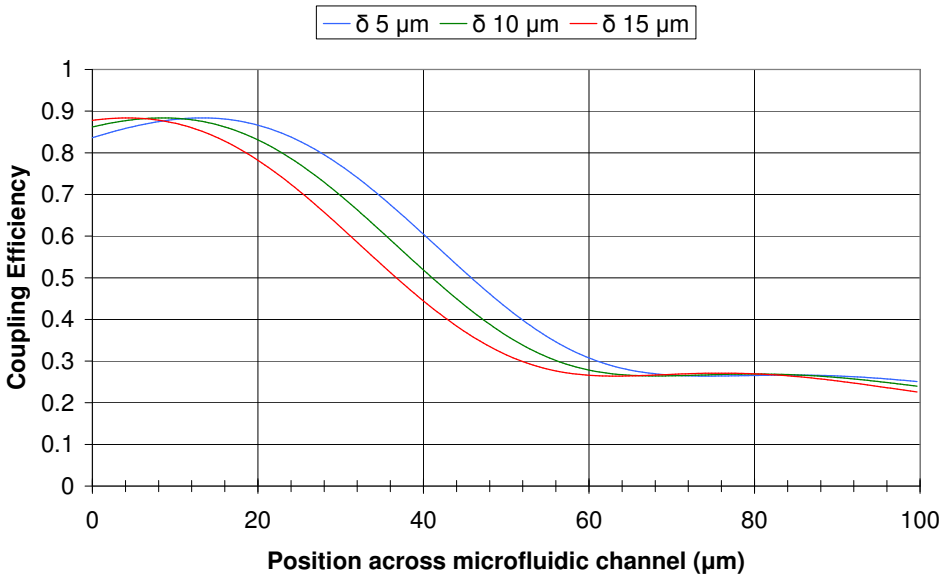

FIGURE 5.13: Coupling efficiency of restricted imaging MMI across the microfluidic channel for δ offset length of 5, 10, and 15 μm.

propagating along the device and focussing into the microfluidic channel for different given inputs, while the right column is the corresponding field amplitude in the middle of the microfluidic channel. The excitation from waveguide input 1 is shown in Figure 5.12(a), but the MMI cannot image non-symmetrical input fields so the field in the middle of the microfluidic channel in Figure 5.12(b) does not resemble the input field. The case of excitation from the middle waveguide, position 2, is given in Figure 5.12(c) with a spotsize of 1.74 μm at the middle of the microfluidic channel. Excitation from input waveguides 1 and 3 is given in Figure 5.12(e) and results in a spotsize of 1.50 μm. The spotsizes are larger than the launch spotsize of 1.25 μm, but smaller than the spotsizes for the general self-imaging MMI. This can be explained as the light has propagated for a shorter distance in the restricted self-imaging MMI than the general self-imaging MMI, so that the modes have not accumulated as much relative phase shift due to the analytical approximations of the design.

Figure 5.13 shows the coupling efficiency in a restricted imaging MMI across the microfluidic channel width of 100 μm for the offset length of 5, 10, and 15 μm for an excitation at input waveguide 2. The MMI was optimised for a microfluidic channel of 20 μm width and this is shown by the optimum offset length of 10 μm peaking at 10 μm across the microfluidic channel width, which corresponds well with the optimum offset length in Figure 5.11(a). The shape of the curves gives information on the free beam across the microfluidic channel, where lower efficiency from the peak efficiency corresponds to lower local peak intensity. The curves decay more rapidly than for the general self-imaging, shown in Figure 5.10, MMI due to the shorter restricted self-imaging MMI lengths lowering the effects of the Goos-Hähnchen shift and giving a better quality beam.

The curves are similar, but shifted along the microfluidic channel width at approximately -1 μm of microfluidic channel width per 1 μm offset length.

5.3.3 Discussion of the MMI

The MMI is essentially a multimode waveguide of suitable length to utilise the self-imaging phenomenon, where the excited modes interfere as they propagate to recreate either single or multiple images of the input field. Though normally used in integrated optics for coupling and power splitting, the MMI has recently been used for LoC detection applications: chemical sensing [234], gas sensing [235], and fluorescence detection [236].

The analytical treatment for weak-guiding waveguides does not describe the behaviour of the MMI perfectly because of the Goos-Hähnchen shift, so that the approximations can become invalid. One solution is to have air gaps [237] on both sides of the multimode region increasing the refractive index contrast without changing the material system. There is loss in image reconstruction as the modes accumulatively become out of phase with one another. The other effect of weak-guiding MMIs is the extraneous or pseudo self-imaging, not predicted by the analytical treatment and not dealt with in this work, which occurs at planes before the desired image plane has been studied [233] and utilised in realised MMIs [238, 239] to make two-wavelength filters.

The MMI has several design advantages over lenses for microfluidics. Imaging from an MMI is along a flat plane ideal for microfluidic integration. The MMI being essentially a wide multimode waveguide allows for high fabrication tolerances. The weak guiding, while reducing the image quality, also improves fabrication tolerances. Simulations of the MMIs compared to simulations of the lenses, in Section 4.9, show that the MMIs have higher efficiencies than the lenses focussing into the middle of the microfluidic channel as the light is guided right up to the microfluidic channel, thus lowering losses. However, the general self-imaging MMI when imaging the middle waveguide has a spotsize of 2.22 μm which is larger than the paraxial kinoform lens' spotsize of 2.05 μm because of the accumulating phase lags between modes. The restricted MMI solves this by reducing the propagation length and the resultant imaging exhibits both higher efficiency and a reduced spotsize of 1.74 μm.

5.4 Conclusion

Two planar integrated optical devices which perform focussing functions into the middle of a microfluidic channel have been presented in this chapter as alternatives to lenses, namely the AWG and the MMI. The AWG and MMI have the potential to be used in

several complex detection systems such as scattering, LTRS, or thermal lens where bulk optical components are normally used.

The AWG is a transmission grating that can be used for integration with a microfluidic channel with the advantage of focussing for a several wavelengths with low aberrations. The AWG could provide high flexibility for microfluidics. The geometry of the AWG does not have to be based on the Rowland mounting and can be designed to focus at having different wavelengths along a straight line, which is ideal for working with a straight microchannel detection region. However, only recently has an AWG operating in the visible range been demonstrated and fabrication tolerances tend to be stringent for AWGs to function efficiently. For these reasons, the MMI was preferred for experimental studies and has been designed and simulations presented as a device for focussing into a microfluidic channel for subsequent fabrication.

The MMI is a device that uses the *self-imaging* phenomenon and is relatively simple to design and fabricate because it is essentially a multimode waveguide with given length to image the input plane to the output plane. If only certain modes are excited at the input plane of the multimode region of the MMI, such as a symmetrical modes, then the MMI can have its length reduced by a factor of 4 which improves its imaging by reducing the accumulating phase lags between modes caused by the paraxial approximation used for design and the Goos-Hähnchen shift.

Chapter 6

Fabrication of Integrated Optics for Microfluidic Devices in Glass

6.1 Introduction

Increased integration of optics in microfluidic devices is required to further LoC technology as reviewed in Chapters 1 and 2. A higher level of optical integration to manipulate free beams in microfluidic channels for direct excitation of cells or particles was identified as an area of improvement. To achieve this, integration of optical functionality using waveguides, lenses, and MMI devices was studied theoretically for focussing of the free beam from the end of a channel waveguide into a microfluidic channel to improve performances in optical detection at the micronscale. This chapter describes the planar fabrication procedure developed for integrating optical components, namely, waveguides, lenses and MMIs, for a detection device in a SiO_2-based system. The basic structure is simple and flexible, using a two-mask process with minimal alignment in fabrication.

To simplify fabrication a simple design ethos was employed. A flexible waveguide "sandwich" structure of a buried optical layer aligned to the centre of the microfluidic channel is proposed, so that optimisation of the microfluidic method of focussing the particle to the centre of the microfluidic channel is available. The deposited optical waveguiding layer can then be patterned to make a wide range of planar integrated optical components for microfluidic analysis. The first stage of the fabrication optimisation is to make slab waveguides and optically characterise them by measuring the refractive index of the waveguide layer. Once this is known, the optical components can be designed. Microfluidic channels need to be from a few microns up to a hundred microns in cross-sectional dimensions to study micron-sized particles, such as biological cells. On top of the waveguides, there must be a deposited cladding layer to protect the waveguides, achieve symmetry, and bury the waveguides to the middled of the microfluidic

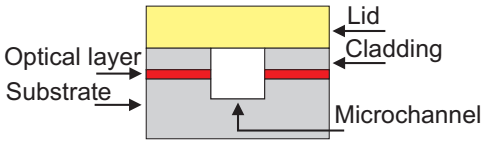

FIGURE 6.1: Illustration of the cross-section of the flexible sandwich structure. The base is the substrate (white), the optical waveguiding layer is deposited on top (red), the cladding (white), the etched microfluidic channel (blue) and the lid fixed on top (yellow).

channel sidewall. Finally, a lid is attached to seal the microfluidic channel; the device cross-section is illustrated in Figure 6.1.

Patterning the waveguide layer can create either rib or channel waveguides similar to configurations mentioned in the literature [166, 212]. This layer can also be patterned to include waveguide lenses and MMIs to manipulate light by focussing, so that, for example, the effects of divergence of an incoming beam can be controlled in the microfluidic channel.

6.2 SiO_2-Based Material System

6.2.1 Glass for Integration

Use of glass technology from the communications field can result in high quality optical microfluidic devices [159]. Silica glasses have good optical properties, such as low absorption in the visible range and the autofluorescence which contributes to background signals in detection systems is lower than in most commonly used polymers [240]. Glass has proven to have good bio-compatibility and existing MEMS technology can be used for microfabrication.

The fabrication process selected here was silica based due to silica glass having the good properties forementioned. A waveguide system with a microfluidic channel as shown in Figure 6.1, would ideally require smooth walls to reduce unwanted scattering of light at the interfaces and vertical walls for the light to propagate towards the collecting waveguide. In practice, a compromise is usually met which depends on the selectivity of any necessary masks and the material to be etched to the etchant used, and dimensions to be achieved. To achieve straight sidewalls an anisotropic etch such as ion beam milling, reactive-ion etching (RIE) or deep RIE (DRIE) process can be used, but the choice is strongly dependent on required aspect ratio.

6.2.2 Waveguides in Glass

The buried waveguide layer should have a selectivity for etching of ideally 1:1 with respect to the substrate and cladding, so that there is a smooth wall and not an undercut or notch feature produced by the etching, to minimise scattering loss at the interface and loss due to unwanted refraction. One way to achieve a material with similar properties to the silica cladding is to have a two glass mixture of mostly silica. Germania (GeO_2) which is commonly used material systems to make fibre-optics [241] may be used as a dopant. Germanium is the next element of group IV in the periodic table from silicon and germania has similar chemical properties to silica with its refractive index being higher. An alternative is to use a material such as tantala (Ta_2O_5). While it is molecularly much larger than silica and has a very high refractive index of approximately 2.1 at 633 nm [242, 243], only a very small concentration would have to be used as dopant.

Percentage weights for SiO_2:GeO_2 of 75:25 %wt and for SiO_2:Ta_2O_5 of 89:11 %wt targets were selected for the doped silica to give a deposited film of refractive index difference to undoped silica of ~ 0.015. The concentrations used were estimated from data in the literature [242–245]. The refractive index of the deposited films are described in Section 6.4 and Section 6.5. The value of ~ 0.015 was chosen using the modelling of rectangular waveguides in Chapter 3. The core of the waveguide has to have a high enough refractive index to guide the mode mostly in the core of the waveguide to able to have good control over the spotsize.

6.2.3 Other Material Systems

The material systems used for microfluidics and integrated optics systems fit into three categories: glasses, polymers, and silicon. Glass has already been discussed as the material of choice for this work. Here though, the latter two categories are briefly described for completeness.

Although silicon processes are well established, it is not a good optical material for propagating light in planar waveguides at the visible wavelengths, so it is not normally used in optical detection in microfluidics, unless the microfluidic channel and optical waveguides are made on a glass layer [39]. This of course does not apply to microfluidics with no on-chip optics.

Polymers, such as polydimethylsiloxane (PDMS) and polymethylmethacrylate (PMMA), have become very popular materials to work with for microfluidics. PDMS has a low autofluorescence, is transparent from wavelengths of 235 nm to the infra-red, and is considered non-toxic to cells and proteins [246, 247]. Becker and Locascio [248] published a review on the use of polymers for microfluidics. Polymers are considered to have advantages for microfluidics, such as quicker fabrication allowing for rapid prototyping for

low number of devices, usually not requiring a cleanroom facility, and cheap fabrication costs. Although polymers are generally considered to give poorer optical performance than traditional materials, in Becker and Locascio's opinion this may not always be the case with advances in polymer technology.

TABLE 6.1: Steps for fabrication of devices.

Step	Description
Buried Optical Layer	
Step 1	Acetone and IPA wash of substrate.
Step 2	Deposit 2 μm of doped silica by sputtering.
Step 3†	Anneal for 1 hr at 500 °C.
Step 4	Spin on positive photoresist (S1818).
Step 5	Photolithography.
Step 6	Etch 2 μm deep pattern by ion beam.
Step 7	Acetone and IPA wash of substrate.
Step 8	Plasma clean using RIE.
Step 9	Deposit 4 μm layer of silica by sputtering.
Step 10†	Anneal for 6 hr at 950 °C.
*Microfluidic Channel**	
Step 11	Spin on negative photoresist (SU-8 10).
Step 12	Photolithography.
Step 13	Etch 8 - 9 μm deep pattern by ion beam.
Step 14	Remove residue in fuming nitric for 10 min.
Dicing & Polishing	
Step 15	Attach samples together with wax.
Step 16	Saw the substrate to separate the two chips.
Step 17	Lap and polish device ends.
*Seal Microfluidic Channel**	
Step 18	Glass cover-slips 150 - 170 μm thick cut to size.
Step 19	UV glue applied.
Step 20	Flood with UV for 30 s to set glue.
	† The anneal steps' difference is explained in Subsection 6.3.3.
	* Steps which were modified from original plan, discussed in Section 6.6.

6.3 Fabrication Process Used

6.3.1 Fabrication Steps

The choice of using SiO_2-based material system was made because of its optical quality and robustness, the standard processing used, chemical compatibility, and compatibility with fibre-optics. The fabrication process for the device is outlined in Table 6.1, though fine details of steps, such as the photolithographic steps, have been omitted from the table for clarity.

The fabrication is accomplished in only a two-mask process, one for etching and patterning the optical layer and the other for etching the microfluidic channel. The process can be thought of as being split into four main phases: fabrication of the buried optical layer, steps 1 to 10, fabrication of the microfluidic channel, steps 11 to 14, dicing and polishing of the samples, steps 15 to 20, and sealing of the channel steps 18 to 20. The remainder of Section 6.3 describes the methods used and elaborates on complicated steps.

6.3.2 Sputtering for the Deposition of Films

The first necessary step was to obtain an optical waveguiding layer for the optical components to be patterned in. Subsection 6.2.2 mentions GeO_2 and Ta_2O_5 as dopants for silica. Both composite materials were deposited on fused silica substrates. Deposition was done by sputtering from the custom-made targets (from Testbourne Ltd).

Radio frequency (RF) sputtering of thin films of composite materials such as GeO_2:SiO_2 [249] and Ta_2O_5:SiO_2 [242] has been successful at producing films of controllable refractive index. RF sputtering is depicted in Figure 6.2 and works by creating a 13.56 MHz alternating voltage across two electrodes in a vacuum chamber. For sputtering to deposit material from a target to a substrate the target must be on the cathode and the substrate on the anode. Ions are accelerated towards the cathode and bombard the

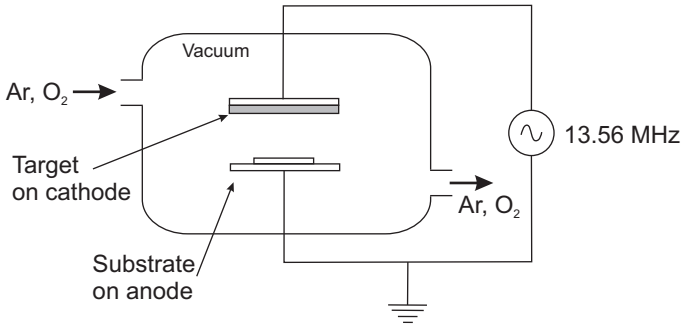

FIGURE 6.2: Illustration of an RF sputterer.

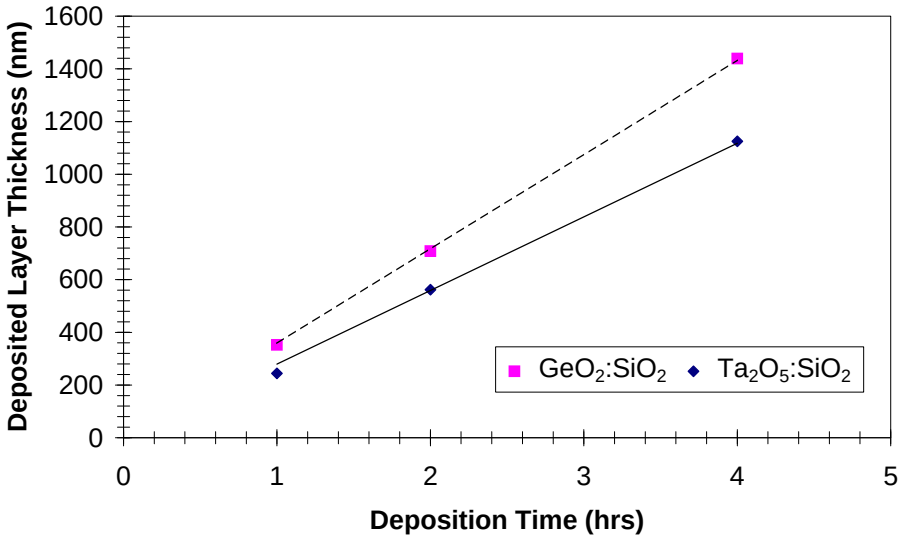

FIGURE 6.3: Deposited thickness of GeO_2:SiO_2 and Ta_2O_5:SiO_2 films versus time.

TABLE 6.2: Sputtered deposition rates of GeO_2:SiO_2, Ta_2O_5:SiO_2, and SiO_2 films.

Material	Deposition Rate (nm hr^{-1})
GeO_2:SiO_2	358
Ta_2O_5:SiO_2	279
SiO_2	207

target dislodging material which deposits on to the surface of the substrate. In standard plasmas Ar gas is used, but O_2 gas is also pumped into the chamber to oxidise any Ge and Ta atoms.

The conditions used were a magnetron power of 300 W, the gases pumped in at 20 sccm and 5 sccm for Ar and O_2 respectively, and a chamber temperature of 20 °C. The measured deposition thickness with respect to time for GeO_2:SiO_2 and Ta_2O_5:SiO_2 films are shown in Figure 6.3, and for SiO_2 in Figure 6.4. The corresponding deposition rates are given in Table 6.2. It is notable that the composite films are deposited at a faster rate than pure SiO_2 and that GeO_2:SiO_2 has a faster deposition rate than Ta_2O_5:SiO_2. From the deposition rates it was calculated that for an optical film thickness of ~ 2 μm, the GeO_2:SiO_2 would require deposition time of 5.5 hours and the Ta_2O_5:SiO_2 a time of 7.0 hours. The cladding of 4 μm is seen from the graph to need 20 hours.

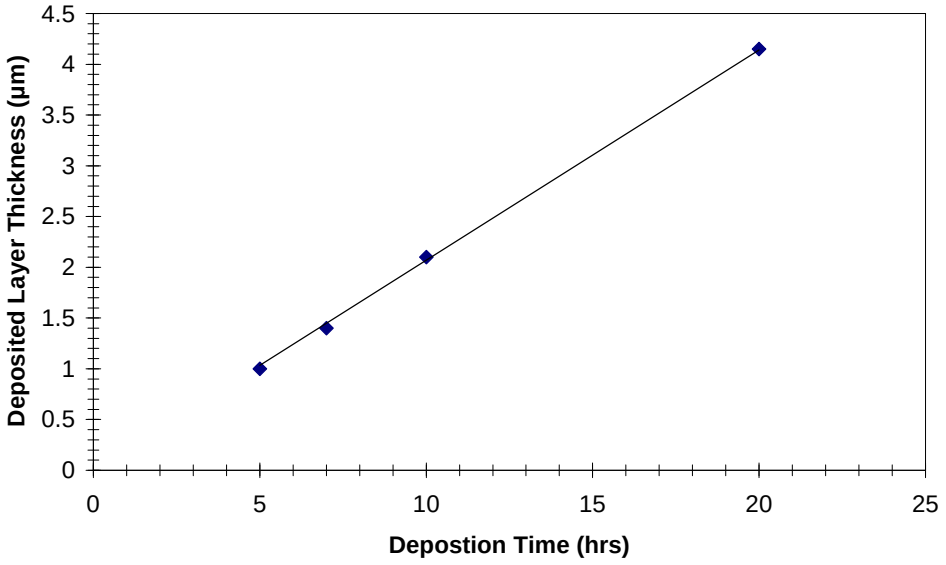

FIGURE 6.4: Deposited thickness of SiO_2 film versus time.

6.3.3 Annealing

In glasses, annealing is useful to oxidise the material and reduce stresses within the materials of newly deposited layers, which serves to reduce optical losses within the material by lowering scattering, homogenising the refractive index of the film to that of the oxides, and reduces absorption due to oxygen vacancies. A tube furnace was used to anneal with an oxygen flow of 2 L min^{-1}. Step 3 was based on the scattering losses of slab waveguides obtained in Section 6.4. The tube furnace was pumped at a rate of 10 °C min^{-1} and left to dwell at 500 °C for 60 mins. The cooling was not controllable by the tube furnace, but was programmed nonetheless at a cool rate of 10 °C min^{-1} and cooled naturally.

While this process yielded acceptable results for step 3, at step 10, however, patterned channel waveguides did not guide after the cladding was deposited and step 3 was repeated. Films of GeO_2:SiO_2 have been annealed for longer at higher temperatures [250], so the devices were put in the tube furnace at 950 °C for 6 hours.

6.3.4 Photolithography

Photolithography was used for patterning of the optical components in the deposited composite film and the microfluidics, once the cladding is deposited, in the device. The designed masks for the optical components and microfluidic channels were made. The process steps for photolithography are illustrated in Figure 6.5.

The first step is to spin photoresist on top of the substrate with deposited film and softbake. For patterning the optical layer a positive photoresist were used. Spinning of

S1818 was ramped up to 500 RPM for 2 s, then to 5000 RPM for 60 s. Softbaking was done in a convection oven for 30 minutes at 90 °C. The softbaked photoresist is firm enough for exposure. The mask is aligned and placed in hard contact with the photoresist in a mask aligner which then exposes it to UV light with energy density of 90 J cm^{-2}. The pattern is developed with MF390 developer for 45 s and then a final hardbake at 120 °C for 30 minutes is done a convection oven. The patterned photoresist is not perfectly rectangular in cross-section by inspection from a microscope, which combined with ion beam etching's faceting effect will give waveguides with quasi-trapezoidal cross-sections as described in Subsection 6.7.1.

The reactive ion etcher (RIE) is essentially a sputterer that has as its plasma a reactive gas which can etch materials. A RIE can be used for plasma cleaning (or ashing) using plasma of O_2 and no gas reactive to glass. This removes any organic materials on the surface and is used to remove stubborn deposits of remaining photoresist, the residue, so that the patterned layer is ready for the SiO_2 cladding to be deposited.

The photolithography step for making the microfluidic channel was done using a thick negative photoresist, SU8-10. This was not the original intention, see Section 6.6. The SU8-10 was spun at 500 RPM for 10 s, then to 3000 RPM for 30 s. Softbake was done on a hot plate for one minute at 65 °C, then for two minutes at 95 °C. Exposure in the mask aligner was at an energy density of 100 J cm^{-2}. SU8-10 requires a post-exposure bake, so the procedure for softbaking is repeated. The pattern was developed with EC solvent for two minutes then rinsed with IPA. No hardbake was necessary. SU8-10 residue after ion beam etching was easily removed by soaking in fuming nitric acid for 10 minutes.

6.3.5 Ion Beam Etching

Ion beam etching (or ion beam milling) is a dry plasma etch process. Unlike the plasma in the sputterer, the ion beam is created in separate chamber, decoupling the substrate from the plasma. The ions are then directed as a beam into the chamber on to the substrate being etched. Figure 6.6 illustrates an ion beam setup. The substrate being

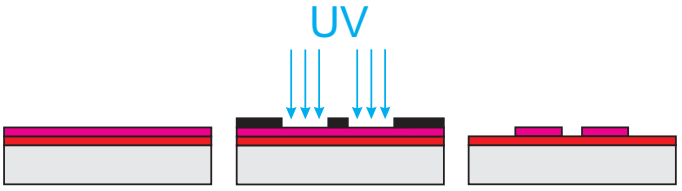

FIGURE 6.5: Photolithography process in positive photoresist. (Left) The photoresist is spun on top of the film and softbaked. (Middle) A mask is placed on top by hard contact and UV light is irradiated. (Right) The exposed photoresist is developed and the patterned photoresist hardbaked.

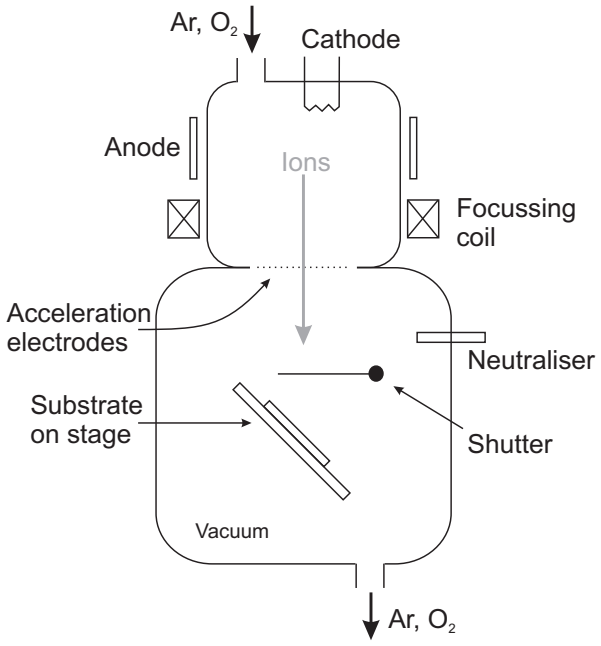

FIGURE 6.6: Diagram of ion beam etching operation.

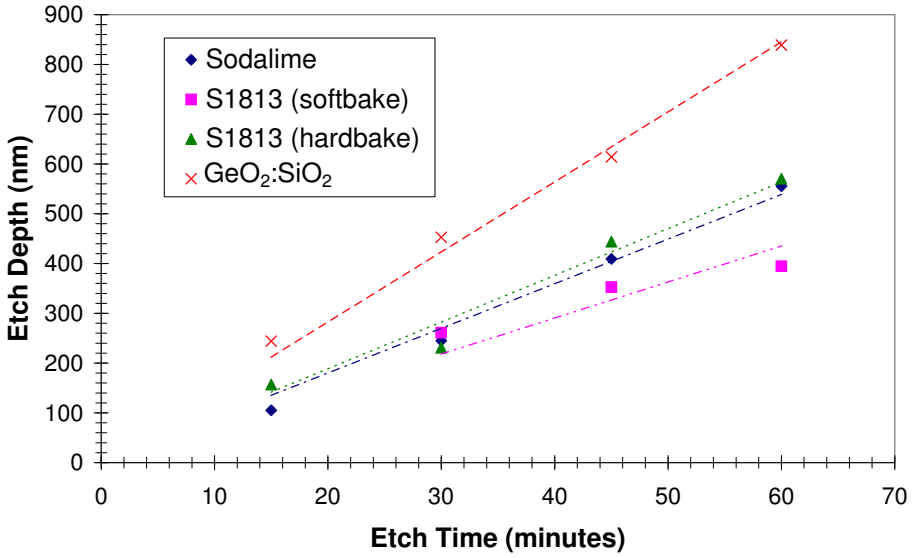

FIGURE 6.7: Graph showing data from etch tests versus time at zero degrees to the beam.

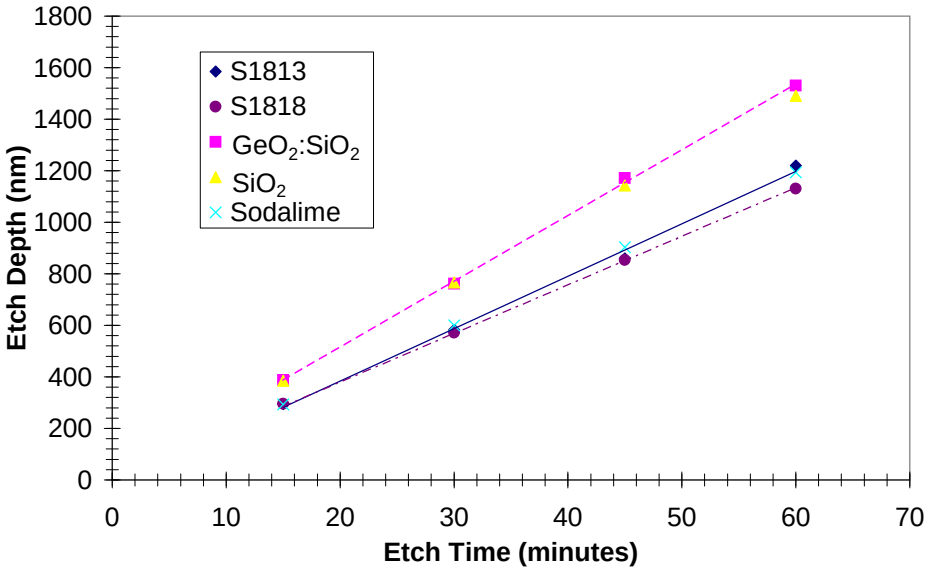

FIGURE 6.8: Graph showing etch tests versus time at 45 degrees to the beam.

TABLE 6.3: Ion beam etch rates for sodalime glass, fused SiO_2, GeO_2:SiO_2 film, S1813 and S1818 photoresist films at 0° and 45° incident angle to the beam.

Material	Etch Rate (nm min^{-1})
At 0 ° to the beam	
Sodalime	14.105
S1813 (hardbaked)	9.406
S1813 (softbake)	8.987
GeO_2:SiO_2	7.260
At 45 ° to the beam	
Sodalime	19.949
S1813 (hardbaked)	19.824
S1818 (hardbaked)	18.929
GeO_2:SiO_2	25.669
SiO_2	25.136

decoupled into a separate chamber allows for tilting the stage to which the substrate is fixed. A faceting effect that occurs in ion beam etching is observable. The etch rate is dependent on tilt angle to the beam and is well understood [251]. Unfortunately, ion beam etching leads to unwanted features such as trapezoidal or quasi-trapezoidal waveguides.

The etch rates were determined under tests by placing samples of sodalime glass, samples with deposited GeO_2:SiO_2 films and sample with deposited Ta_2O_5:SiO_2 films, fused SiO_2 and photoresist films on substrates. The ion beam was set to magnetron power of 500 W and a beam current of 100 mA with Ar and O_2 gases at 6 sccm each and a chamber temperature of 25 °C.

The first etch tests are shown in Figure 6.7 with the ion beam perpendicular to the substrate at zero degrees. Softbaked photoresist does not etch at a constant rate as the graph shows. The data points are not near the line of best fit. The heat generated from the ion beam bakes the photoresist changing its etch rate while being etched. Figure 6.8 shows etch tests for an ion beam at 45° tilt to the beam. Comparing with Figure 6.7, the etch rates at 45° tilt are higher. Figure 6.8 also shows that the etch rates for the photoresist are very similar to the sodalime glass and that the GeO_2:SiO_2 and SiO_2 have similar etch rates. This is made clearer as the etch rates from the lines of best fit are tabulated in Table 6.3. All etching for fabrication was, therefore, done at 45° tilt.

From Table 6.3, it is clear that the selectivity between S1818 photoresist and the GeO_2:SiO_2 film is 1.3:1. This means that for 2 μm thick waveguides the photoresist needs to be a minimum of 1.5 μm thick. The first photoresist tried was S1813 due to

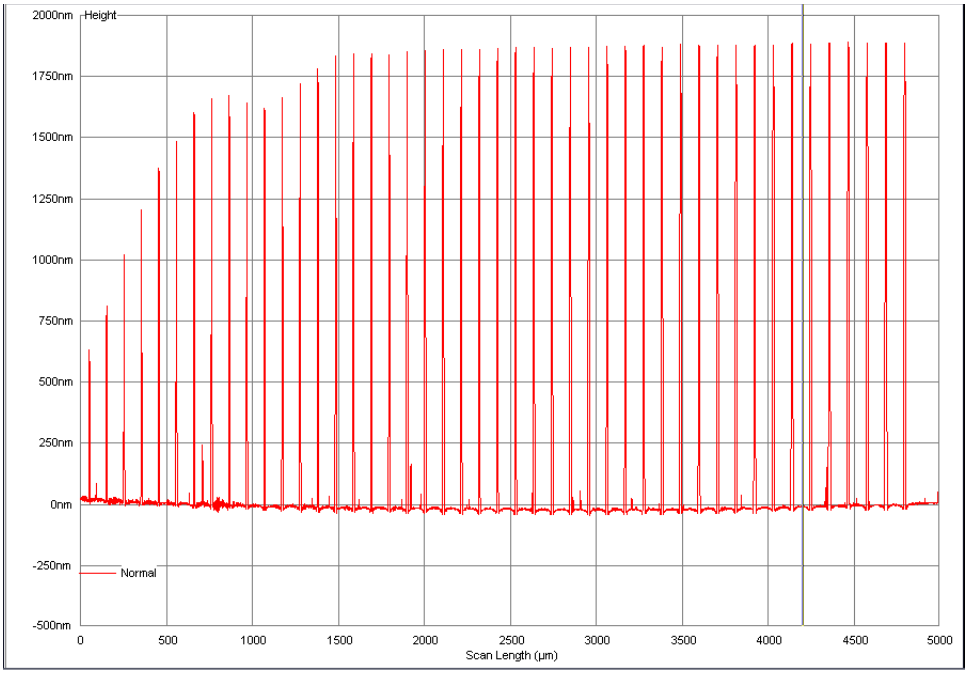

FIGURE 6.9: Trace from step profiler for patterned waveguides of S1813 photoresist.

its abundance in the cleanroom. The photoresist was patterned from a mask of waveguides with varying widths from 1 to 10 μm with an interval of 0.2 μm. Figure 6.9 is a trace from the step profiler of the patterned photoresist. The narrower features with widths of 1 - 2.2 μm, proved too difficult to repeatedly reproduce at the necessary 1.5 μm height and even this result was not easily repeatable. S1818 is reproducible down to 2 μm width (sixth waveguide feature from the left of the trace). The SU8-10 used for patterning the microfluidic channel is not tabulated as there was not enough time to do several etch tests. However, one was made and it was found to have a selectivity of approximately 1:1 with SiO_2.

6.3.6 Sawing, Lapping and Polishing

Polishing must be done on endfaces of the devices to be able to effectively couple light in and out of the optical waveguiding layer. The devices to be polished are first attached together with wax, so that several samples may be polished simultaneously, as the process is tedious and time consuming. The blocks are attached with wax to the jig ready for processing.

The theory of polishing is straight forward. The material to be polished has successive rounds of a fine micro-particles in suspension grinding against the surface to be polished, known as lapping. Lapping was done with 600 grit which is SiC. After inspection under an optical microscope, and the surface deemed suitable, several other lapping stages were done with micro-particles of calcined aluminium oxide of sizes 9, 3, and 1 μm. The final stage is the polishing itself with SF1 polishing fluid (from Logitech Ltd.) which shears the face of the glass to leave an optical finish.

6.4 Prism Coupling and Scattering Losses of Thin Films

Once a film is deposited, it is necessary to know its refractive index as well as that of the substrate. Prism coupling is a non-destructive mode-selective optical technique which determines the effective refractive index of a slab waveguide under characterisation and the refractive index of the substrate [164, 252]. It works by using a prism to couple light into an asymmetric slab waveguide consisting of a substrate and a thin film on top as depicted in Figure 6.10(a). A laser beam is irradiated on to a prism of known dimensions and refractive index.

The prism and waveguide are rotated until light is coupled into the waveguide on rotating stage as shown in the setup in Figure 6.10(b). The laser used is a HeNe (633 nm). The polariser allows selective excitation of TE or TM modes. A beamsplitter is used to sample some of the light for a reference signal. The reflectivity is measured as the sample under test is rotated and is translated by the computer as intensity from the photodiode

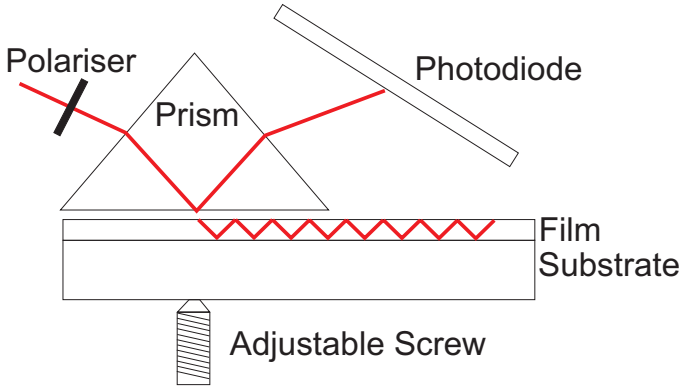

(a) Prism coupling.

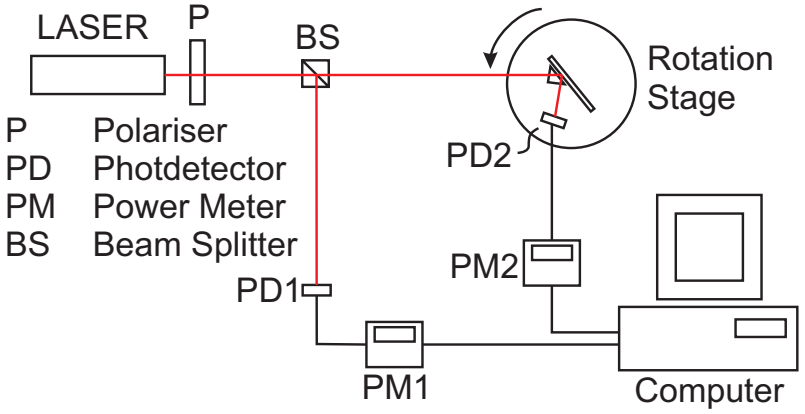

(b) Prism coupler setup.

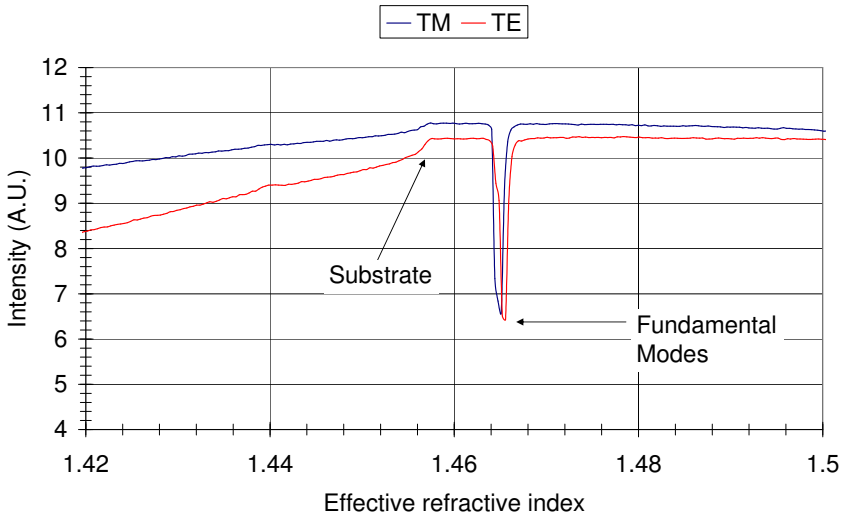

(c) Example trace.

FIGURE 6.10: (a) Prism coupling, (b) prism coupler setup and (c) and example trace from the setup.

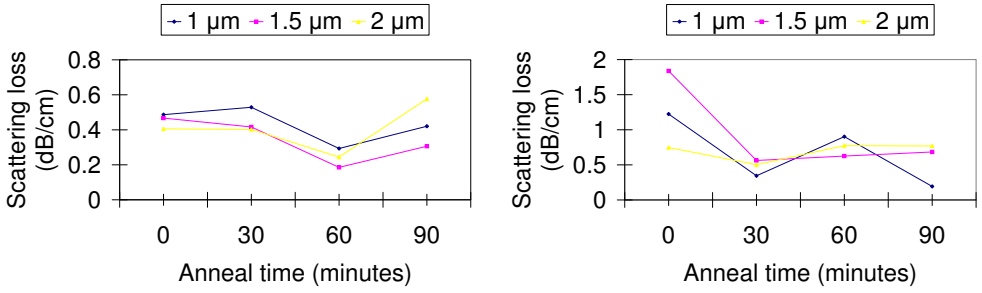

(a) GeO_2:SiO_2 (b) Ta_2O_5:SiO_2

FIGURE 6.11: Slab scattering loss measurements.

beside the sample versus the effective refractive index, as shown by an example trace given in Figure 6.10(c). This is a trace for the sample of GeO_2:SiO_2 film of one micron. The slab waveguide is singlemode as there is only one trough for both TE and TM polarisations. The point at which the trace begins to decrease with decreasing index, because the light is entering the substrate, is the substrate refractive index.

The deposited films of GeO_2:SiO_2 and Ta_2O_5:SiO_2 on fused SiO_2 substrates for thicknesses of 1, 1.5, and 2 μm were tested with prism coupling. Some of the films were annealed for 30, 60, and 90 minutes at 500 °C in the tube furnace. The slabs were found to all be singlemoded in both polarisations apart from the 2 μm unannealed sample which supported two modes. The substrates had an average measured refractive index of 1.458, in agreement with the manufacturer's value. For the GeO_2:SiO_2 film, the effective refractive index for TE mode was found to be 1.4685 and for TM mode, 1.4694. For the Ta_2O_5:SiO_2 film, the effective refractive index for TE mode, 1.4682, and for TM mode, 1.4696. These TE mode values agrees well, within less than 1%, for a film of a refractive index of 1.474 using the analytical theory in Section 3.2 for both GeO_2:SiO_2 and Ta_2O_5:SiO_2 films. A deposited film can be birefringent due to the anisotropy of the material, or due to the solutions of Maxwell's equations, or both [253]. The birefringence of the 2 μm thick films were measured and averaged 8×10^{-4}. This was considered small and therefore negligible.

Scattering losses can be measured by modifying slightly the prism coupling setup in Figure 6.10(b). A lens is used to image the slab waveguide while the prism couples light into the slab mode and the image is collected on a CCD camera. The results for scattering loss versus anneal time for slab waveguides of 1, 1.5, and 2 μm thickness are given in Figure 6.11. The losses reduce slightly with annealing and tend to be lower for the GeO_2:SiO_2 film than Ta_2O_5:SiO_2 film. The Ta_2O_5:SiO_2 film was not further developed device because it showed of the higher losses and the longer deposition rates in Subsection 6.3.2. The graphs for the scattering losses do not show a well behaved trend with anneal time so no conclusion on best anneal time can be made from them.

A time for 60 minutes annealing was chosen based on the values of the scattering loss data obtained.

6.5 Ellipsometry of Thin Films

Knowing the refractive index of the deposited films and substrate is important for designing, simulating, and realising optical components in the film. A second method, ellipsometry, was used to confirm results from the prism coupling in Section 6.4. Ellipsometry is an extremely useful indirect and non-destructive optical technique used to determine optical properties of substrates and films, but its full description is complex and out of scope for this thesis. The reader should refer to Tompkins [254] for further details on the subject. The apparatus is shown conceptually in Figure 6.12. Ellipsometry uses a coherent incoming light source, but results from several wavelengths can give information of a material's dispersion characteristic.

The real part of index of refraction, usually referred to as the refractive index, and the imaginary part of index of refraction, normally referred to as the extinction coefficient, are given by n and k respectively. One ellipsometric measure is Δ, the phase difference, caused by reflection. It is calculated as

$$\Delta = \delta_1 - \delta_2 \tag{6.1}$$

by measuring δ_1 the phase difference between the perpendicular and parallel polarization components of the incident light, and δ_2 the phase difference again, but for the reflected light. This gives Δ a range of $0 \leq \Delta \leq 2\pi$. The second ellipsometric value calculated is Ψ where its tangent is the ratio of the measured amplitude of the perpendicular and parallel polarization components, $|R_p|$ and $|R_s|$ respectively

$$\tan(\Psi) = \frac{|R_p|}{|R_s|}. \tag{6.2}$$

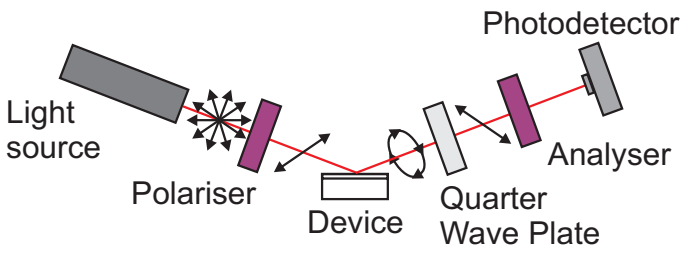

FIGURE 6.12: Conceptual ellipsometry setup.

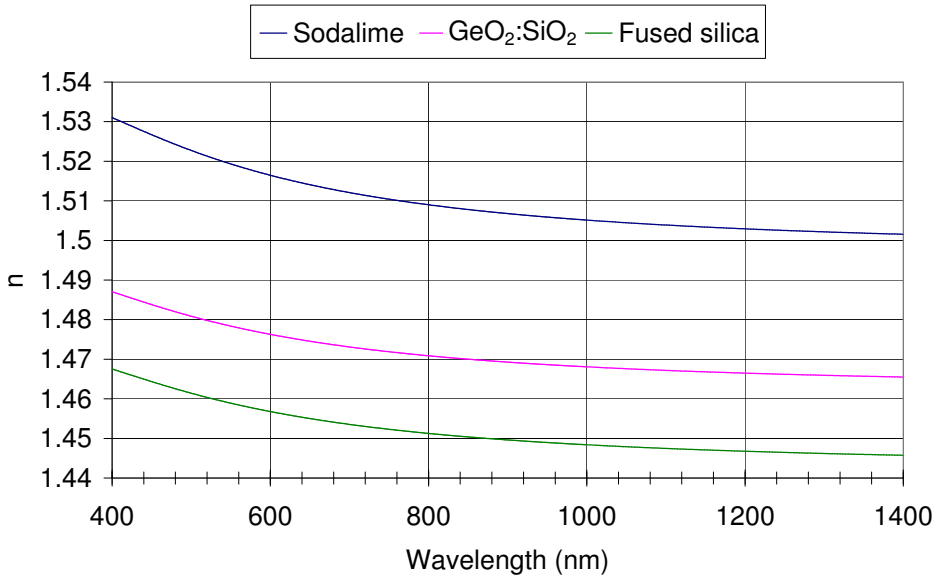

FIGURE 6.13: The dispersion curves for soda lime glass, fused silica, and thin film of GeO_2:SiO_2 on fused silica acquired by ellipsometry.

Ψ then has a range of $0 \leq \Psi \leq \pi/2$. Once the measurements are acquired for a substrate, the parameters can be converted to a dispersion curve. For a thin film on a known substrate, a model can be created and curve fitting is performed. The information from the substrate is then used with the ellipsometric parameters obtained from the film to make dispersion curves of the film. The Cauchy dispersion equation where the refractive index is

$$n(\lambda) = A + \frac{B}{\lambda^2} + \frac{C}{\lambda^4} \tag{6.3}$$

where A, B, and C are coefficients. The Cauchy coefficients obtained from ellipsometry for fused SiO_2, sodalime and GeO_2:SiO_2 film are given in Table 6.4.

The graph in Figure 6.13 shows the dispersion curves from the Cauchy coefficients given in Table 6.4. for a wavelength range from 400 - 1400 nm. The first observation is that the sodalime glass has the highest refractive index, so it cannot be used as a substrate for

TABLE 6.4: Cauchy coefficients.

Material	A	B(μm^2)	C(μm^4)
Sodalime	1.498	7.94×10^{-3}	-4.1×10^{-4}
GeO_2:SiO_2	1.463	5.70×10^{-3}	-2.9×10^{-4}
Fused silica	1.443	5.89×10^{-3}	-3.1×10^{-4}

the devices. The GeO_2:SiO_2 film has a higher refractive index than the fused SiO_2 and at 633 nm the refractive index is 1.475 and 1.456 for film and substrate, respectively. Though these ellipsometry results for the refractive index of substrate and deposited GeO_2:SiO_2 film agree with the results obtained from prism coupling in Section 6.4 with an error less than 0.1%, the Δn values notably differ. The prism coupling gave a Δn of 0.016 within the targeted specification of $\sim$ 0.015, but the ellipsometry suggests a Δn at a higher value of 0.019. The prism coupling values was used in the designs and simulations as the results are considered more accurate for the single wavelength of 633 nm than the ellipsometry measurements, for example, the refractive index of the fused silica substrate by prism coupling is the same as given by the manufacturer.

6.6 Unavailable Fabrication Steps

6.6.1 Modified Steps

Due to time constraints, unforseen problems with machinery, and disruptions with moving into new facilities, it was not possible to use with the original fabrication process that had been planned. The process steps which were actually used have been given in Table 6.1. The microfluidic channel steps and seal steps had to be modified from the original plan. Performance may be improved by employing these steps, once fabrication facilities become available.

Originally, the microfluidic channel was to be made by patterning a Cr sacrificial mask by lift-off to be able to etch in a DRIE to give large aspect ratio than other dry etches such as ion beam etching. The microfluidic channels once made were to be sealed with a PDMS cover with holes for fluidic tubes to be connected to for pumping and removing fluid. Table 6.5 outlines these sets of process steps which were eventually not implemented in the final devices and this section describes lift-off and DRIE.

6.6.2 Lift-off

Metal sacrificial masks are commonly used for reactive etches because metals such as Cr give better selectivity with the materials to be etched than photoresists due to reactive species involved in etching. The lift-off technique achieves a better profile for the contact Cr mask [251] for DRIE than a wet etch of Cr. The process is given in Figure 6.14. It is done by first patterning the substrate with photoresist then depositing a thin metal layer is deposited on top. The removal of unwanted metal is achieved by cleaning with acetone and removing the photoresist with the metal on top of it, leaving only the metal that is deposited directly onto the substrate.

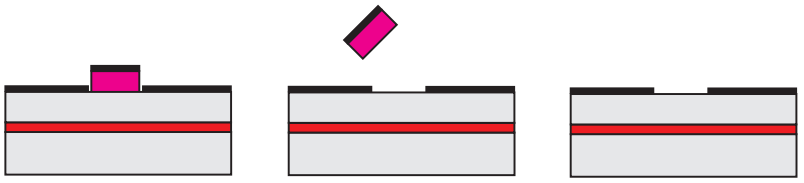

FIGURE 6.14: Lift-off technique. (Left) Metal is deposited on top of the patterned photoresist. (Middle) Resist pattern removed along with metal on top. (Right) Metal layer ready for etching.

Cr is to be used as a mask as the metal has a much slower etch rate than silica and has been used for this type of etching in industry. The value of 1 μm for the Cr thickness has been suggested by communications with Oxford Instruments for an etch of 30 - 40 μm. Therefore, a layer of 0.3 - 0.5 μm of Cr which can be deposited by electron beam evaporation is expected to be adequate for an etch depth of 10 μm.

6.6.3 Deep Reactive Ion Etching

Microfluidic channels are required to be up to hundreds of microns in width and the depth should also be of similar dimensions to accommodate particles passing through. Deep reactive ion etching (DRIE) is used for etching deep trenches with high aspect ratios. This is the best dry etch process to give straight walls. Etch rates of 600 and 750 nm min^{-1} have been reported [255]. Surfaces can be made smoother at the expense of etch rate by addition of inert gases during the DRIE process [255–257].

TABLE 6.5: Steps unavailable for fabrication of devices.

Step	Description
Microfluidic Channel	
Step 1	Spin on positive photoresist.
Step 2	Photolithography.
Step 3	Deposit Cr 1 μm thick.
Step 4	Lift-off resist by acetone wash.
Step 5	DRIE 10 μm microfluidic channel.
Step 6	Remove leftover Cr with etchant.
Seal Microfluidic Channel	
Step 1	PDMS slab with drilled holes.
Step 2	Attach tubes to the holes with adhesive to seal.
Step 3	Clamp PDMS to top of the microfluidic channel.

6.7 Realised Devices

6.7.1 Channel Waveguides

Scanning electron microscope (SEM) images of channel waveguides with cladding were taken from above, shown in Figure 6.15(a), and from the polished waveguide endfaces, shown in Figure 6.15(b). From above, the waveguides appear sunken in the middle. This is due to the darker core as seen from the endface image. The waveguides have quasi-trapezoidal profiles due the photoresist profile in cross-section not being completely rectangular and to the ion beam etch process facet effect. Optical microscope images of the waveguides from above, before cladding, were used for measuring the waveguide widths and the height was measured with a step profiler. The average waveguide widths were measured as 5.3 ± 0.3 μm bottom width, 2.6 ± 0.3 μm top width, and 1.95 ± 0.02 μm height. The waveguides have a cladding of ~ 4 μm as shown in Figure 6.15(b).

The channel waveguides do not have the ideal rectangular cross-sections or the trapezoidal cross-sections simulated in Chapter 3, but quasi-trapezoidal cross-sections. The top widths are slightly larger than the 2 μm wanted from Chapter 3. The shape of the cross-section is a closer approximation to a rectangle than a true trapezoid. However, there can still be improvements in fabrication to make the channel waveguide cross-section more rectangular. The cross-section that has been realised makes it difficult to measure the top width from optical microscope images, as the top width is not well defined. This is clear seen from the SEM images showing the channel waveguide cross-section, where the waveguide height continuously decreases from the middle of the channel waveguide. The characterisations of the realised waveguides in Chapter 7 show that the waveguides function as required and, thus, can be used for purpose.

6.7.2 Paraxial Kinoform Lenses

One of the chips comprising waveguides, paraxial kinoform lenses and a simple microfluidic channel is shown in Figure 6.16. A microscope image, Figure 6.17, shows a typical paraxial kinoform lens on the chip before cladding was deposited. The central zones on the lens are well defined, but the central part of the lens in the outer zones were not transferred perfectly because of resolution limits of photolithography. An evident effect is a gap in the centre along the centre of the lens increasing from the central zones to the outer zones.

The lens thickness for the paraxial kinoform lens should be constant, as derived in Subsection 4.6.2, but the realised lens thickness in Figure 6.17 is tapered, decreasing from the central zones to the outer zones. The tapering is due to the mask where the lens pattern is tapered due to the limits of resolution of mask makers (Compugraphics

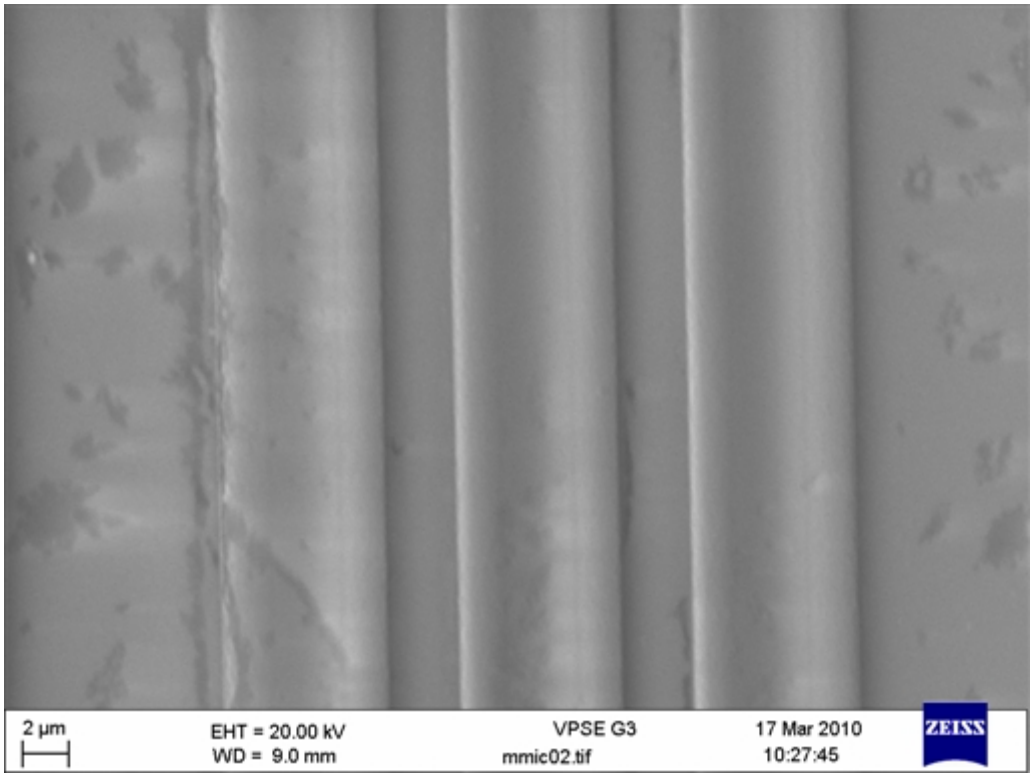

(a) Top of waveguides.

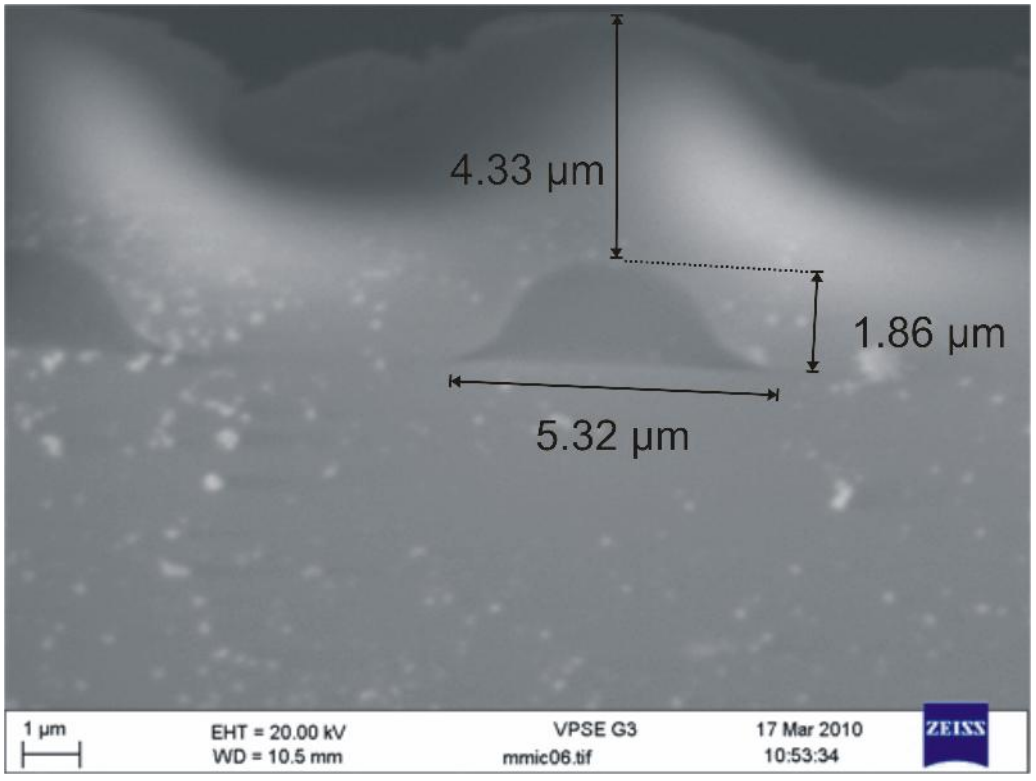

(b) Endface of waveguides.

FIGURE 6.15: SEM images of channel waveguides.

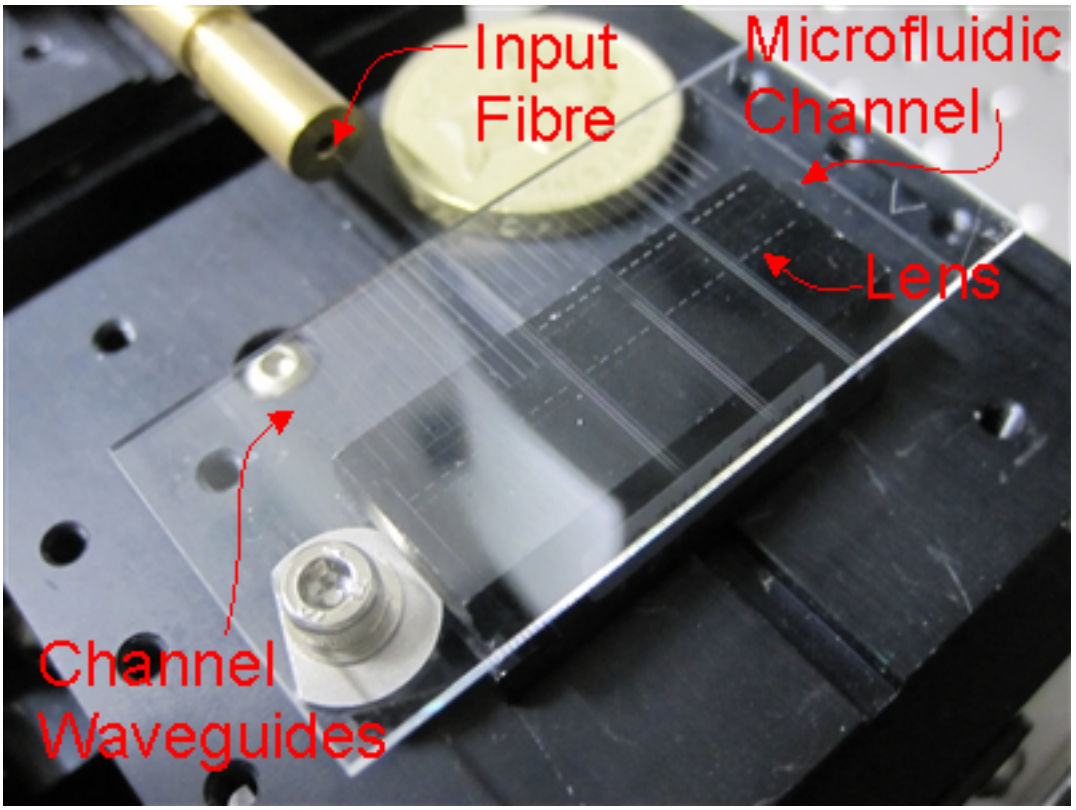

FIGURE 6.16: Paraxial kinoform lenses on a chip with microfluidic channel.

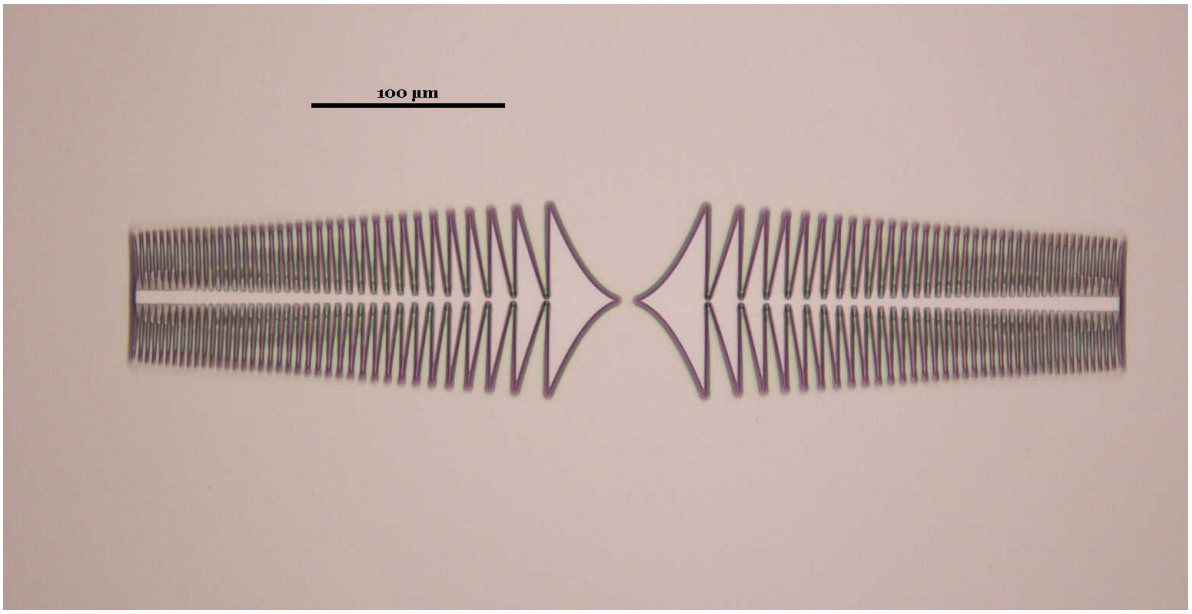

FIGURE 6.17: Optical microscope image of paraxial kinoform lens taken from above.

Intl. Ltd.), meaning that the pattern does not replicate the paraxial kinoform lens design in Chapter 4 exactly.

Since most of the light diverging from the channel waveguide into the slab region is contained in the centre of the beam, the well defined central zones are expected to focus the light to a small enough spotsize to show the proof of principle of the function of the lens.

6.7.3 MMI devices

One of the chips comprising waveguides, general self-imaging MMIs, restricted self-imaging MMIs, and a microfluidic channel is shown in Figure 6.18. A microscope image of a typical MMI on the chip before cladding was deposited is shown in Figure 6.19; it is only a partial image as the MMI is too long to be fully imaged by the microscope objective. The MMI is well defined and it is observable that the slab region as well as the channel waveguides have quasi-trapezoidal cross-section.

The average widths, taken from optical microscope images, are for the MMI slab region are 20.7 ± 1.0 μm for top 24.5 ± 0.5 μm for the bottom. The equivalent rectangular cross-section is, therefore, 22.6 μm. The height is the same as the channel waveguides, 1.95 ± 0.02 μm, taken by step profiler. These dimensions are close to the 22 μm width

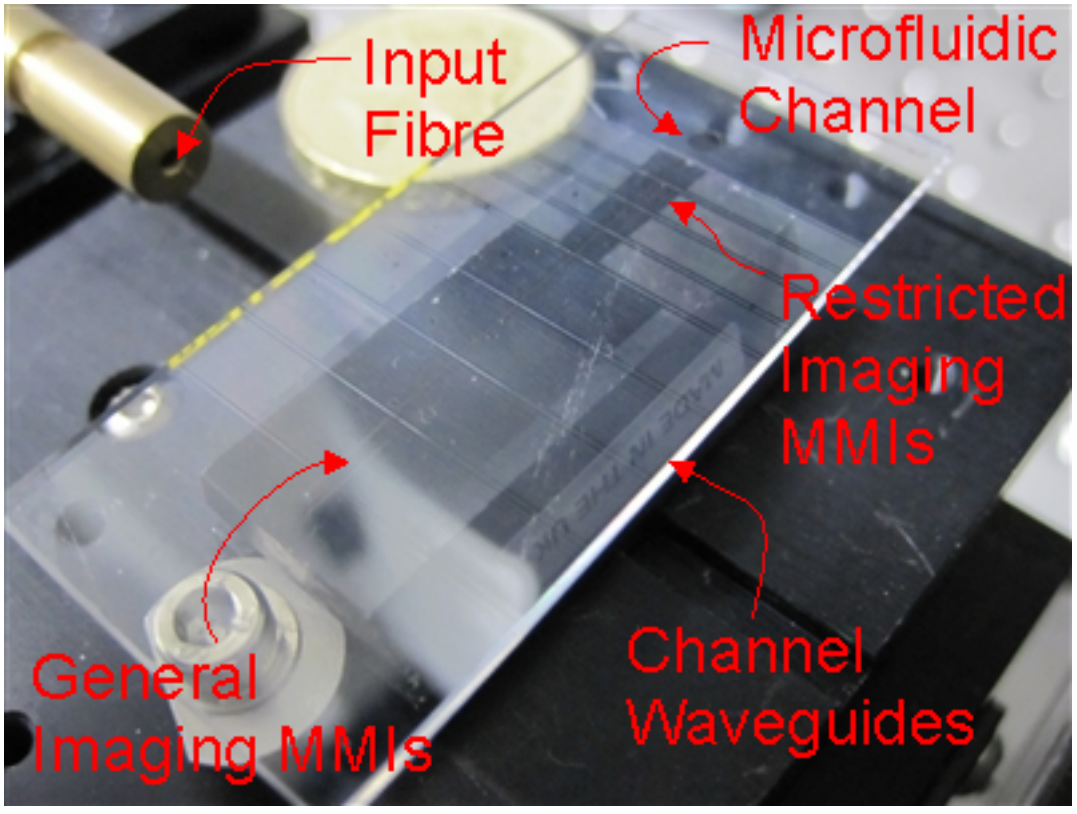

FIGURE 6.18: MMIs on a chip with microfluidic channel.

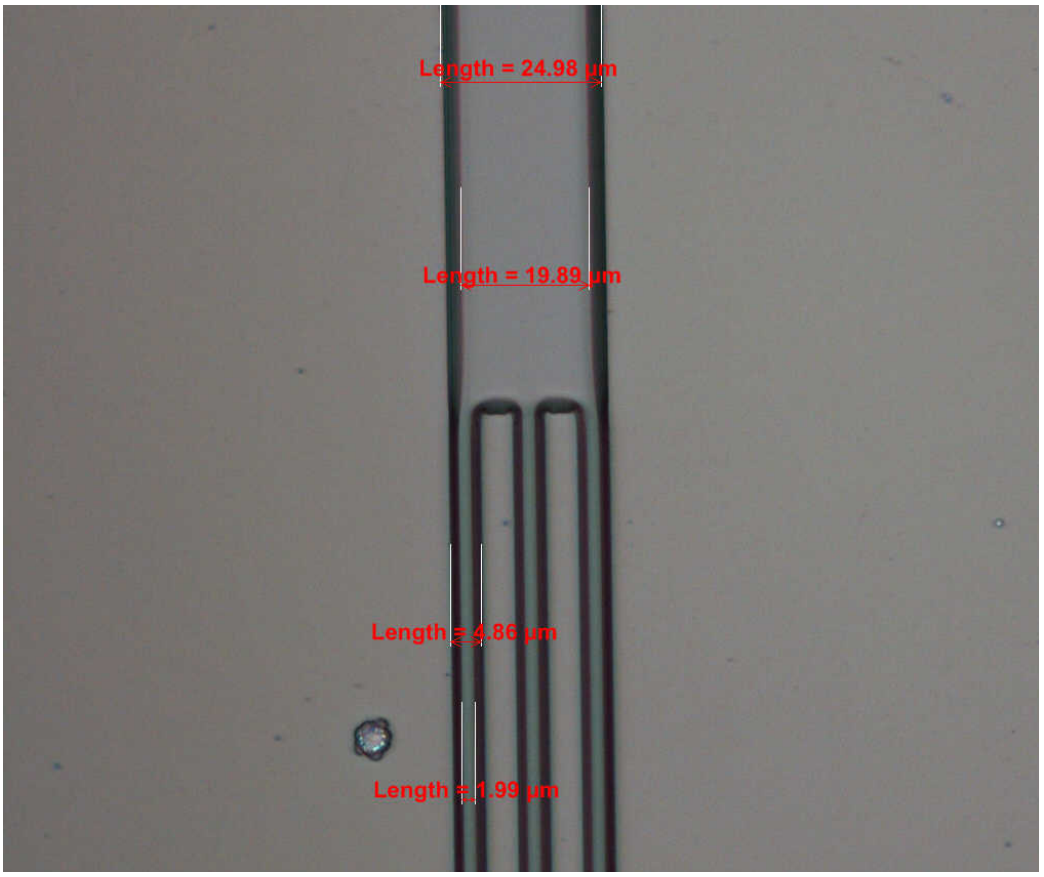

FIGURE 6.19: Optical microscope image of one end of an MMI device taken from above.

used in the design and simulations in Chapter 5. The MMI is known for high fabrication tolerances and with the dimensions that have been achieved in this fabrication for the MMIs means that imaging should happen as expected along the multimode region.

6.8 Conclusion

A two-mask process for flexible planar fabrication of integrated optics and microfluidics on a single chip has been described. The structure comprises a buried optical waveguide layer that can be patterned to make planar optical components such as waveguides, lenses, and MMIs. A glass material system was chosen because of its compatibility with standard planar fabrication process, its good optical qualities, and its good chemical compatibility in microfluidics. Two composite SiO_2 glasses were chosen, GeO_2:SiO_2 and Ta_2O_5:SiO_2, at concentrations to give a refractive index contrast, Δn of ~ 0.015, while simultaneously keeping the material chemically compatible with pure SiO_2 as possible for etching.

The GeO_2:SiO_2 and Ta_2O_5:SiO_2 films were measured to have a refractive index of 1.474 compared to fused silica substrates of 1.458 by prism coupling at a wavelength of 633

nm, giving a Δn of 0.016. From the two composite materials, GeO_2:SiO_2 was found to be simpler to fabricate having higher deposition rates, etch rates and forming slab waveguides with lower losses than Ta_2O_5:SiO_2. Therefore, the decision to discontinue development of devices using Ta_2O_5:SiO_2 was made. Ellipsometric measurements were made to confirm prism coupling measurements of refractive index and were in good agreement.

The realised channel waveguides have quasi-trapezoidal cross-sections due to the photoresist cross-sections not being completely rectangular and the faceting caused by ion beam etching. The waveguide cross-sectional dimensions were measured as 5.3 $\pm$ 0.3 μm bottom width, 2.6 $\pm$ 0.3 μm top width, and 1.95 $\pm$ 0.02 μm height. The quasi-trapezoidal cross-section is better than a true trapezoidal cross-section as it is closer in shape to the ideal rectangular. The top width is difficult to measure since the quasi-trapezoidal cross-section is a continuous irregular shape on the top.

The realised paraxial kinoform lenses, designed in Chapter 4, had well defined central zones, but the outer zones were less well defined because of the resolution limit of the mask and and resolution limit of photolithography. However, since most of the optical power diverging from the channel waveguide into the slab region is contained in the centre of the beam, the well defined central zones are expected to focus the light to a small enough spotsize to demonstrate proof of principle of the function of the lens.

The realised MMIs were well defined and, in common with the channel waveguides, have quasi-trapezoidal cross-sections with dimensions for the widths of 20.7 ± 1.0 μm for top 24.5 ± 0.5 μm for the bottom, and the same height as the channel waveguides. The equivalent rectangular cross-section is, therefore, 22.6 μm. These dimensions are close to the designed 22 μm width. The MMI is known for high fabrication tolerances and with the dimensions that have been achieved in this fabrication for the MMIs means that imaging is expected along the multimode region.

The next chapter describes characterisation of the optical function of the realised channel waveguides, paraxial kinoform lenses, and MMIs that were made using the process described in this chapter.

Chapter 7

Characterisation of Waveguides, Kinoform Lenses, and MMIs

7.1 Introduction

The problem of how to introduce light into the middle of a microfluidic channel with a small spotsize in a planar device using integrated solutions of lenses, AWGs, and MMIs, has been considered in previous chapters. Chapter 4 described the theory of candidate lens designs and after simulating several candidate lenses clarified that a paraxial kinoform lens was best suited for fabrication. Chapter 5 has considered alternatives to lenses, namely, AWGs and MMIs, and concluded that MMIs would be suitable for fabrication to compare with lenses. Channel waveguides, paraxial kinoform lenses and MMIs were fabricated using the fabrication processes described in Chapter 6.

This chapter describes the characterisation of the realised devices in terms of spotsizes achievable in the waveguides, by mode profiling, and in the slab regions of the paraxial kinoform lenses and MMIs, by imaging the scattering intensities from above. Channel waveguide losses are also characterised to confirm that sufficient power is transmitted through the device to observe the detection functions. Characterisation results are then given for spotsizes in the microfluidic channel by fluorescence imaging from above demonstrating that light can be focussed or imaged into a small spot in the middle of a microfluidic channel, as required.

7.2 Channel Waveguides

7.2.1 Mode Profiling of Channel Waveguides

In Chapter 3 mode analysis by BPM for channel waveguides was carried out to confirm that appropriate single-mode waveguides with Gaussian-like mode intensity profiles could be made in the material system described in Chapter 6. Mode profiling characterisation was done to confirm that the realised waveguides have the mode properties comparable to those waveguides simulated. Prism coupling with slab waveguides with no cladding, as used in Section 6.4, can determine which modes are supported. Unfortunately, prism coupling is difficult to do with channel waveguides and not possible with a cladding on top. Mode profiling can give a good indication of how many modes are supported practically for waveguides with few modes and those simulated here were designed for singlemode or a few-mode operation.

Very accurate optical setups for mode profiling have been established with alignment of the endfaces of the samples and use of telecentric imaging as demonstrated by Fatadin *et al.* [258]. Such a setup would be ideal but more time consuming and for the accuracy required the more standard setup shown in Figure 7.1 was used. A HeNe laser emitting at 633 nm wavelength with an attenuator at the front is coupled into a singlemode fibre using a x25 objective. The fibre is then butt coupled to the waveguide under test. The imaging optics comprises a x25 objective with a tube to stop stray light entering the camera attached to it on the output end of the waveguide. The camera is a CMOS camera, model Motic Moticam 2300, connected to a computer for control and capture.

The image of the mode profile is taken when the mode is excited and observed, and then analysed after data collection. The analysis of the fundamental mode profile data was done using a program written in the MATLAB environment which is given in Appendix B. The realised quasi-trapezoidal channel waveguides realised in the final devices had an average cross-section of 5.3 ± 0.3 μm bottom width, 2.6 ± 0.3 μm top width, and

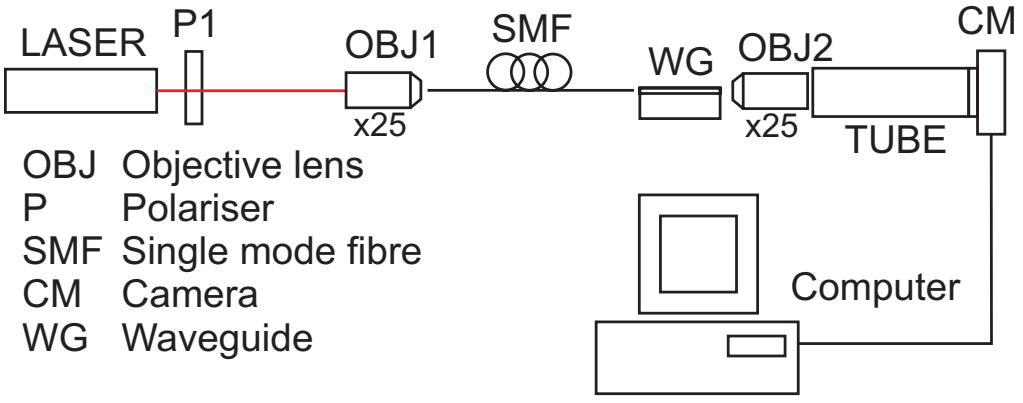

FIGURE 7.1: Mode profiling setup.

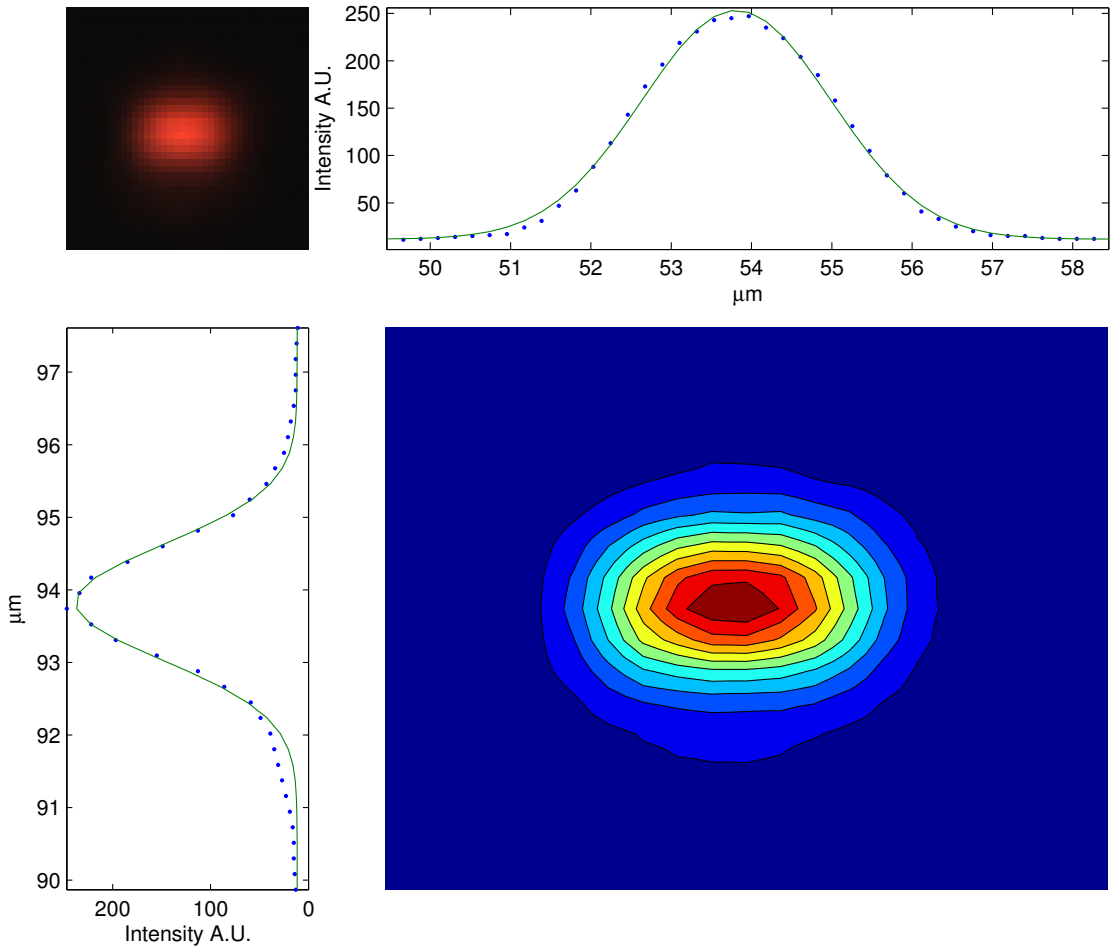

FIGURE 7.2: Screenshot of example mode profile. On the top left corner is the raw image. On the bottom right the contour representation of the intensity and two graphs top and left fitting a gaussian to the cross-section of the profile through its peak. The spotsize was 2.35 μm horizontally and 1.59 μm vertically.

1.95 $\pm$ 0.02 μm height on the paraxial kinoform lens devices and the MMI devices. A representative example of the data collected is given in Figure 7.2. The intensity contour representation of the image is analysed using a Gaussian fit on the cross-section of the profile through its peak with

$$I = I_0 \exp\left(\frac{-2x^2}{\omega^2}\right), \tag{7.1}$$

for the horizontal and vertical directions, where I_0 is the peak intensity, ω is the spotsize.

Two sets of channel waveguides were made when developing the fabrication described in Chapter 6. The first set used a mask with varying waveguide widths which was employed to find the smallest width that could be used to repeatedly make channel waveguides. The choice of the 2 μm wide waveguides from Chapter 3 could be made once the dimension was shown to be repeatable in Chapter 6. The modal spotsizes for waveguides against width is shown in Figure 7.3 for widths where the fundamental mode

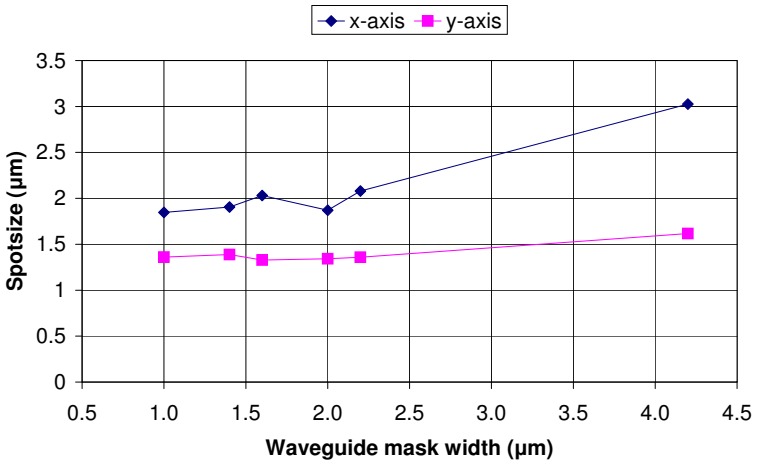

FIGURE 7.3: Spotsizes in the x-axis and y-axis for waveguides of varying width.

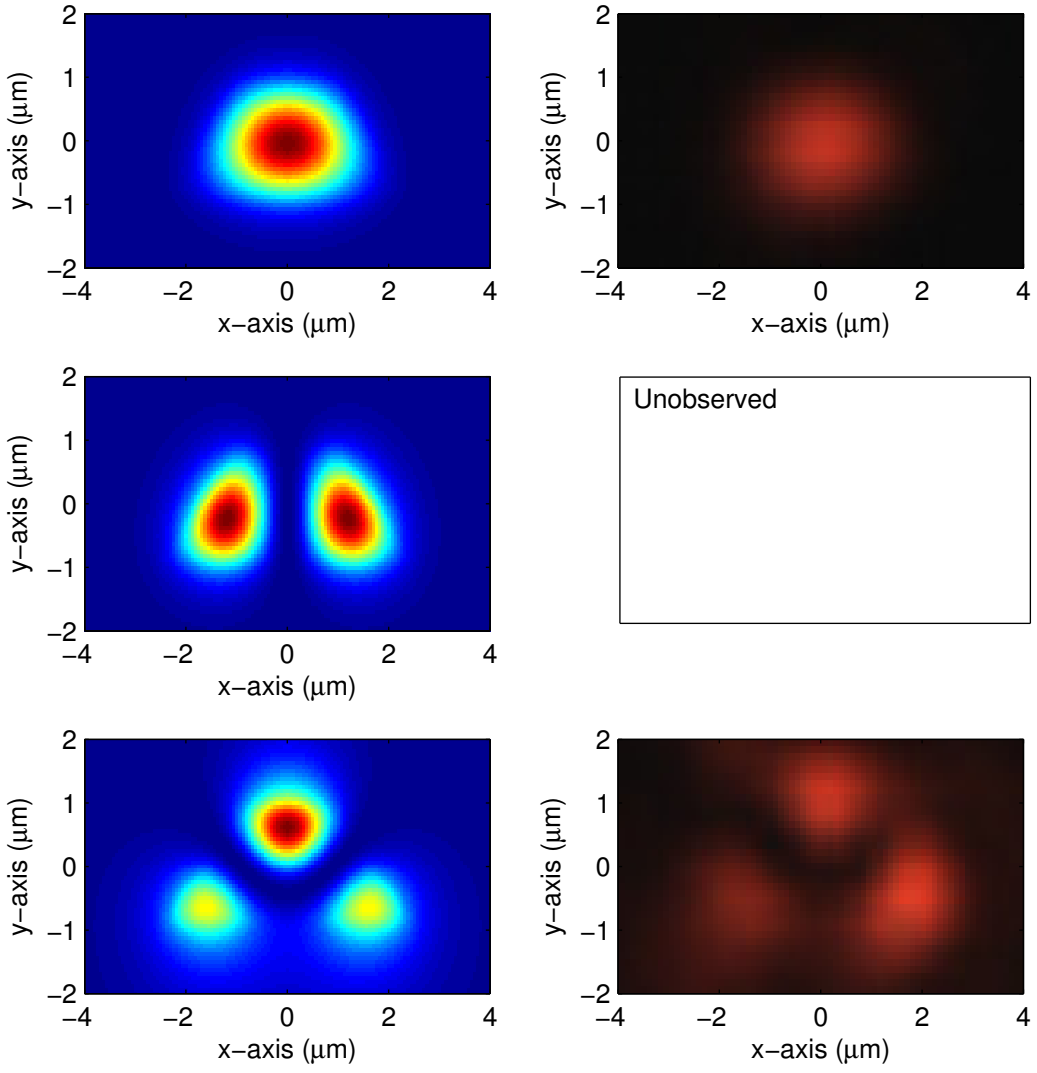

FIGURE 7.4: Mode profiles of simulated modes on the left and the observed modes on the right.

could be excited. The results show that the fundamental is confined approximately to the dimensions of the waveguide as expected in the second regime discussed in Chapter 3 and that the mode width does not change greatly with small changes in mask width. The mode sizes around 2 μm agree well with simulation of trapezoidal waveguide. The simulated mode profiles for a trapezoidal cross-section of 2 μm, 5 μm, and 2 μm, for top width, bottom width, and height, respectively, are compared with observed mode profiles shown in Figure 7.4. The mode profiles agree well with simulations, although the second mode (the next from the fundamental) was not observed.

The second set of waveguides were 2 μm in width and were the final waveguide design used for lens and MMI devices. From Chapter 3 it was known that the waveguides would have trapezoidal or quasi-trapezoidal cross-sections due to fabrication methods. This was shown to be the case in the SEM images in Chapter 6. The average spotsize of the fundamental mode from 14 measurements made on the final devices for the channel waveguides were 2.5 ± 0.5 μm and 1.5 ± 0.1 μm for the horizontal and vertical dimensions respectively. Mode size appear larger than the first set of waveguides, which may be due to the extra annealing lowering the core refractive index and this would also explain why only the fundamental mode was observed in the second set.

7.2.2 Channel Waveguide Losses

Loss measurements on the waveguides were done to confirm that sufficient power would reach the microfluidic channel using a standard HeNe laser available for experiments to observe required focussing function for detection. Insertion loss and propagation losses were measured. The setup used to do the insertion loss measurements is shown in Figure 7.5 and to take scattering images for propagation loss discussed in Section 7.3.

A 10 mW HeNe laser of 633 nm wavelength is used for input into a singlemode fibre using a x25 objective. The fibre is butt coupled into the waveguide under test. A x25

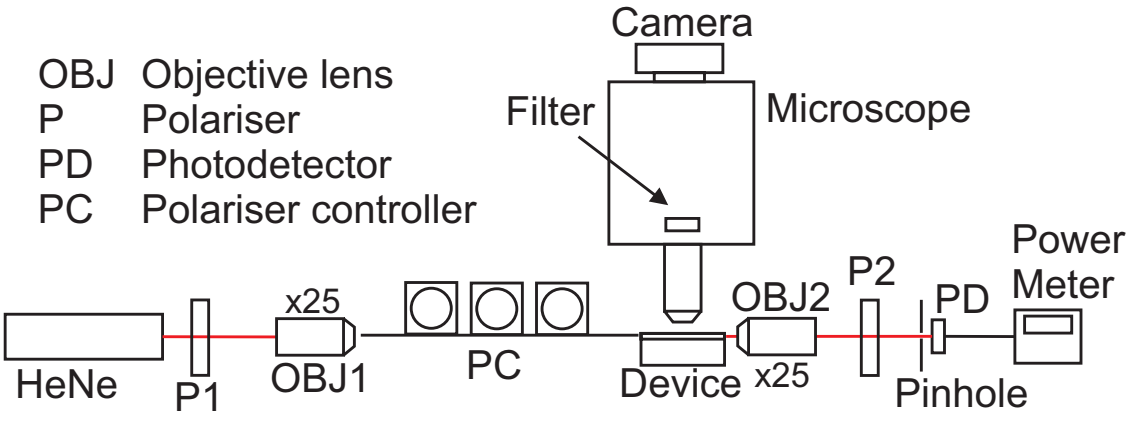

FIGURE 7.5: Setup for imaging scattering along the device and fluorescence in the microfluidic channel.

objective collects the output light and detected through a pinhole, to minimise stray light, by a photodetector. For polarised measurements, polarisers are placed before the input objective and after the output objective and the polarisation from the fibre is changed using a polarisation controller [259].

The total insertion loss is calculated from measuring the input light power coming out of the fibre, P_i, and the output of the waveguide, P_o, which in decibels is

$$L_T = -10 \log_{10} \frac{P_o}{P_i}. \tag{7.2}$$

A mean average of 12.2 $\pm$ 2.5 dB loss was measured for waveguides approximately 2.5 cm long for unpolarised light and no significant difference observed when changing from TE to TM polarisations. The total insertion loss measured can, in decibels, be equated to

$$L_T = L_C + L_P, \tag{7.3}$$

where L_C is the coupling loss of the butt-coupled fibre to the waveguide and L_P is the propagation loss along the waveguide. The coupling loss is determined by the mode mismatch of the fibre and waveguide, imperfections at the endfaces, and Fresnel reflections. The propagation loss is due to any scattering and absorption along the waveguide.

To know whether the coupling loss or propagation loss is the main contributor to the insertion losses, one of them must be measured. The loss due to scattering can be measured by adding a few components to the setup shown in Figure 7.5. The setup takes images of the scattering along the waveguides from above. The scattering images were taken by a microscope using a x10 objective and a CCD camera (Q Imaging, Regita 1300) as it was more sensitive than the CMOS camera used for mode profiling. The setup for scattering losses takes several images along waveguide for reliable measurement. These images span 1 cm and overlap so that that entire length is covered. The images are analysed after acquisition.

The analysis involves processing the pixel intensities by accumulating the pixel values in the columns of the images. A dark background image taken as a reference is removed from the data and the accumulated data is transformed to decibels. This can be done as the pixel value is proportional to intensity. A line-of-best-fit is then fitted onto the data where its gradient is the propagation loss per propagation length. Figure 7.6(a) shows representative example of the raw images captured and Figure 7.6(b) is the generated from the data collected in the image showing the propagation loss in per propagation length. The tilt of the waveguide is due to the alignment of the microscope, but this is negligible as the angle is only $1.75 \times 10^{-4\circ}$. The colourmap in Figure 7.7 is used for plotting the intensity in scattering images.

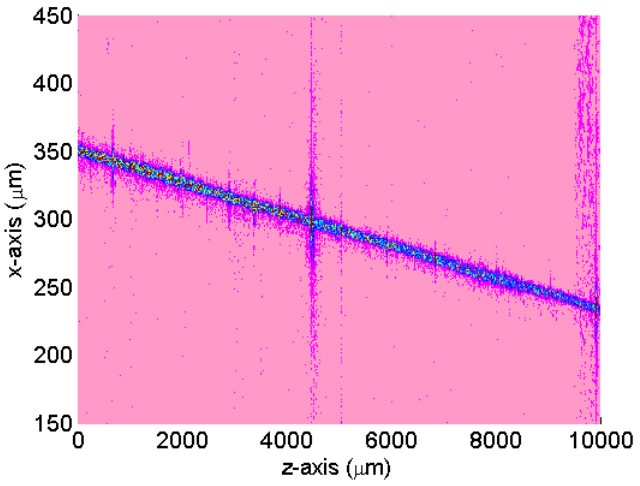

(a)

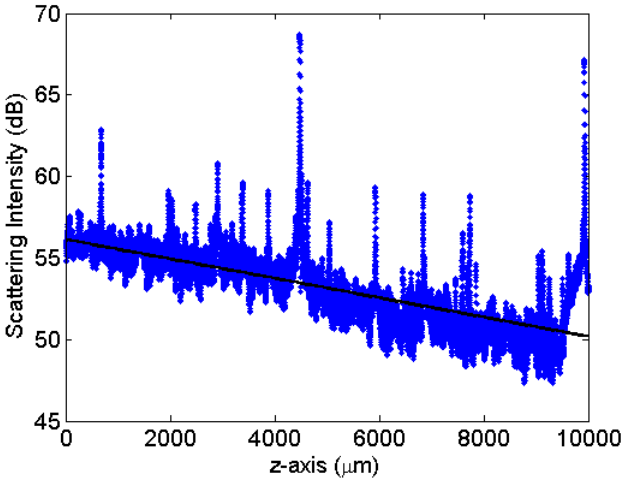

(b)

FIGURE 7.6: (a) Stitched raw images of propagating light in a waveguide being scattered. (b) Propagation loss for a channel waveguide in decibels versus propagation length up to 1 cm and line of best fit shown a propagation loss of 5.9 dB cm^{-1}.

FIGURE 7.7: Colour map of intensity used for scattering raw images and scattering and fluorescence processed images.

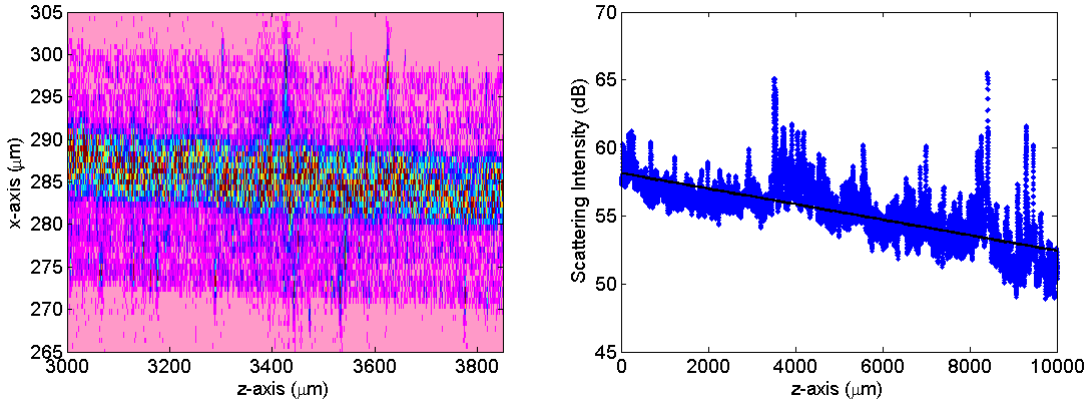

(a) TE (b) TE

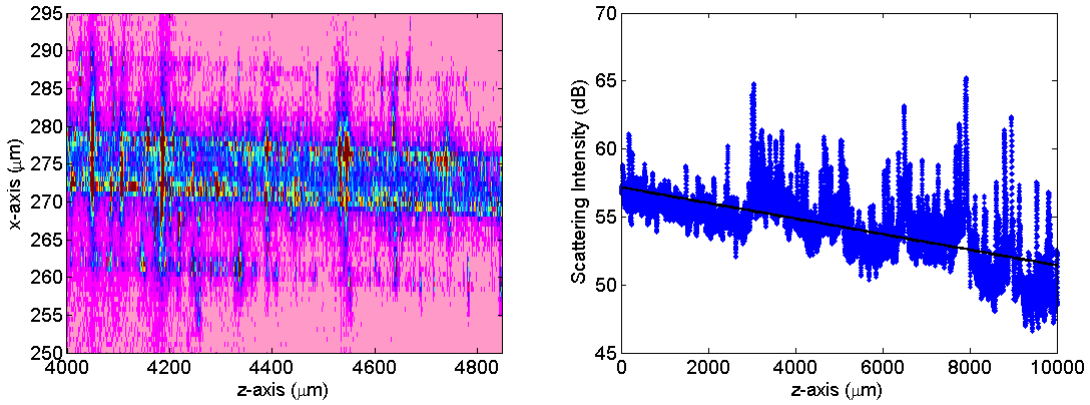

(c) TM (d) TM

FIGURE 7.8: Image of a section of scattering for (a)TE and (c)TM polarisations with a propagation loss of 5.7 dB cm^{-1} for (b)TE and 6.0 dB cm^{-1} for (b)TM.

The average propagation loss of the waveguides is 7.1 ± 2.0 dB cm^{-1}. The waveguides are approximately 2.5 cm, though slightly less due to polishing the endfaces, giving a propagation loss, L_P, of 17.75 dB. It has also shown that, L_P is the dominant term in equation 7.3 and its value is higher than that of L_T which may be due to higher error of measurement and the propagation distance being less than 2.5 cm in the real devices due to dicing and polishing. There was not a notable difference in quantity between the propagation losses of the TE and TM polarisations in the channel waveguide with propagation losses agreeing with no polarisation. However, images shown in Figures 7.8(a) and 7.8(c) reveal that more light is scattered from the top of the waveguide when operated in TE polarisation and more light scatters from the sides of the waveguide when operated in TM polarisation.

The losses are quite high for a waveguide, but low loss in the waveguide was not a priority in this work and the scattering from the waveguides is enough to be able to image the operation of the lens and MMI devices from above in the following section. The main

source of scattering in waveguides is Rayleigh scattering and this scattering is polarisation dependent [120]. This explains the scattering from different waveguide surfaces dependent on polarisation and accurate birefringent measurements on silica waveguides have been done using this fact [260]. The largest improvements in lowering channel waveguide loss would be to have a through study of annealing times and temperatures.

7.3 Focussing in the Slab Region

7.3.1 Approach to Imaging the Focussing

Before carrying out the fabrication of microfluidic channels on the devices, images of scattering from the kinoform lenses and MMIs were taken using the setup shown in Figure 7.5 to observe their focussing function. Analysis on the images was done by first identifying the focal point, then smoothing the image with a 16-tap running average filter, and finally performing Gaussian fits to find spotsizes along the beam to be able to fit to the Gaussian beam equation.

7.3.2 Kinoform Lenses

Figure 7.9(a) shows a representative example of a raw image made from the stitching of images taken of the scattering from the top of a paraxial kinoform lens. It shows, from the left, TE polarised light entering from a channel waveguide into a slab waveguide and the beam diverging up to the lens 2 mm away. Once at the lens, the light interacts with the lens and focusses to a focal point 2 mm away. This is the first order focus. There is a second focus found at 1 mm away from the lens which is most likely light going into the second order. Figure 7.9(b) shows the same lens, but with TM excitation. The two focal points are still visible, but the lens structure is more clearly visible because the scattering is most prominent on the vertical walls. The two images resemble the simulation images shown in Chapter 4. Non-idealities in the devices cause light to be scattered away from the first order focus, which will cause a loss in device transmission.

Figure 7.10 shows the first order focus of a lens fitted to the Gaussian beam equation. There are two columns with a cropped image of the first order focal point on the left, Figure 7.9(a), for TE polarisation and on the right, Figure 7.9(b), for TM polarisation. The first image in each column is the raw cropped image. The second image in each column is the moving average filtered image to smooth out the local fluctuations that scattering provides. A 16-tap running average filter was applied along the z-axis as the image only changes slowly. The third image in each column are Gaussian fits for the x-axis along each element of the z-axis. The spotsizes acquired from these Gaussian fits and marked by the red dots. The Gaussian beam equation is then fitted on to these

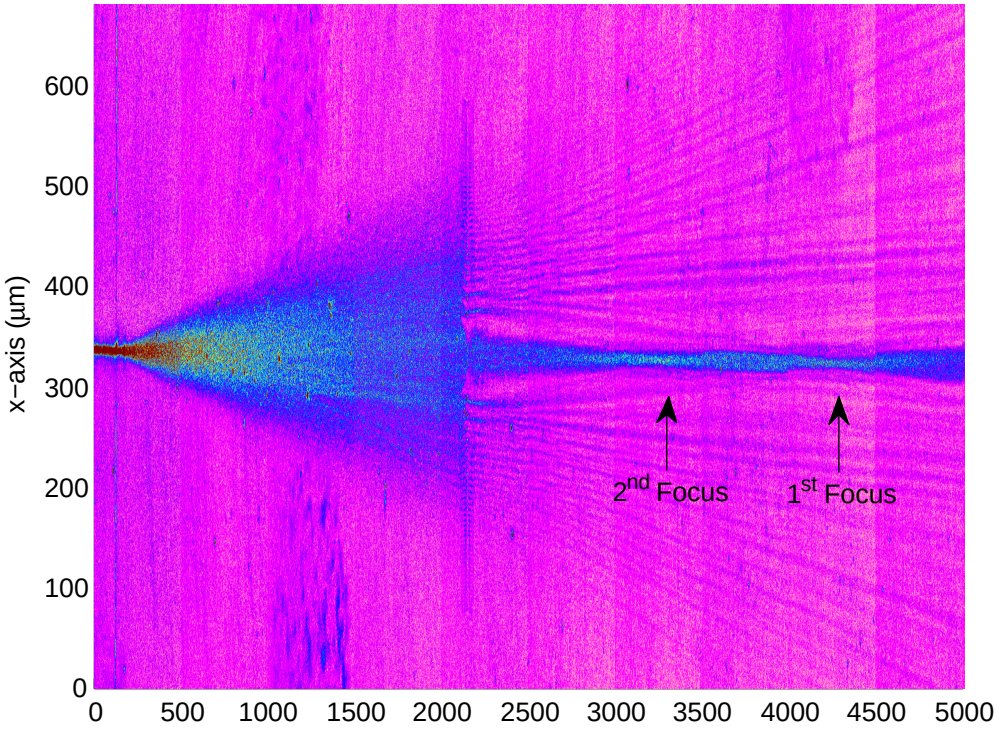

(a) TE

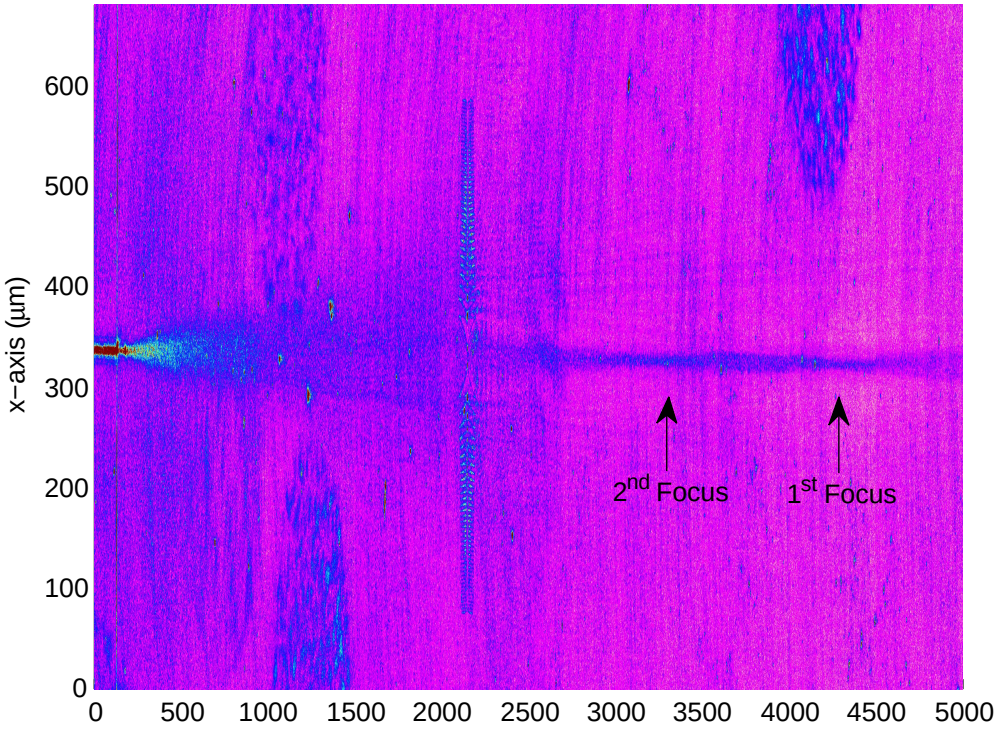

(b) TM

FIGURE 7.9: Scattering images of a paraxial kinoform lens stitched together for (a)TE and (b)TM polarisations.

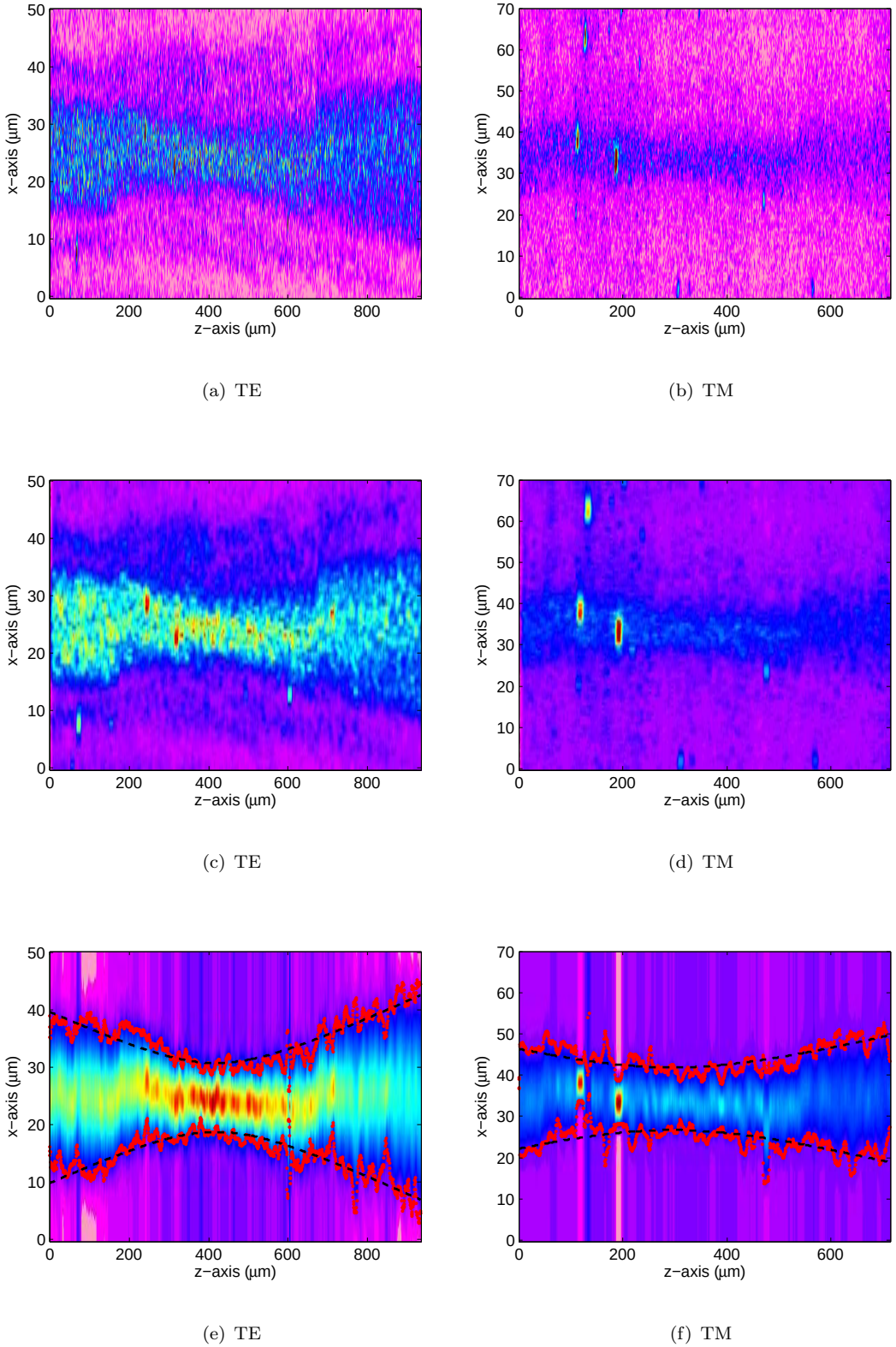

(a) TE (b) TM

(c) TE (d) TM

(e) TE (f) TM

FIGURE 7.10: Scattering image of the kinoform lens focussing in the in slab waveguide. The cropped raw image of the first order focus for TE(a) and TM(b). The image processed by smoothing by moving average filter for TE(c) and TM(d). The images Gaussian fits and spotsizes shown by red dotted line and the fit of a Gaussian beam for TE(e) and TM(f).

TABLE 7.1: Gaussian beam parameters for focussing scattering image in a slab waveguide by a paraxial kinoform lens for both TE and TM polarisations.

Beam Parameter	TE	TM
ω_0	6.2 ± 0.6 μm	6.2 ± 1.9 μm
z_R	173.8 ± 23.6 μm	177.6 ± 84.8 μm

spotsizes to give quantitative values for the focussing properties, namely, the spotsize, ω_0, and the Rayleigh range, z_R, which are given in Table 7.1.

The paraxial kinoform lenses have been demonstrated to focus to a small spotsize at the focal distance designed at 2 mm in both TE and TM polarisations with high Rayleigh ranges. The spotsizes given in Table 7.1 at the focus are larger than the channel waveguide spotsize of 2.5 μm due to limits in scattering imaging and non-idealities due to fabrication. However, the spotsizes are small and useful for optical detection.

7.3.3 MMIs

Figure 7.11 is a representative of the scattering images captured of an MMI. It is a raw image of the scattering from the top of a restricted MMI being excited by its central channel waveguide input with TE polarisation, Figure 7.11(a), and with TM polarisation, Figure 7.11(b). The MMI is 3 mm long and images the input in the middle of the MMI along the z-axis. It then re-images it back into the central output channel. Figure 7.11(b) is the same MMI, but with a TM polarisation at the input.

Figure 7.12 is in two columns with a cropped image of the imaging in the middle of the MMI from, on the left, Figure 7.11(a) and, on the right, Figure 7.11(b). The first image in each column is the raw cropped image and the second image in each column is the moving average filtered image. The third image in each column are Gaussian fits for the x-axis along each element of the z-axis with the spotsizes marked by the red dots. The Gaussian beam equation fit from the spotsizes to give quantitative values for the focussing properties, spotsize and Rayleigh range, which are given in table 7.2.

The same non-idealities which affect the scattering images of channel waveguides and lenses affect MMIs. However, the MMIs have demonstrated to have a better spotsizes at the imaging plane than the paraxial kinoform lens for both TE and TM polarisations.

TABLE 7.2: Gaussian beam parameters for scattering image in the MMI for both TE and TM polarisations.

Beam Parameter	TE	TM
ω_0	3.1 ± 0.33 μm	2.9 ± 0.5 μm
z_R	42.6 ± 7.1 μm	36.7 ± 10.8 μm

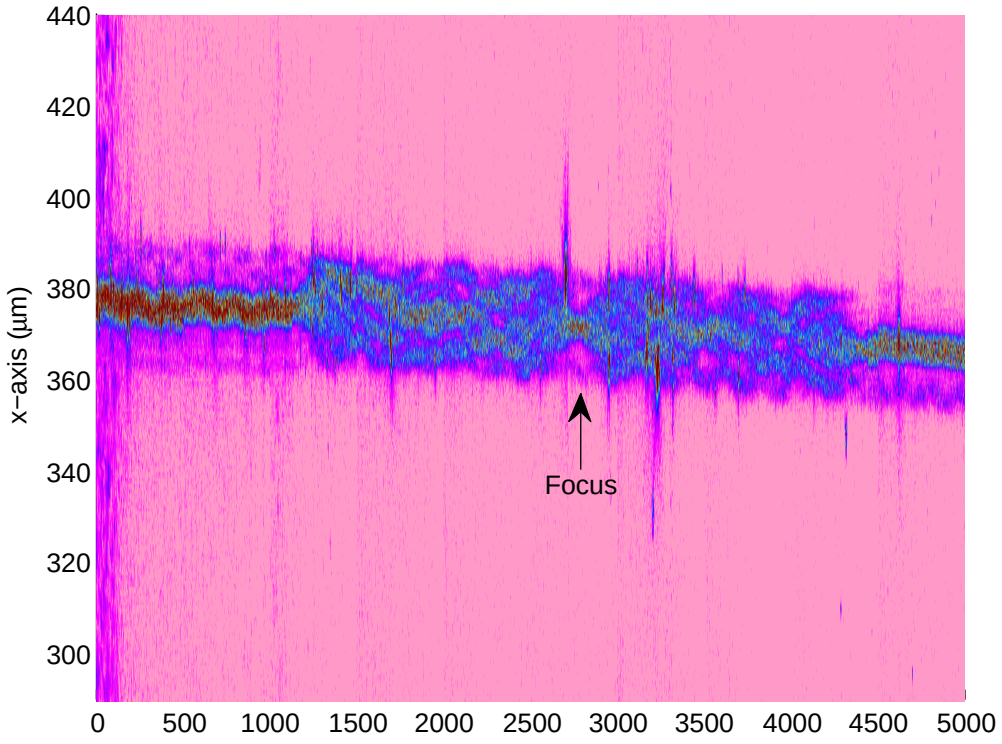

(a) TE

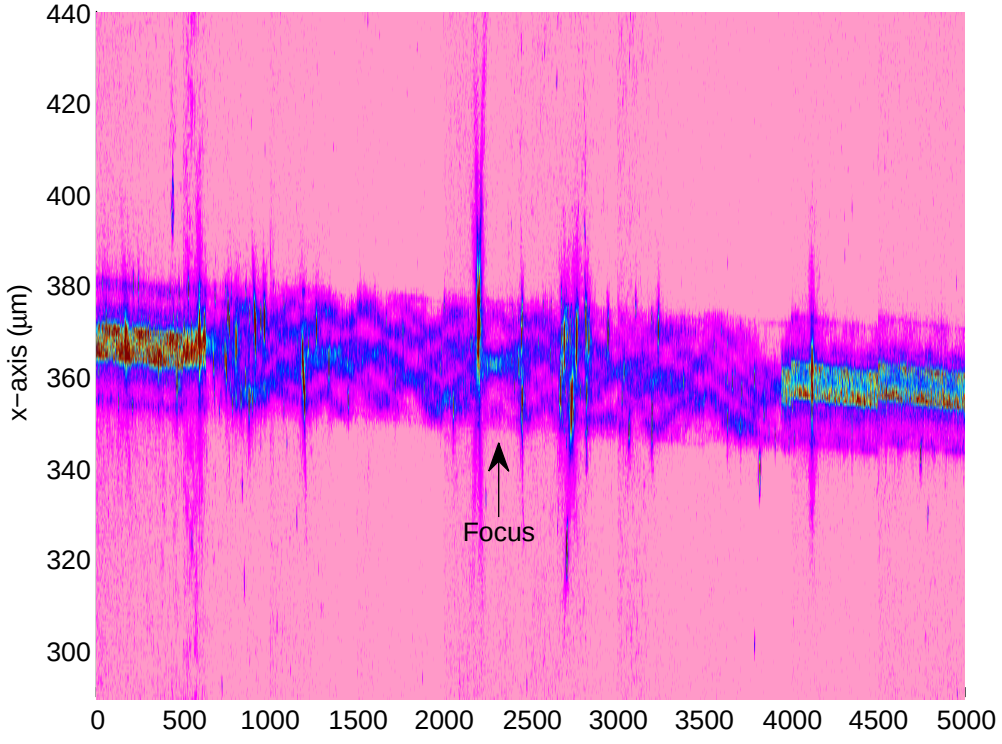

(b) TM

FIGURE 7.11: Scattering images of a restricted MMI stitched together for (a)TE and (b)TM polarisations.

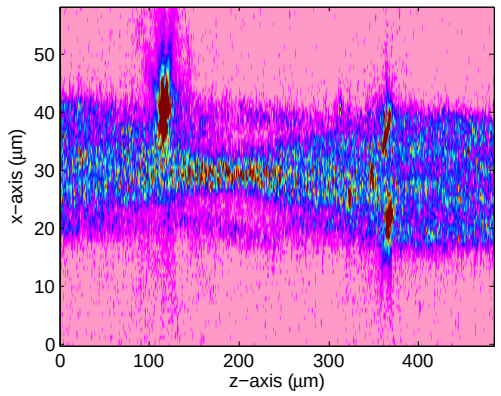

(a) TE

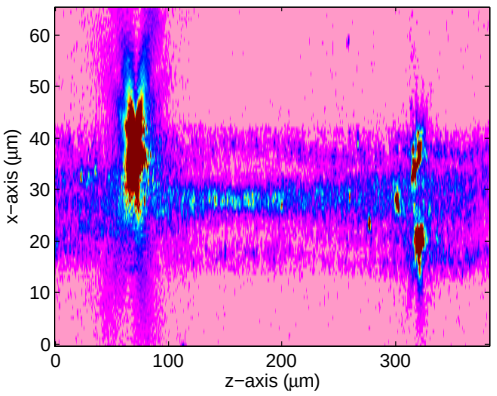

(b) TM

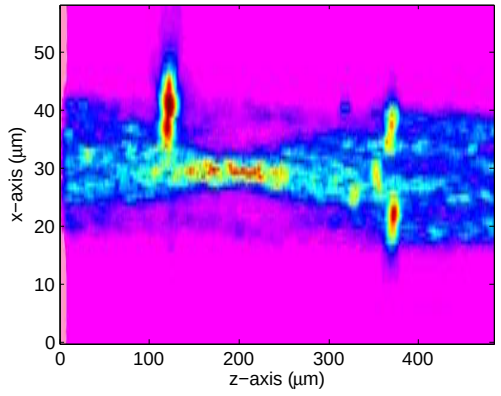

(c) TE

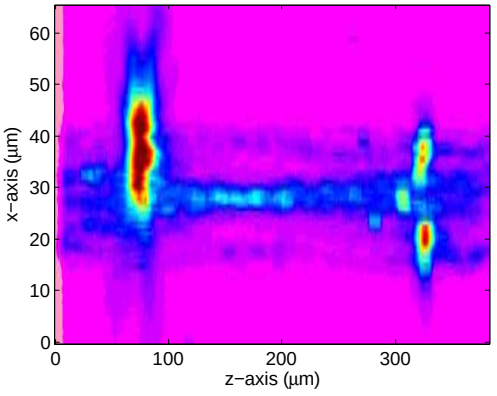

(d) TM

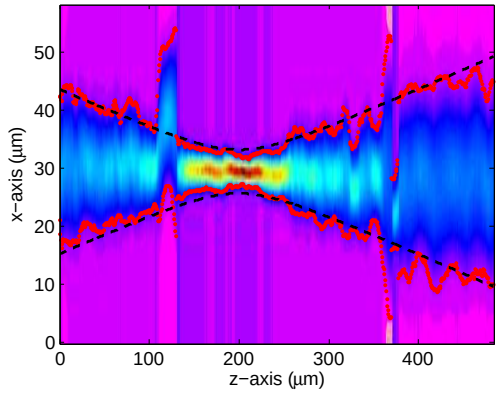

(e) TE

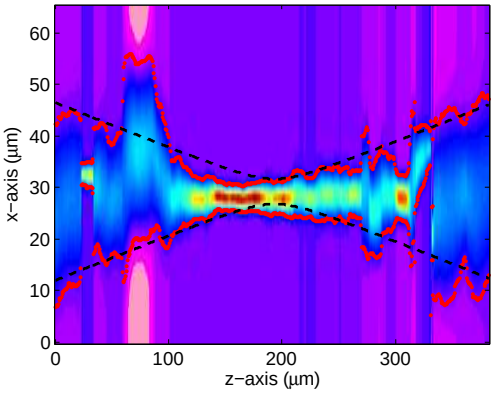

(f) TM

FIGURE 7.12: Scattering image of the MMI focussing its middle. The cropped raw image of the first order focus for TE(a) and TM(b). The image processed by smoothing by moving average filter for TE(c) and TM(d). The images Gaussian fits and spotsizes shown by red dotted line and the fit of a Gaussian beam for TE(e) and TM(f).

The lenses focus to a spotsize of $\sim$ 6.2 μm while the MMI focusses to $\sim$ 3.0 μm and channel waveguides spotsize of 2.5 μm in Section 7.2.1. The Rayleigh range for the MMI is lower than that of the lenses. Both the improved spotsize and shorter Rayleigh range of the MMIs when compared with kinoform lenses was expected by following the simulations in Chapter 5.

7.4 Focussing in a Microchannel

The the kinoform lenses and MMIs have been demonstrated to focus in the slab waveguides from which they are constructed. The purpose of this work is to focus light into the microfluidic channel which is etched through the slab waveguide region and this section characterises the beam in the microfluidic channel. The focussing in the channel was characterised by inserting a fluorescing solution into the microfluidic channel. Fluorescence in the microfluidic channel was achieved by using Cy 5.5 fluorophore which can absorb the excitation light from the HeNe at 633 nm and emits at approximately 700 nm. Since the concentration of Cy5.5 was small, it was assumed that the solution would have a the same refractive index as water which is what the devices were designed to have in the microfluidic channels.

The Cy5.5 concentration of 4.96×10^{-5} M was prepared by Dr. P. Hua. Since a pumping system had not been developed due to time constraints a coverslip of approx 150-170 μm thick was cut to size and glued on top of the chip covering the microfluidic channel. This then allowed the liquid to be placed on one of the microfluidic reservoirs and through capillary action flow to the other reservoir filling the channel with solution. The same setup to measure scattering was used for the imaging of fluorescence in the channel, Figure 7.5, except that the microscope had a x20 objective for imaging. The filter is used to block excitation light in the fluorescence measurements.

A working general MMI had its three inputs coupled to sequentially and Figure 7.13 shows the raw images of the focussing in the channel. This indicates that the MMI can be used to provide a moving focus in the channel. The central focus is well formed, but the side focusses exhibit angled propagation and contain light not contributing to the focussed beam.

Figure 7.14 show representative fluorescence images taken of the microfluidic channel for channel waveguides, paraxial kinoform lenses, and both general and restricted MMIs. The left column of images are the cropped original fluorescence images as seen by the camera through the filter. The images in the right column are of Gaussian fits in the x-axis for each element in the z-axis as was done with the focussing in scattering images. The black dashed line shows the best fit for the Gaussian beam equation parameters. The results for the measurements od several devices are tabulated in Table 7.3.

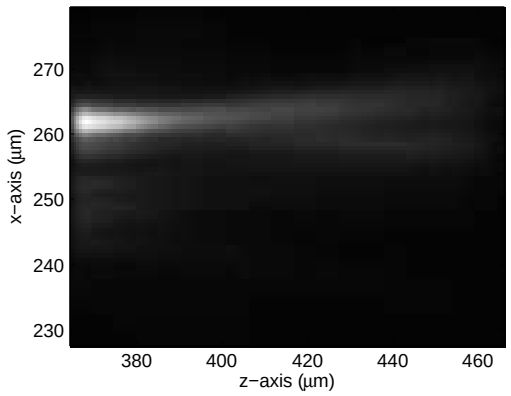

(a)

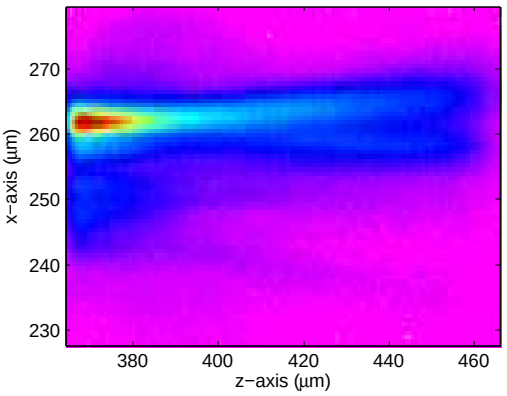

(b)

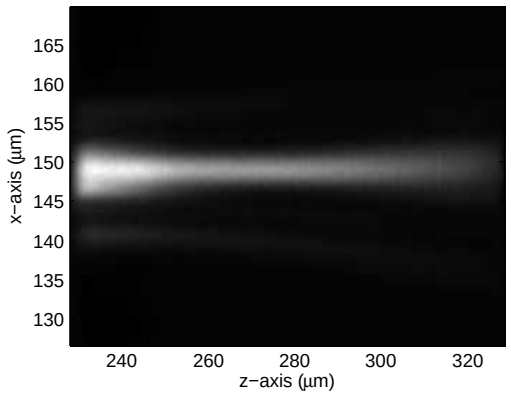

(c)

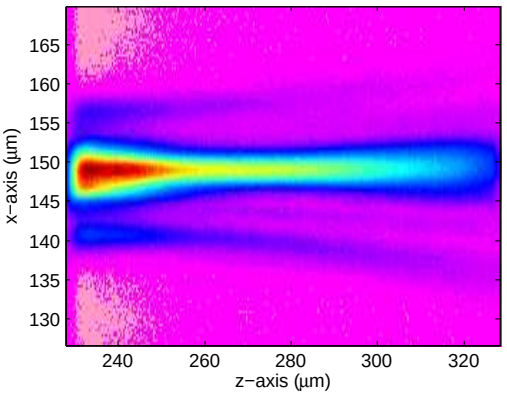

(d)

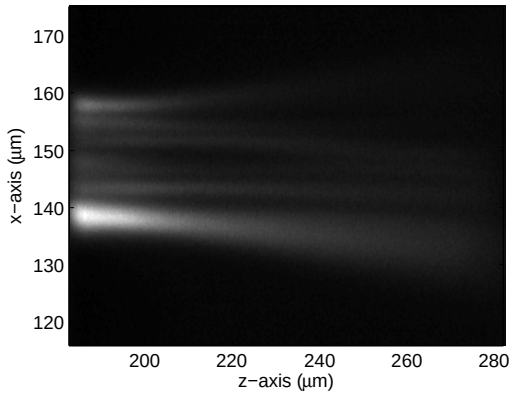

(e)

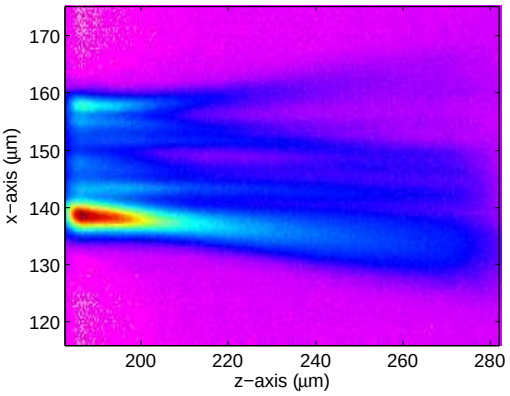

(f)

FIGURE 7.13: Focussing of MMI into the middle of a microfluidic channel with input in (a) the bottom waveguide, (b) the middle waveguide, and (c) the top waveguide.

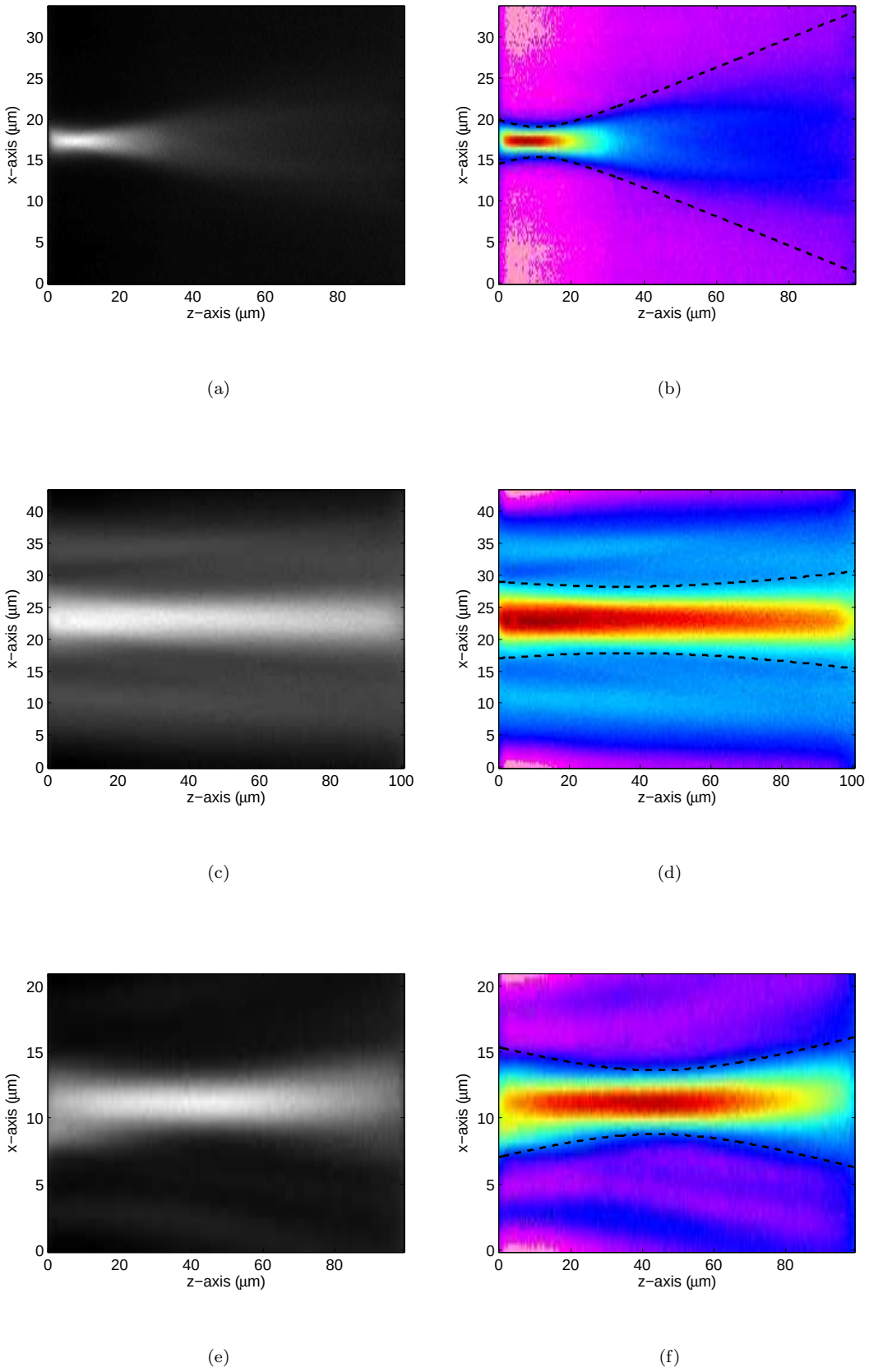

(a) (b)

(c) (d)

(e) (f)

FIGURE 7.14: Fluorescence of the beam in microchannel due to (a)waveguide, (b)paraxial kinoform lens, and (c)MMI. Images on the left are cropped raw with a grayscale colour map and on the right is are the corresponding processed images of Gaussian beam fits shown as the black dashed lines.

TABLE 7.3: Gaussian beam parameters for fluorescence images in the microfluidic channel for a channel waveguide, a paraxial kinoform lens, and an MMI. The table also includes the values of the simulations of the devices for comparison.

Beam Parameter	Waveguide (Rect./Trap.)	Lens	MMI (Gen./Res.)
ω_0	2.5 ± 0.5 μm	5.6 ± 1.6 μm	2.6 ± 0.3 μm
(Sim. ω_0)	(1.17/1.70 μm)	(2.05 μm)	(2.22/1.74 μm)
z_R	12.0 ± 1.3 μm	90.7 ± 27.0 μm	25.6 ± 11.1 μm
z_c	14.8 ± 3.8 μm	56.0 ± 23.1μm	29.2 ± 14.1 μm

The lenses and MMIs can be used as devices for focussing light into the middle of a microfluidic channel. The spotsize of the focus is well formed and almost the size of the input waveguide. The Gaussian beam fit for light transmitted into the microfluidic channel by the channel waveguide, paraxial kinoform lenses, and MMIs are given in Table 7.3. The values given are focus spotsize, ω_0, the Rayleigh range, and the distance into the microfluidic channel, z_c. The channel waveguide spotsize is 6.1 μm at the distance of 29.2 μm and 8.9 μm at the distance of 56.0 μm. The lens can focus into the middle of the microfluidic channel as this work required and though it has a larger focus spotsize than the channel waveguides' initial spotsize it does it is smaller than the spotsize of the diverging beam from the channel waveguide in the middle of the microfluidic channel. The MMIs that could be characterised do not focus as far into the microfluidic channel as the lens. However, the focus spotsize is both smaller than the spotsize of the diverging channel waveguide and the focus spotsize of the lens.

7.5 Summary and Discussion

This section is a summary of the results and a discussion of the implications. The purpose of this chapter was to characterise channel waveguides and to determine how well the realised paraxial kinoform lenses and MMIs focus the light into the middle of a microfluidic channel.

The characterisation of the channel waveguides included mode profiling to provide a direct measurement of the spotsize; the average size being 2.5 μm and 1.5 μm for the horizontal and vertical dimensions in the final devices, respectively. These spotsizes are larger than the simulations for 2 μm top width trapezoidal waveguide in Chapter 3 which were 1.7 μm and 1.1 μm for horizontal and vertical dimensions, respectively. The total insertion loss of the channel waveguides was measured and found to be 12.2 dB. Though the loss is high for waveguides they provide sufficient power to characterise the lenses and MMI devices. To discover whether this loss was predominantly coupling loss from the input fibre or propagation, scattering measurements from above the waveguides were taken. Scattering images were taken along the device and post-processing them to

have a plot of relative propagation power, which gave an average loss of 7.1 dB cm^{-1}. For a waveguide of approximately 2.5 cm, this is a high value showing that coupling loss is not the dominant loss, but this study also showed that scattering would allow for characterisation of lens and MMI function. Low-loss waveguides were not a priority in this work, but of course, there is room for future work in improvement of losses.

The focussing function of the lenses and MMIs without a microfluidic channel, but in the slab regions was characterised by taking scattering images along the device. Post-processing allowed the overall function of the lenses and MMIs to be observed. The images show that the function agrees with that seen in the simulations in Chapter 4 and Chapter 5, respectively. The focus was then fitted to a Gaussian beam equation to extract the spotsize. The average spotsizes for the lenses were 6.2 μm for both TE and TM polarisations and for the MMIs were 3.1 μm and 2.9 μm for TE and TM polarisations, respectively. The waveguides function as required and the lenses and MMIs focus in slabs, though scattering properties differ in the images taken for TE and TM polarisations scattering more from different surfaces on the channel waveguides the losses are similar and focussing properties negligible considered polarisation independent. The lenses and MMIs function as designed. Unfortunately, due to fabrication tolerances being too stringent, the lenses have been shown to focus some power into the second order and that the outer zones do not contribute to focussing the light. If the fabrication tolerances could be improved and features made more accurately more light would go to the first order focus and more of the higher spatial frequencies on the outer zones would contribute to making the focus have a smaller spotsize. The MMIs achieve a smaller spotsize than that of the lenses and lose less light in transmission.

The final characterisation was to observe focussing in a 100 μm wide microfluidic channel. For this, fluorescence images were taken by inserting Cy5.5 into the microfluidic channel. Post-processing of the fluorescent images for channel waveguides, paraxial kinoform lenses, and MMI devices bringing light to the microfluidic channel showed that the channel waveguides only diverge in the channel, whilst the lenses and MMIs focus into the microfluidic channel. Spotsizes in the microfluidic channel were 2.5 μm, 5.6 μm, and 2.6 μm for the channel waveguides, lenses, and MMIs, respectively. The devices on average could move the foci 56.0 μm and 29.2 μm into the microfluidic channels by the lenses and MMIs, respectively. The channel waveguides in comparison have a divergent beam with a spotsizes of 6.1 μm at the distance of 29.2 μm and 8.9 μm at the distance of 56.0 μm, much larger than the spotsizes made at those distances by the lenses and MMIs. The lenses can focus further into the channel, but the MMIs can focus into a smaller spotsize in the channel almost the size of channel waveguide spotsize. Therefore, future work would mostly involve reducing the empirical spotsize by improving fabrication tolerances of the lenses and changing MMI design to image further into the microfluidic channel.

7.6 Conclusion

Singlemode operation of channel waveguides is vital to making more complex microfluidic optical detection systems. However, multimode channel waveguides with few modes can operate in singlemode. For the devices presented in this work, the channel waveguide's fundamental mode determines the minimum spotsize achievable and allows it to function as designed. The channel waveguide has an average spotsize of 2.5 μm and 1.5 μm for horizontal and vertical dimensions, respectively, with total losses of 12.2 dB for a length of $\backsim$ 2.5 cm and a propagation loss of 7.1 dB cm^{-1}.

The paraxial kinoform lenses and MMIs realised have been shown to work in the GeO_2:SiO_2 material system. Both devices focus into the microfluidic channel with average spotsizes at the foci for the paraxial kinoform lenses of 5.6 μm and for the MMIs of 2.6 μm. The devices on average could move the foci 56.0 μm and 29.2 μm into the microfluidic channels by the lenses and MMIs, respectively. The spotsize of the channel waveguide is initially 2.5 μm, but for comparison the channel waveguide's divergent beam increases this spotsize to 6.1 μm at the distance of 29.2 μm and 8.9 μm at the distance of 56.0 μm, which is much larger than the spotsizes made at those distances by the lenses and MMIs. Polarisation dependence on the channel waveguide loss or the focussing functions of lens and MMI devices were found to be negligible.

The ability for both devices to focus light in the channel allow for greater control of the beam position, and its spotsize, in the microfluidic channel and now have the capability to build upon these devices and fully integrate optical detection methods that have currently little or no integration in optics for microfluidics.

Chapter 8

Conclusions and Future Work

8.1 Conclusions

The work in this thesis aimed to advance detection in lab-on-a-chip (LoC) technology and in particular μflow cytometry. The area of research was chosen to be the integrated optics as optical detection techniques are preferred in microfluidic systems due to their high sensitivities. A review of the literature led to the conclusion that the integrated optics used for microfluidic systems was in its infancy for many of the optical detection methods currently used in the analytical chemistry laboratory.

The literature review found that the most mature integrated microfluidic detection methods are fluorescence and absorption. Absorption is an attractive method as it is label-free, but poses the problem in microfluidics that it needs long path lengths or enhancement by multipass systems. The most dominant technique in use for optical detection is fluorescence due to its high sensitivity, but it often requires labelling by the use of fluorophores. Scattering is still being developed and has been used to acquire size and shape information on cells in flow cytometry and when combined with fluorescence can yield a more powerful detection system. Surface enhanced Raman scattering (SERS) is gaining ground as a competitor to fluorescence as a direct label-free method for detection and identification of species. However, SERS requires an integrated metal nanostructure or nanoparticle because normally the Raman signal is too weak. This creates other obstacles to development such as difficulties in fabrication, degradation of the nanostructures, blocking of the microfluidic channel or the inability subsequently to separate nanoparticles from the analyte. Laser tweezer Raman spectroscopy (LTRS) which may be used to trap and analyse large particles such as cells or species attached to enhancing metallic particles without extra enhancement may prove capable of solving the inherent problems of SERS for certain particles. Refractive index detection techniques are label-free but require sample separation methods such as capillary electrophoresis

(CE) to give adequate specificity of detection of particle species. The thermal lens technique performs detection in absorption assays and does not require long path lengths, but has the same drawback. Direct excitation, a beam of light illuminated on to the analyte, as opposed to evanescent excitation methods are found in the majority of optical detection in microfluidic systems as it provides greater flexibility to incorporate many optical detection methods. The review concluded that the higher integration of optical components and different configurations is necessary as the route to achieving integration for optical detection methods with little or no integration yet, such as the thermal lens, LTRS, and SERS.

A theoretical study of an integrated device with the most basic integrated optics combined with a microfluidic channel was carried out to highlight its limitations and determine what is necessary for greater optical integration. The most basic function is a waveguide delivering the excitation light as a free beam into the microfluidic channel. The 3D waveguide is the basic building block for integrated optics. Operation in only the fundamental mode (achievable even in waveguides with few modes) was identified early on as absolutely necessary to make complex optical systems predictable and to make repeatable spotsizes as small as possible. Analytical methods were used to have an intuition to the modal behaviour of the channel waveguide of rectangular cross-section. However, numerical simulations were carried out using BPM in a commercial package (*BeamPROP*$^{\mathrm{TM}}$) to study the behaviour of rectangular and trapezoidal cross-section channel waveguides with the values of the material system used to realise the devices as the analytical methods are limited to certain geometries. Channel waveguides with rectangular cross-section are ideal as simulations show good symmetrical mode profiles and the ability to make singlemode waveguides up to 2 μm in both width and height. Lager dimensions allow for easier coupling to fibre. Trapezoidal cross-section channel waveguides were also simulated because device dimensions are ultimately dependent on fabrication which tends to produce waveguides with such cross-sections. The cross-channel coupling efficiencies drop to 0.5 after 25 μm of propagation along the microfluidic channel width for simulations of the free beam diverging from rectangular channel waveguides in the microfluidic channel and coupling to channel waveguides of the same dimensions of the other side of 2 μm height and widths of 2, 3, and 4 μm. The width of the microfluidic channel for acceptable free-beam loss from a waveguide is determined by the width of the waveguide which controls divergence. However, this leads to either narrow microfluidic channels and larger spotsizes not ideal for fluorescence or scattering measurements. The Rayleigh range was used as the prime measure of whether microfluidic systems need more complex optics than only channel waveguides, but an increase of Rayleigh range involves increasing the spotsize which for many systems may be unacceptable.

Channel waveguides are convenient to guide the light to the microfluidic channel, but the divergence of the free beam in the microfluidic channel is not ideal. There is a

need to shift the tight intensity distribution at the end of the channel waveguide to the middle of the microfluidic channel without greatly increasing the spotsize. This can be achieved by integrating waveguide lenses. The waveguide lenses considered in this thesis were to be made using standard planar fabrication methods. Negative lenses, where the surrounding medium has higher refractive index than the lens, were chosen due to the better configuration for fabrication by etching. Ideal refractive lenses are designed using Fermat's principle which gives ideal collimating and focussing lens geometries of hyperbolas for positive lenses and ellipses for negative lenses. Diffractive lenses were found to overcome problems with refractive lenses such as poor lens aperture collection and large thickness. The diffractive lenses designed here improve upon the Fresnel zone plate (FZP), which has a diffraction efficiency of only ∼40% into the first order focus. The Bragg lens is an extension of the FZP which can focus the light into one diffractive order by operating in the Bragg regime. Unfortunately, its major flaw is that the central zones of the lens do not meet the Bragg regime condition, severely limiting its practical efficiency. The alternative improvement on the FZP is the kinoform profile, essentially a blazing that concentrates the power into one focussed order. The derivation of analytical kinoform profile was generated and extended to the the negative kinoform profile not found in the literature by the author. Candidate lenses for fabrication were chosen, namely, the elliptical refractive lens, the elliptical McGaugh kinoform lens, the elliptical kinoform lens, and the paraxial kinoform lens and simulations by BPM showed, unexpectedly, that the paraxial kinoform lens was the most efficient at imaging the end of a channel waveguide. The discrepancy is because of the limitations of the analytical methods used for designing the lenses.

At the micronscale other structures may be employed to image the end of a channel waveguide into a microfluidic channel as alternatives to lenses. Two devices were proposed, the arrayed waveguide grating (AWG) which works as a transmission grating and the multimode interference (MMI) device which uses the *self-imaging* phenomenon. The AWG can focus for a several wavelengths with low aberrations which could provide high flexibility for microfluidics. However, only recently has an AWG operating in the visible range been demonstrated and even in infra-red fabrication tolerances tend to be stringent for AWGs to function efficiently. For these reasons, the MMI was preferred for experimental studies and has been designed and simulated for focussing into a microfluidic channel for subsequent fabrication. The main advantage of the MMI compared to the lens is its relative simplicity to design and fabricate, because MMIs are essentially a multimode waveguide with a given length to image the input plane to the output plane. Excitation of only certain modes, such as a symmetrical modes, at the input plane of the multimode region of the MMI allows for its length to be reduced by a factor of 4 which improves its imaging by reducing the accumulating phase lags between modes caused by the paraxial approximation used for design and the Goos-Hähnchen shift.

Devices were fabricated comprising channel waveguides, paraxial kinoform lenses and

MMIs. A two-mask process for flexible planar fabrication of integrated optics and microfluidics on a single chip was developed. The structure comprises a buried optical waveguide layer that can be patterned to make a wide range of optical devices. A glass material system was chosen because of its compatibility with standard planar fabrication process, its good optical qualities, and its good chemical compatibility in microfluidics. Two composite SiO_2 glasses were chosen for study, GeO_2:SiO_2 and Ta_2O_5:SiO_2, for the optical waveguiding layer. However, GeO_2:SiO_2 was found to be simpler to fabricate having higher deposition rates, etch rates and forming slab waveguides with lower losses than Ta_2O_5:SiO_2, so the latter was discontinued. Film deposition by RF sputtering gave GeO_2:SiO_2 films with a refractive index of 1.474 at a wavelength of 633 nm and on fused silica substrates of refractive index of 1.458 giving a Δn of 0.016. The realised channel waveguides have quasi-trapezoidal cross-sections due to the photoresist cross-sections not being completely rectangular and the faceting caused by ion beam etching. The waveguide cross-sectional dimensions were measured as 5.3 $\pm$ 0.3 μm bottom width, 2.6 $\pm$ 0.3 μm top width, and 1.95 $\pm$ 0.02 μm height. The paraxial kinoform lenses realised had well defined central zones, but the outer zones were less well defined because of the resolution limit of the mask and and resolution limit of photolithography. However, since most of the optical power diverging from the channel waveguide into the slab region is contained in the centre of the beam, the well defined central zones are expected to focus the light to a sufficiently small enough spotsize. The MMIs realised were well defined and, in common with the channel waveguides, have quasi-trapezoidal cross-sections with equivalent rectangular cross-sectional width is 22.6 μm; this dimension is close to the 22 μm width used in the design.

The channel waveguides were observed to guide and could be operated in the fundamental mode. The channel waveguide determines the minimum spotsize achievable and allows it to function as designed. The final devices had channel waveguides with an average spotsize of 2.5 μm and 1.5 μm for horizontal and vertical dimensions, respectively. Both the paraxial kinoform lenses and MMIs were shown to image the end of a channel waveguide and form a focus into the microfluidic channel and polarisation dependence on the devices was found to be negligible. The paraxial kinoform lenses and MMIs realised have been demonstrated successfully in the GeO_2:SiO_2 material system. The average spotsizes in the microfluidic channel for the paraxial kinoform lenses of 5.6 μm at a distance of 56.0 μm into the microfluidic channel and for the MMIs were 2.6 μm at a distance of 29.2 μm, where, for comparison, the channel waveguide's divergent beam had a spotsize to 6.1 μm at the distance of 29.2 μm and 8.9 μm at the distance of 56.0 μm, which is much larger than the spotsizes made at those distances by the lenses and MMIs.

The devices were shown to focus the free beam in a microfluidic channel and potentially offer great flexibility to be used in several complex detection systems with little or no optical integration furthering the LoC and making progress in miniaturisation towards

portable, robust, cheaper, and even increased sensitivity. It is challenging to develop optical detection systems for microfluidics as high specifications are placed upon the optics, due to the extremely small sample volumes and small optical path lengths. However, the work in this thesis provides two optical devices that can manipulate the free beam in a microfluidic channel paving the way to more complex optical detection systems to be integrated with microfluidics to make more advanced μflow cytometers.

8.2 Future work

8.2.1 Improvement of Waveguides

Now that the devices have been realised, improvements in making more robust and efficient devices such as lowering waveguide losses can be addressed. For example, further studies into the annealing of the buried structure and the use of alternative deposition methods such as plasma-enhanced chemical vapor deposition (PECVD) or flame hydrolysis for layer deposition instead of sputtering to give better quality depositions should be conducted.

Use of higher index material systems, such as Ta_2O_5, would allow optical components on the devices to be scaled down. However, efficient coupling between fibre and on-chip waveguides would have to be overcome and singlemode behaviour achieved. One possibility may be to use rib waveguides to achieve singlemode behaviour, if reproducible channel waveguides are too large, and to use tapered waveguides to couple light to fibre efficiently. Rib waveguides do not have symmetrical mode profiles in both cross-sectional dimensions, but with careful design the asymmetry may be minimised. If these difficulties are overcome, the final device may be able to achieve a focus spotsize of a ~ 1 μm in the centre of a microfluidic channel.

The channel waveguides were found to have quasi-trapezoidal cross-sections. An analytical or numerical method to analyse the realised waveguide cross-sections be useful for more accurate modelling. Although the birefringence was found to be negligible, more detailed, birefringence measurements on the channel waveguides could carried out for completeness using the simple experimental setup by Janz *et al.* [260].

8.2.2 Work on Lenses

The kinoform lenses are dependent on their profiles and need the smallest feature sizes achievable. This can be remedied by the use of a focussed ion beam (FIB) for direct etching and patterning of the planar waveguide lenses, which has been reported to make feature sizes down to tens of nanometers [261]. However, FIB is time consuming for large features or for mass production.

Other kinoform profiles were simulated, but not realised in this work. The theory in Chapter 4 when deriving the elliptical kinoform design considers the lens' finite thickness with no paraxial approximation, thus this design is intuitively expected to be the most efficient; however, simulation showed otherwise. Fabrication with FIB would allow for an empirical comparison since the elliptical kinoform lens differs from the paraxial kinoform lens mostly at the outer zones where photolithography is limited. Another design route to explore is the realisation of hybrid lenses [214], where the central zones have kinoform profiles and the outer zones have Bragg gratings to reduce the stringent fabrication tolerances of the kinoform. Improvements in lens design may be possible with genetic algorithms which have successfully been used to design optical devices such as MMIs [262, 263], starting with analytical lenses as initial solutions.

During this work another type of lens device has emerged in the literature promising small footprint; these are known as photonic crystal lenses or"nano-lenses" [264]. The FIB would allow for comparison of easy of fabrication, focussing efficiency, and flexibility of design between diffractive lenses and the nano-lenses.

8.2.3 Work on AWGs and MMIs

The AWG was identified as a very flexible device for use in optical detection, but was not realised due to stringent fabrication tolerances. The AWG has imaging properties comparable to the MMI and the bonus of working at several wavelengths, which would allow to make devices that employ optical detection methods with little or no integration. Though MMIs do not have these stringent fabrication tolerances, the same fabrication issues apply for both devices, which consist of essentially only waveguides, albeit a wide multimode waveguide, so the future work on the devices should discuss both.

Fine tuning could be achieved in MMI devices improving performance after fabrication. The effective width of the MMI could be changed actively by making microfluidic channels on sidewalls of MMIs and changing the refractive index contrast between core and side liquid allowing for control of the free beam's focus position along the width of the microfluidic channel.

The AWG is a relatively large integrated optical device. It can be made more compact by reducing the length of the arrayed waveguides using air trenches to allow for larger bend angles without major increase from bend loss [265]. AWGs are made using star couplers. Interestingly, MMIs can be used to make a type of AWG known as an MMI-AWG [222], which are simpler to make given the less stringent fabrication tolerances to make MMIs. The MMI-AWG has two MMIs instead of star couplers and the number of waveguides in the waveguide array is equal to the number of output waveguides of the MMI. The MMI-AWG would have the advantages of the AWG dispersion but be simpler to fabricate with the MMIs having less stringent tolerances.

Buried ion-exchanged alternatives to the waveguide and MMI fabrication could be explored providing the advantage of using cheap sodalime glasses as substrates [266], and even AWG have been fabricated this way [267]. One limitation that is difficult to control is the waveguide width, which is affected by the depth to which the waveguide is buried [268]. Alternatively, UV direct writing, which has recently provided a novel way of making MMIs [269] could be explored giving more control on dimensions than buried ion-exchanged and could be applied to making AWGs. However, both these technologies would have to achieve high-performance devices at visible wavelengths. MMIs have been written by femtosecond laser to function at visible wavelengths [270]. Refractive index of the femtosecond-written waveguides can be controlled by writing speed [271] allowing the possibility for straight AWGs and MMI-AWGs where the arrayed waveguides are in a straight configuration all of equal length and the phase change for dispersion is achieved by differing refractive index.

The devices discussed so far can all focus or image small spotsizes into the middle of microfluidic channels. However, none of these devices can control the diffraction in the vertical (y-axis) dimension within the microfluidic channel. The obvious solution is to have 3D devices, but planar fabrication for lenses in the vertical dimension is too difficult. On the other hand, 3D AWGs are plausible but, as with the lenses, curvature in the vertical dimension would still be too difficult with stringent tolerances. MMIs having less stringent tolerances and flat input and output faces could overcome this and 3D MMI-AWGs [272] could be made. Designs of 3D MMIs have been studied [273] and demonstrated in silicon [274] and ARROW [275] waveguides, but with no channel waveguides connected to the multimode regions. To achieve 3D operations, the basic building block, the waveguide, would have to be made in 3D upon which to build 3D devices. This is difficult to achieve using conventional planar fabrication methods are difficult. Polymers could be used [276], but these methods involve partial exposures and mask shadowing effects to be able to produce vertical features; this fabrication is too complex. Direct writing is a more suitable method and 3D waveguides have been created by direct writing using a femtosecond laser, in both glass [277] and polymers [278]. Photopolymers allow for an inexpensive alternative using continuous lasers for direct writing [279].

8.2.4 Biological Applications

The devices realised in this work have demonstrated that a free beam in a microfluidic channel for optical detection can be manipulated on chip using integrated optics at the micronscale and this forms a strong basis on which to build improved devices. However, this requires a fully sealed lid and the introduction of a pumping system to be put in place. Once there is a pumping system in place, hydrodynamic focussing can be implemented to focus particles in the microfluidic channel so that the particles pass

the beam at the focal point away from the sidewalls. Particle detection experiments can then also be carried out. Particle fluorescence and scattering experiments using latex microspheres of a few microns in size should be characterised first, followed by biological particles of similar sizes such as cells. The results would build a library of signal signatures of known particles, which could then be used in detection and discrimination of particles in mixed or unknown analytes. Results can then be compared between devices and with the literature. The next stage of a practical μflow cytometer could be added, namely, on-chip sorting.

The capability of devices being able to perform optical trapping in addition to detection increases the complexities of μflow cytometers. Optical trapping in a microfluidic channel by a free beam has been demonstrated in AWGs [230], but this could also be done by the MMIs and waveguide lenses. Integration of optical trapping configurations could lead to fully integrated devices for optical detection methods such as LTRS and thermal lensing. The realised devices may be able to trap particles at the focus in the microfluidic channel.

The improvements to the integrated optics in microfluidic systems will lead to techniques not yet realised on chip. The focussing devices would for collection show fluorescence and scattering distributions giving information on the shape, size, surface roughness and detection of constituent parts (for example, organelles in biological cells) of the particles which could be used to discriminate at a higher accuracy, especially when distinguishing biological cells of different similar sizes but of different type. The possibility of multiple optical detection methods simultaneously done would provide μflow cytometry with extremely high yield. Furthermore, progress into 3D imaging devices will lead this ultimately to a form of on-chip microscopy, the ability to discriminate biological cells by imaging, but also to perform optical analysis not easily achieved with bulk setups.

Appendix A

Sodalime Glass and Fused Silica Chemical Compositions

The substrates used in this work have the following chemical compositions according to the manufacturers given in the tables below.

TABLE A.1: The approximate chemical composition MENZEL-GLÄSER sodalime glass

Compound	Concentration
SiO_2	72.20%
Na_2O	14.30%
K_2O	1.20%
CaO	6.40%
MgO	4.30%
AL_2O_3	1.20%
Fe_2O_3	0.03%
SO_3	0.30%

The information from Table A.1 was taken from `www.menzel.de/Objekttraeger.687.0.html?id=687&L=1`.

The information from Table A.2 was taken from `www.uqgoptics.com/materials_optical_spectosil.aspx`.

TABLE A.2: The approximate chemical composition Spectrosil fused silica glass

	Spectrosil 1000	Spectrosil 2000
Typical trace elements in ppb		
Al	< 20	< 10
Ca	< 10	< 10
Co	< 10	< 10
Cr	< 10	< 10
Cu	< 10	< 10
Fe	< 10	< 10
K	< 10	< 10
Li	< 10	< 10
Mg	< 10	< 10
Mn	< 10	< 10
Na	< 10	< 10
Ti	< 10	< 10
V	< 10	< 10
Zn	< 10	< 10
Zr	< 10	< 10
ppm		
Cl	< 1	< 1
OH	1000	1000

Appendix B

Mode Profile Analyser

This appendix provides the MATLAB source code, Listing B.1, used for the mode profile analyser (MPA) program. To get it to work a .fig file is also needed with a layout given in Figure B.1 and can be generated with the GUIDE command in MATLAB.

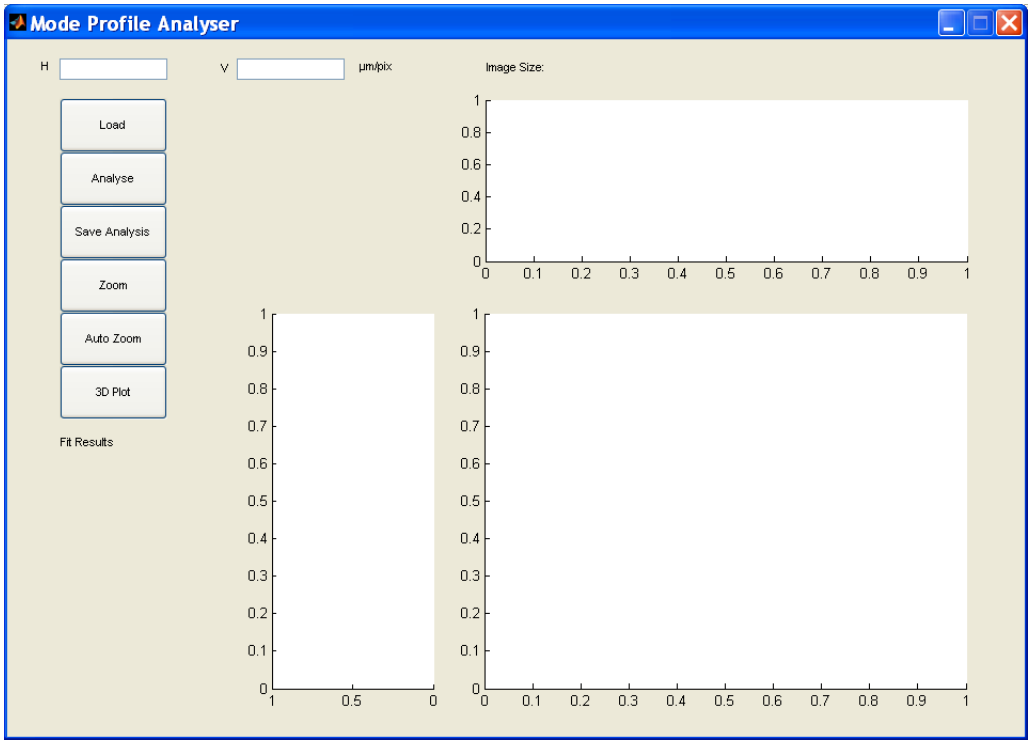

FIGURE B.1: Screenshot of layout of the MPA program.

LISTING B.1: MATLAB source code of the mode profile analyser (MPA) program.

```
function varargout = mpa(varargin)
% MPA M-file for mpa.fig
%      MPA, by itself, creates a new MPA or raises the existing
%      singleton*.
%
%      H = MPA returns the handle to a new MPA or the handle to
%      the existing singleton*.
%
%      MPA('CALLBACK',hObject,eventData,handles,...) calls the local
%      function named CALLBACK in MPA.M with the given input arguments.
%
%      MPA('Property','Value',...) creates a new MPA or raises the
%      existing singleton*.  Starting from the left, property value pairs are
%      applied to the GUI before mpa_OpeningFcn gets called.  An
%      unrecognized property name or invalid value makes property application
%      stop.  All inputs are passed to mpa_OpeningFcn via varargin.
%
%      *See GUI Options on GUIDE's Tools menu.  Choose "GUI allows only one
%      instance to run (singleton)".
%
% See also: GUIDE, GUIDATA, GUIHANDLES

% Edit the above text to modify the response to help mpa

% Author: Hamish Hunt
% Last Modified by GUIDE v2.5 09-Feb-2010 16:27:57

% Begin initialization code - DO NOT EDIT
gui_Singleton = 1;
gui_State = struct('gui_Name',       mfilename, ...
                   'gui_Singleton',  gui_Singleton, ...
                   'gui_OpeningFcn', @mpa_OpeningFcn, ...
                   'gui_OutputFcn',  @mpa_OutputFcn, ...
                   'gui_LayoutFcn',  [] , ...
                   'gui_Callback',   []);
if nargin && ischar(varargin{1})
    gui_State.gui_Callback = str2func(varargin{1});
end

if nargout
    [varargout{1:nargout}] = gui_mainfcn(gui_State, varargin{:});
else
    gui_mainfcn(gui_State, varargin{:});
end
% End initialization code - DO NOT EDIT


% --- Executes just before mpa is made visible.
function mpa_OpeningFcn(hObject, eventdata, handles, varargin)
% This function has no output args, see OutputFcn.
% hObject    handle to figure
% eventdata  reserved - to be defined in a future version of MATLAB
% handles    structure with handles and user data_axes (see GUIDATA)
% varargin   command line arguments to mpa (see VARARGIN)

% Choose default command line output for mpa
handles.output = hObject;
handles.data = [];          % User data
```

```
59  handles.Hum_pix = NaN;      % Calibration um per pix
    handles.Vum_pix = NaN;      % Default must be NaN
61
    % Update handles structure
63  guidata(hObject, handles);

65  % Switch axis off for contour
    axes(handles.data_axes); % Select the proper axes
67  axis off;

69  % Clear command line for errors!
    %clc;
71
    % UIWAIT makes mpa wait for user response (see UIRESUME)
73  % uiwait(handles.thegui);

75
    % --- Outputs from this function are returned to the command line.
77  function varargout = mpa_OutputFcn(hObject, eventdata, handles)
    % varargout  cell array for returning output args (see VARARGOUT);
79  % hObject    handle to figure
    % eventdata  reserved - to be defined in a future version of MATLAB
81  % handles    structure with handles and user data_axes (see GUIDATA)

83  % Get default command line output from handles structure
    varargout{1} = handles.output;
85

87  % --- Executes on button press in pushbutton1. Load
    function pushbutton1_Callback(hObject, eventdata, handles)
89  % hObject    handle to pushbutton1 (see GCBO)
    % eventdata  reserved - to be defined in a future version of MATLAB
91  % handles    structure with handles and user data_axes (see GUIDATA)

93  % Load data
    [handles.data, raw] = openfile();
95
    % Put picture on axes
97  axes(handles.picture); % Select the proper axes
    set(handles.picture,'Visible','on');
99  image(raw);
    axis off;
101
    % Print size of matrix for user since no axis
103 dimens = size(handles.data);
    set(handles.text6,'String',['Image Size: '...
105                             num2str(dimens(2))...
                                ' x '...
107                             num2str(dimens(1))...
                                ' pixels']);
109
    % Update handles structure
111 guidata(hObject, handles);
    % Contour of data
113 contour_of_data(handles);

115 % --- Executes on button press in pushbutton2. Analyse
    function pushbutton2_Callback(hObject, eventdata, handles)
117 % hObject    handle to pushbutton2 (see GCBO)
```

```
% eventdata  reserved - to be defined in a future version of MATLAB
% handles    structure with handles and user data_axes (see GUIDATA)

% Get cm/pix value to turn pix to cm
Hum_pix = handles.Hum_pix;
Vum_pix = handles.Vum_pix;

% Estimate peak location
[I,J] = est_peak(handles.data);

% Horizontal fit
x = 1:length(handles.data(I,:));
if ~(isnan(Hum_pix))
    x = Hum_pix*x;
end
[xthefit, xsummary] = fitgauss(handles.data(I,:),x,x(I));

% Plot the orig and fit
axes(handles.hori_sptsz); % Select the proper axes
plot(x,handles.data(I,:),'.',x,xthefit);
axis tight
if ~(isnan(Hum_pix))
    xlabel('\mum');
else
    xlabel('pixel');
end
ylabel('Intensity A.U.');

% Vertical fit
y = 1:length(handles.data(:,J));
if ~(isnan(Vum_pix))
    y = Vum_pix*y;
end
[ythefit, ysummary] = fitgauss(handles.data(:,J)',y,y(J));

% Plot the orig and fit
axes(handles.vert_sptsz); % Select the proper axes
plot(handles.data(:,J),y,'.',ythefit,y);
set(handles.vert_sptsz,'XDir','reverse'); % Set reverse direction axis
axis tight
if ~(isnan(Vum_pix))
    ylabel('\mum');
else
    ylabel('pixel');
end
xlabel('Intensity A.U.');

% Publish fit results.
handles = fitresults(handles,xsummary,ysummary);
% Update handles structure
guidata(hObject, handles);

% --- Executes on button press in pushbutton3. Save
function pushbutton3_Callback(hObject, eventdata, handles)
% hObject    handle to pushbutton3 (see GCBO)
% eventdata  reserved - to be defined in a future version of MATLAB
% handles    structure with handles and user data_axes (see GUIDATA)

% Bring up pop-up box to save
```

```
177 [filename, pathname] = uiputfile('*.fig', 'Save session as','untitled.fig');
    % If box was cancelled do nothing else save.
179 if ischar(filename)
        set(hObject,'Value',0);% Stops button being down when saving
181     saveas(gcbf, [pathname filename], 'fig');
    end
183
    % --- Executes on button press in togglebutton1. Zoom
185 function togglebutton1_Callback(hObject, eventdata, handles)
    % hObject    handle to togglebutton1 (see GCBO)
187 % eventdata  reserved - to be defined in a future version of MATLAB
    % handles    structure with handles and user data (see GUIDATA)
189
    % Hint: get(hObject,'Value') returns toggle state of togglebutton1
191
    if get(hObject,'Value')
193     zoom on;
    else
195     zoom off;
    end
197
    % --- Executes on button press in togglebutton4. Auto zoom
199 function togglebutton4_Callback(hObject, eventdata, handles)
    % hObject    handle to togglebutton4 (see GCBO)
201 % eventdata  reserved - to be defined in a future version of MATLAB
    % handles    structure with handles and user data (see GUIDATA)
203
    % Hint: get(hObject,'Value') returns toggle state of togglebutton4
205
    if get(hObject,'Value')
207     % --- Code for peak
        a = handles.data; % a for "a matrix"
209     [I,J] = est_peak(a);

211     % Get cm/pix value to turn pix to cm
        Hum_pix = handles.Hum_pix;
213     Vum_pix = handles.Vum_pix;

215     % Horizontal
        x = 1:length(handles.data(I,:));
217     if ~(isnan(Hum_pix))
            x = Hum_pix*x;
219     end

221     % Vertical
        y = 1:length(handles.data(:,J));
223     if ~(isnan(Vum_pix))
            y = Vum_pix*y;
225     end

227     % Take peak
        peak = a(I,J);
229
        % Take estimate spotsize
231     temp = find(sign(a(I,:) - peak*exp(-2)) == 1);
        spot_est = (temp(end)-temp(1))/2;
233     % Take a range of 2 spotsizes
        elminx = round(min(temp)-spot_est);
235     elmaxx = round(max(temp)+spot_est);
```

```
237     % Take estimate spotsize
        temp = find(sign(a(:,J) - peak*exp(-2)) == 1);
239     spot_est = (temp(end)-temp(1))/2;
        % Take a range of 2 spotsizes
241     elminy = round(min(temp)-spot_est);
        elmaxy = round(max(temp)+spot_est);
243
        % Select the proper axes
245     axes(handles.data_axes);
        % Zooms by changing the axis viewed.
247     axis([elminx elmaxx elminy elmaxy]);
        % Select other axes proper axes
249     axes(handles.hori_sptsz);
        axis([x(elminx) x(elmaxx) 0 max(a(I,:))]);
251     axes(handles.vert_sptsz);
        axis([0 max(a(:,J)) y(elminy) y(elmaxy)]);
253     % Don't forget the picture
        axes(handles.picture);
255     axis([elminx elmaxx length(a(:,J))-elmaxy length(a(:,J))-elminy]);

257 else
        % Select the proper axes
259     axes(handles.data_axes);
        % Returns to MATLAB auto control NB.
261     %normal does nothing auto goes beyond data
        axis tight;
263     % For the other axes
        axes(handles.hori_sptsz);
265     axis tight;
        axes(handles.vert_sptsz);
267     axis tight;
        axes(handles.picture);
269     axis tight;
    end
271
    % --- Executes on button press in pushbutton6. 3D plot
273 function pushbutton6_Callback(hObject, eventdata, handles)
    % hObject    handle to pushbutton6 (see GCBO)
275 % eventdata  reserved - to be defined in a future version of MATLAB
    % handles    structure with handles and user data (see GUIDATA)
277
    surf_of_data(handles);
279
    % --- Opening File
281 function [data,raw] = openfile()

283 if exist('predir.mat','file') %File with previous path used.
        load('predir.mat');
285 else
        Dir=''; % Incase of no predir
287 end

289 %Returns 0(zero) if cancelled
    %args: 1st file types, 2nd is title, 3rd path
291 [File,Dir] = uigetfile({'*.bmp','(*.bmp) Bitmap'},'',Dir);

293 %Stops non char DIR being saved
    if ischar(Dir)
```

```
295     save('predir.mat','Dir'); % updates the path

297     % --- Save data to variable in guidata
        raw = imread([Dir File], 'bmp');
299     data = raw(end:-1:1,:,1);     % Takes R from RGB
        %data(:,:,2:3) = [];
301     data = double(data);    % Make data usable by converting to double.
    else                        % Also stops problems plotting eg. mesh.
303     raw = [];
        data = [];
305 end

307 % --- Contour of data
    function contour_of_data(handles)
309 if ~isempty(handles.data)

311     % Plot contour
        axes(handles.data_axes); % Select the proper axes
313     contourf(handles.data,10);
        axis off;
315 end

317 % --- Surf of data
    function surf_of_data(handles)
319 if ~isempty(handles.data)
        figure('name','3D Plot','numbertitle','off')  % Create new figure window
321     mesh(handles.data);
    end
323
    % --- Writes to the Results Box
325 function handles = fitresults(handles,xsummary,ysummary)
    % String with results
327 summary = {'Fit Results:','',...
        'Horizontal:', xsummary{1:end}, '',...
329     'Vertical:', ysummary{1:end}};
    %get(handles.fitresults,'String')
331 set(handles.fitresults,'String',summary);

333 % --- Estimate peak position
    function [I,J] = est_peak(a)
335
    % Takes the average found good estimate
337 [I,J] = find(a == max(max(a)));
    I = round(mean(I));
339 J = round(mean(J));

341 % --- Gaussian parametric fit - NB. uses curve fitting toolbox!
    function [thefit, summary] = fitgauss(signal,x,gmu)
343
    % Type to fit
345 f = fittype('A*exp(-0.5.*(((x-mu)/std_dev).^2)) + B');
    [f1,out] = fit(x','signal',f,'Startpoint',[200 10 gmu 0.3*gmu],'MaxFunEvals',1e4);
347
    % Ouput the fit as vector
349 coeffs = coeffvalues(f1);
    thefit = coeffs(1)*exp(-0.5.*(((x-coeffs(3))/coeffs(4)).^2)) + coeffs(2);
351
    % Fill out summary cell - NB. std_dev can be -ve so take abs()
353 % NB. Not sqrt(2)because it is fitted to intensity.
```

```
summary = {['R^2 = ' num2str(out.rsquare)],...
           ['mu = ' num2str(coeffs(3))],...
           ['std_dev = ' num2str(abs(coeffs(4)))],...
           ['spotsize = ' num2str(2.*abs(coeffs(4)))],...
           ['amp = ' num2str(coeffs(1))],...
           ['thres = ' num2str(coeffs(2))]};

function edit2_Callback(hObject, eventdata, handles)
% hObject    handle to edit2 (see GCBO)
% eventdata  reserved - to be defined in a future version of MATLAB
% handles    structure with handles and user data (see GUIDATA)

% Hints: get(hObject,'String') returns contents of edit2 as text
%        str2double(get(hObject,'String')) returns contents of edit2 as a
%        double

handles.Hum_pix = str2double(get(hObject,'String'));
% Update handles structure
guidata(hObject, handles);

% --- Executes during object creation, after setting all properties.
function edit2_CreateFcn(hObject, eventdata, handles)
% hObject    handle to edit2 (see GCBO)
% eventdata  reserved - to be defined in a future version of MATLAB
% handles    empty - handles not created until after all CreateFcns called

% Hint: edit controls usually have a white background on Windows.
%       See ISPC and COMPUTER.
if ispc && isequal(get(hObject,'BackgroundColor'), ...
        get(0,'defaultUicontrolBackgroundColor'))
    set(hObject,'BackgroundColor','white');
end

function edit4_Callback(hObject, eventdata, handles)
% hObject    handle to edit4 (see GCBO)
% eventdata  reserved - to be defined in a future version of MATLAB
% handles    structure with handles and user data (see GUIDATA)

% Hints: get(hObject,'String') returns contents of edit4 as text
%        str2double(get(hObject,'String')) returns contents of edit4 as a
%        double

handles.Vum_pix = str2double(get(hObject,'String'));
% Update handles structure
guidata(hObject, handles);

% --- Executes during object creation, after setting all properties.
function edit4_CreateFcn(hObject, eventdata, handles)
% hObject    handle to edit4 (see GCBO)
% eventdata  reserved - to be defined in a future version of MATLAB
% handles    empty - handles not created until after all CreateFcns called

% Hint: edit controls usually have a white background on Windows.
%       See ISPC and COMPUTER.
if ispc && isequal(get(hObject,'BackgroundColor'), ...
        get(0,'defaultUicontrolBackgroundColor'))
    set(hObject,'BackgroundColor','white');
end
```

Bibliography

[1] T. Thorsen, S. Maerkl, and S. Quake, "Microfluidic large-scale integration," *Science*, vol. 298, no. 5593, pp. 580–584, 2002.

[2] M. Smit, M. Hill, R. Baets, E. Bente, H. Dorren, F. Karouta, P. Koenraad, T. Koonen, X. Leijtens, R. Nötzel, S. Oei, H. de Waardt, J. van der Tol, and D. Khoe, "How complex can integrated optical circuits become?" in *ECIO*, Copenhagen, Denmark, 2007.

[3] D. Psaltis, S. Quake, and C. Yang, "Developing optofluidic technology through the fusion of microfluidics and optics," *Nature*, vol. 442, no. 7101, pp. 381–386, 2006.

[4] J. El-Ali, P. Sorger, and K. Jensen, "Cells on chips," *Nature*, vol. 442, no. 7101, pp. 403–411, 2006.

[5] A. Manz, N. Graber, and H. Widmer, "Miniaturized total chemical-analysis systems - a novel concept for chemical sensing," *Sensors and Actuators B - Chemical*, vol. 1, no. 1-6, pp. 244–248, 1990.

[6] A. deMello, "Control and detection of chemical reactions in microfluidic systems," *Nature*, vol. 442, no. 7101, pp. 394–402, 2006.

[7] H. Craighead, "Future lab-on-a-chip technologies for interrogating individual molecules," *Nature*, vol. 442, no. 7101, pp. 387–393, 2006.

[8] Y. Xia and G. Whitesides, "Soft lithography," *Annual Review of Materials Science*, vol. 28, pp. 153–184, 1998.

[9] D. Erickson and D. Q. Li, "Integrated microfluidic devices," *Analytica Chimica Acta*, vol. 507, no. 1, pp. 11–26, 2004.

[10] C. Yi, C. Li, S. Ji, and M. Yang, "Microfluidics technology for manipulation and analysis of biological cells," *Analytica Chimica Acta*, vol. 560, no. 1-2, pp. 1–23, 2006.

[11] D. Breslauer, P. Lee, and L. Lee, "Microfluidics-based systems biology," *Molecular Biosystems*, vol. 2, no. 2, pp. 97–112, 2006.

[12] K. Huikko, R. Kostiainen, and T. Kotiaho, "Introduction to micro-analytical systems: bioanalytical and pharmaceutical applications," *European Journal of Pharmaceutical Sciences*, vol. 20, no. 2, pp. 149–171, 2003.

[13] P. Auroux, D. Iossifidis, D. Reyes, and A. Manz, "Micro total analysis systems. 2. analytical standard operations and applications," *Analytical Chemistry*, vol. 74, no. 12, pp. 2637–2652, 2002.

[14] P. Dittrich and A. Manz, "Single-molecule fluorescence detection in microfluidic channels - the Holy Grail in μTAS?" *Analytical and Bioanalytical Chemistry*, vol. 382, no. 8, pp. 1771–1782, 2005.

[15] T. Vilkner, D. Janasek, and A. Manz, "Micro total analysis systems. recent developments," *Analytical Chemistry*, vol. 76, no. 12, pp. 3373–3385, 2004.

[16] K. Dholakia and P. Reece, "Optical micromanipulation takes hold," *Nano Today*, vol. 1, no. 1, pp. 18–27, 2006.

[17] L. Lechuga, "New frontiers in optical biosensing," in *ECIO*, Copenhagen, Denmark, 2007.

[18] S. Balslev, A. Jorgensen, B. Bilenberg, K. Mogensen, D. Snakenborg, O. Geschke, J. Kutter, and A. Kristensen, "Lab-on-a-chip with integrated optical transducers," *Lab on a Chip*, vol. 6, no. 2, pp. 213–217, 2006.

[19] S. Ibrahim and G. van den Engh, "High-speed cell sorting: fundamentals and recent advances," *Current Opinion in Biotechnology*, vol. 14, no. 1, pp. 5–12, 2003.

[20] D. Mattanovich and N. Borth, "Applications of cell sorting in biotechnology," *Microbial Cell Factories*, vol. 5, no. 12, 2006.

[21] D. Huh, W. Gu, Y. Kamotani, J. Grotberg, and S. Takayama, "Microfluidics for flow cytometric analysis of cells and particles," *Physiological Measurement*, vol. 26, no. 3, pp. R73–R98, 2005.

[22] D. Ateya, J. Erickson, P. Howell, L. Hilliard, J. Golden, and F. Ligler, "The good, the bad, and the tiny: a review of microflow cytometry," *Analytical and Bioanalytical Chemistry*, vol. 391, no. 5, pp. 1485–1498, 2008.

[23] J. Godin, C. Chen, S. Cho, W. Qiao, F. Tsai, and Y. Lo, "Microfluidics and photonics for bio-system-on-a-chip: A review of advancements in technology towards a microfluidic flow cytometry chip," *Journal of Biophotonics*, vol. 1, no. 5, pp. 355–376, 2008.

[24] J. Leary, "Ultra high-speed sorting," *Cytometry Part A*, vol. 67A, no. 2, pp. 76–85, 2005.

[25] M. Toner and D. Irimia, "Blood-on-a-chip," *Annual Review of Biomedical Engineering*, vol. 7, pp. 77–103, 2005.

[26] O. Krichevsky and G. Bonnet, "Fluorescence correlation spectroscopy: the technique and its applications," *Reports on Progress in Physics*, vol. 65, no. 2, pp. 251–297, 2002.

[27] N. Pamme, R. Koyama, and A. Manz, "Counting and sizing of particles and particle agglomerates in a microfluidic device using laser light scattering: application to a particle-enhanced immunoassay," *Lab on a Chip*, vol. 3, no. 3, pp. 187–192, 2003.

[28] S. Gotz and U. Karst, "Recent developments in optical detection methods for microchip separations," *Analytical and Bioanalytical Chemistry*, vol. 387, no. 1, pp. 183–192, 2007.

[29] C. Yi, Q. Zhang, C. Li, J. Yang, J. Zhao, and M. Yang, "Optical and electrochemical detection techniques for cell-based microfluidic systems," *Analytical and Bioanalytical Chemistry*, vol. 384, no. 6, pp. 1259–1268, 2006.

[30] P. Viskari and J. Landers, "Unconventional detection methods for microfluidic devices," *Electrophoresis*, vol. 27, no. 9, pp. 1797–1810, 2006.

[31] P. Lambeck, "Integrated optical sensors for the chemical domain," *Measurement Science & Technology*, vol. 17, no. 8, pp. R93–R116, 2006.

[32] D. Schrum, C. Culbertson, S. Jacobson, and J. Ramsey, "Microchip flow cytometry using electrokinetic focusing," *Analytical Chemistry*, vol. 71, no. 19, pp. 4173–4177, 1999.

[33] M. McClain, C. Culbertson, S. Jacobson, and J. Ramsey, "Flow cytometry of escherichia coli on nucrifluidic devices," *Analytical Chemistry*, vol. 73, no. 21, pp. 5334–5338, 2001.

[34] M. Witek, S. Wei, B. Vaidya, A. Adams, L. Zhu, W. Stryjewski, R. McCarley, and S. Soper, "Cell transport via electromigration in polymer-based microfluidic devices," *Lab on a Chip*, vol. 4, no. 5, pp. 464–472, 2004.

[35] N. Pamme, J. Eijkel, and A. Manz, "On-chip free-flow magnetophoresis: Separation and detection of mixtures of magnetic particles in continuous flow," *Journal of Magnetism and Magnetic Materials*, vol. 307, no. 2, pp. 237–244, 2006.

[36] Z. Wang, J. El-Ali, M. Engelund, T. Gotsaed, I. R. Perch-Nielsen, K. B. Mogensen, D. Snakenborg, J. P. Kutter, and A. Wolff, "Measurements of scattered light on a microchip flow cytometer with integrated polymer based optical elements," *Lab on a Chip*, vol. 4, no. 4, pp. 372–377, 2004.

[37] Z. Wang, O. Hanson, P. Petersen, A. Rogeberg, J. P. Kutter, D. Bang, and A. Wolff, "Dielectrophoresis microsystem with integrated flow cytometers for on-line monitoring of sorting efficiency," *Electrophoresis*, vol. 27, no. 24, pp. 5081–5092, 2006.

[38] S. Moring, R. Reel, and R. Van Soest, "Optical improvements of a Z-shaped cell for high-sensitivity UV absorbency detection in capillary electrophoresis," *Analytical Chemistry*, vol. 65, no. 23, pp. 3454–3459, 1993.

[39] K. Mogensen, F. Eriksson, O. Gustafsson, R. Nikolajsen, and J. Kutter, "Pure-silica optical waveguides, fiber couplers, and high-aspect ratio submicrometer channels for electrokinetic separation devices," *Electrophoresis*, vol. 25, no. 21-22, pp. 3788–3795, 2004.

[40] Z. Liang, N. Chiem, G. Ocvirk, T. Tang, K. Fluri, and D. Harrison, "Microfabrication of a planar absorbance and fluorescence cell for integrated capillary electrophoresis devices," *Analytical Chemistry*, vol. 68, no. 6, pp. 1040–1046, 1996.

[41] K. Mogensen, N. Petersen, J. Hubner, and J. Kutter, "Monolithic integration of optical waveguides for absorbance detection in microfabricated electrophoresis devices," *Electrophoresis*, vol. 22, no. 18, pp. 3930–3938, 2001.

[42] K. Mogensen, J. El-Ali, A. Wolff, and J. Kutter, "Integration of polymer waveguides for optical detection in microfabricated chemical analysis systems," *Applied Optics*, vol. 42, no. 19, pp. 4072–4079, 2003.

[43] M. Grumann, J. Steigert, L. Riegger, I. Moser, B. Enderle, K. Riebeseel, G. Urban, R. Zengerle, and J. Ducree, "Sensitivity enhancement for colorimetric glucose assays on whole blood by on-chip beam-guidance," *Biomedical Microdevices*, vol. 8, no. 3, pp. 209–214, 2006.

[44] H. Salimi-Moosavi, Y. Jiang, L. Lester, G. McKinnon, and D. Harrison, "A multireflection cell for enhanced absorbance detection in microchip-based capillary electrophoresis devices," *Electrophoresis*, vol. 21, no. 7, pp. 1291–1299, 2000.

[45] N. Mortensen and S. Xiao, "Slow-light enhancement of Beer-Lambert-Bouguer absorption," *Applied Physics Letters*, vol. 90, no. 14, p. 141108, 2007.

[46] M. Duggan, T. McCreedy, and J. Aylott, "A non-invasive analysis method for on-chip spectrophotometric detection using liquid-core waveguiding within a 3D architecture," *Analyst*, vol. 128, no. 11, pp. 1336–1340, 2003.

[47] A. Datta, I. Eom, A. Dhar, P. Kuban, R. Manor, I. Ahmad, S. Gangopadhyay, T. Dallas, M. Holtz, F. Temkin, and P. Dasgupta, "Microfabrication and characterization of Teflon AF-coated liquid core waveguide channels in silicon," *IEEE Sensors Journal*, vol. 3, no. 6, pp. 788–795, 2003.

[48] K. Ro, K. Lim, B. Shim, and J. Hahn, "Integrated light collimating system for extended optical-path-length absorbance detection in microchip-based capillary electrophoresis," *Analytical Chemistry*, vol. 77, no. 16, pp. 5160–5166, 2005.

[49] L. Zhu, C. Lee, and D. DeVoe, "Integrated microfluidic UV absorbance detector with attomol-level sensitivity for BSA," *Lab on a Chip*, vol. 6, no. 1, pp. 115–120, 2006.

[50] A. Llobera, R. Wilke, and S. Buttgenbach, "Poly(dimethylsiloxane) hollow abbe prism with microlenses for detection based on absorption and refractive index shift," *Lab on a Chip*, vol. 4, no. 1, pp. 24–27, 2004.

[51] A. Llobera, R. Wilke, and S. Buttgenbach, "Optimization of poly(dimethylsiloxane) hollow prisms for optical sensing," *Lab on a Chip*, vol. 5, no. 5, pp. 506–511, 2005.

[52] B. Ma, X. Zhou, G. Wang, H. Huang, Z. Dai, J. Qin, and B. Lin, "Integrated isotachophoretic reconcentration with zone electrophoresis separation on a quartz microchip for UV detection of flavonoids," *Electrophoresis*, vol. 27, no. 24, pp. 4904–4909, 2006.

[53] L. Jiang and S. Pau, "Integrated waveguide with a microfluidic channel in spiral geometry for spectroscopic applications," *Applied Physics Letters*, vol. 90, no. 11, p. 111108, 2007.

[54] J. Hu, V. Tarasov, A. Agarwal, L. Kimerling, N. Carlie, L. Petit, and K. Richardson, "Fabrication and testing of planar chalcogenide waveguide integrated microfluidic sensor," *Optics Express*, vol. 15, no. 5, pp. 2307–2314, 2007.

[55] G. Veldhuis, O. Parriaux, H. Hoekstra, and P. Lambeck, "Sensitivity enhancement in evanescent optical waveguide sensors," *Journal of Lightwave Technology*, vol. 18, no. 5, pp. 677–682, 2000.

[56] D. Holmes, H. Morgan, and N. Green, "High throughput particle analysis: Combining dielectrophoretic particle focussing with confocal optical detection," *Biosensors & Bioelectronics*, vol. 21, no. 8, pp. 1621–1630, 2006.

[57] M. Gong, K. Wehmeyer, P. Limbach, F. Arias, and W. Heineman, "On-line sample preconcentration using field-amplified stacking injection in microchip capillary electrophoresis," *Analytical Chemistry*, vol. 78, no. 11, pp. 3730–3737, 2006.

[58] J. Dishinger and R. Kennedy, "Serial immunoassays in parallel on a microfluidic chip for monitoring hormone secretion from living cells," *Analytical Chemistry*, vol. 79, no. 3, pp. 947–954, 2007.

[59] Y. Sun and X. Yin, "Novel multi-depth microfluidic chip for single cell analysis," *Journal of Chromatography A*, vol. 1117, no. 2, pp. 228–233, 2006.

[60] H. Morgan, D. Holmes, and N. Green, "High speed simultaneous single particle impedance and fluorescence analysis on a chip," *Current Applied Physics*, vol. 6, no. 3, pp. 367–370, 2006.

[61] B. Jung, Y. Zhu, and J. Santiago, "Detection of 100 aM fluorophores using a high-sensitivity on-chip CE system and transient isotachophoresis," *Analytical Chemistry*, vol. 79, no. 1, pp. 345–349, 2007.

[62] S. Yang, S. Hsiung, Y. Hung, C. Chang, T. Liao, and G. Lee, "A cell counting/-sorting system incorporated with a microfabricated flow cytometer chip," *Measurement Science & Technology*, vol. 17, no. 7, pp. 2001–2009, 2006.

[63] C. Simonnet and A. Groisman, "High-throughput and high-resolution flow cytometry in molded microfluidic devices," *Analytical Chemistry*, vol. 78, no. 16, pp. 5653–5663, 2006.

[64] T. Kamei and T. Wada, "Contact-lens type of micromachined hydrogenated amorphous Si fluorescence detector coupled with microfluidic electrophoresis devices," *Applied Physics Letters*, vol. 89, no. 11, p. 114101, 2006.

[65] T. Kamei, N. Toriello, E. Lagally, R. Blazej, J. Scherer, R. Street, and R. Mathies, "Microfluidic genetic analysis with an integrated a-Si : H detector," *Biomedical Microdevices*, vol. 7, no. 2, pp. 147–152, 2005.

[66] J. Fu, Q. Fang, T. Zhang, X. Jin, and Z. Fang, "Laser-induced fluorescence detection system for microfluidic chips based on an orthogonal optical arrangement," *Analytical Chemistry*, vol. 78, no. 11, pp. 3827–3834, 2006.

[67] R. Mazurczyk, J. Vieillard, A. Bouchard, B. Hannes, and S. Krawczyk, "A novel concept of the integrated fluorescence detection system and its application in a lab-on-a-chip microdevice," *Sensors and Actuators B-Chemical*, vol. 118, no. 1-2, pp. 11–19, 2006.

[68] R. Bernini, E. De Nuccio, F. Brescia, A. Minardo, L. Zeni, P. Sarro, R. Palumbo, and M. Scarfi, "Development and characterization of an integrated silicon micro flow cytometer," *Analytical and Bioanalytical Chemistry*, vol. 386, no. 5, pp. 1267–1272, 2006.

[69] N. Yamaguchi, H. Ohba, and M. Nasu, "Simple detection of small amounts of pseudomonas cells in milk by using a microfluidic device," *Letters in Applied Microbiology*, vol. 43, no. 6, pp. 631–636, 2006.

[70] K. Inatomi, S. Izuo, and S. Lee, "Application of a microfluidic device for counting of bacteria," *Letters in Applied Microbiology*, vol. 43, no. 3, pp. 296–300, 2006.

[71] Q. Xiang, G. Hu, Y. Gao, and D. Li, "Miniaturized immunoassay microfluidic system with electrokinetic control," *Biosensors & Biolectronics*, vol. 21, no. 10, pp. 2006–2009, 2006.

[72] H. Li, Z. Cai, and J. Lin, "Separation of catecholamines by microchip electrophoresis with a simple integrated laser-induced fluorescence detector," *Analytica Chimica Acta*, vol. 565, no. 2, pp. 183–189, 2006.

[73] H.-C. Yeh, C. Puleo, T. Lim, Y.-P. Ho, P. Giza, R. Huang, and T.-H. Wang, "A microfluidic-FCS platform for investigation on the dissociation of Sp1-DNA complex by doxorubicin," *Nucleic Acids Research*, vol. 34, no. 21, pp. e144–e152, 2006.

[74] Y. Zhang, J. Bahns, Q. Jin, R. Divan, and L. Chen, "Toward the detection of single virus particle in serum," *Analytical Biochemistry*, vol. 356, no. 2, pp. 161–170, 2006.

[75] C. Hollars, J. Puls, O. Bakajin, B. Olsan, C. Talley, S. Lane, and T. Huser, "Bioassay based on single molecule fluorescence detection in microfluidic channels," *Analytical and Bioanalytical Chemistry*, vol. 385, no. 8, pp. 1384–1388, 2006.

[76] Q. Yan, R. Chen, and J. Cheng, "Highly sensitive fluorescence detection with Hg-lamp and photon counter in microchip capillary electrophoresis," *Analytica Chimica Acta*, vol. 555, no. 2, pp. 246–249, 2006.

[77] S. Gotz and U. Karst, "Wavelength-resolved fluorescence detector for microchip capillary electrophoresis separations," *Sensors and Actuators B-Chemical*, vol. 123, no. 1, pp. 622–627, 2007.

[78] T. Revermann, S. Gotz, and U. Karst, "Quantitative analysis of thiols in consumer products on a microfluidic CE chip with fluorescence detection," *Electrophoresis*, vol. 28, no. 7, pp. 1154–1160, 2007.

[79] S. Gotz, T. Revermann, and U. Karst, "Quantitative on-chip determination of taurine in energy and sports drinks," *Lab on a Chip*, vol. 7, no. 1, pp. 93–97, 2007.

[80] B. Mitra, C. Wilson, L. Que, P. Selvaganapathy, and Y. Gianchandani, "Microfluidic discharge-based optical sources for detection of biochemicals," *Lab on a Chip*, vol. 6, no. 1, pp. 60–65, 2006.

[81] E. Destandau, J. Lefevre, A. Eddine, S. Desportes, M. Jullien, R. Hierle, I. Leray, B. Valeur, and J. Delaire, "A novel microfluidic flow-injection analysis device with fluorescence detection for cation sensing. Application to potassium," *Analytical and Bioanalytical Chemistry*, vol. 387, no. 8, pp. 2627–2632, 2007.

[82] Y. Kim, K. Shin, J. Kang, E. Yang, K. Paek, D. Seo, and B. Ju, "Poly(dimethylsiloxane)-based packaging technique for microchip fluorescence detection system applications," *Journal of Microelectromechanical Systems*, vol. 15, no. 5, pp. 1152–1158, 2006.

[83] O. Hofmann, X. Wang, A. Cornwell, S. Beecher, A. Raja, D. Bradley, A. deMello, and J. deMello, "Monolithically integrated dye-doped PDMS long-pass filters for disposable on-chip fluorescence detection," *Lab on a Chip*, vol. 6, no. 8, pp. 981–987, 2006.

[84] R. Irawan, C. Tay, S. Tjin, and C. Fu, "Compact fluorescence detection using in-fiber microchannels - its potential for lab-on-a-chip applications," *Lab on a Chip*, vol. 6, no. 8, pp. 1095–1098, 2006.

[85] Z. Shen, X. Liu, Z. Long, D. Liu, N. Ye, J. Qin, Z. Dai, and B. Lin, "Parallel analysis of biomolecules on a microfabricated capillary array chip," *Electrophoresis*, vol. 27, no. 5-6, pp. 1084–1092, 2006.

[86] D. Liu, X. Zhou, R. Zhong, N. Ye, G. Chang, W. Xiong, X. Mei, and B. Lin, "Analysis of multiplex PCR fragments with PMMA microchip," *Talanta*, vol. 68, no. 3, pp. 616–622, 2006.

[87] B. Huang, H. Wu, D. Bhaya, A. Grossman, S. Granier, B. Kobilka, and R. Zare, "Counting low-copy number proteins in a single cell," *Science*, vol. 315, no. 5808, pp. 81–84, 2007.

[88] J. Edgar, C. Pabbati, R. Lorenz, M. He, G. Fiorini, and D. Chiu, "Capillary electrophoresis separation in the presence of an immiscible boundary for droplet analysis," *Analytical Chemistry*, vol. 78, no. 19, pp. 6948–6954, 2006.

[89] S. Oh, S. Lee, S. Kenrick, P. Daugherty, and H. Soh, "Microfluidic protein detection through genetically engineered bacterial cells," *Journal of Proteome Research*, vol. 5, no. 12, pp. 3433–3437, 2006.

[90] W. Hellmich, D. Greif, C. Pelargus, D. Anselmetti, and A. Ros, "Improved native UV laser induced fluorescence detection for single cell analysis in poly(dimethylsiloxane) microfluidic devices," *Journal of Chromatography A*, vol. 1130, no. 2, pp. 195–200, 2006.

[91] K. Yea, S. Lee, J. Choo, C. Oh, and S. Lee, "Fast and sensitive analysis of DNA hybridization in a PDMS micro-fluidic channel using fluorescence resonance energy transfer," *Chemical Communications*, no. 14, pp. 1509–1511, 2006.

[92] S. Kim, L. Chen, S. Lee, G. Seong, J. Choo, E. Lee, C. Oh, and S. Lee, "Rapid DNA hybridization analysis using a PDMS microfluidic sensor and a molecular beacon," *Analytical Sciences*, vol. 23, no. 4, pp. 401–405, 2007.

[93] P. Liu, T. Seo, N. Beyor, K. Shin, J. Scherer, and R. Mathies, "Integrated portable polymerase chain reaction-capillary electrophoresis microsystem for rapid forensic short tandem repeat typing," *Analytical Chemistry*, vol. 79, no. 5, pp. 1881–1889, 2007.

[94] D. Pregibon, M. Toner, and P. Doyle, "Multifunctional encoded particles for high-throughput biomolecule analysis," *Science*, vol. 315, no. 5817, pp. 1393–1396, 2007.

[95] F. Huang, C. Liao, and G. Lee, "An integrated microfluidic chip for DNA/RNA amplification, electrophoresis separation and on-line optical detection," *Electrophoresis*, vol. 27, no. 16, pp. 3297–3305, 2006.

[96] K. Yun, D. Lee, H. Kim, and E. Yoon, "A microfluidic chip for measurement of biomolecules using a microbead-based quantum dot fluorescence assay," *Measurement Science & Technology*, vol. 17, no. 12, pp. 3178–3183, 2006.

[97] L. Riegger, M. Grumann, T. Nann, J. Riegler, O. Ehlert, W. Bessler, K. Mittenbuehler, G. Urban, L. Pastewka, T. Brenner, R. Zengerle, and J. Ducree, "Read-out concepts for multiplexed bead-based fluorescence immunoassays on centrifugal microfluidic platforms," *Sensors and Actuators A-Physical*, vol. 126, no. 2, pp. 455–462, 2006.

[98] A. Haes, A. Terray, and G. Collins, "Bead-assisted displacement immunoassay for staphylococcal enterotoxin B on a microchip," *Analytical Chemistry*, vol. 78, no. 24, pp. 8412–8420, 2006.

[99] C. Costin, R. Olund, B. Staggemeier, A. Torgerson, and R. Synovec, "Diffusion coefficient measurement in a microfluidic analyzer using dual-beam microscale-refractive index gradient detection - application to on-chip molecular size determination," *Journal of Chromatography A*, vol. 1013, no. 1-2, pp. 77–91, 2003.

[100] S. Leung, J. Edel, R. Wootton, and A. DeMello, "Continuous real-time bubble monitoring in microchannels using refractive index detection," *Measurement Science & Technology*, vol. 15, no. 1, pp. 290–296, 2004.

[101] H. Shao, D. Kumar, and K. Lear, "Single-cell detection using optofluidic intracavity spectroscopy," *IEEE Sensors Journal*, vol. 6, no. 6, pp. 1543–1550, 2006.

[102] W. Song, X. Zhang, A. Liu, C. Lim, P. Yap, and H. Hosseini, "Refractive index measurement of single living cells using on-chip fabry-perot cavity," *Applied Physics Letters*, vol. 89, no. 20, p. 203901, 2006.

[103] K. Phillips and Q. Cheng, "Recent advances in surface plasmon resonance based techniques for bioanalysis," *Analytical and Bioanalytical Chemistry*, vol. 387, no. 5, pp. 1831–1840, 2007.

[104] G. Quigley, R. Harris, and J. Wilkinson, "Sensitivity enhancement of integrated optical sensors by use of thin high-index films," *Applied Opitcs*, vol. 38, no. 28, pp. 6036–6039, 1999.

[105] R. Heideman and P. Lambeck, "Remote opto-chemical sensing with extreme sensitivity: design, fabrication and performance of a pigtailed integrated optical

phase-modulated mach-zehnder interferometer system," *Sensors and Actuators B-Chemical*, vol. 61, no. 1-3, pp. 100–127, 1999.

[106] F. Blanco, M. Agirregabiria, J. Berganzo, K. Mayora, J. Elizalde, A. Calle, C. Dominguez, and L. Lechuga, "Microfluidic-optical integrated CMOS compatible devices for label-free biochemical sensing," *Journal of Micromechanics and Microengineering*, vol. 16, no. 5, pp. 1006–1016, 2006.

[107] B. Sepulveda, J. del Rio, M. Moreno, F. Blanco, K. Mayora, C. Dominguez, and L. Lechuga, "Optical biosensor microsystems based on the integration of highly sensitive Mach-Zehnder interferometer devices," *Journal of Optics A-Pure and Applied Optics*, vol. 8, no. 7, pp. S561–S566, 2006.

[108] A. Ymeti, J. Kanger, J. Greve, G. Besselink, P. Lambeck, R. Wijn, and R. Heideman, "Integration of microfluidics with a four-channel integrated optical Young interferometer immunosensor," *Biosensors & Bioelectronics*, vol. 20, no. 7, pp. 1417–1421, 2005.

[109] A. Ymeti, J. Greve, P. Lambeck, T. Wink, S. van Hovell, T. Beumer, R. Wijn, R. Heideman, V. Subramaniam, and J. Kanger, "Fast, ultrasensitive virus detection using a Young interferometer sensor," *Nano Letters*, vol. 7, no. 2, pp. 394–397, 2007.

[110] G. Duveneck, A. Abel, M. Bopp, G. Kresbach, and M. Ehrat, "Planar waveguides for ultra-high sensitivity of the analysis of nucleic acids," *Analytica Chimica Acta*, vol. 469, no. 1, pp. 49–61, 2002.

[111] P. Yuen, N. Fontaine, M. Quesada, P. Mazumder, R. Bergman, and E. Mozdy, "Self-referencing a single waveguide grating sensor in a micron-sized deep flow chamber for label-free biomolecular binding assays," *Lab on a Chip*, vol. 5, no. 9, pp. 959–965, 2005.

[112] Y. Sarov, T. Ivanov, K. Ivanova, V. Sarova, I. Capek, and I. Rangelow, "Diffraction under total internal reflection for micro-fluidic analysis," *Applied Physics A-Materials Science & Processing*, vol. 84, no. 1-2, pp. 191–196, 2006.

[113] C. Choi and B. Cunningham, "Single-step fabrication and characterization of photonic crystal biosensors with polymer microfluidic channels," *Lab on a Chip*, vol. 6, no. 10, pp. 1373–1380, 2006.

[114] M. Malmqvist, "Biospecific interaction analysis using biosensor technology," *Nature*, vol. 361, no. 6408, pp. 186–187, 1993.

[115] M. Furuki, J. Kameoka, H. Craighead, and M. Isaacson, "Surface plasmon resonance sensors utilizing microfabricated channels," *Sensors and Actuators B-Chemical*, vol. 79, no. 1, pp. 63–69, 2001.

[116] A. Wheeler, S. Chah, R. Whelan, and R. Zare, "Poly(dimethylsiloxane) microfluidic flow cells for surface plasmon resonance spectroscopy," *Sensors and Actuators B-Chemical*, vol. 98, no. 2-3, pp. 208–214, 2004.

[117] S. Huang, G. Lee, F. Chien, S. Chen, W. Chen, and M. Yang, "A microfluidic system with integrated molecular imprinting polymer films for surface plasmon resonance detection," *Journal of Micromechanics and Microengineering*, vol. 16, no. 7, pp. 1251–1257, 2006.

[118] K. Lei, W. Law, Y. Suen, W. Li, Y. Yam, H. Ho, and S. Kong, "A vortex pump-based optically-transparent microfluidic platform for biotech and medical applications," *Proceedings of the Institutionof Mehcanical Engineers Part H-Journal of Engineering in Medicine*, vol. 221, no. H2, pp. 129–141, 2007.

[119] R. Kurita, Y. Yokota, Y. Sato, F. Mizutani, and O. Niwa, "On-chip enzyme immunoassay of a cardiac marker using a microfluidic device combined with a portable surface plasmon resonance system," *Analytical Chemistry*, vol. 78, no. 15, pp. 5525–5531, 2006.

[120] E. Hecht, *Optics (International Edition)*, 4th ed. Addison Wesley, 2002.

[121] K. Kneipp, H. Kneipp, I. Itzkan, R. Dasari, and M. Feld, "Surface-enhanced Raman scattering and biophysics," *Journal of Physics-Condensed Matter*, vol. 14, no. 18, pp. R597–R624, 2002.

[122] R. Connatser, L. Riddle, and M. Sepaniak, "Metal-polymer nanocomposites for integrated microfluidic separations and surface enhanced Raman spectroscopic detection," *Journal of Separation Science*, vol. 27, no. 17-18, pp. 1545–1550, 2004.

[123] G. L. Liu and L. P. Lee, "Nanowell surface enhanced Raman scattering arrays fabricated by soft-lithography for label-free biomolecular detections in integrated microfluidics," *Applied Physics Letters*, vol. 87, no. 7, p. 074101, 2005.

[124] W. Nirode, G. Devault, and M. Sepaniak, "On-column surface-enhanced Raman spectroscopy detection in capillary electrophoresis using running buffers containing silver colloidal solutions," *Analytical Chemistry*, vol. 72, no. 8, pp. 1866–1871, 2000.

[125] K. Strehle, D. Cialla, P. Rosch, T. Henkel, M. Kohler, and J. Popp, "A reproducible surface-enhanced Raman spectroscopy approach. online SERS measurements in a segmented microfluidic system," *Analytical Chemistry*, vol. 79, no. 4, pp. 1542–1547, 2007.

[126] K. Yea, S. Lee, J. Kyong, J. Choo, E. Lee, S. Joo, and S. Lee, "Ultra-sensitive trace analysis of cyanide water pollutant in a PDMS microfluidic channel using surface-enhanced Raman spectroscopy," *Analyst*, vol. 130, no. 7, pp. 1009–1011, 2005.

[127] T. Park, S. Lee, G. Seong, J. Choo, E. Lee, Y. Kim, W. Ji, S. Hwang, D. Gweon, and S. Lee, "Highly sensitive signal detection of duplex dye-labelled DNA oligonucleotides in a PDMS microfluidic chip: confocal surface-enhanced Raman spectroscopic study," *Lab on a Chip*, vol. 5, no. 4, pp. 437–442, 2005.

[128] D. Lee, S. Lee, G. Seong, J. Choo, E. Lee, D. Gweon, and S. Lee, "Quantitative analysis of methyl parathion pesticides in a polydimethylsiloxane microfluidic channel using confocal surface-enhanced Ramanspectroscopy," *Applied Spectroscopy*, vol. 60, no. 4, pp. 373–377, 2006.

[129] J. Jung, L. Chen, S. Lee, S. Kim, G. Seong, J. Choo, E. Lee, C. Oh, and S. Lee, "Fast and sensitive DNA analysis using changes in the FRET signals of molecular beacons in a PDMS microfluidic channel," *Analytical and Bioanalytical Chemistry*, vol. 387, no. 8, pp. 2609–2615, 2007.

[130] R. Keir, E. Igata, M. Arundell, W. Smith, D. Graham, C. McHugh, and J. Cooper, "SERRS. In situ substrate formation and improved detection using microfluidics," *Analytical Chemistry*, vol. 74, no. 7, pp. 1503–1508, 2002.

[131] F. Docherty, P. Monaghan, R. Keir, D. Graham, W. Smith, and J. Cooper, "The first SERRS multiplexing from labelled oligonucleotides in a microfluidics lab-on-a-chip," *Chemical Communications*, no. 1, pp. 118–119, 2004.

[132] A. Ashkin, J. Dziedzic, J. Bjorkholm, and S. Chu, "Observation of a single-beam gradient force optical trap for dielectric particles," *Optics Letters*, vol. 11, no. 5, pp. 288–290, 1986.

[133] R. Thurn and W. Kiefer, "Raman-microsampling technique applying optical levitation by radiation pressure," *Applied Spectroscopy*, vol. 38, no. 1, pp. 78–83, 1984.

[134] C. Xie, D. Chen, and Y. Li, "Raman sorting and identification of single living micro-organisms with optical tweezers," *Optics Letters*, vol. 30, no. 14, pp. 1800–1802, 2005.

[135] C. Creely, G. Singh, and D. Petrov, "Dual wavelength optical tweezers for confocal Raman spectroscopy," *Optics Communications*, vol. 245, no. 1-6, pp. 465–470, 2005.

[136] G. Rusciano, A. De Luca, A. Sasso, and G. Pesce, "Phase-sensitive detection in Raman tweezers," *Applied Physics Letters*, vol. 89, no. 26, p. 261116, 2006.

[137] R. Gessner, C. Winter, P. Rosch, M. Schmitt, R. Petry, W. Kiefer, M. Lankers, and J. Popp, "Identification of biotic and abiotic particles by using a combination of optical tweezers and in situ Raman spectroscopy," *ChemPhysChem*, vol. 5, no. 8, pp. 1159–1170, 2004.

[138] K. Ramser, K. Logg, M. Goksor, J. Enger, M. Kall, and D. Hanstorp, "Resonance Raman spectroscopy of optically trapped functional erythrocytes," *Journal of Biomedical Optics*, vol. 9, no. 3, pp. 593–600, 2004.

[139] K. Ramser, J. Enger, M. Goksor, D. Hanstorp, K. Logg, and M. Kall, "A microfluidic system enabling Raman measurements of the oxygenation cycle in single optically trapped red blood cells," *Lab on a Chip*, vol. 5, no. 4, pp. 431–436, 2005.

[140] C. Xie and Y. Li, "Raman spectra and optical trapping of highly refractive and nontransparent particles," *Applied Physics Letters*, vol. 81, no. 6, pp. 951–953, 2002.

[141] T. Kitamori, M. Tokeshi, A. Hibara, and K. Sato, "Thermal lens microscopy and microchip chemistry," *Analytical Chemistry*, vol. 76, no. 3, pp. 52A–60A, 2004.

[142] K. Mawatari, M. Tokeshi, and T. Kitamori, "Quantitative detection and fixation of single and multiple gold nanoparticles on a microfluidic chip by thermal lens microscope," *Analytical Sciences*, vol. 22, no. 5, pp. 781–784, 2006.

[143] M. Tokeshi, M. Uchida, A. Hibara, T. Sawada, and T. Kitamori, "Determination of subyoctomole amounts of nonfluorescent molecules using a thermal lens microscope: Subsingle molecule determination," *Analytical Chemistry*, vol. 73, no. 9, pp. 2112–2116, 2001.

[144] Y. Kikutani, H. Hisamoto, M. Tokeshi, and T. Kitamori, "Micro wet analysis system using multi-phase laminar flows in three-dimensional microchannel network," *Lab on a Chip*, vol. 4, no. 4, pp. 328–332, 2004.

[145] A. Smirnova, K. Mawatari, A. Hibara, M. Proskurnin, and T. Kitamori, "Micromultiphase laminar flows for the extraction and detection of carbaryl derivative," *Analytica Chimica Acta*, vol. 558, no. 1-2, pp. 69–74, 2006.

[146] E. Tamaki, A. Hibara, M. Tokeshi, and T. Kitamori, "Tunable thermal lens spectrometry utilizing microchannel-assisted thermal lens spectrometry," *Lab on a Chip*, vol. 5, no. 2, pp. 129–131, 2005.

[147] M. Goto, K. Sato, A. Murakami, M. Tokeshi, and T. Kitamori, "Development of a microchip-based bioassay system using cultured cells," *Analytical Chemistry*, vol. 77, no. 7, pp. 2125–2131, 2005.

[148] S. Hiki, K. Mawatari, A. Hibara, M. Tokeshi, and T. Kitamori, "UV excitation thermal lens microscope for sensitive and nonlabeled detection of nonfluorescent molecules," *Analytical Chemistry*, vol. 78, no. 8, pp. 2859–2863, 2006.

[149] K. Sato, A. Egami, T. Odake, M. Tokeshi, M. Aihara, and T. Kitamori, "Monitoring of intercellular messengers released from neuron networks cultured in a microchip," *Journal of Chromatography A*, vol. 1111, no. 2, pp. 228–232, 2006.

[150] M. Yamauchi, K. Mawatari, A. Hibara, M. Tokeshi, and T. Kitamori, "Circular dichroism thermal lens microscope for sensitive chiral analysis on microchip," *Analytical Chemistry*, vol. 78, no. 8, pp. 2646–2650, 2006.

[151] M. Tokeshi, J. Yamaguchi, A. Hattori, and T. Kitamori, "Thermal lens micro optical systems," *Analytical Chemistry*, vol. 77, no. 2, pp. 626–630, 2005.

[152] M. Yamauchi, M. Tokeshi, J. Yamaguchi, T. Fukuzawa, A. Hattori, A. Hibara, and T. Kitamori, "Miniaturized thermal lens and fluorescence detection system for microchemical chips," *Journal of Chromatography A*, vol. 1106, no. 1-2, pp. 89–93, 2006.

[153] M. Kakuta, H. Takahashi, S. Kazuno, K. Murayama, T. Ueno, and M. Tokeshi, "Development of the microchip-based repeatable immunoassay system for clinical diagnosis," *Measurement Science & Technology*, vol. 17, no. 12, pp. 3189–3194, 2006.

[154] J. Quirino and S. Terabe, "Exceeding 5000-fold concentration of dilute analytes in micellar electrokinetic chromatography," *Science*, vol. 282, no. 5388, pp. 465–468, 1998.

[155] K. Mawatari, Y. Naganuma, and K. Shimoide, "Portable thermal lens spectrometer with focusing system," *Analytical Chemistry*, vol. 77, no. 2, pp. 687–692, 2005.

[156] K. Mawatari and K. Shimoide, "Reflective thermal lens detection device," *Lab on a Chip*, vol. 6, no. 1, pp. 127–130, 2006.

[157] K. Ghaleb and J. Georges, "Photothermal spectrometry for detection in miniaturized systems: relevant features, strategies and recent applications," *Spectrochimica Acta Part A-Molecular and Biomolecular Spectroscopy*, vol. 60, no. 12, pp. 2793–2801, 2004.

[158] K. Ghaleb and J. Georges, "Signal optimisation in cw-laser crossed-beam photothermal spectrometry: influence of the chopping frequency, sample size and flow rate," *Spectrochimica Acta Part A-Molecular and Biomolecular Spectroscopy*, vol. 61, no. 13-14, pp. 2849–2855, 2005.

[159] P. Friis, K. Hoppe, O. Leistiko, K. Mogensen, J. Hubner, and J. Kutter, "Monolithic integration of microfluidic channels and optical waveguides in silica on silicon," *Applied Optics*, vol. 40, no. 34, pp. 6246–6251, 2001.

[160] J. McMullin, H. Qiao, S. Goel, C. Ren, and D. Li, "Integrated optical measurement of microfluid velocity," *Journal of Micromechanics and Microengineering*, vol. 15, no. 10, pp. 1810–1816, 2005.

[161] D. Chang-Yen, R. Eich, and B. Gale, "A monolithic PDMS waveguide system fabricated using soft-lithography techniques," *Journal of Lightwave Technology*, vol. 23, no. 6, pp. 2088–2093, 2005.

[162] K. Mogensen, Y. Kwok, J. Eijkel, N. Petersen, A. Manz, and J. Kutter, "A microfluidic device with an integrated waveguide beam splitter for velocity measurements of flowing particles by Fourier transformation," *Analytical Chemistry*, vol. 75, no. 18, pp. 4931–4936, 2003.

[163] J. Ruano, A. Glidle, A. Cleary, A. Walmsley, J. Aitchison, and J. Cooper, "Design and fabrication of a silica on silicon integrated optical biochip as a fluorescence microarray platform," *Biosensors & Bioelectronics*, vol. 18, no. 2-3, pp. 175–184, 2003.

[164] H. Nishihara, M. Haruna, and T. Suhara, *Optical Integrated Circuits*. McGraw-Hill, 1989.

[165] K. Okamoto, *Fundamentals of Optical Waveguides*, 2nd ed. Academic Press, 2006.

[166] D. Lee, *Electromagnetic Principles of Integrated Optics*. John Wiley & Sons, Inc., 1986.

[167] A. Ghatak and K. Thyagarajan, *Optical Electronics*. Cambridge University Press, 1989.

[168] A. Ghatak and K. Thyagarajan, *An Introduction to Fiber Optics*. Cambridge University Press, 1998.

[169] R. März, *Integrated Optics Design and Modeling*. Artech House, Inc., 1995.

[170] R. Scarmozzino, A. Gopinath, R. Pregla, and S. Helfert, "Numerical techniques for modeling guided-wave photonic devices," *IEEE Journal of Selected Topics in Quantum Electronics*, vol. 6, no. 1, pp. 150–162, 2000.

[171] E. Marcatili, "Dielectric rectangular waveguide and directional coupler for integrated-optics," *Bell System Technical Journal*, no. 48, pp. 2071–2102, 1969.

[172] A. Kumar, K. Thyagarajan, and A. Ghatak, "Analysis of rectangular-core dielectric waveguides - an accurate perturbation approach," *Optics Letters*, vol. 8, no. 1, pp. 63–65, 1983.

[173] K. Chiang, "Analysis of rectangular dielectric wave-guides - effective-index method with built-in perturbation," *Electronics Letters*, vol. 28, no. 4, pp. 388–390, 1992.

[174] C. Ma, H. Zhang, D. Zhang, Z. Cui, and S. Liu, "Effects of trapezoid core cross-sections on transmission characteristics of polymer arrayed waveguide grating multiplexers," *Optics Communications*, vol. 241, no. 4-6, pp. 321–331, 2004.

[175] E. Popescu and S. Song, "Trapezoidal waveguides: first-order propagation equivalence with rectangular waveguides," *Journal of Physics A-Mathematical and Theoretical*, vol. 40, no. 48, pp. 14 555–14 574, 2007.

[176] BeamProp, *BeamProp Version 5.0a User Manual*. RSoft, 2001.

[177] Nufern, "Nufern 630 nm select cut-off single-mode fiber," 13 July 2007.

[178] G. Benazzi, D. Holmes, T. Sun, M. C. Mowlem, and H. Morgan, "Discrimination and analysis of phytoplankton using a microfluidic cytometer," *IET Nanobiotechnology*, vol. 1, no. 6, pp. 94–101, 2007.

[179] D. Marcuse, "Loss analysis of single-mode fiber splices," *Bell System Technical Journal*, vol. 56, no. 5, pp. 703–718, 1977.

[180] K. Suzuki, Y. Hida, T. Shibata, Y. Inoue, H. Takahashi, and K. Okamoto, "Silica-based arrayed-waveguide gratings for the visible wavelength range," *NTT Technical Review*, vol. 4, no. 6, pp. 48–52, 2006.

[181] P. Prasad, *Introduction to Biophotonics*. John Wiley & Sons Inc, 2003.

[182] S. Hsiung, C. Lin, and G. Lee, "A microfabricated capillary electrophoresis chip with multiple buried optical fibers and microfocusing lens for multiwavelength detection," *Electrophoresis*, vol. 26, no. 6, pp. 1122–1129, 2005.

[183] S. Camou, H. Fujita, and T. Fujii, "PDMS 2D optical lens integrated with microfluidic channels: principle and characterization," *Lab on a Chip*, vol. 3, no. 1, pp. 40–45, 2003.

[184] J. Seo and L. Lee, "Disposable integrated microfluidics with self-aligned planar microlenses," *Sensors and Actuators B-Chemical*, vol. 99, no. 2-3, pp. 615–622, 2004.

[185] J. Godin, V. Lien, and Y. Lo, "Demonstration of two-dimensional fluidic lens for integration into microfluidic flow cytometers," *Applied Physics Letters*, vol. 89, no. 6, p. 061106, 2006.

[186] S. Hsiung, C. Lee, and G. Lee, "Microcapillary electrophoresis chips utilizing controllable micro-lens structures and buried optical fibers for on-line optical detection," *Electrophoresis*, vol. 29, no. 9, pp. 1866–1873, 2008.

[187] W. Chang and P. Ashley, "Fresnel lenses in optical-waveguides," *IEEE Journal of Quantum Electronics*, vol. 16, no. 7, pp. 744–754, 1980.

[188] T. Suhara, K. Kobayashi, H. Nishihara, and J. Koyama, "Graded-index Fresnel lenses for integrated optics," *Applied Optics*, vol. 21, no. 11, pp. 1966–1971, 1982.

[189] C. Pitt, S. Reid, S. Reynolds, and J. Skinner, "Waveguiding Fresnel lenses - modeling and fabrication," *Journal of Modern Optics*, vol. 35, no. 6, pp. 1079–1111, 1988.

[190] K. Spaulding and G. Morris, "Achromatic wave-guide lenses," *Applied Optics*, vol. 30, no. 18, pp. 2558–2569, 1991.

[191] H. Hopkins, *Wave Theory of Aberrations*. Clarendon Press, 1950.

[192] P. Mouroulis and J. MacDonald, *Geometrical Optics and Optical Design*. Oxford University Press, 1997.

[193] W. Born and E. Wolf, *Principle of Optics*, 7th ed. Cambridge University Press, 1999.

[194] M. Maesumi, "Parabolic-mirrors, elliptic and hyperbolic lenses," *American Mathematical Monthly*, vol. 99, no. 6, pp. 558–562, 1992.

[195] V. Moreno, J. Roman, and J. Salgueiro, "High efficiency diffractive lenses: Deduction of kinoform profile," *American Journal of Physics*, vol. 65, no. 6, pp. 556–562, 1997.

[196] J. Goodman, *Fourier Optics*, 3rd ed. Roberts & Company Publishers, 2005.

[197] D. Buralli, G. Morris, and J. Rogers, "Optical-performance of holographic kinoforms," *Applied Optics*, vol. 28, no. 5, pp. 976–983, 1989.

[198] L. Hazra, Y. Han, and C. Delisle, "Imaging by zone plates - axial stigmatism at a particular order," *Journal of the Optical society of America A-Optics Image Science and Vision*, vol. 11, no. 10, pp. 2750–2754, 1994.

[199] L. Hazra, O. Meknassi, and C. Delisle, "Zone characteristics of planar kinoform lenses of any specific order for stigmatic imaging between extra-axial conjugate points," *Journal of the Optical Society of America A-Optics Image Science and Vision*, vol. 12, no. 11, pp. 2463–2470, 1995.

[200] D. Faklis and G. Morris, "Spectral properties of multiorder diffractive lenses," *Applied Optics*, vol. 34, no. 14, pp. 2462–2468, 1995.

[201] T. Sales and G. Morris, "Diffractive-refractive behavior of kinoform lenses," *Applied Optics*, vol. 36, no. 1, pp. 253–257, 1997.

[202] L. Solymar and D. Cooke, *Volume Holography and Volume Gratings*. Academic Press Inc., 1981.

[203] F. Pfeiffer, C. David, J. van der Veen, and C. Bergemann, "Nanometer focusing properties of Fresnel zone plates described by dynamical diffraction theory," *Physical Review B*, vol. 73, no. 24, p. 245331, 2006.

[204] S. Yao and D. Thompson, "Chirp-grating lens for guided-wave optics," *Applied Physics Letters*, vol. 33, no. 7, pp. 635–637, 1978.

[205] C. Warren, S. Forouhar, W. Chang, and S. Yao, "Double ion exchanged chirp grating lens in lithium niobate waveguides," *Applied Physics Letters*, vol. 43, no. 5, pp. 424–426, 1983.

[206] L. Lesem, P. Hirsch, and J. Jordan, "The kinoform: A new wavefront reconstruction device," *IBM Journal of Research and Development*, vol. 13, no. 2, pp. 150–155, 1969.

[207] Z. Jaroszewicz, R. Staronski, J. Sochacki, and G. Righini, "Planar Fresnel lens with multiple phase jump," *Pure and Applied Optics*, pp. 667–677, 1994.

[208] M. McGaugh, C. Verber, and R. Kenan, "Modified integrated optic Fresnel lens for waveguide-to-fiber coupling," *Applied Optics*, vol. 34, no. 9, pp. 1562–1568, 1995.

[209] G. Boole, *Calculus of Finite Differences*, 4th ed. New York: Chelsea Publishing Company, 1958.

[210] J. Harvey, A. Krywonos, and D. Bogunovic, "Nonparaxial scalar treatment of sinusoidal phase gratings," *Journal of the Optical Society of America A-Optics Image Science and Vision*, vol. 23, no. 4, pp. 858–865, 2006.

[211] T. Suhara and H. Nishihara, "Integrated-optics components and devices using periodic structures," *IEEE Journal of Quantum Electronics*, vol. 22, no. 6, pp. 845–867, 1986.

[212] H. Nishihara and T. Suhara, "Micro Fresnel lenses," *Progress in Optics*, vol. 24, pp. 1–37, 1987.

[213] L. d'Auria, J. Huignard, A. Roy, and E. Spitz, "Photolithographic fabrication of thin film lenses," *Optics Communications*, vol. 5, no. 4, pp. 232–235, 1972.

[214] T. Vu, J. Norris, and C. Tsai, "Formation of negative-index-change wave-guide lenses in $LiNbO_3$ by using ion milling," *Optics Letters*, vol. 13, no. 12, pp. 1141–1143, 1988.

[215] G. Hatakoshi and S. Tanaka, "Grating lenses for integrated-optics," *Optics Letters*, vol. 2, no. 6, pp. 142–144, 1978.

[216] K. Spaulding and G. Morris, "Achromatic wave-guide couplers," *Journal of Lightwave Technology*, vol. 10, no. 10, pp. 1513–1518, 1992.

[217] S. Winnall, A. Lindsay, M. Austin, J. Canning, and A. Mitchell, "A microwave channelizer and spectroscope based on an integrated optical Bragg-grating Fabry-Perot and integrated hybrid Fresnel lens system," *IEEE Transactions on Microwave Theory and Techniques*, vol. 54, no. 2, pp. 868–872, 2006.

[218] T. Suhara, S. Fujiwara, and H. Nishihara, "Proton-exchanged Fresnel lenses in Ti-$LiNO_3$ waveguides," *Applied Optics*, vol. 25, no. 19, pp. 3379–3383, 1986.

[219] J. Albert, J. Huttunen, and J. Saarinen, "Planar Fresnel lens photoimprinted in a germanium-doped silica optical waveguide," *Optics Letters*, vol. 20, no. 10, pp. 1136–1138, 1995.

[220] Y. Hibino, "Recent advances in high-density and large-scale AWG multi/demultiplexers with higher index-contrast silica-based PLCs," *IEEE Journal of Selected Topics in Quantum Electronics*, vol. 8, no. 6, pp. 1090–1101, 2002.

[221] J. S. Yu, J. Y. Moon, S. M. Choi, and Y. T. Lee, "Fabrication of 1×8 multimode-interference optical power splitter based on InP using CH_4/H_2 reactive ion etching," *Japanese Journal of Applied Physics Part 1-Regular Papers Short Notes & Review Papers*, vol. 40, no. 2A, pp. 634–639, 2001.

[222] M. Smit and C. van Dam, "PHASAR-based WDM-devices: Principles, design and applications," *IEEE Journal of Selected Topics in Quantum Electronics*, vol. 2, no. 2, pp. 236–250, 1996.

[223] H. Takahashi, K. Oda, H. Toba, and Y. Inoue, "Transmission characteristics of arrayed-wave-guide N × N wavelength multiplexer," *Journal of Lightwave Technology*, vol. 13, no. 3, pp. 447–455, 1995.

[224] D. Wang, G. Jin, Y. Yan, and M. Wu, "Aberration theory of arrayed waveguide grating," *Journal of Lightwave Technology*, vol. 19, no. 2, pp. 279–284, 2001.

[225] R. März and C. Cremer, "On the theory of planar spectrographs," *Journal of Lightwave Technology*, vol. 10, no. 12, pp. 2017–2022, 1992.

[226] S. Lu, C. Yang, Y. Yan, G. Jin, Z. Zhou, W. Wong, and E. Pun, "Design and fabrication of a polymeric flat focal field arrayed waveguide grating," *Optics Express*, vol. 13, no. 25, pp. 9982–9994, 2005.

[227] Y. Komai, H. Nagano, K. Kodate, K. Okamoto, and T. Kamiya, "Application of arrayed-waveguide grating to compact spectroscopic sensors," *Japanese Journal of Applied Physics Part 1 - Regular Papers Short Notes & Review Papers*, vol. 43, no. 8B, pp. 5795–5799, 2004.

[228] Y. Komai, H. Nagano, K. Okamoto, and K. Kodate, "Compact spectroscopic sensor using a visible arrayed waveguide grating," *Japanese Journal of Applied Physics*, vol. 45, no. 8B, pp. 6742–6749, 2006.

[229] K. Kodate and Y. Komai, "Compact spectroscopic sensor using an arrayed waveguide grating," *Journal of Optics A-Pure and Applied Optics*, vol. 10, no. 4, p. 044011, 2008.

[230] T. Saida, T. Shibata, M. Ishii, and H. Takahashi, "Integrated optical tweezers using arrayed waveguide grating," *2005 Conference on Lasers & Electro-Optics (CLEO), Vols 1-3*, pp. 556–558 2350, 2005.

[231] H. Talbot, "Facts relating to optical science," *Philisophical Magazine*, vol. 9, pp. 289–290, 1836.

[232] L. B. Soldano and E. C. M. Pennings, "Optical multimode interference devices based on self-imaging - principles and applications," *Journal of Lightwave Technology*, vol. 13, no. 4, pp. 615–627, 1995.

[233] B. West and D. Plant, "Optimization of non-ideal multimode interference devices," *Optics Communications*, vol. 279, no. 1, pp. 72–78, 2007.

[234] K. Kribich, R. Copperwhite, H. Barry, B. Kolodziejczyk, J. Sabattie, K. O'Dwyer, and B. MacCraith, "Novel chemical sensor/biosensor platform based on optical multimode interference (MMI) couplers," *Sensors and Actuators B - Chemical*, vol. 107, no. 1, pp. 188–192, 2005.

[235] T. Mazingue, R. Kribich, P. Etienne, and Y. Moreau, "Simulations of refractive index variation in a multimode interference coupler: Application to gas sensing," *Optics Communications*, vol. 278, no. 2, pp. 312–316, 2007.

[236] A. Cleary, S. Garcia-Blanco, A. Glidle, J. S. Aitchison, P. Laybourn, and J. M. Cooper, "An integrated fluorescence array as a platform for lab-on-a-chip technology using multimode interference splitters," *IEEE Sensors Journal*, vol. 5, no. 6, pp. 1315–1320, 2005.

[237] C. Kaalund and Z. Jin, "Novel multimode interference devices for low index contrast materials systems featuring deeply etched air trenches," *Optics Communications*, vol. 250, no. 4-6, pp. 292–296, 2005.

[238] J. Hong and S. Lee, "1×2 wavelength multiplexer with high transmittances using extraneous self-imaging phenomenon," *Journal of Lightwave Technology*, vol. 25, no. 5, pp. 1264–1268, 2007.

[239] J. Hong, S. Lee, and S. Lee, "Extraneous self-imaging phenomenon with weak-guiding condition," *Optics Letters*, vol. 32, no. 10, pp. 1311–1313, 2007.

[240] A. Piruska, I. Nikcevic, S. Lee, C. Ahn, W. Heineman, P. Limbach, and C. Seliskar, "The autofluorescence of plastic materials and chips measured under laser irradiation," *Lab on a Chip*, vol. 5, no. 12, pp. 1348–1354, 2005.

[241] E. Dianov and V. Mashinsky, "Germania-based core optical fibers," *Journal of Lightwave Technology*, vol. 23, no. 11, pp. 3500–3508, 2005.

[242] M. Kobayashi and H. Terui, "Refractive-index and attenuation characteristics of SiO_2-Ta_2O_5 optical-waveguide film," *Applied Optics*, vol. 22, no. 19, pp. 3121–3127, 1983.

[243] M. Cevro, "Ion-beam sputtering of $(Ta_2O_5)_{(x)}$-$(SiO_2)_{(1-x)}$ composite thin-films," *Thin Solid Films*, vol. 258, no. 1-2, pp. 91–103, 1995.

[244] C. Ho, K. Pita, N. Ngo, and C. Kam, "Optical functions of (x)GeO_2:(1-x)SiO_2 films determined by multi-sample and multi-angle spectroscopic ellipsometry," *Optics Express*, vol. 13, no. 3, pp. 1049–1054, 2005.

[245] S. Chu, W. Pan, S. Sato, B. Little, T. Kaneko, and Y. Kokubun, "ARROW-type vertical coupler filter: Design and fabrication," *Journal of Lightwave Technology*, vol. 17, no. 4, pp. 652–658, 1999.

[246] A. Ros, W. Hellmich, T. Duong, and D. Anselmetti, "Towards single molecule analysis in PDMS microdevices: from the detection of ultra low dye concentrations to single DNA molecule studies," *Journal of Biotechnology*, vol. 112, no. 1-2, pp. 65–72, 2004.

[247] K. Miyaki, Y. L. Guo, T. Shimosaka, T. Nakagama, H. Nakajima, and K. Uchiyama, "Fabrication of an integrated PDMS microchip incorporating an LED-induced fluorescence device," *Analytical and Bioanalytical Chemistry*, vol. 382, no. 3, pp. 810–816, 2005.

[248] H. Becker and L. E. Locascio, "Polymer microfluidic devices," *Talanta*, vol. 56, no. 2, pp. 267–287, 2002.

[249] E. Quartarone, P. Mustarelli, F. Marabelli, M. Battagliarin, and S. Turato, "GeO_2-doped SiO_2 sputtered thin films: Microstructure, stoichiometry, and optical properties," *Journal of Vacuum Science & Technology A*, vol. 22, no. 6, pp. 2234–2238, 2004.

[250] S. Sebastiani, S. Berneschi, M. Brenci, G. Conti, S. Pell, and G. Righini, "Simple approach to calculate the refractive index profile of ion-exchanged waveguides," *Optical Engineering*, vol. 44, no. 5, p. 054602, 2005.

[251] M. Madou, *Fundamentals of Microfabrication: The Science of Miniaturization*, 2nd ed. CRC Press Inc.,U.S, 2002.

[252] P. Tien and R. Ulrich, "Theory of prism-film coupler and thin-film light guides," *Journal of the Optical Society of America*, vol. 60, no. 10, pp. 1325–1337, 1970.

[253] I. Hodgkinson and Q.-H. Wu, *Birefringent Thin Films and Polarizing Elements*. World Scientific Publishing Co Pte Ltd, 1998.

[254] H. Tompkins, *A User's Guide to Ellipsometry*. Dover, 2006.

[255] J. Park, N. Lee, J. Lee, J. Park, and H. Park, "Deep dry etching of borosilicate glass using SF_6 and SF_6/Ar inductively coupled plasmas," *Microelectronic Engineering*, vol. 82, no. 2, pp. 119–128, 2005.

[256] L. Li, T. Abe, and M. Esashi, "Smooth surface glass etching by deep reactive ion etching with SF_6 and Xe gases," *Journal of Vacuum Science & Technology B*, vol. 21, no. 6, pp. 2545–2549, 2003.

[257] T. Ichiki, Y. Sugiyama, T. Ujiie, and Y. Horiike, "Deep dry etching of borosilicate glass using fluorine-based high-density plasmas for microelectromechanical system fabrication," *Journal of Vacuum Science & Technology B*, vol. 21, no. 5, pp. 2188–2192, 2003.

[258] I. Fatadin, D. Ives, and M. Wicks, "Accurate magnified near-field measurement of optical waveguides using a calibrated CCD camera," *Journal of Lightwave Technology*, vol. 24, no. 12, pp. 5067–5074, 2006.

[259] H. Lefevre, "Single-mode fiber fractional wave devices and polarization controllers," *Electronics Letters*, vol. 16, no. 20, pp. 778–780, 1980.

[260] S. Janz, P. Cheben, H. Dayan, and R. Deakos, "Measurement of birefringence in thin-film waveguides by Rayleigh scattering," *Optics Letters*, vol. 28, no. 19, pp. 1778–1780, 2003.

[261] S. Reyntjens and R. Puers, "A review of focused ion beam applications in microsystem technology," *Journal of Micromechanics and Microengineering*, vol. 11, no. 4, pp. 287–300, 2001.

[262] Q. Wang, J. Lu, and S. L. He, "Optimal design of a multimode interference coupler using a genetic algorithm," *Optics Communications*, vol. 209, no. 1-3, pp. 131–136, 2002.

[263] B. R. West and S. Honkanen, "MMI devices with weak guiding designed in three dimensions using a genetic algorithm," *Optics Express*, vol. 12, no. 12, pp. 2716–2722, 2004.

[264] J. Marques-Hueso, L. Sanchis, B. Cluzel, F. de Fornel, and J. P. Martinez-Pastor, "Genetic algorithm designed silicon integrated photonic lens operating at 1550 nm," *Applied Physics Letters*, vol. 97, no. 7, p. 071115, 2010.

[265] Y. B. Lin, N. Rahmanian, S. Kim, G. P. Nordin, C. Topping, D. W. Smith, and J. Ballato, "Ultracompact AWG using air-trench bends with perfluorocyclobutyl polymer waveguides," *Journal of Lightwave Technology*, vol. 26, no. 17-20, pp. 3062–3070, 2008.

[266] M. Blahut and D. Kasprzak, "Gradient index multimode interference structures - technology and applications," *Acta Physica Polonica A*, vol. 116, no. 3, pp. 257–260, 2009.

[267] B. Buchold and E. Voges, "Polarisation insensitive arrayed-waveguide grating multiplexers with ion-exchanged waveguides in glass," *Electronics Letters*, vol. 32, no. 24, pp. 2248–2250, 1996.

[268] P. Madasamy, B. R. West, M. M. Morrell, D. F. Geraghty, S. Honkanen, and N. Peyghambarian, "Buried ion-exchanged glass waveguides: burial-depth dependence on waveguide width," *Optics Letters*, vol. 28, no. 13, pp. 1132–1134, 2003.

[269] C. Holmes, H. E. Major, J. C. Gates, C. B. E. Gawith, and P. G. R. Smith, "Period adapted bragg mirror multimode interference device," *2009 Conference on Lasers and Electro-Optics and Quantum Electronics and Laser Science Conference (CLEO/QELS 2009), Vols 1-5*, pp. 2865–2866, 2009.

[270] W. Watanabe, Y. Note, and K. Itoh, "Fabrication of multimode interference waveguides in glass by use of a femtosecond laser," *Optics Letters*, vol. 30, no. 21, pp. 2888–2890, 2005.

[271] D. Blömer, A. Szameit, F. Dreisow, T. Schreiber, S. Nolte, and A. Tünnermann, "Nonlinear refractive index of fs-laser-written waveguides in fused silica," *Optics Express*, vol. 14, no. 6, pp. 2151–2157, 2006.

[272] A. Yehia and D. Khalil, "Design of a compact three-dimensional multimode interference phased array structures (3-D MMI PHASAR) for DWDM applications," *IEEE Journal of Selected Topics in Quantum Electronics*, vol. 11, no. 2, pp. 444–451, 2005.

[273] D. Khalil and A. Yehia, "Two-dimensional multimode interference in integrated optical structures," *Journal of Optics A-Pure and Applied Optics*, vol. 6, no. 1, pp. 137–145, 2004.

[274] H. Chen and D. T. K. Tong, "Two-dimensional symmetric multimode interferences in silicon square waveguides," *IEEE Photonics Technology Letters*, vol. 17, no. 4, pp. 801–803, 2005.

[275] R. Bernini, E. De Nuccio, A. Minardo, L. Zeni, and P. M. Sarro, "2-D MMI devices based on integrated hollow ARROW waveguides," *IEEE Journal of Selected Topics in Quantum Electronics*, vol. 13, no. 2, pp. 194–201, 2007.

[276] S. M. Garner, S. S. Lee, V. Chuyanov, A. T. Chen, A. Yacoubian, W. H. Steier, and L. R. Dalton, "Three-dimensional integrated optics using polymers," *IEEE Journal of Quantum Electronics*, vol. 35, no. 8, pp. 1146–1155, 1999.

[277] S. Nolte, M. Will, J. Burghoff, and A. Tuennermann, "Femtosecond laser writing of waveguides in glass: A new way to 3D integrated," *Glass Science and Technology*, vol. 76, pp. 23–28, 2003.

[278] W. Watanabe, S. Sowa, T. Tamaki, K. Itoh, and J. Nishii, "Three-dimensional waveguides fabricated in poly(methyl methacrylate) by a femtosecond laser," *Japanese Journal of Applied Physics Part 2-Letters & Express Letters*, vol. 45, no. 29-32, pp. L765–L767, 2006.

[279] A. C. Sullivan, M. W. Grabowski, and R. R. McLeod, "Three-dimensional direct-write lithography into photopolymer," *Applied Optics*, vol. 46, no. 3, pp. 295–301, 2007.